A STUDY OF THE SENSITIVITY OF COASTAL OCEAN MODELS TO VERTICAL MIXING

by

MARCIA T. HSU

(Under the Direction of Daniela Di Iorio)

ABSTRACT

The evolution of buoyant plumes in the coastal ocean is intimately related to the vertical mixing within the plumes. The sensitivity of three mixing parameterizations used to approximate the vertical viscosity and diffusivity - the constant scheme, Mellor-Yamada Level 2.5, and the Pacanowski and Philander scheme - was investigated in an idealized coastal ocean model. Two types of coastal current systems were first investigated with variations in background viscosity/diffusivity magnitude, and then subjected to variations in tidal forcing. The effects of the schemes were examined using parameters that provided a quantitative description of the plume; these were the downshelf, upshelf, and across-shelf distances, the depth, and the integrated horizontal and vertical salt fluxes. Results from this study revealed that depending on the user-defined background viscosity/diffusivity, type of plume, and amplitude of tide, the choice of vertical mixing scheme can have a measurable effect on the behavior of the plume.

INDEX WORDS: vertical mixing, vertical mixing parameterizations, modeling, ECOM3d, coastal current, surface-advected plume, bottom-advected plume, buoyancy forcing, tidal forcing, stratification, destratification

A STUDY OF THE SENSITIVY OF COASTAL OCEAN MODELS TO VERTICAL MIXING

by

MARCIA T. HSU

B.S., The University of Georgia, 2005

A Thesis Submitted to the Graduate Faculty of The University of Georgia in Partial Fulfillment of the Requirements for the Degree

MASTER OF SCIENCE

ATHENS, GEORGIA

2008

A STUDY OF THE SENSITIVITY OF COASTAL OCEAN MODELS TO VERTICAL MIXING

by

MARCIA T. HSU

Major Professor: Daniela Di Iorio

Committee: Charles Tilburg
Adrian Burd

Electronic Version Approved:

Maureen Grasso
Dean of the Graduate School
The University of Georgia
August 2008

DEDICATION

To my blood, sweat, and tears.

ACKNOWLEDGEMENTS

I would like to thank my committee members, Dr. Charles Tilburg, Dr. Daniela Di Iorio, and Dr. Adrian Burd for all their wonderful advice, support, and help on this project. This has been an incredible learning experience.

Thank you, Georgia Sea Grant and NSF for funding my project, and to the University of Delaware for housing the two-processor Sun Blade 2000 used to run the ECOM3d model.

Also, thanks to the faculty, staff, and my friends in University of Georgia's Marine Sciences department for departmental, intellectual, and moral support. Thanks to Lanny Miller for all the help on this project and all of its related presentations. Thanks to Jennie Seay, Heather Reader, Jorn Lakowski, Christine Hladik, Sylvia Schaefer, and Mr. Dobbs for intellectual advice and entertainment.

Finally and most importantly, I would like to give a special thanks to my parents and Teresa for all their support and encouragement for the past three years.

TABLE OF CONTENTS

LIST OF TABLES

Page

LIST OF FIGURES

CHAPTER 1

INTRODUCTION

1.1 Background

River plumes and their subsequent coastal current systems play a major role in the across-shelf transport of land and river-borne materials, such as nutrients, larvae, and pollutants. The transport behaviors of these materials are essential determinates of the condition of the coastal environment. Nutrients transported by rivers into the ambient ocean sustain the development of coastal ecosystems, resulting in proliferate productivity near the coast (Libes 1992). Larvae, due to their lack of mobility, rely on physical coastal transport processes for survival, creating a strong correlation between the adult population size and the transport of larvae (Epifanio and Garvine 2001). A significant amount of dissolved and particulate pollutants originate from rivers, and the export of these contaminants through the water column is related to the coastal processes that exist (e.g. Harms et al. 2000).

The dynamics responsible for the movement of water within coastal systems are well understood. In the absence of winds or other forcings, the buoyant water moves out of the river or estuary, turns anticyclonically, due to the influence of the Coriolis effect, and moves downshelf in geostrophic balance. The coastal current system, consists of two parts, an anticyclonic flowing bulge and a downstream coastal current. An example of this coastal system is the Delaware Coastal Current, seen in Figure 1.1.

The main mechanisms for material transport within the current systems are advection and mixing. Studies have shown that nutrient, sediment, and larval movement in or out of the estuaries follow the flow and mixing of the buoyant waters (Kourafalou et al. 1996a, Epifanio and Garvine 2001, Tilburg et al. 2006, Childs et al. 2002). While the effects of advection on the coastal system can be empirically analyzed and calculated using the derived velocity field, mixing is much more complex due to its irregular, multiple-scale eddies that create an exchange of properties. A few of the major mechanisms responsible for mixing freshwater into the ambient ocean water are direct stirring from winds, Ekman circulation, instabilities in the flow field, and tidal mixing. The speed, pathway, and distance which materials and organisms travel in the coastal current system are all influenced by the amount of turbulence and the mixing processes encountered.

The lack of sufficient mixing in a coastal plume can have severe consequences for the coastal environment, shown in Figure 1.2. The northern coastal region of the Gulf of Mexico experiences extreme seasonal hypoxia due to the combination of strong stratification and large inorganic nitrogen input during the summer months of higher freshwater discharge from the Mississippi River into the region (Childs et al. 2002). The increased nitrogen load dramatically enhances biological productivity, increasing the sinking flux of organic matter for bacterial respiration; this creates a large oxygen depletion in the water column. Because of the strong stratification, mixing between the layers is suppressed, and oxygen in the lower layer cannot be replenished. Therefore, a lower layer hypoxic, dead zone is created, suffocating non-motile organisms (Feber 2001).

Mixing is a function of the stratification and the vertical shear in the water column (Dyer 1997). The Richardson number, *Ri*, is often used to describe the stability of the environment and the mixing present. This number is expressed as the ratio of the magnitude of stratification to the magnitude of vertical shear:

$$Ri = \frac{-\frac{g}{\rho}\frac{\partial\rho}{\partial z}}{\left(\frac{\partial U}{\partial z}\right)^2 + \left(\frac{\partial V}{\partial z}\right)^2} \tag{1.1}$$

where g is the gravitational acceleration, ρ is the density, U and V are mean horizontal velocities, and z is the vertical component of the water column. A Ri value above the critical value of 0.25 indicates the likelihood of the presence of entrainment in the water column, where mixing only exists in one direction; denser and saltier water moves into the upper level freshwater region (Dyer 1997). However, when Ri is less than 0.25, Kelvin-Helmholtz instabilities may be present, and the region is dominated by shear, indicating that turbulent mixing is present in the area (Dyer 1997). This type of mixing is more efficient at overturning and mixing the saltier water and freshwater through the equal volume exchange of the differing waters (Dyer 1997). This 0.25 critical Ri value represents an energy ratio where the buoyancy term maintains potential energy while vertical shear maintains kinetic energy that must oppose the stratification (Cushman-Roisin 1994). Therefore, if there is enough vertical shear, meaning the potential energy to kinetic energy ratio is less than 0.25, this stratification may be destroyed and mixed by the vertical shear.

Tides can greatly influence the mixing present in the water column. Tides are shallow water waves, and the tidal wave properties change with variations in water depth. As the wave moves into areas of shallow water, the tidal amplitude will increase and the wave speed will decrease due to friction and the conservation of energy. Tides are barotropically forced, where higher tidal amplitudes create a larger pressure gradient and faster velocities that are decreased by bottom friction. Thus, a vertically sheared environment is created, resulting in enhanced vertical mixing (Garvine 1999), which is frequently described as tidal stirring; thus, tidal stirring is defined as the mixing directly produced from tidal forcing and bottom friction. With an increase in vertical mixing, higher vertical eddy viscosity (which will be defined later) values can be found near the bottom and can cause the buoyant outflow to expand to the bottom topography (Guo and Valle-Levinson 2007).

Tides alter coastal current stratification, and can weaken the overall stratification of the system and/or induce periodic stratification corresponding to the tidal flow (Guo and Valle-Levinson 2007, Simpson 1997, Simpson and Souza 1995, Simpson et al. 1990). Tidal stirring occurs during both ebb and flood currents due to the continual presence of bottom friction created vertical shear, where the mixing opposes the stratification on ebb through the sheared mixing and helps destratify the water column on flood, enhancing mixing (Simpson et al. 1990). Changes in the vertical shear from tidal velocities may also create mixing events. Sanders and Garvine (2001) showed that near the end of ebb tide within the Delaware plume, vertical shear can reach a maximum, where velocities are slower and begin changing to slack at depth, and the Richardson number decreases below 0.25, resulting in a mixing event with a duration of a few hours. Therefore, maximum differences in vertical shear from the change in tidal acceleration may play a role in increased mixing.

Mixing may also be generated through a special case of tidal forcing, called tidal straining. This phenomenon has been observed in regions of freshwater influences such as the Rhine River and Liverpool Bay (Simpson and Souza 1995, Simpson et al. 1990) in which the effects of tides and freshwater flow result in extended mixing. Tidal straining may be described in terms of the baroclinic forcing and the resulting turbulent mixing when interacting with the barotropic driven flow. During ebb tide, the baroclinic and barotropic flows induce a stratified environment with less turbulent mixing, where the density gradient is strained from enhanced stratification; surface freshwater moves over denser water at the bottom. However, during flood tide, ‘overstraining’ of the system occurs; denser water is pushed over freshwater creating an unstable situation. Thus, the combination of convective mixing from the unstable water column and the tidal stirring created from tidal forcing effectively destratifies the water column. The competition between the buoyancy forcing and the tidal forcing is known to induce periodic stratification on ebb and enhanced mixing on short timescales during flood for tidal straining (Simpson et al. 2005, Simpson 1997, Simpson and Souza 1995). Simpson et al. (1990) developed a criterion to determine the occurrence of Strain-Induced Periodic Stratification (SIPS) that was reformulated into a horizontal Richardson number by Stacey et al. (2001), calculated in the offshore direction as,

$$Ri_y = \frac{g\beta\Gamma(h_1)^2}{v_*} \tag{1.2}$$

where β is the saline expansivity calculated from the equation of state, $\Gamma \sim (\partial s/\partial y)$, s is the salinity, h_1 is the depth, and v_* is the friction velocity (calculated as the square root of the momentum stress terms, discussed later). The horizontal Richardson number describes the interaction of shear, stratification, and mixing in the estuary. A $Ri_y > 1$ indicates the increase in stratification and shear with the decrease of mixing, thus, increasing the baroclinic flow of the system, with the largest stratification is usually found near the end of ebb tide. A value < 1 indicates destratification of the water column, where convective mixing combined with tidal stirring dominates the system. Stacey et al. (2001) used a threshold value of 3 on ebbing tide for their observations from the northern San Francisco Bay area, above which, to describe the times in which the estuary was dominated by stratification and shear.

The amount of mixing present heavily affects the overall shape of the coastal current plume. Kourafalou et al. (1996a) used a numerical model to conclude that the most influential parameters determining the shape of the plume were the freshwater discharge rate, the depth of the receiving basin, and the horizontal and vertical eddy viscosity/diffusivity. They found that increased freshwater discharge rates create higher stratification which suppresses mixing and cause the plume to extend farther and faster downshelf. However, extremely high freshwater discharge rates can result in the instability of the coastal current and episodic mixing events. Additionally, they discovered that the depth of the coastal ocean is directly related to the amount of mixing within the region. Shallow bottom depths increase vertical mixing in the coastal system when the Ekman depth is greater than the bottom. Of particular importance were the mixing terms. Kourafalou et al. (1996a) found that increased horizontal eddy viscosity causes an increase in material exchange across horizontal gradients in the coastal current while increased vertical eddy viscosity causes plumes to deepen and slow down the widening of the coastal system across-shelf. Larger values of these parameters decreased the meandering behavior of the coastal current, which has been noted as an indication of current baroclinic instability.

Consequently, a better understanding of mixing is necessary to gain insight into the dynamics of coastal current systems. Mixing transfers mass, momentum, and heat in a flow of three-dimensional rotational eddies and is a direct consequence of turbulence. Wind stress, tides, internal waves, shear, and radiative heating are a few catalysts for turbulent flow and mixing. Turbulent flow is characterized by diffusion, dissipation, and random movement (Tennekes and Lumley 1972). Diffusion is the property that moves energy and mass from areas of higher concentrations to areas of lower concentrations. The diffusive property of turbulence energy is important for the transfer and continuance of the turbulent motions through the water. Dissipation is the decay of turbulence. Turbulent energy continuously dissipates as it is lost to work done by molecular viscosity to increase the internal energy of the fluid. If the source of the turbulent motions disappears, turbulence eventually dissipates into heat and is eliminated

(Tennekes and Lumley 1972). The random movement of the flow field creates problems for the investigation of turbulence and has hindered a detailed explanation of turbulent behavior. Turbulence is typically represented by the total energy, the mean turbulent energy, or the turbulent kinetic energy (TKE), of the system (Tennekes and Lumley 1972). The calculation of these energies in any given flow field is difficult, and their estimation relies on a large number of different relationships and assumptions, depending on the method of investigation, either observational or computational.

1.2 Purpose and importance of investigation

This investigation aims to improve the understanding of the relationship between mixing schemes within numerical models and the mixing of the coastal current system. Most models separate parameterizing methods for the horizontal and vertical mixing in coastal waters since horizontal scales are typically much larger than vertical scales. Horizontal mixing has been widely parameterized with the use of the Smagorinsky (1963) scheme, which solves for horizontal diffusivity using horizontal shear and has been shown to produce generally effective results (used in Whitney and Garvine 2006, Tilburg et al. 2006). However, a reliable and universally accepted parameterization scheme to calculate vertical mixing is nonexistent. This study compares three well-known turbulence closure schemes in an attempt to examine the behavior of each sub-model to changes in physical parameters.

In modeling, the accuracy of calculating the amount of mixing in a coastal current system is extremely important, since the resulting plume structure depends on the mixing. The dimensions of the freshwater plume are affected by the amount of water mixed. For example, in an upwelling situation where plumes are expected to be thin, an underestimation of mixing could lead to a modeled plume that is thicker than expected. A second consequence is the result of inaccurate calculation of particle path and transport distances due to miscalculations in velocities.

The closure scheme can also affect the mixing outcome of the coastal system. In a directed study of two different turbulence closure schemes, Chapman (2002) demonstrated that coastal environments, more specifically, coastal shelfbreak fronts, are highly dependent on the mixing schemes applied. The investigation concluded that while coastal features, such as the presence of a plume front and the location of associated velocities, were present when using both vertical mixing schemes, they differed in frontal spatial area and in the magnitude of mixing. Figure 1.3 is from Chapman (2002) demonstrating the differences in frontal structure and velocity magnitudes between the two parameterizations, where u is the alongshelf velocities with positive values out of the page drawn with solid contours, v is the across-shelf velocities with positive values moving offshore, and w is the vertical velocities with positive values moving upwards. The negative velocity values are indicated by dotted contours, and the front is identified by the dashed lines. The graphs on the left show the constant scheme compared to the second-order parameterization scheme graphs on the right. In these graphs, the second-order scheme results in larger upward velocities on the shoreward edge of the plume caused by the narrow front with stronger horizontal gradients in the u and v velocities to create a large vertical shear to drive the circulation in the front, where mixing is then focused near the surface. The constant scheme however, has weaker horizontal gradients creating vertical shear and upwards motion and also a prominent reversal of flow in the across-shelf direction at the bottom. Chapman (2002) states that weak reversal is also seen in the second-order scheme, but due to the selected contour ranges, this is not present in the figures. Therefore, using constant viscosity and diffusivity produced stronger mixing near the bottom and a wider front while the use of a second-order turbulence closure scheme resulted in weaker mixing near the bottom and a narrower front (Chapman 2002). The difference in the results show that coastal regions are sensitive to the closure scheme chosen for the model (Chapman 2002).

Because the selected turbulence closure scheme can heavily influence the resulting coastal flow field, a number of studies have compared turbulence closure schemes in coastal environments (i.e. Burchard et al. 1998, Durski et al. 2004, Umlauf and Burchard 2005, Wijesekera et al. 2003). Many authors have compared specific closure schemes to observational data. Stacey et al. (1999) obtained ADCP data for the northern San Francisco Bay and compared his dataset to a commonly used closure scheme. Li et al. (2005) compared the results of four turbulent mixing schemes to two-year measurements of the Chesapeake Bay estuary. Tilburg et al. (2007) examined the Delaware River plume during an upwelling event first using Rhodamine dye and then comparing the mixing observations to model output. These studies showed that model predictions are comparable to observational data, but differences to observational data still persist. In addition, variations within mixing parameterizations or the use of different parameterizations can affect the resulting coastal environment, causing the model to result differently from observation.

Research has also been done on turbulence closure schemes in idealized environments. Kourafalou et al (1996a) and Garvine (1999) briefly examined the effects of vertical eddy viscosity/diffusivity on coastal current systems. Hetland (2005) used a model with a salinity coordinate system to study the plume mixing caused by wind stress when using two different turbulence closure schemes derived from the same method. Davies and Xing (1999) examined two length scale based turbulence submodels and the constant scheme when subjected to changes in depth and magnitudes of viscosity/diffusivity using an idealized model with salinity, latitudinal, and discharge properties of the Ebro River. These studies have shown that changing environmental variables, such as the amount of mixing, mixing scheme, and bottom depth, can influence the resulting freshwater plume behavior.

This study expands on the above previous work by focusing on two different types of coastal current systems and using a variety of schemes that are either empirically or numerically based, allowing for a broader scope for comparison. Two scenarios, one with only buoyancy forcing and the other with buoyancy forcing and tides, are then investigated to determine the effects of the different schemes on an idealized coastal environment. The plume growth is quantitatively and qualitatively compared across the mixing parameterizations in order to analyze the discrepancies between the mixing produced from each scheme. The purpose of this investigation is not to determine the best turbulence scheme, but instead to examine the effects of different vertical mixing schemes. The goal of this study is to answer, how does an idealized coastal ocean respond when subjected to different vertical mixing calculations?

1.3 Thesis outline

The next chapter, chapter 2, focuses on the model used for this study, going into detail about the different submodels and how they are calculated within the model. Next, the three mixing schemes are presented, with information describing the formation of these schemes. More detail on coastal current systems and the classification of the systems are then discussed, leading into an explanation on the creation of the coastal current systems used for testing and how the coastal plumes will be analyzed. After the methods are discussed, results from a timestep sensitivity analysis are shown. Chapter 3 presents the model results from only buoyancy forcing, followed by the results from the combination of buoyancy forcing and tides in

Chapter 4. Near the end of manuscript, the discussion, conclusions, (Chapter 5) and future recommendations (Chapter 6) for the investigation are presented in detail.

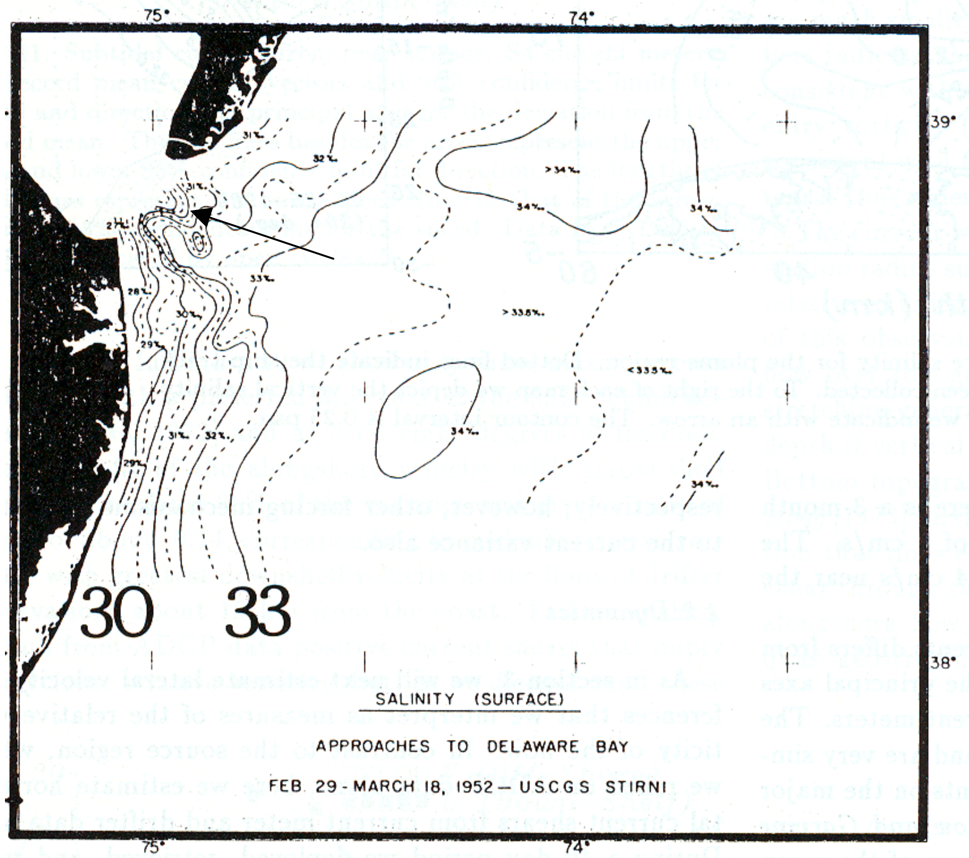

Figure 1.1 : Salinity field of the Delaware Coastal Current as graphed by Münchow and Garvine (1993). A small anticyclonic bulge exists immediately out of the bay area (black arrow) and the coastal current moves downshelf along the barrier islands.

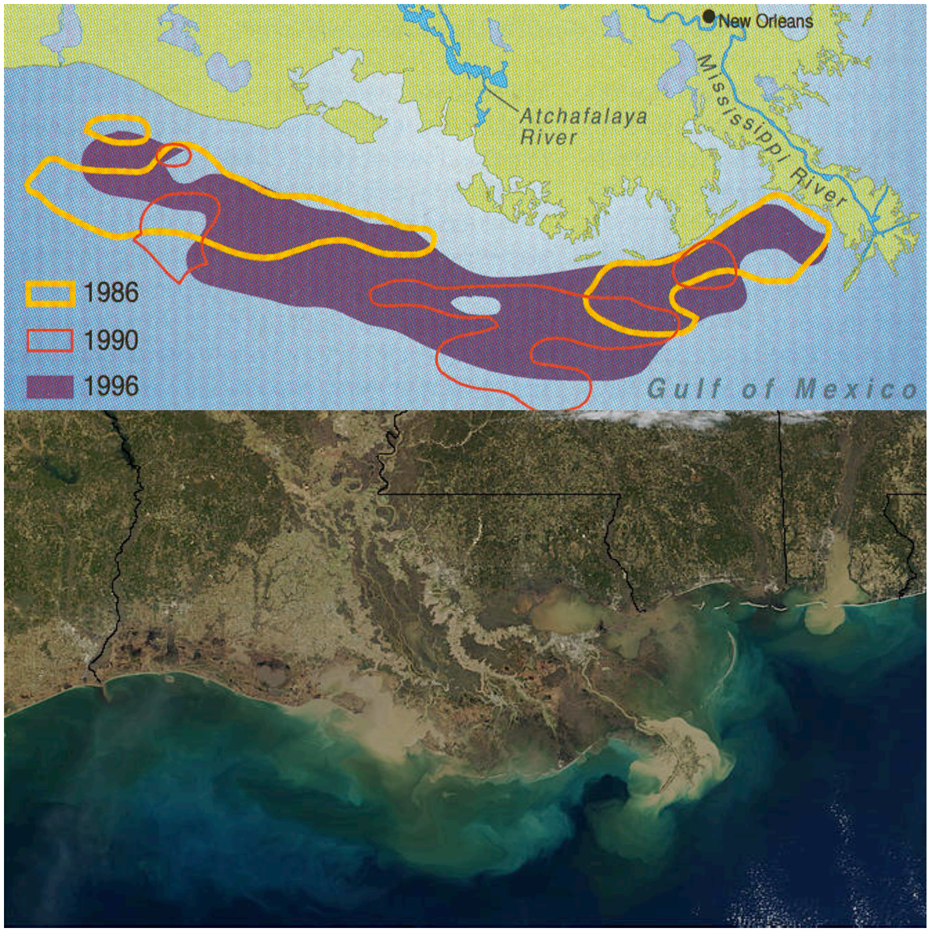

Figure 1.2 :

TOP: An image showing the changes in hypoxic areas with years (Ferber 2001).

BOTTOM: An image showing the large sediment transport into the hypoxic areas from the Mississippi River during January 2004. The sediment transport reaches its max during the summer months (NASA/GSFC 2003).

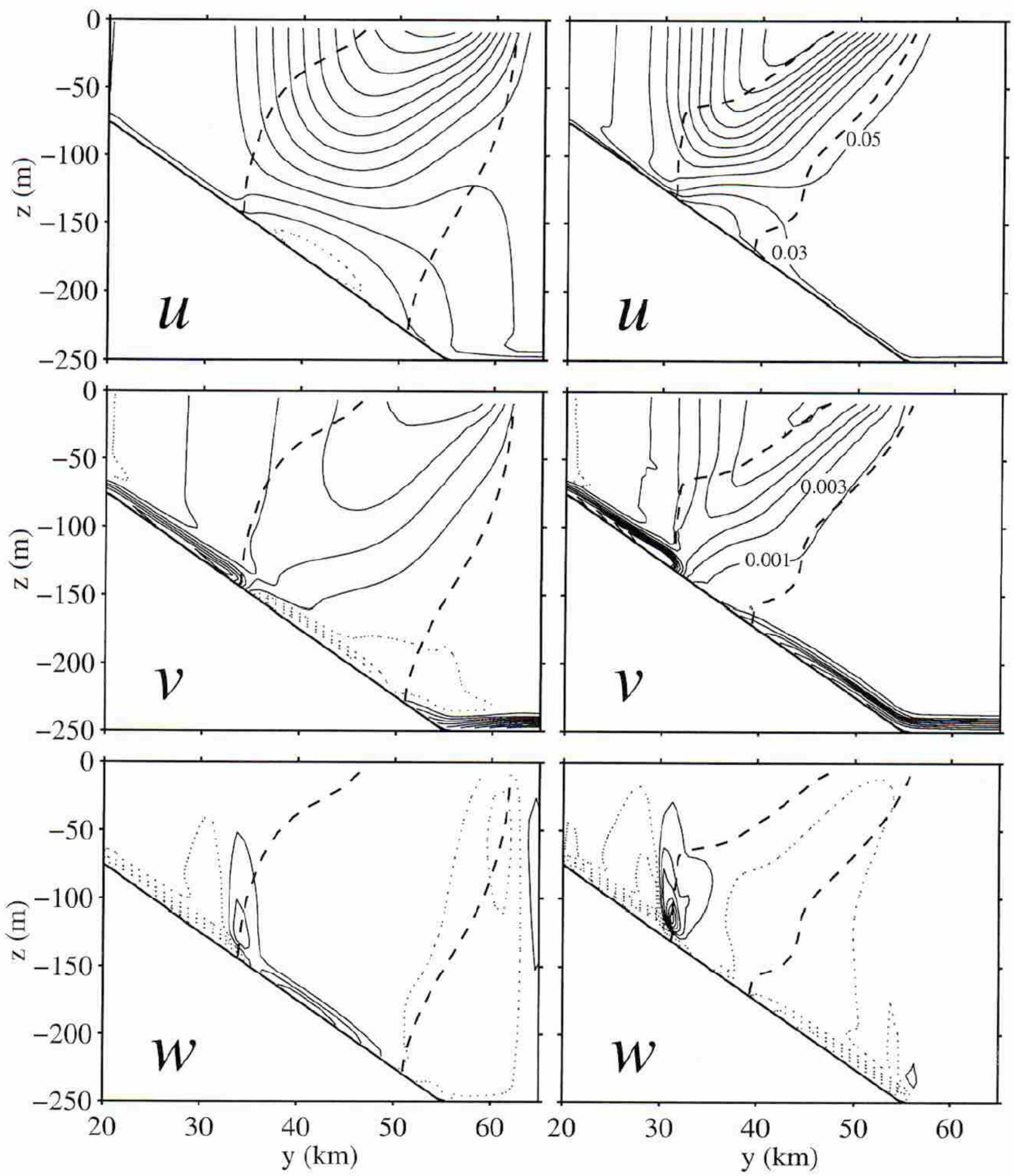

Figure 1.3 : From Chapman (2002), the graphs on the left show the constant scheme compared to the second-order parameterization scheme graphs on the right, where u is the alongshelf velocities with positive values out of the page, v is the across-shelf velocities with positive values moving offshore, and w is the vertical velocities with positive values moving upwards. Solid contours are positive, dotted contours are negative, and dashed line indicates the location of the plume front. Contour values for *u* begin with –0.01 m s^{-1} and end at 0.23 m s^{-1} with an interval of 0.02 m s^{-1} while *v* is from –0.007 to 0.017 m s^{-1} with 0.002 m s^{-1} intervals, and *w* is from –0.8 x 10^{-4} to 10^{-4} m s^{-1} with intervals of 1.5 x 10^{-5} m s^{-1}.

CHAPTER 2

METHODS

2.1 The numerical model

ECOM3d, a similar model to the Princeton Ocean Model (POM), is a three-dimensional estuarine, coastal, and ocean model developed by Blumberg and Mellor (1995). This investigation utilizes the version of ECOM3d as described by Whitney and Garvine (2006). The model solves the three dimensional equations of momentum, continuity, temperature, salinity, and turbulence on a sigma coordinate system in the vertical and on a staggered finite difference grid scheme in the horizontal (Blumberg 1995). The sigma coordinate system maintains constant depth proportions throughout the water column, shown in Figure 2.1. For example, if the second sigma level is set to 0.02, 2% of the water volume lies above this level throughout the entire model. This type of system is ideally suited for coastal modeling due to its increased resolution at shallow depths.

ECOM3d uses a staggered grid system that allows the model to quickly and efficiently solve differential equations for transport of variables of interest across grid domains. The Arakawa C staggered grid calculates variables at different locations as shown in Figure 2.2, based on Kantha and Clayson (2000); notice the locations of the alongshelf velocity variable, $\hat{u}$, the across-shelf velocity variable, $\hat{v}$ (where $\hat{u} = U + u$ and $\hat{v} = V + v$, representing the sum of the mean and fluctuating velocities), and the surface elevation, η. The Arakawa C grid results in highly accurate calculations of pressure gradients and divergence at the expense of Coriolis, and the grids applies finite differencing to approximate the shallow water equations. The divergence term is calculated by the addition of the two unidirectional components at the center of the grids. Pressure gradients are represented by elevation and require no averaging, as shown with the shallow water equations and Figure 2.2. The Coriolis is a two-dimensional phenomenon requiring the simultaneous use of both directions for calculation at a specified location; thus, it is more accurately calculated when information for both dimensions is collocated (Kantha and Clayson 2000). In the Arakawa C grid, the calculation of the Coriolis term is compromised by averaging the horizontal terms.

Due to the various temporal scales required to model coastal current systems, ECOM3d steps between two modes of calculations that use two different time steps, i.e. internal and external time steps. The user specifies the time step of each mode based on the Courant-Friedrichs-Lewy (CFL) criterion (Courant, Friedrichs, and Lewy 1967 *translated reprint*, Blumberg 1995, Mellor 1998). This criterion identifies the largest time step possible for stable calculations. The external mode time step, Δt_E, is often chosen to be 90% of the external CFL limit:

$$\Delta t_E \leq \frac{1}{C_t}\left|\frac{1}{\Delta x^2}+\frac{1}{\Delta y^2}\right|^{-1/2} \tag{2.1}$$

where Δx and Δy represents the grid spacing, $C_t = 2(gH_M)^{1/2} + U_{max}$, g is equal to 9.81 m s^{-2}, H_M is the maximum depth of the water column, and U_{max} is the maximum downshelf velocity. Barotropic variables that change over shorter time scales, such as elevation and vertically averaged velocities, are solved in the external mode and then passed over to the internal mode. The internal mode in turn, calculates bottom stress, and vertical variations of velocity, potential temperature, salinity, and turbulence variables. Information on advection, density, and bottom stress of the water column is then fed back to the external mode for the next set of external time steps. The internal mode is larger than the external mode and focuses on the three-dimensional, baroclinic forcing in the model. The internal time step, Δt_I, must meet the requirements of the internal CFL criterion:

$$\Delta t_I \le \frac{1}{C_T}\left|\frac{1}{\Delta x^2}+\frac{1}{\Delta y^2}\right|^{-1/2} \tag{2.2}$$

where $C_T = 2C + U_{max}$, U_{max} is the maximum velocity and $C = \sqrt{g' H_C}$; g' is the reduced gravity ($g' = g\Delta\rho/\rho_0$) and H_C is the depth at the coast (Blumberg 1995, Mellor 1998).

ECOM3d allows the user to select one of four built-in advection or solver algorithms: upwind difference, central difference, smolar_2, and smolar_r. The upwind scheme is a first order approximation scheme that tends to create heavily diffuse coastal current systems due to its inclusion of numerical diffusion in the calculations. The central difference scheme is second order and does not allow for numerical diffusion; however, this scheme is not positive definite and may create numerical ripples that propagate away from frontal zones. The second order Multidimensional Positive Definite Advection Transport Algorithms (MPDATA) are much more accurate and do not suffer from the same problems as the other two schemes; nevertheless, they require considerably more computational resources and time. Two MPDATA schemes are found in ECOM3d, smolar_2 and smolar_r. Smolar_2 uses the upwind transport algorithm and then applies the upwind scheme using an anti-diffusion velocity twice. Antidiffusive velocities are used to correct for the numerical diffusion of the upwind scheme (Smolarkiewicz 1984). The smolar_2 scheme calculates the antidiffusive velocities using a function derived from the previous computated concentration field (Smolarkiewicz and Clark 1986). Smolar_r calculates these velocities using a function derived from original concentrations using a recursion relation; the resulting velocities are then similar to those that have been corrected with infinite iterations (Blumberg 1995). Although smolar_r requires the most amount of computational time, the increased accuracy outweighs this disadvantage since accuracy is of great importance and the models will be run on the timescale of months in this study.

ECOM3d uses the Smagorinsky (1963) formula to parameterize the horizontal mixing coefficients needed to solve for the variable transport equations, which is:

$$A_m = C_h \Delta x \Delta y \left[\left(\frac{\partial \hat{u}}{\partial x} \right)^2 + \left(\frac{\partial \hat{v}}{\partial y} \right)^2 + \frac{1}{2} \left(\frac{\partial \hat{u}}{\partial y} + \frac{\partial \hat{v}}{\partial x} \right)^2 \right]^{1/2} \tag{2.3}$$

where $\hat{u}$ and $\hat{v}$ are instantaneous velocities, and C_h is a constant that is set to 0.05; this value has been set between 0.01 to 0.5 (Blumberg 1995). In ECOM3d, the Prandtl number is currently set equal to one by the user, indicating that eddy viscosity and eddy diffusivity are the same value for horizontal and vertical parameterization. Therefore, Smagorinsky's (1963) formula assumes that the horizontal parameterization of diffusion and viscosity can be represented with the same value, A_m, for this set Prandtl number.

ECOM3d uses a second moment turbulence closure sub-model to calculate vertical mixing coefficients. The turbulence closure scheme included within the model is the Mellor-Yamada Level 2.5 scheme (Mellor and Yamada 1982, Galperin et al. 1988); this scheme will be further discussed in the next section. It is important to note that ECOM3d can also be easily set to use constant viscosity/diffusivity in the model as an alternative method to approximate the mixing coefficients.

The boundary conditions used for this investigation are based on alterations to the ECOM3d model developed by Whitney and Garvine (2006). Salt and heat flux are zero for the surface, bottom, and land boundaries. The surface boundary flux is influenced only by wind stress, if winds are present. The bottom boundary is controlled by the quadratic drag law, where the calculated bed shear stress depends on the ambient density, a drag coefficient, and the bottom velocities (Tilburg 2003, Dyer 1997). A partial slip condition is utilized along land boundaries. The velocity component normal to the coast is set to zero while the velocity component tangent to the coast is half of the velocity of the adjoining interior grid. Although there is no physical backing for this condition, the partial slip condition has been shown to be highly functional for different coastline geometries (Whitney 2003).

To prevent artificial, buoyancy-driven flow, the open boundaries are not given specific temperature and salinity values; instead, smooth conditions are used. The water properties do not change when crossing in and out of the boundary. A composite Clamped/Gravity-Wave Radiation, or CLP/GWI, condition is applied for the upshelf, downshelf, and across-shelf boundaries to solve for boundary surface elevation (Chapman 1985, Whitney 2003). The CLP condition 'clamps' tidal information to the surface elevation. The surface elevation, η_T, for the CLP condition is shown below:

$$\eta_T = \sum_i \eta_i \cos(\omega_i t - \varphi_i) \text{ for } i \text{ tidal constituents} \tag{2.4}$$

where η_i is the tidal surface elevation, ω_i is the tidal frequency, t is time in seconds, and φ_i is the tidal phase. This condition allows for better representation of tidal behavior within the model realm. GWI solves for surface changes due to radiating gravity waves using the equation,

$$\frac{\partial \eta_R}{\partial t} - c_w \frac{\partial \eta_R}{\partial x} = 0 \tag{2.5}$$

where $c_w = \sqrt{g h_z}$ is the phase speed of an exiting wave, g is the gravitational acceleration, and h_z is the water column depth. Since the surface elevation includes the passage of waves through the boundary, there is a smoother transition at the boundary that will not unnaturally disrupt the simulated flow field. These conditions, CLP and GWI, combined, allow for the surface elevation at the open boundaries to be calculated as

$$\eta = \eta_T + \eta_R. \tag{2.6}$$

ECOM3d is used in this investigation due to its previous success in depicting various aspects of coastal current systems. Garvine (1999) used ECOM3d to demonstrate the effects of latitude, bottom slope, and tides on plumes. In addition, a number of successful studies using ECOM3d exist that compare model output to observations (Kourafalou et al. 1996a&b, Fong and Geyer 2001, Whitney and Garvine 2006).

2.2 Closure schemes

A variety of methods are used to calculate turbulence for numerical simulations. This investigation focuses on several numerical schemes, ranging from empirical methods that rely on the Richardson number, to more complex methods that rely on numerous transport equations. All schemes aim to solve for the vertical Reynolds stress terms from the Reynolds decomposed Navier-Stokes equations. The Navier-Stokes equations, as well as the conservation of mass and salinity transport equation, are expressed in three dimensional vector notation as,

$$\rho\left(\frac{\partial \hat{u}_i}{\partial t} + \hat{u}_k \frac{\partial \hat{u}_i}{\partial x_k} + \varepsilon_{ijk} f_j \hat{u}_k\right) - \nu\nabla^2 \hat{u}_i = -\frac{\partial \hat{P}}{\partial x_i} - g_i\rho \tag{2.7}$$

$$\frac{\partial \rho}{\partial t} + \frac{\partial}{\partial x_k}\left(\rho \hat{u}_k\right) = 0 \tag{2.8}$$

$$\frac{\partial \hat{S}}{\partial t} + \hat{u}_k \frac{\partial \hat{S}}{\partial x_k} = \gamma\nabla^2 \hat{S} \tag{2.9}$$

where t is the time, $f_j = (0,2\Omega cos\theta,2\Omega sin\theta)$ where Ω is Earth's angular velocity and θ is the latitude, ε_{ijk} is the Levi Civita symbol, $g_i = (0,0,g)$ where $g = 9.81$ m s^{-2}, ν is the kinematic viscosity in m^2 s^{-1}, and γ is the molecular diffusivity (based on Mellor 1973). The salinity transport equation is used instead of the temperature transport equation due to model conditions; all temperature is kept constant for the model runs. Applying the Boussinesq approximation and the hydrostatic balance assumptions, as well as the Reynolds decomposition and averaging of velocity, pressure, density, and salinity in the above equations, results in the following:

$$\frac{\partial U_i}{\partial t} + U_k \frac{\partial U_i}{\partial x_k} + \varepsilon_{ijk} f_j U_k = -\frac{1}{\rho_0}\frac{\partial p}{\partial x_i} - \frac{\partial}{\partial x_k}\left(\overline{u_i u_k}\right) - g_i \frac{\rho'}{\rho_0} + \nu \nabla^2 U_i \tag{2.10}$$

$$\frac{\partial S}{\partial t} + u_k \frac{\partial S}{\partial x_k} = -\frac{\partial}{\partial x_k}\left(\overline{u_k s}\right) + \gamma \nabla^2 S \tag{2.11}$$

where $\hat{u} = U + u$, $\hat{S} = S + s$, and overbars represent the ensemble means of turbulence variables (based on Mellor 1973, Mellor and Yamada 1974). The lower case variables are fluctuating components of the variable and the upper case variables are the mean component of the variable. If the momentum and salinity flux terms in the equations above are defined as,

$$\begin{aligned} \overline{uw} &= -K_z \frac{\partial U}{\partial z} \\ \overline{vw} &= -K_z \frac{\partial V}{\partial z} \\ \overline{ws} &= -K_s \frac{\partial S}{\partial z} \end{aligned} \tag{2.12}$$

where K_z is the eddy viscosity, the transfer of momentum, and K_s is the eddy diffusivity, the transfer of salinity, a method to determine these two parameters is needed to close the equations.

However, solving for these Reynolds stress terms is no easy task. In order to solve these equations, a number of assumptions and approximations must be used to close the equations. Three different turbulence closure schemes will be analyzed in this study: a scheme with constant viscosity/diffusivity, a Richardson number based scheme by Pacanowski and Philander (1981), and Mellor-Yamada Level 2.5.

2.2.1 Constant Viscosity/Diffusivity Scheme

The first and least complex of the methods to parameterize K_z and K_s, viscosity and diffusivity, is to use constant values, which uses the same viscosity and diffusivity coefficients throughout the water column. While the scheme tends to produce unrealistic mixing in areas of high shear and varied stratification, the scheme benefits from a simple implementation and clear interpretation of the viscosity/diffusivity coefficients used.

2.2.2 Pacanowski and Philander (1981) Scheme

Although, the next scheme, the Pacanowski and Philander (1981) scheme, was originally formulated based on characteristics of the equatorial and open ocean regions, Houghton et al. (2004) found that this model has the potential to successfully simulate mixing in coastal regions. This closure scheme formulated by Pacanowski and Philander (1981) is based on empirical studies in the Equatorial region by Robinson (1966) and Jones (1973). Jones (1973) used in-situ measurements to develop a mathematical relationship between the vertical eddy coefficient and the Richardson number. From this point on in the manuscript, the scheme presented in Pacanowski and Philander (1981) will be identified as the Pacanowski and Philander scheme.

The Pacanowski and Philander scheme assumes that vertical eddy viscosity and diffusivity are dependent on the effects of stratification and vertical shear and rely on the Richardson number, *Ri*, shown in (1.1). The Richardson number dependent eddy viscosity and diffusivity are calculated using,

$$K_z = \frac{K_{z_0}}{(1+\varpi(Ri))^n} + K_{z_b} \qquad (2.13)$$

$$K_s = \frac{K_z}{(1+\varpi(Ri))} + K_{s_b}$$

where K_{z_b} and K_{s_b} represent background viscosity and diffusivity, and K_{z_0} (the null viscosity), ϖ, and n represent adjustable parameters. Figure 2.3 shows the relationship between the calculated eddy viscosity and the Richardson number when using various parameter values; lower Richardson numbers, indicating more vertical shear, creates higher eddy viscosity. Since eddy diffusivity is calculated using the eddy viscosity value, higher eddy viscosity values would produce higher eddy diffusivity values as well.

In their experiments and using previous investigations on the Equatorial Undercurrent, Pacanowski and Philander (1981) proposed that K_{z_0} be set between 50 and 150 cm^2 s^{-1}, n to equal 2, and ϖ be set to 5 (Robinson 1966, Jones 1973). They also found that the variables n and ϖ can change the speed of the jet while K_{z_0} can alter the speed and shear of the jet. Therefore, these variables have the potential to influence the simulation outcome and must be carefully assigned.

2.2.3 Mellor-Yamada Scheme

The last scheme to be studied is the Mellor-Yamada Level 2.5; this second moment method utilizes statistical methods to model turbulence (Mellor and Yamada 1982, Galperin 1988). The appendix section follows through, in more detail, the derivations and assumptions leading to the creation of the Mellor-Yamada Level 2.5 closure scheme used in ECOM3d, based on Mellor and Yamada 1974 and 1982. However, for this section, a brief overview of the scheme will be presented.

This scheme is originally derived from the Navier-Stokes equation, (2.7) to (2.9), to form the foundation of the Mellor-Yamada scheme, the equations below:

$$\frac{\partial \overline{u_i u_j}}{\partial t} + U_k \frac{\partial \overline{u_i u_j}}{\partial x_k} + \overline{u_j u_k}\frac{\partial U_i}{\partial x_k} + \overline{u_i u_k}\frac{\partial U_j}{\partial x_k} + \frac{\partial \overline{u_i u_j u_k}}{\partial x_k} + f_k(\varepsilon_{jkl}\overline{u_l u_i} + \varepsilon_{ikl}\overline{u_l u_j})$$
$$= -\frac{1}{\rho_o}\frac{\partial \overline{p u_j}}{\partial x_i} - \frac{1}{\rho_o}\frac{\partial \overline{p u_i}}{\partial x_j} + \overline{\frac{p}{\rho_o}\frac{\partial u_j}{\partial x_i}} + \overline{\frac{p}{\rho_o}\frac{\partial u_i}{\partial x_j}} - \frac{g_i}{\rho_o}\overline{u_j \rho'} - \frac{g_j}{\rho_o}\overline{u_i \rho'} + \nu\frac{\partial}{\partial x_k}\left(\frac{\partial \overline{u_i u_j}}{\partial x_k}\right) - 2\nu\overline{\frac{\partial u_i}{\partial x_k}\frac{\partial u_j}{\partial x_k}} \tag{2.14}$$

$$\frac{\partial \overline{u_i s}}{\partial t} + U_k \frac{\partial \overline{u_i s}}{\partial x_k} + \overline{u_k s}\frac{\partial U_i}{\partial x_k} + \overline{u_i u_k}\frac{\partial S}{\partial x_k} + \frac{\partial \overline{u_i u_k s}}{\partial x_k} + \varepsilon_{ikl} f_k \overline{u_l s}$$
$$= \frac{1}{\rho_o}\frac{\partial \overline{ps}}{\partial x_i} + \overline{\frac{p}{\rho_o}\frac{\partial s}{\partial x_i}} - \frac{g_i}{\rho_o}\overline{s\rho'} + \gamma \frac{\partial}{\partial x_k}\left(\overline{u_i \frac{\partial s}{\partial x_k}}\right) - \gamma \overline{\frac{\partial u_i}{\partial x_k}\frac{\partial s}{\partial x_k}} + \nu \frac{\partial}{\partial x_k}\left(\overline{s\frac{\partial u_i}{\partial x_k}}\right) - \nu \overline{\frac{\partial u_i}{\partial x_k}\frac{\partial s}{\partial x_k}} \tag{2.15}$$

$$\frac{\partial \overline{s^2}}{\partial t} + U_k \frac{\partial \overline{s^2}}{\partial x_k} + 2\overline{u_k s}\frac{\partial S}{\partial x_k} + \frac{\partial \overline{u_k s^2}}{\partial t} = \gamma \frac{\partial}{\partial x_k}\left(\frac{\partial \overline{s^2}}{\partial x_k}\right) - 2\gamma \overline{\frac{\partial s}{\partial x_k}\frac{\partial s}{\partial x_k}} \tag{2.16}$$

where $\rho' = (\partial\rho/\partial S) * s$ (based on Mellor and Yamada 1974). These three equations, (2.14) to (2.16), are then subjected to a number of assumptions, such as the Rotta hypothesis and Kolmogorov's hypothesis of local isotropy, to form the highest Mellor-Yamada Level 4. With each descending Mellor-Yamada Level, different assumptions are made for the scaling of the terms, and terms with a specified order of magnitude of anisotropy, or directional dependence, are neglected. The significance of this is that turbulence by nature, has anisotropic features, where all three dimensional directions change characteristics.

One of the major assumptions in the Mellor-Yamada closure schemes is that all length scales are set to be proportional for simplicity, shown below as,

$$(l_1, \Lambda_1, l_2, \Lambda_2) = (A_1, B_1, A_2, B_2)l \tag{2.17}$$

where the variables on the left hand side of the equation are various length scales used in the various Mellor-Yamada equations, and the variables on the right hand side, except for the master length scale, l, are constants measured from data (Mellor and Yamada 1982). This assumption greatly simplifies the need to individually calculate each length scale; however, it then results in the dependence of all length scales on one master length scale and previously measured data. Mellor and Yamada have pointed out this assumption to be the 'weakest link' in their scheme (Mellor and Yamada 1982).

The Mellor-Yamada Level 2.5 scheme derives from the Mellor-Yamada Level 2 scheme, where Level 2 is subjected to the boundary layer approximation and Coriolis terms are neglected. The eddy viscosity and diffusivity coefficients in Mellor-Yamada Level 2.5 may be calculated with the equations below,

$$\begin{aligned} K_z &= lqS_M \\ K_s &= lqS_H \end{aligned} \tag{2.18}$$

where S_M and S_H are stability functions dependent on Ri, q can be solved from the turbulent transport equation and is the square root of the turbulent kinetic energy ($\frac{1}{2}q^2 = \frac{1}{2}\overline{u_k^{\ 2}}$), and l is the master length scale (the equation, (A.11), is presented in the appendix).

Although a number of studies have been successful using the Mellor-Yamada Level 2.5 scheme (i.e. Tilburg et al. 2006, Whitney 2003, Kourafalou 1996a&b, Garvine 1999), it is interesting to note that as stratification increases and the Richardson number becomes large, the scheme automatically shuts down and instead, uses constant background vertical viscosity (K_{z_b}) and diffusivity (K_{s_b}), specified by the user, to depict the situation (Garvine 1999, Hetland 2005). Therefore, the user must use careful consideration when determining these background values since this choice can greatly influence the behavior of the plume.

2.2.4 Other Vertical Mixing Schemes

The well-known turbulence closure scheme, k-ε, was not used in this investigation due to its similarity to the Mellor-Yamada Level 2.5 scheme. The k-ε scheme, like the Mellor-Yamada Level 2.5 scheme, is a statistical second-order method that is derived from transport equations. Burchard et al. (1998) show that the fundamental difference between the two schemes is the derivation and calculation of the length scale. This difference has little influence on the results of the two schemes; Burchard and Petersen (1999) and Li et al. (2005) have shown a similarity in performance when applying both schemes in idealized situations or in a marine environment. Therefore, in this study, the use of the Mellor-Yamada Level 2.5 serves as a good representative for this genre of closure scheme, those based on transport equations.

Initially, the use of a fourth vertical mixing scheme, the modified K profile parameterization scheme (KPP), was originally intended for this investigation (Large 1994, Wijesekera 2003, Durski 2004). This scheme divides the water column into three sections based on the idea that different factors affect the boundaries and the interior of the coastal water column. The surface and bottom boundary mixing layers are calculated with a cubic polynomial shape function and the turbulent velocity scale (based on a number of variables, including the turbulent friction velocity and a function of the stability parameter). The interior is dependent on the shear instability and internal wave breaking found in this region. This scheme is efficient for approximating the viscosity and diffusivity coefficient when the interior region separates the top and bottom boundary layers. However, the modified KPP scheme becomes highly complex in situations where the surface and bottom boundary layers tend to overlap, such as the innershelf and shallow areas on the coast. The cubic polynomial shape function must then be reconfigured to include the effects of both layers and the new physical factors important in determining the viscosity and diffusivity coefficients [*Wijesekera, H., personal communication*]. In this study, one of plumes that are created, discussed in the next section, has much interaction between the surface and bottom boundaries, which would then represent a large problem if using the KPP scheme.

2.3 Coastal current classification

Since the focus of this project is to compare different turbulence closure schemes among a variety of coastal regions in an idealized model, a method to create and represent existing coastal current systems is necessary. Several studies using different classification systems have been developed. Kourafalou et al. (1996a) divided plumes based on the third root of the Fischer et al. (1979) Richardson number (R_3) and the densimetric Froude number (F); the two terms are calculated as,

$$R_3 = \frac{u_F}{u_{*1}} \qquad (2.19)$$

$$F = \frac{u_F}{u_D}$$

where $u_F = (g' Q_F)^{1/3}$ is the velocity of freshwater discharge, Q_F is the inlet discharge divided by inlet width, u_{*1} is the shear velocity, and $u_D = ((g' h)^{1/2})/\pi$ is the densimetric velocity (Kourafalou 1996a). Plumes were considered supercritical when $R > 1$ and distinguished by the meandering of the coastal current while the plumes were categorized as subcritical when $R < 1$, an indicator of the dominance of mixing and/or the influence of a shallow bottom; when $R \sim 1$, the densimetric Froude number determined the classification of the plume. If $F > 1$, the plume was supercritical, and when $F < 1$, the plume was subcritical (Kourafalou 1996a).

Garvine (1995) based his classification method on the Kelvin number, where the numerator represents the across-shelf distance of the plume and the denominator is the Rossby radius, as will be shown in (2.23). The Kelvin number is mathematically represented below as,

$$K = \frac{\tau L_H}{c / f} \qquad (2.20)$$

where c is the wave speed, f is the Coriolis parameter, L_H is the alongshelf length scale of the plume and τ is, as Garvine (1995) describes, the 'slenderness' of the plume, and so, τL_H is the across-shore length scale. Plumes with a very small Kelvin number were small-scale plumes with weak Coriolis and faster flow, such as the Amazon River, while plumes with very large

Kelvin numbers had elongated alongshore structure with stronger Coriolis and slower speeds, such as the Delaware Coastal Current (Garvine 1995).

These methods describe the characteristics of the plume after its formation. Since this investigation attempts to control the type of plume prior to plume development, Avicola and Huq's (2002) classification scheme was the method of choice. Avicola and Huq (2002) used two nondimensional numbers to predict the type of plume commonly found in coastal environments: surface-advected, intermediate, and bottom-advected plumes. Surface-advected plumes are characterized by the absence of bottom influence on the plume while bottom-advected plumes are heavily affected by interactions with the bottom. Intermediate plumes show characteristics of both.

The two nondimensional parameters are the ambient depth parameter, h/H, and the bottom slope parameter, R/y_b, adapted from Chapman and Lentz (1994) and Yankovsky and Chapman (1997). The ambient depth parameter describes the thickness of the plume, h, in relation to the depth of the column at one Rossby radius, H. The bottom slope parameter is the Rossby radius divided by the width of the current in contact with the bottom topography, describing the horizontal compression or expansion of the plume along the bottom. Both of these nondimensional parameters are used to describe characteristics exhibited by the current system and may be calculated with knowledge of only five parameters: the freshwater discharge rate (Q), the reduced gravity ($g' = g * \Delta\rho/\rho_0$), the Coriolis parameter (f), the bottom slope (α), and the coastal wall depth (H_c).

The ambient depth parameter, h/H, may be calculated using,

$$h = \sqrt{\frac{2Qf}{g'}} \tag{2.21}$$

$$H = depth@1R = H_c + \alpha R \tag{2.22}$$

$$R = \frac{c}{f} = \frac{\sqrt{g'h}}{f} \tag{2.23}$$

where h is the scale depth and R is the Rossby radius. Surface-advected currents are those systems with ambient depth parameter values less than 1. Figure 2.4A, from Avicola and Huq (2002), is a schematic representation of a surface-advected current; the current is free from boundary effects, except for the coastline. Intermediate currents are those currents with ambient depth parameter values around 0.4, and they present characteristics of both, surface-advected and bottom-trapped currents. The bottom-trapped currents are those currents with ambient depth parameter values greater than 1. These currents are shaped by the bottom topography, as shown in Figure 2.4B (Avicola and Huq 2002). The name 'bottom-trapped' refers to the dynamics within the current that causes the discontinuation of offshore progression of the coastal current density front when the bottom no longer displays offshore buoyant flux, the cause for bottom trapping will be discussed later (Chapman and Lentz 1994). These types of plumes are also referred to as bottom-advected plumes in this study.

The nondimensional bottom slope parameter, R/y_b, may be calculated using the Rossby Radius equation, (2.23), and the equation below,

$$y_b \sim \frac{h}{\alpha} \tag{2.24}$$

where y_b is the maximum offshore distance of the bottom-trapped layer. This parameter characterizes coastal currents by their offshore extent. If the parameter value is < 1, the current width against the bottom is much larger than the Rossby radius, indicating horizontal expansion of the coastal current; thus, creating a weaker pressure gradient within the current and leading to a slow geostrophic along-shelf velocity to develop. A parameter value of > 1 describes a current with horizontal compression; these currents have steeper across-shelf pressure gradients and therefore, faster geostrophic along-shelf velocities (Avicola and Huq 2002). Figure 2.5 shows the relationship between the two nondimensional numbers in terms of the type of plume formed.

2.4 Characteristics of coastal current systems

Surface-advected systems are more common than bottom-advected systems. At lower latitudes, surface-advected systems are more commonly found due to the reduction of Coriolis allowing for stronger stratification to develop (Garvine 1999, Yankovsky and Chapman 1997). The main identifying features of surface-advected plumes are in the side view, the buoyancy of the plume with the bottom located far beneath the plume's depth, and in the plan view, the asymmetry in the across-shelf extent of the coastal current system, where the bulge widens much further offshore than the subsequent coastal current. Surface-advected systems typically have an expanding bulge that is a few internal Rossby radii, (2.25), across-shelf (Garvine 1999). Yankovsky and Chapman (1997), however, show that the plume should extend a minimum of more than four internal Rossby radii offshore.

Bottom-advected systems are more limited in their development. They are typically found in areas with high freshwater discharge and/or with a small density anomaly, causing the system to come into contact and interact with the bottom (Yankovsky and Chapman 1997). As previously discussed, as freshwater moves out of its source region and into the ambient ocean, it forms a buoyant plume that turns anticyclonically and moves downshelf along the coast. In bottom-advected systems, the influence of the bottom stress coupled with the geostrophic current results in a bottom Ekman layer, whose net transport is offshelf. The combination of the offshore movement of the bottom Ekman layer and the vertical mixing of the lighter water within the front with the heavier ambient ocean water results in an offshore movement of the plume and the density front (Chapman and Lentz 1994). The plume continues to expand in the offshore direction until it reaches a depth in which the vertical shear in the density front reverses the alongshelf velocities near the bottom and therefore, the bottom Ekman layer no longer has a net offshore transport. At this point, the density front as well as the plume becomes 'bottom-trapped' and no longer moves offshore (Chapman and Lentz 1994). Figure 2.6 shows the across-shelf velocity field when the bottom-advected plume becomes trapped offshore.

Examples of each type of coastal current system is as follows. The Connecticut River, the Hudson River, and the Chesapeake Bay discharges are surface-advected currents, when disregarding winds and tidal forcing (Yankovsky and Chapman 1997). The Labrador shelf is a true bottom-advected current (Yankovsky and Chapman 1997). Other systems may fall in all three categories depending on season; the Delaware Bay discharge normally is shown to be a bottom-advected current, but during spring, with high runoff, the plume may become an intermediate or even a surface-advected plume (Yankovsky and Chapman 1997).

In this study, only the surface- and bottom-advected plumes are analyzed due to having individual traits that may be clearly identified.

2.5 Upshelf propagation and anticyclonic shedding

Although modeling coastal current systems have been successful, previous investigators have noted the existence of a numerical model generated feature, the upshelf propagation of the coastal plume (Garvine 2001, Yankovsky 2000, Garvine 1999, Yankovsky and Chapman 1997, Kourafalou et al. 1996a, Chapman and Lentz 1994). Yankovsky (2000) investigated this feature and concluded that the cyclonic turning and propagation is due to the lack of baroclinic adjustment of the freshwater inflow boundary condition, creating a cyclonic disturbance in the mid to bottom layer of the model.

In the model, the inlet boundary conditions do not change along with the changing conditions in the interior of the model domain; the inflow remains independent of time and depth, thus, the inflow velocities at the boundary remain unchanged. However, the grid points immediately offshore of the inlet boundary have the potential to change baroclinically due to freshwater forcing and other mechanisms. Shortly after initiating freshwater inflow, the across-shelf velocities at the bottom reverse to the onshore direction, due to the bottom friction, strong vertical shear, and maintaining thermal wind balance, where the reversal of the direction of the pressure gradient causes the velocity direction to turn around. The generalized flow field cartoon is shown on the left in Figure 2.7. Notice at the surface, the inflow first turns upshelf and then moves offshore and downshelf; this phenomenon will be discussed later. In Figure 2.7, the surface flow is mainly offshore and downshelf while the mid to bottom flow is onshore and upshelf. Because freshwater inflow at the inlet is invariant in time and depth, this set up causes the water to form a strong cyclonic feature and converge mid-depth near the inlet, shown on the right in Figure 2.7, and water to diverge at the surface in all directions near the inlet (Yankovsky 2000). Figure 2.8 shows the same phenomenon but are the model run results from Yankovsky (2000) at Day 5 of the run at the surface on the left and at mid-depth on the right; the inlet location is shown by the bold line on the alongshelf direction axis.

The initial upshelf turning of freshwater as it enters the model at the surface is created by the large horizontal density gradient at the plume front as the freshwater enters the ocean (Yankovsky 2000). The freshwater then moves anticyclonically due to the Coriolis effect and moves downshelf in geostrophic balance.

Yankovsky (2000) experimented with many different model runs to support these conclusions. Using barotropic inflow into the model, the resulting plume proved to have no upstream propagation, however, when using freshwater inflow, the upshelf movement of the plume was consistently present.

The reason for continued upshelf movement after the initial freshwater input into the ocean has also been investigated (Yankovsky 2000 and Garvine 2001). As freshwater flows out into the model domain, the water initially turns upshelf and then anticyclonically due to the Coriolis effect, and forms a bulge. The inlet freshwater is subjected to mixing as it enters the domain due to horizontal and vertical salinity gradients; in addition over time and distance, the freshwater becomes more saline while circulating around the bulge and into the coastal current, as shown in Figure 2.9. Therefore, as the bulge expands, the bulge is no longer able to sustain the buoyant water filling in the center due to mixing, so the freshest pool of discharged water shifts to the upstream portion of the inlet, following the flow field. As time further progresses, the bulge grows and the lightest water continuously shifts upshelf (Yankovsky 2000). When a weak upstream current is present in this type of situation, shedding of anticyclonic bulges can occur; weak upstream currents may be created by winds and tides, and upstream propagation can also produce currents. The bulge grows to an extent where advection can cause new anticyclones to be pushed upstream of the coastal current bulge and propagate upshelf (Yankovsky 2000). Therefore, the upshelf movement is dependent on mixing.

The continued upshelf propagation has been specifically attributed as a consequence of higher magnitudes of vertical diffusivity when using the Mellor-Yamada Level 2.5 and constant schemes. Yankovsky (2000) showed that using constant diffusivity with a magnitude of 10^{-4} m^2 s^{-1}, compared to 10^{-5} m^2 s^{-1}, creates enhanced vertical mixing and therefore, the freshwater bulge shifts upstream with time. In addition, Garvine (2001) showed that the upshelf propagation speed increases with increasing diffusivity and decreasing viscosity, showing that both mixing coefficients have an effect on the upshelf movement.

A rare example of upshelf propagation has been shown in an observational study of the Changjiang plume (Beardsley et al. 1985). In the summer during high discharge, the combination of topographic features partially blocking the inlet and strong tidal velocities creating strong mixing in the area results in upshelf propagation of the Changjiang plume (Beardsley et al. 1985, Yankovsky 2000).

Because of the unrealistic nature of upstream propagation, variables that could avoid or limit the development of upshelf movement have been tested. Yankovsky (2000) identified the freshwater inflow boundary dynamics to be the root of this modeling phenomenon. Therefore, he developed inlet boundary conditions that could adjust to model interior conditions to counteract the upshelf movement; his efforts were successful in minimizing upshelf development but not completely resolving the upshelf movement issue. Adding a downshelf current has been a popular method to eliminate or minimize upshelf propagation, however, Garvine (2001) showed that the upshelf movement still occurred when realistic periodic wind forcing was added as well. Garvine (2001) suggested three adjustments to be made to reduce upshelf intrusion. Like Yankovsky (2000), he showed that a more realistic estuarine inlet would minimize the upshelf propagation. The second suggestion recommended usage of a minimal coastal wall for the realistic inlet since coastlines typically consist of only continental shelves that slope into the ocean; Garvine (2001) used a coastal wall depth of 0.1 m. In addition, similar to riverine inlets, freshwater discharge leaving the estuary at an angle less than 90° downstream proved to decrease upshelf movement. Note that this study does not adjust any parameters to limit the growth upstream but does include investigation of upshelf propagation with time for all model runs.

2.6 Model Setup

The total model domain consists of 450 x 40 x 15 grid cells, and represents approximately 739 km x 57 km in the horizontal. The across-shelf magnitudes are representative of the typical range of coastal shelves found on the east and west United States coasts, O(100 km) and O(10 – 30 km), respectively (Battisti and Clarke 1982). Figure 2.10 shows the dimensions of the model domain used in the simulations, where x represents the alongshelf direction and y is the across-shelf direction.

The interior of the model, with the size of 400 x 40 grid cells, is approximately 600 km x 57 km, and individual grid spacing is 1.5 km in this region. The alongshelf edge boundaries of the model starts at x = 25 grids or ~ 65 km and x = 425 grids or ~ 665 km, and the grid size exponentially increases across 25 grid points towards the model edges, from 65 km to -1.5 km and from 665 km to 739 km. Therefore, at the alongshelf edge of the model, when x ~ 0 km and x ~ 739 km, the grid size is approximately 5 km (top, Figure 2.10).

A sigma coordinate system with 15 sigma levels is used in the vertical direction (Figure 2.1). Each sigma level is set to a percentage, where the level divides the water column; above the level is the percentage of the water column depth and below the level is the remaining depth of the water column. Therefore, resolution decreases with distance away from the coast (Figure 2.1). The depth at the coastal wall, maximum depth at the offshore edge of the model, and bottom slope depends on the type of coastal current system, are shown in Table 2.1.

The river inlet is located between 282.3 km and 292.8 km (equivalent to x = 170 to 177) from the upshelf boundary; freshwater discharge is the only physical forcing mechanism present in the buoyancy forcing simulations. The variations in river discharge and freshwater buoyancy

Table 2.1: This table contains information on the values used to create the different types of plumes as well as the various timesteps used in the model. Note that the internal Rossby radius values are calculated from (2.25), and these values are used in the analysis section.

Variables	***Surface-advected***	***Bottom-advected***
Internal time step (baroclinic)	614.68 s	550.00 s (buoy) 200.00 s (tides)
External time step (barotropic)	13.97 s	11.00 s (buoy) 200.00 s (tides)
H_c *- Coastal wall depth*	10 m	2 m
α *- Bottom slope*	2 x 10^{-3}	1 x 10^{-4}
Max depth	118.0 m	7.4 m
S_a *- Ambient salinity*	32	32
S_i *- Freshwater salinity*	25	22
g' – adjusted gravity	0.0522 m s^{-2}	0.0746 m s^{-2}
Q - Freshwater discharge	800 m^3 s^{-1}	2000 m^3 s^{-1}
Latitude	35°	35°
R_i *- Rossby Radius (internal)*	8.6369 km	4.6175 km
Ambient depth parameter	0.0947	0.8556
Bottom slope parameter	4.3168	0.2244

between the types of coastal current systems, surface- and bottom-advected, are shown in Table 2.1. The buoyant discharge rate, *Q*, and salinity of the inlet discharge, S_i, located from x = 174 to 177, refer to the freshwater input into the ambient coastal environment across 3 grids spanning 4.5 km. The other half of the inlet grids, x = 170 to 174, allows water to flow back into the river inlet. The total width of the inlet consists of 7 grids, or 10.5 km in the alongshelf direction (Figure 2.10).

Because local scales change on shorter timescales due to the presence of smaller features, only 50 days of simulation was run, and the model output data for every 60-hour period (20 snapshots of data) of the model runs was analyzed for buoyancy forcing runs. Simulations subjected to M2 tidal amplitudes of 0.1 m, 0.2 m, or 0.5 m were tidally averaged for a tidal period, 12.42 hours, for each day. A tidal amplitude of 0.1 m refers to the input of 0.1 m tidal amplitude at the offshore most boundary, with linearly decreasing elevations towards the coast on the downstream and upstream boundary edges of the model; the interior of the model initially has an elevation of zero. The tidal phase angle for all tides was set to 0; therefore, all offshore boundary elevation grid points are on the same cotidal line. The model was run on a two-processor Sun Blade 2000 computer housed at the University of Delaware.

2.7 Viscosity/diffusivity magnitudes

The range of magnitudes used for each vertical mixing scheme with only buoyancy forcing is shown in Table 2.2; these values have been used by several previous authors (a few examples: Garvine 1999, Li et al. 2005, and Yankovsky 2000). Values for the constant viscosity/diffusivity represent the magnitude entered into the model and used throughout the model domain without modification. The variables altered in the Pacanowski and Philander (1981) scheme are the null viscosity value, K_{z_0}, and the background viscosity and diffusivity. The null viscosity values used are those proposed in their study and are the default calculated viscosity value when *Ri* goes to zero. The Pacanowski and Philander scheme from henceforth will be known as P&P (A) when using a null viscosity of 5 x 10^{-3} m^2 s^{-1} and P&P (B) when using a null viscosity of 1.5 x 10^{-2} m^2 s^{-1}. The Mellor-Yamada Level 2.5 values represent the background viscosity/diffusivity that was added after first calculating the viscosity/diffusivity from the complex equations discussed in previous sections. The Mellor-Yamada Level 2.5 scheme, from this point further, will be abbreviated as MY2.5, and the background viscosity/diffusivity for all schemes will now be shown as K_{z_b} and K_{s_b}.

For all tidally forced runs, a K_{z_b} and K_{s_b} of 5 x 10^{-4} m^2 s^{-1} is used. One of the purposes of imposing tides is to increase the mixing in the model domain in order to investigate the schemes with an increase of mixing. Increasing the K_{z_b} and K_{s_b} used in the model will help promote more mixing due increasing the viscous shear on the tidal velocities. This study forces the principal lunar M2 semidiurnal tides, with a period of 12.42 hours.

Table 2.2: Ranges of the variables that will be tested in each of the turbulence closure schemes. Note that not all schemes have the same variables, and values are based on previous studies (Garvine 1999 and Pacanowski and Philander 1981). There are a total of 24 runs.

Turbulence Closure Schemes: Variables	***Constant viscosity/diffusivity***	***Pacanowski and Philander (1981)***	***Mellor-Yamada Level 2.5***
K_{z_0} $(m^2\ s^{-1})$		$5x10^{-3}$ and $1.5x10^{-2}$	
K_{z_b} $(m^2\ s^{-1})$	$5x10^{-6}$ to $5x10^{-4\dagger}$	$5x10^{-6}$ to $5x10^{-4}$	$5x10^{-6}$ to $5x10^{-4\dagger}$
K_{s_b} $(m^2\ s^{-1})$		$5x10^{-6}$ to $5x10^{-4}$	
Total runs:	***6***	***12***	***6***

† The Prandlt number is set to 1.0 in these schemes, so only one variable represents both the viscosity and diffusivity.

2.8 Closure scheme verification

Two of the three vertical mixing schemes investigated in this project were available for immediate use in ECOM3d, the constant viscosity/diffusivity and the MY2.5, however, the third scheme, P&P, was not included. Therefore, this scheme was written, implemented, and verified in the model for use in this investigation; only the verification process will be presented in this manuscript to demonstrate successful implementation of the scheme into ECOM3d.

Pacanowski and Philander (1981) presented multiple runs of their scheme using different magnitudes for the null viscosity term, K_{z_0}, shown in Figure 2.3, and in their manuscript, they proposed n to be set to 2 and ϖ to be set to 5. Therefore, cases B, C, D, and F in Figure 2.3 were used for the verification of this scheme. These runs were replicated in ECOM3d and then compared to the empirically calculated viscosity values. The results of the four model simulations are shown in Figure 2.11. Calculations for the validation were performed using values from sigma level 3, since it contained a larger range of viscosity and Richardson numbers.

2.9 Creation of coastal current systems

The two types of coastal current systems were created using the internal Rossby radius, (2.25) and Avicola and Huq's (2002) equations, (2.21) to (2.24). The internal Rossby radius equation describing the coastal region is shown below,

$$R_i = \frac{c}{f} = \frac{\sqrt{g' H_c}}{f} \tag{2.25}$$

This internal Rossby radius calculation differs from Avicola and Huq's (2.23), in that it uses the coastal wall depth, H_c, instead of the plume scale depth, h, and therefore is more representative of the model domain as the plume expands and develops over the model run. In order for the interior model grid resolution to be suitable for these coastal current systems, each internal Rossby radius was set to be 3 or more times larger than the grid resolution; see Table 2.1 for values. The latitude set for all simulations was 35° in the Northern Hemisphere, a representative latitude of the range of prominent river latitudes, 0° - 60°, and the coastal wall depth was set to 10 m for surface-advected plumes and 2 m for bottom-advected plumes. Therefore, the reduced gravity term was calculated using (2.25) to be used in Avicola and Huq's (2002) Equations, (2.21) and (2.23). The freshwater discharge term and the bottom slope term were then both adjusted in Avicola and Huq's (2002) Equations, (2.21) and (2.22), until the plume could be clearly categorized into a type, as seen in Figure 2.5. The surface-advected plume is a loose replication of Garvine's (1999) plume; the only differences are the latitude and discharge magnitudes.

Test runs with various timesteps for each type of coastal current system were then run to determine the maximum u-velocity found in these types of plumes for the CFL condition. The maximum u-velocities among several runs were 0.26 m s^{-1} for surface-advected and 0.20 m s^{-1} for bottom-advected. These values are comparable with typical tidal current speeds for the United States Atlantic coast, which has magnitudes O(0.10 – 0.25 m s^{-1}). As for the Pacific coast, typically O(0.02 - 0.08 m s^{-1}), the magnitudes are comparably larger (Battisti and Clarke 1982).

2.10 Analysis of data

After completing the model simulations, the model outputs were imported into MATLAB and analyzed with code written for this investigation to study the nondimensional downshelf, upshelf, and across-shelf propagation with time, as well as the changes in integrated vertical and horizontal salt fluxes and depth extent with time. Each item of study focused on a selected salinity anomaly contour located close to the edge of the plume, where more mixing with the ambient salinity water is known to occur (Wright and Coleman 1971 and Hetland 2005). The salinity anomaly was calculated based on Garvine (1999) and is expressed as,

$$s_g = \frac{S_a - S_g}{S_a - S_i} \tag{2.26}$$

where S_g is the output salinity from the model, S_a is the ambient ocean salinity (32), and S_i is the salinity of the freshwater (25 for surface-advected plumes; 22 for bottom-advected plumes). Salinity anomaly ranges from 0 to 1; the lower values indicate a smaller difference between the salinities and thus, the salinity value is closer to the ambient value. Therefore smaller salinity anomaly values were selected, 0.1 for surface-advected plumes and 0.25 for bottom-advected plumes, to represent the salinity anomaly contour of interest in the vicinity of the plume edge.

The evolution of the metrics for the specified salinity contour was used to analyze the dimensional changes in the coastal current system through time. The three regions representing these dimensions, in the plan view, are defined as and shown in Figure 2.12. The downshelf distance was the location of the farthest distance of the salinity contour of interest in the positive alongshelf direction from the x = 176 grid, or x ~ 291 km, the center of the freshwater discharge. The upshelf propagation was described as the farthest distance of the salinity contour of interest in the negative alongshelf direction from the x = 176 grid. The across-shelf bulge region, Figure 2.12 region A, was identified as the across-shelf distance of the selected salinity anomaly contour averaged across 2 internal Rossby Radii downshelf of x = 176, where the internal Rossby Radius varies depending on the plume type.

These three locations are important indicators of the growth of the plume through time. Figure 2.13 demonstrates the growth of the parameters with time for the surface-advected plume using a K_{z_b} and K_{s_b} magnitude of 5 x 10^{-6} m^2 s^{-1} and using MY2.5; remember, the surface-advected plume follows the 0.1 salinity anomaly contour. As shown, there is an increase in the size of the plume with time. The most growth is shown in the downshelf direction of the coastal current while changes in the upshelf distance and across-shelf distance are not as large. Therefore, these three parameters, downshelf, upshelf, and across-shelf distances, are useful for describing the key areas of growth for the plume in the various directions of growth. In addition, because plumes mix with ambient waters as they grow with time, the parameters also give information on the mixing coefficients calculated from the mixing scheme.

Depth is an important parameter to record in that the depth of the plume also changes with time. The depth extent of the surface-advected plume was calculated as the average depth of the contour of interest at 80% of the average across-shelf distance over the same alongshelf distance of the bulge (Figure 2.13 and 2.14), used in the across-shelf dimensional analysis, through time. Therefore, the depth of the plume is calculated at the same region of the plume, the across-shore edge, at all times. Comparisons in depth will focus on only the offshore edge of the plume. Figure 2.14 shows the side view of a surface-advected plume at various snapshots in time with a K_{z_b} and K_{s_b} magnitude of 5 x 10^{-6} m^2 s^{-1} and using MY2.5. The white line indicates the across-shelf distances where depth is recorded at 300 km downshelf. These graphs show an increase of depth with time for the depth parameter location. Depth is an important parameter used to examine the vertical mixing of the plume. With more vertical mixing, the plume will mix vertically, expand, and increase in salinity. Therefore, analyzing depth can be a useful indictor of the mixing within the plume.

Note that there is no calculation for depth for the bottom-advected plume. Since the bottom-advected plume extends to the bottom topography, the depth parameter calculation would always be the depth of the water column. Therefore, the calculation of depth for the bottom-advected plume is quite unnecessary since it would follow the bottom topography with time.

After these four metrics were recorded through time, they were nondimensionalized by dividing by the internal Rossby Radius (shown in Table 2.1). The internal Rossby Radius was used as a length scale to allow for ease in analyzing and comparing the results. The schemes were also quantitatively compared through a percent difference, to emphasize differences across schemes, using the equation below:

$$\%diff = 100 * \frac{metric_1 - metric_2}{metric_1} \tag{2.27}$$

where $metric_1$ is the average of the larger metric across the last ten days of simulation while $metric_2$ is the average of the lowest metric across the same time period. Therefore, the percentage values are only descriptive of Days 40 to 50.

Integrated horizontal and vertical salinity fluxes are also useful indictors of mixing in the coastal plumes. Salinity flux is defined as the flow of salt either in the horizontal or vertical directions, in this study. Therefore, salt can be used as a material tracer for mixing.

The integrated horizontal and vertical salinity fluxes with time for the selected contour anomaly were calculated using the equations,

$$S_{F_V} = \int_{y_{\min}}^{y_{\max}} \left(-K_s \frac{\partial S}{\partial z} \right) \partial y \qquad (2.28)$$
$$S_{F_H} = \int_{z_{\min}}^{z_{\max}} \left(A_m \frac{\partial S}{\partial y} \right) \partial z$$

where S_{F_V} solves for the vertical salt flux using the vertical diffusivity produced from the turbulence closure schemes, and S_{F_H} solves for the horizontal salt flux using the horizontal diffusivity produced from the Smagorinsky scheme. These flux calculations were located roughly one internal Rossby radius downshelf from the center of the freshwater outflow (at 300 km for the surface-advected currents and 297 km for the bottom-advected currents). The salt flux for the vertical and horizontal directions were assumed to be zero at the coast, across-shelf edge, bottom, and top. The salt flux was also assumed to decrease linearly from the last salt flux point within these boundaries to the last contour point on the boundary inner edge. The boundary for these calculations were considered to be values greater than the points on the second sigma level and values less than the points on the fourteenth sigma level; recall that z is negative. As for the y-direction, the boundaries started at the coast to 2.5 km and from 54.5 km to the across-shelf edge of the domain, shown in Figure 2.15.

In order to compare the plumes through time, all the metrics were also recorded for the salinity anomaly contours that were 10% above and 10% below the contour of interest; therefore, the salinity anomalies of 0.09 and 0.11 were used for the surface-advected and 0.275 and 0.225 were used for the bottom-advected plume. These values were then plotted as bars for each snapshot, where the bar range gives information on the changes in the metric. Larger ranges may be interpreted as the presence of a weaker salinity gradient, and smaller ranges indicate a stronger salinity gradient. When comparing across multiple runs for a metric, overlapping ranges are considered similar metric results. These comparisons will be presented in the next chapter.

2.11 Timestep sensitivity analysis

A timestep sensitivity test for the nondimensional downshelf, upshelf, and across-shelf distances was performed for the plumes and the vertical mixing schemes using a K_{z_b} and K_{s_b} magnitude of 5 x 10^{-6} m^2 s^{-1}, where this value was directly applied to the constant scheme and used as the background value for the other schemes. The timestep analysis added 24 more model runs to the study. These tests showed that variations in timestep, within each scheme and type of plume, had no major effect on the resulting metrics. However changes in scheme had a larger effect on the plume than changes in timestep.

The next two subsections focus on the nondimensional downshelf distance and briefly cover the upshelf and offshore distances, shown in Figures 2.16 through 2.23, which compare various internal timestep (DTI) and external timestep (DTE) pairs. In future sections, the effects of the schemes on the resulting nondimensional distances will be discussed.

2.11.1 Surface-advected timestep analysis

The nondimensional downshelf distance for three timestep pairs for the surface-advected plume using MY2.5 is shown in Figure 2.16. The resulting downshelf distance for DTI = 614.68 s with a DTE = 13.97 s is similar to that of DTI = 550.00 s with DTE = 11.00 s. A much more drastic change occurs when the timesteps are further decreased to DTI = 92.00 s and DTE = 9.20 s. While all simulations result in a similar growth curve shape, the smallest timestep pair is about 2% larger than the other two timesteps.

Figure 2.17 shows the nondimensional downshelf distance results from the three timesteps for the two P&P. Like the timestep comparison for MY2.5, the results for DTI = 614.68 s and DTI = 550.00 s are similar, but when DTI = 92.00 s, higher nondimensional distance results. In this graph, P&P (B) is affected more by the timestep changes than P&P (A); the runs with DTI = 92.00 s reaches a difference of 3% larger for P&P (A) and 5% larger for P&P (B), when compared to the other timesteps.

The overall effect of changes in timestep and changes in mixing scheme is demonstrated in Figure 2.18. The difference between schemes, constant and P&P (A), is about 10% for a DTI = 614.68, where the behaviors of the individual schemes are distinct even with changes in timestep. A grouping pattern for all the mixing schemes exists, where each scheme timestep results are grouped with DTI = 92.00 s as the highest nondimensional distance and the timesteps, DTI = 614.68 s and 550.00 s, are close and lower in downshelf extent. In general, the constant scheme timesteps have the least extents while P&P (B) timesteps have the greatest extent. However, the difference between the three timestep pairs varies according to the scheme used.

Figure 2.19 shows an ordering of timestep results due to scheme changes for the nondimensional upshelf and across-shelf for the bulge. While these timestep and scheme orderings are different from the nondimensional downshelf results, the trends are consistent across the schemes. This observation suggests that even with changes in timestep, differences in results among the closure schemes for the surface-advected plume are still present when comparing across schemes; the ordering of the mixing schemes and the ordering of the timesteps are the same when comparing the results. In this investigation, to account for any uncertainties, all surface-advected plumes, including buoyancy forcing with and without tides, had DTI = 614.68 s and DTE = 13.97 s.

2.11.2 Bottom-advected timestep analysis

Four timestep pairs were examined for bottom-advected plumes. The bottom-advected nondimensional downshelf distance results while using MY2.5 is shown in Figure 2.20. The run with the largest nondimensional downshelf distance, DTI = 200.00 s, is 2% larger than the smallest, DTI = 981.56 s.

Figure 2.21 shows the downshelf distance results for the P&P schemes. The choice of timestep has little effect on the downshelf distance but does result in significant differences in other metrics (Figure 2.22, which is discussed later). Similar to the surface-advected plumes, P&P (B) has more of an effect due to timestep changes than P&P (A) for bottom-advected plumes. The timestep differences are 6% for P&P (B) and a 3% for P&P (A).

All bottom-advected timestep runs are shown in Figure 2.23. Note that the large decrease in the constant scheme runs at Day 32 is due to the break of a downstream eddy from the plume; eddy mixing will be presented in future sections. The difference between the schemes is much larger than the discrepancies between the timesteps; when looking at a DTI equal to 200.00 s, MY2.5 is 13% larger than P&P (B). The maximum difference between timesteps for the downshelf distance was shown in Figure 2.21 with 6%. The nondimensional upshelf and across-shelf for the bulge timestep comparisons also emphasize the effect of the schemes compared to the effect of timestep on the plume, shown in Figure 2.22. The upshelf graph has a 59% difference across the schemes while within a scheme with various timesteps, the difference grows up to 27%. The across-shelf also results in the same, where within a scheme, the timestep results vary only about half as much in extent as when comparing across schemes with the same timestep.

Therefore, inherent differences between the schemes are not affected by the use of different timesteps, shown in Figures 2.23 and 2.22. Like the surface-advected plumes, the schemes appear to group according to the scheme rather than the timestep variations. In Figure 2.23, MY2.5 and constant schemes are grouped as the higher distances while both P&P schemes show the least extent. A different grouping behavior is shown in Figure 2.22, but the schemes are still individualistic in behavior.

In this investigation, the bottom-advected plumes used DTI = 550.00 s and DTE = 11.00 s for the buoyancy forcing portion of the study. However, with the introduction of tidal forcing, a timestep of DTI = 200.00 s and DTE = 4.00 s was utilized to account for changes in the CFL criteria.

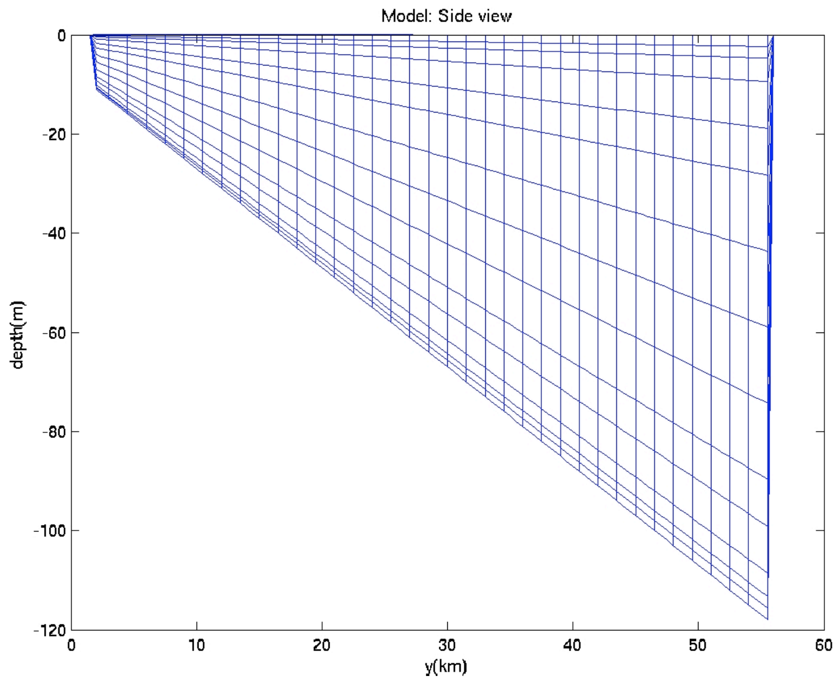

Figure 2.1: The model side view shows the sigma level coordinate system, with 15 levels. It is important to note that the vertical resolution decreases with distance farther offshore.

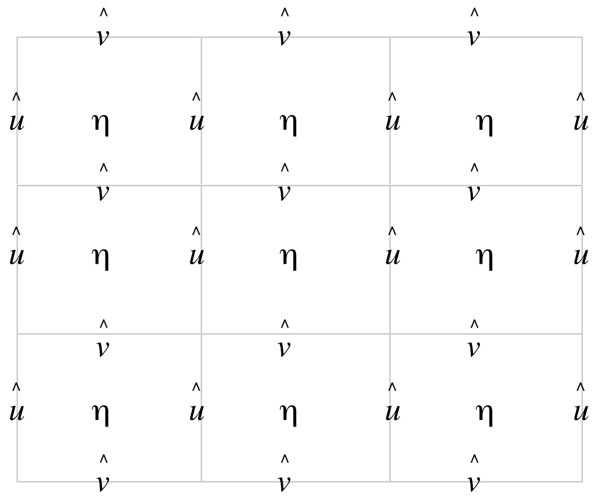

Figure 2.2: The Arakawa C staggered grid based on Kantha and Clayson (2000). Note the different locations of alongshelf velocity variable, $\hat{u}$, the across-shelf velocity variable, $\hat{v}$, and the surface elevation, η on the grid.

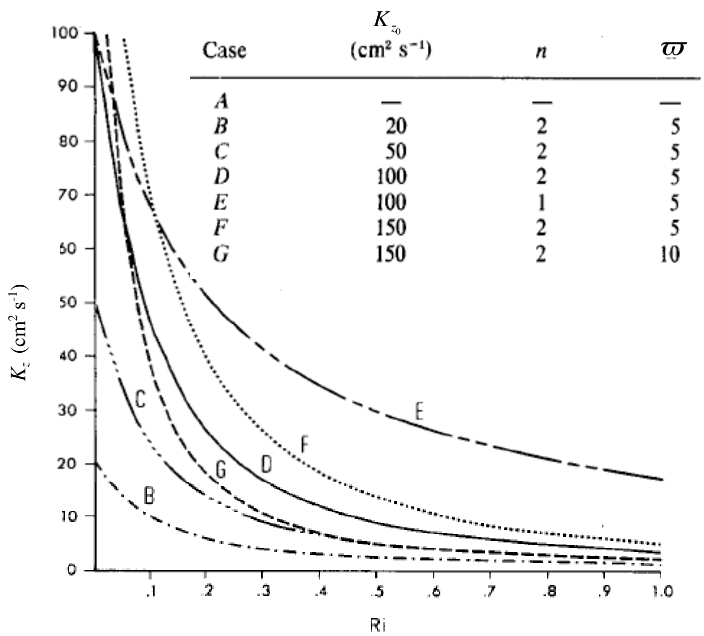

Case	K_{z_0} (cm^2 s^{-1})	n	ϖ
A	—	—	—
B	20	2	5
C	50	2	5
D	100	2	5
E	100	1	5
F	150	2	5
G	150	2	10

Figure 2.3: A table and graph from Pacanowski and Philander (1981) showing the dependence of the viscosity on the Richardson number. This graph will be used to validate the implementation of the Pacanowski and Philander (1981) turbulence closure scheme, discussed later in this section.

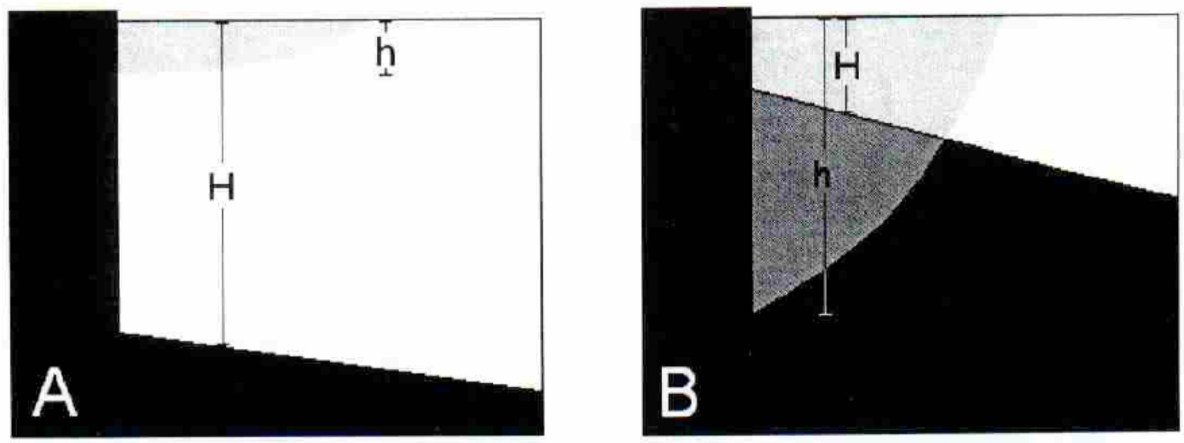

Figure 2.4: Avicola and Huq (2002) show a schematic representation of the surface-advected and bottom-advected plumes in A and B. The figures, however, show a spatial representation of the nondimensional numbers and their resulting behavior. The lightly shaded regions illustrate the plume area and the solid line shows the location of the plume front.

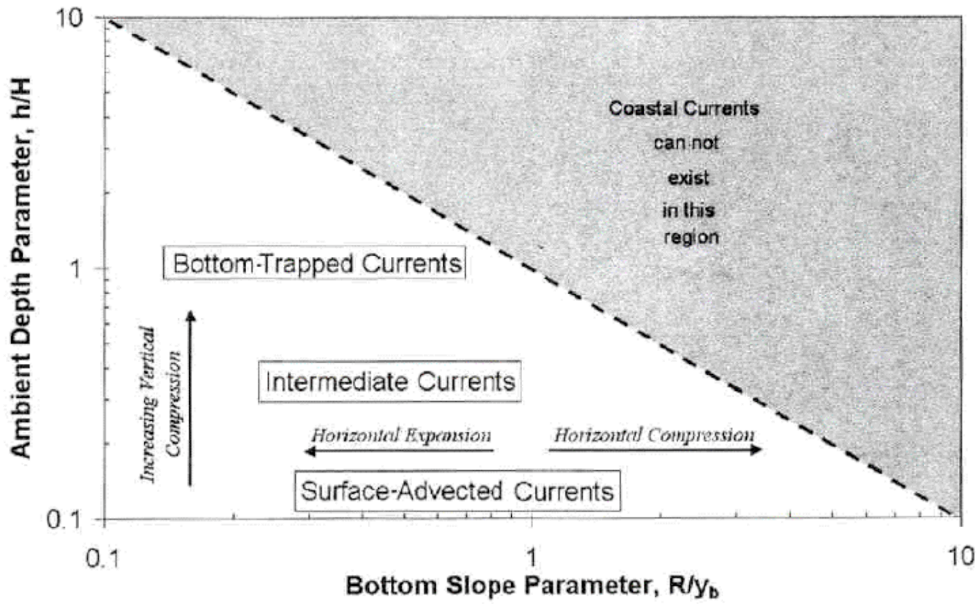

Figure 2.5: Diagram from Avicola and Huq (2002) that describes the types of coastal current plumes depending on the two nondimensional values.

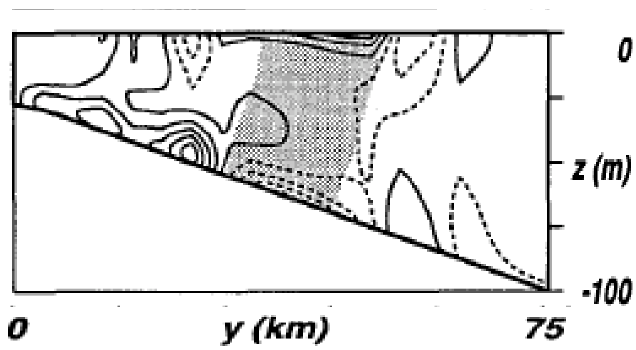

Figure 2.6: A bottom-trapped plume is shown from Chapman and Lentz (1994), where cross-shore velocities are shown at Day 60 of their model run. The contours show the across-shelf velocities with contours from -0.0225 to 0.0375 m s^{-1} and intervals of 0.005 m s^{-1}. Positive, offshore contours are solid lines and negative, onshore contours are dashed lines. The shaded region represents the location of the density front.

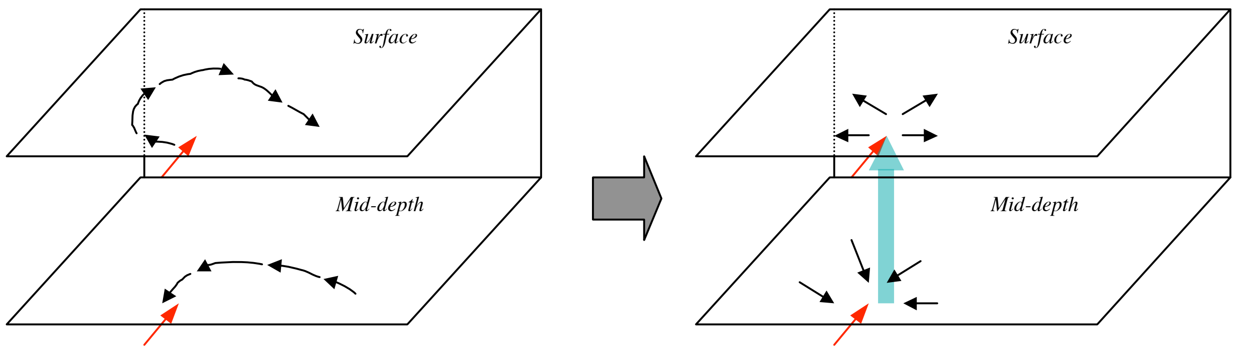

Figure 2.7: The cause for upshelf movement is shown for the surface and at mid-depth (based on Yankovsky 2000). Cyclonic movement develops at mid-depth and creates convergence near the inlet. At the surface, due to continuity, the water diverges. The red arrow shows the location of the freshwater discharge, the black arrows show the coastal plume flow, and the larger blue arrow shows the movement of water due to continuity.

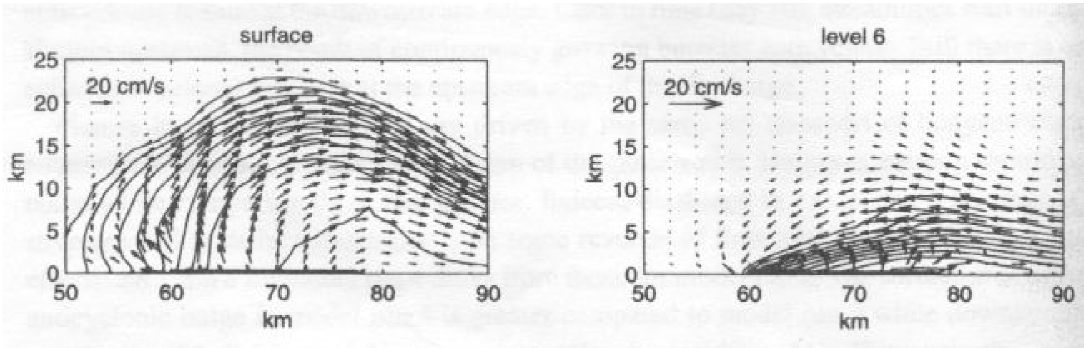

Figure 2.8: From Yankovsky (2000), Day 5 of the model run is graphed at the surface and at mid-depth. The velocity field (cm s^{-1}) is shown by the black arrows while the contours show the salinity anomaly. The bold line along the x-axis represents the location of the freshwater inlet.

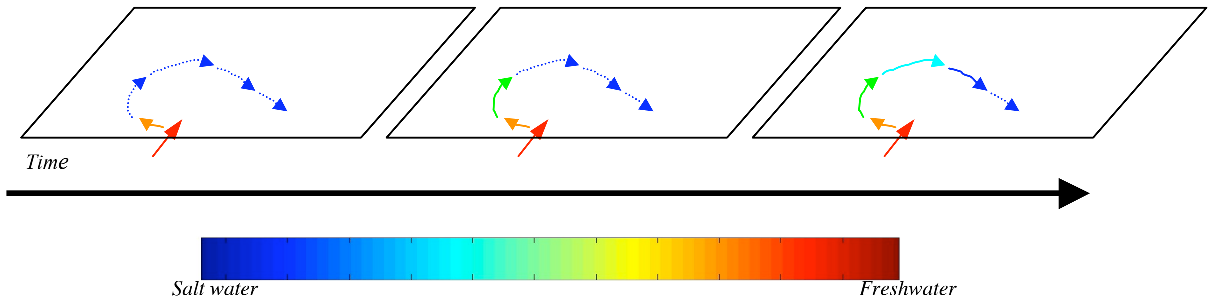

Figure 2.9: This cartoon explains the shift of the freshest water to move upshelf of the inlet with time. The dotted arrows show the flow field before the water parcel reaches the specific location. The solid arrow shows the salinity of the water as it circulates around the bulge. With time and distance, mixing causes the freshest water to remain upshelf of the inlet.

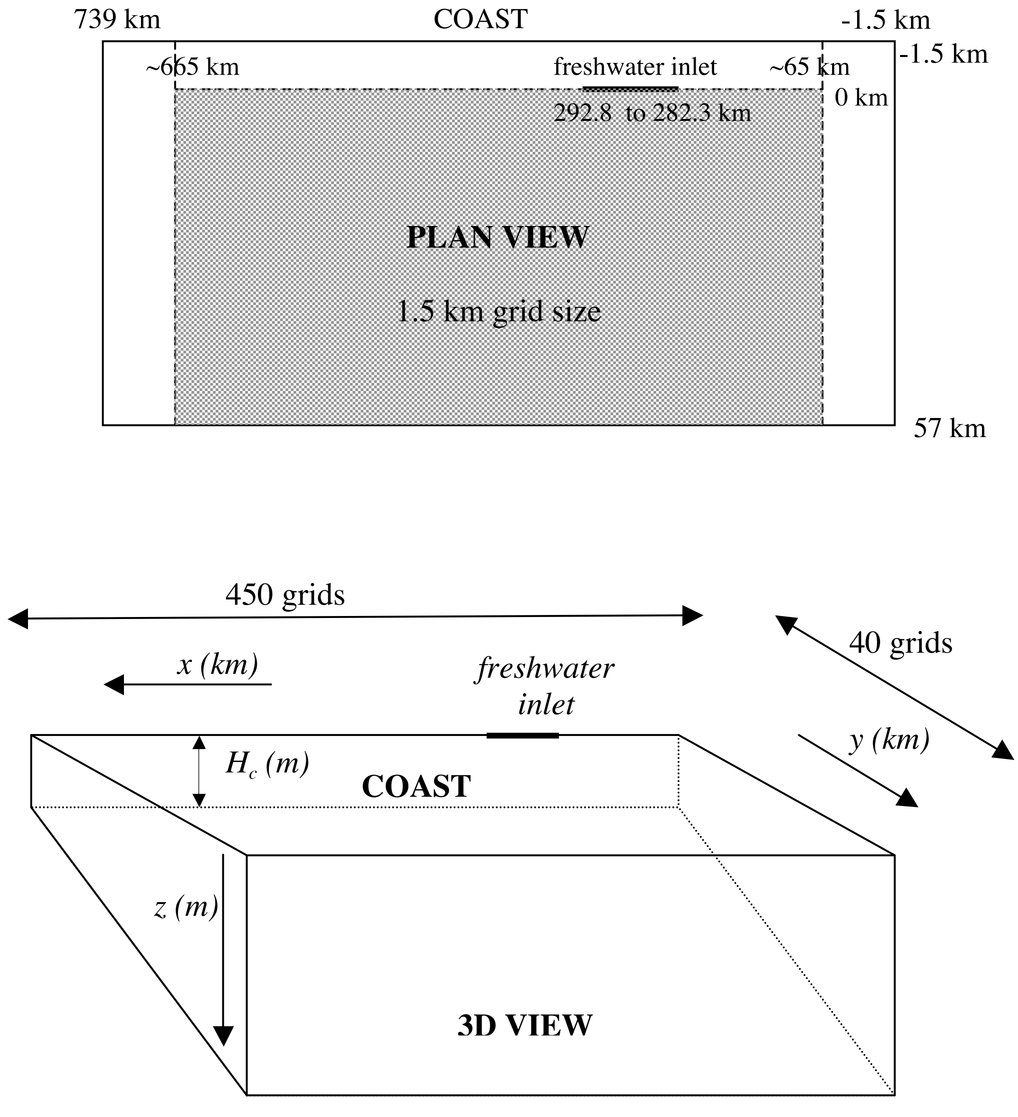

Figure 2.10: The idealized model domain in plan view (top) and three-dimensional view (bottom). The model extends 739 km alongshelf and 57 km across-shelf. The coastal wall depth, H_c, and bottom depth, z, of the domain vary depending on the type of plume. The freshwater inlet is located at x = 170 or 282.3 km from the boundary.

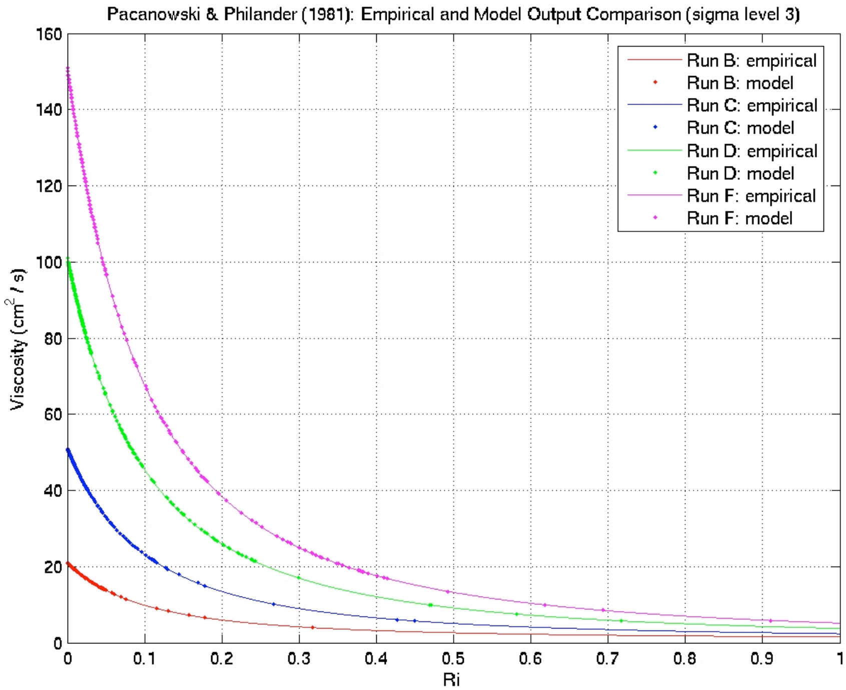

Figure 2.11: Verification of P&P implementation into the model. The graph compares the Ecom3d model output of the viscosity to the empirically calculated results using (2.13).

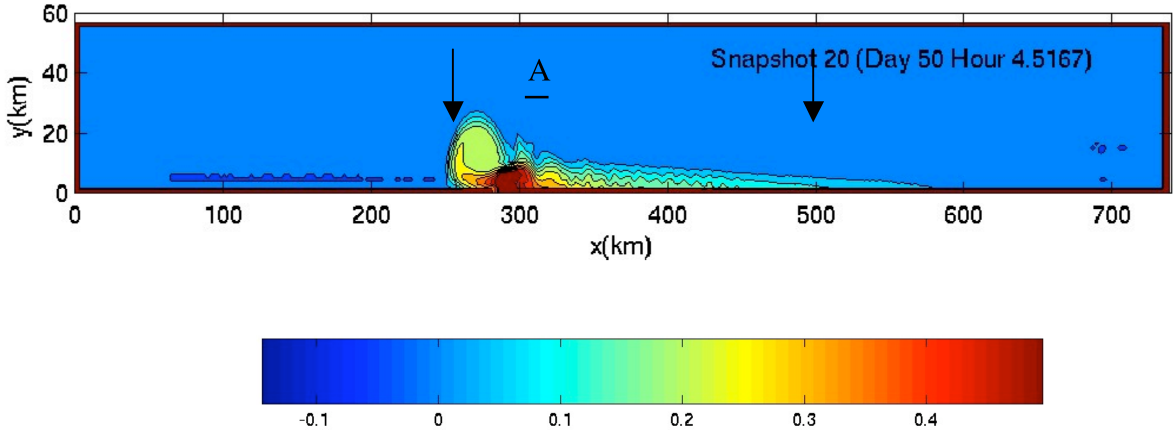

Figure 2.12: Snapshot of buoyant plume showing the four areas of focus for plume dimensional analysis through time are shown by the black arrows and black lines. The arrow located roughly around 250 km indicates the upshelf extent of the surface-advected plume while the arrow roughly around 500 km shows the downshelf extent. Region A represents the area covered by the bulge across-shelf distance.

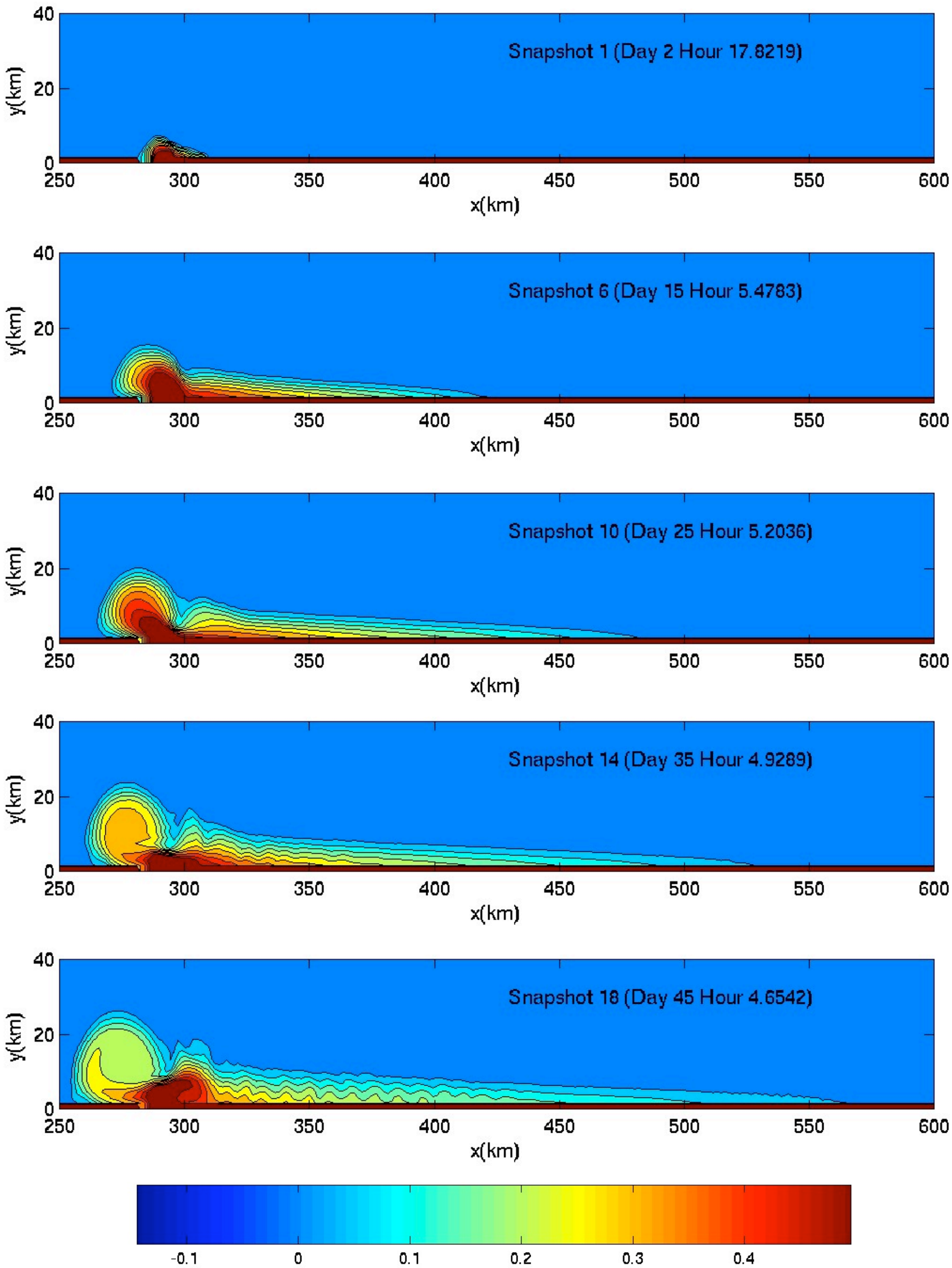

Figure 2.13: Plan view of the evolution of the surface-advected plume using the Mellor-Yamada 2.5 scheme with a K_{z_b} and K_{s_b} of 5 x 10^{-6} m^2 s^{-1}. The salinity anomaly is shown by the colored contours.

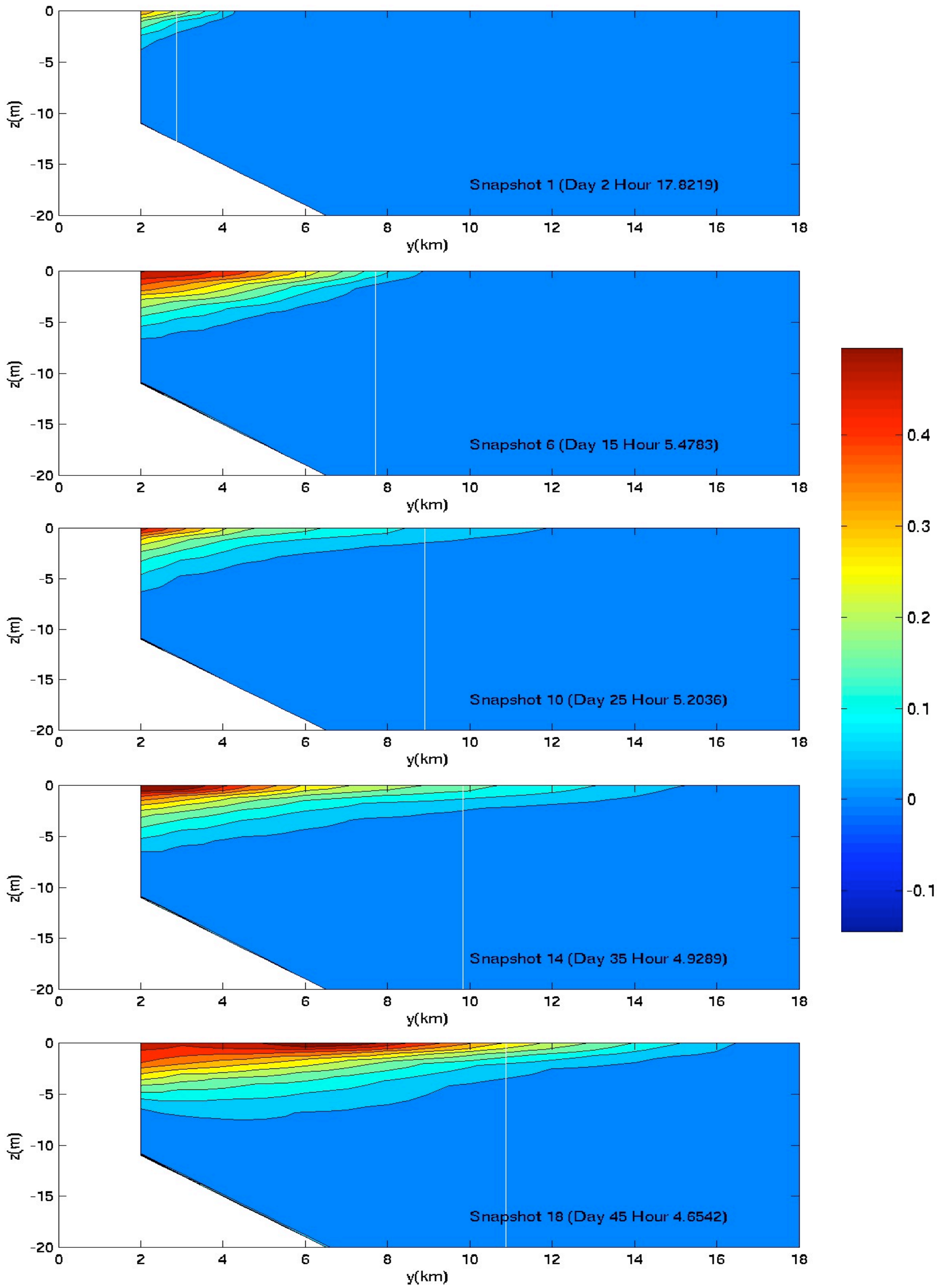

Figure 2.14: Cross-sectional view at 300 km of the evolution of the surface-advected plume using the Mellor-Yamada 2.5 scheme and a K_{z_b} and K_{s_b} of 5 x 10^{-6} m^2 s^{-1}. The colored contours represent the salinity anomaly. The vertical white line indicates the position at which the depth of the plume is calculated. This cross-section is located approximately one internal Rossby Radius downshelf of the inlet.

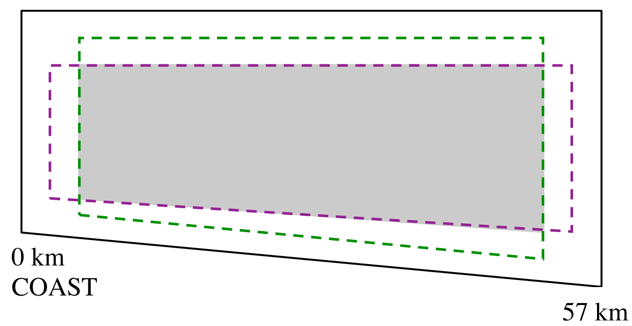

Figure 2.15: The region of calculated salt flux for integration is shown in the shaded region. Note that both point-by-point salt fluxes are in between grid points. The dashed regions are areas where distance values were utilized for integration purposes (green dashed for integrated horizontal salt flux and purple dashed for integrated vertical salt flux) and where salt flux is assumed to be zero. The white region was not used in the integrated salt flux calculations.

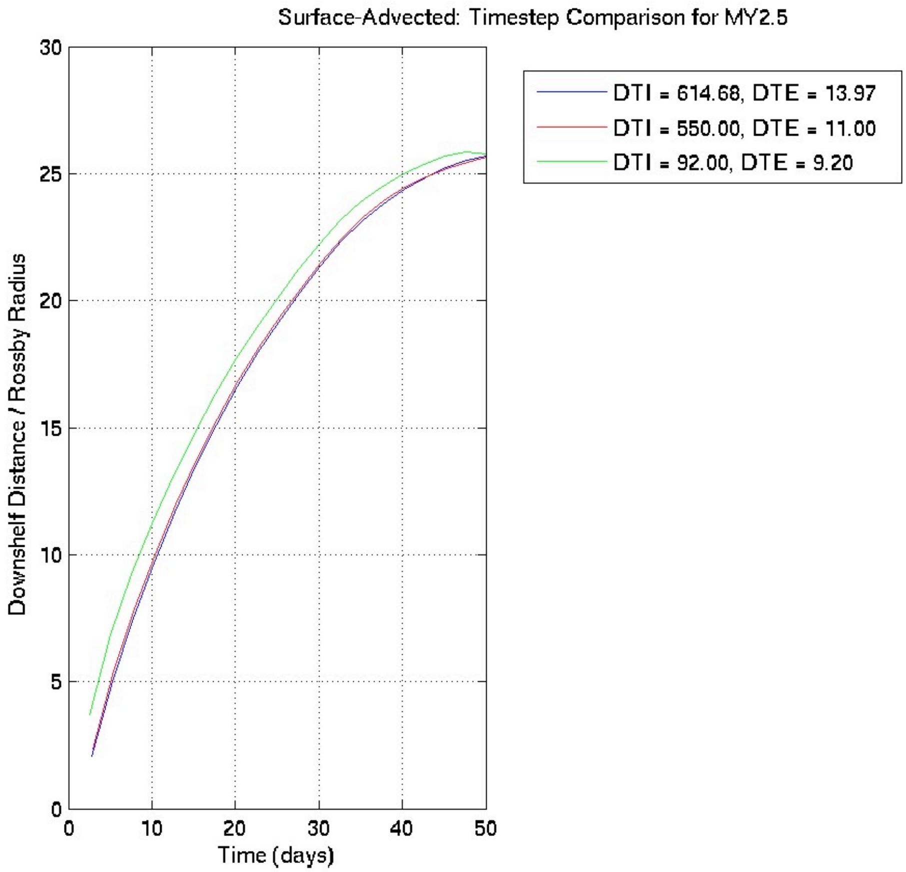

Figure 2.16: The temporal evolution for the nondimensionalized downshelf distance of the surface-advected plume for various timesteps using MY2.5 with a K_{z_b} and K_{s_b} of 5 x 10^{-6} m^2 s^{-1}.

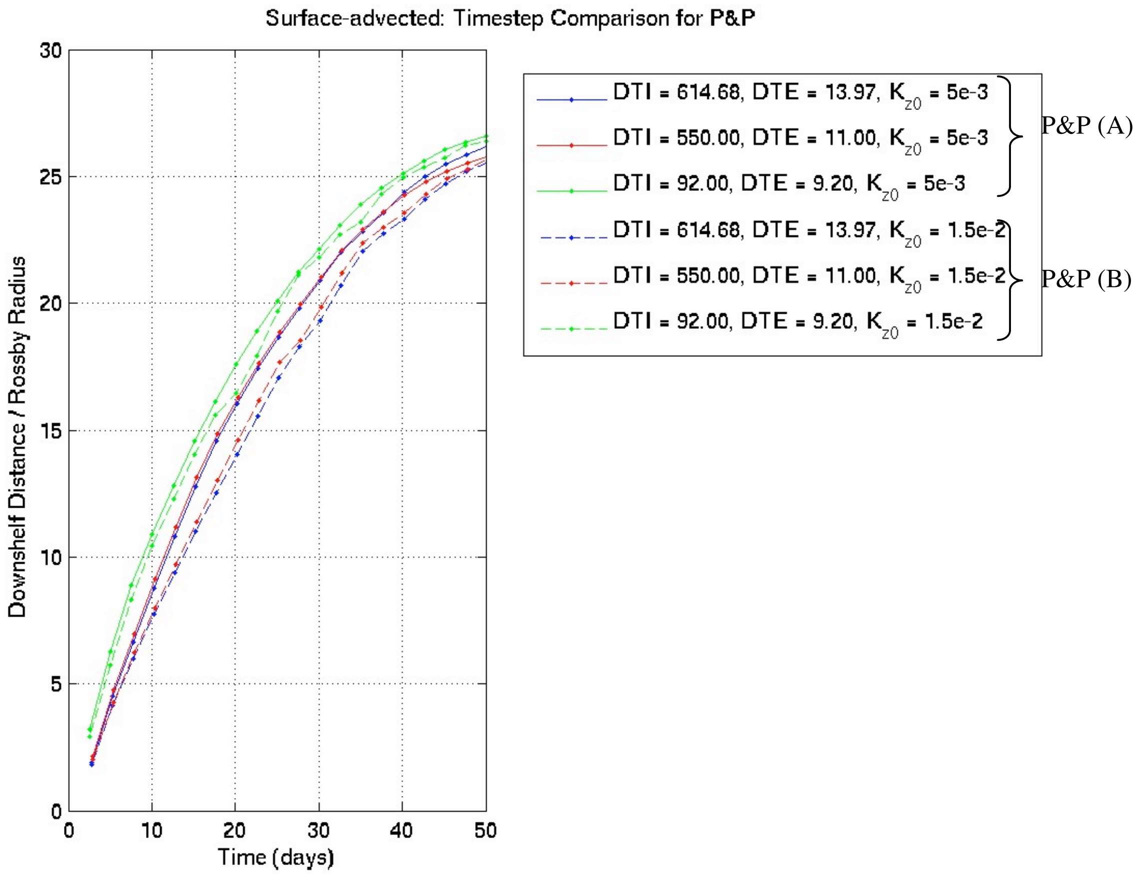

Figure 2.17: The temporal evolution for the nondimensionalized downshelf distance of the surface-advected plume for various timesteps using both P&P with a K_{z_b} and K_{s_b} of 5 x 10^{-6} m^2 s^{-1}.

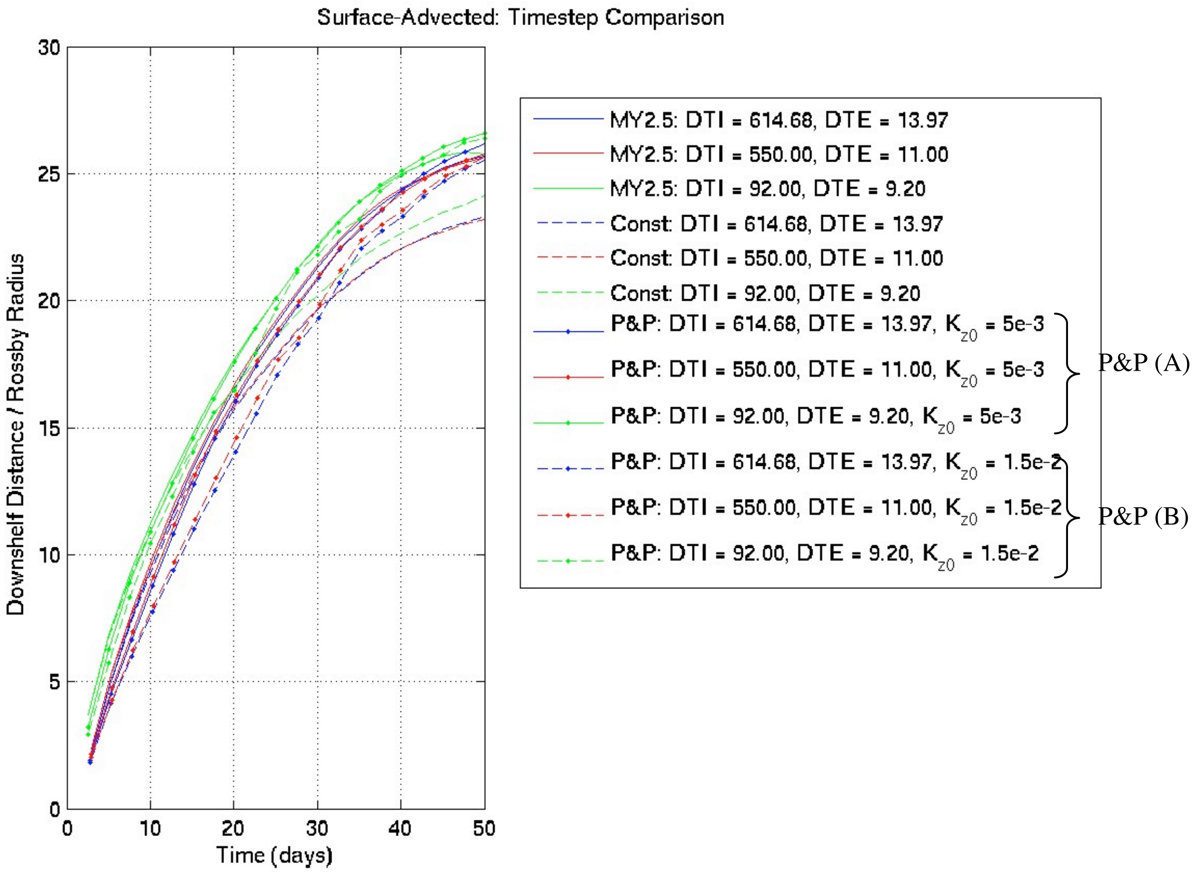

Figure 2.18: The temporal evolution for the nondimensionalized downshelf distance of the surface-advected plume for various timesteps when using all schemes with a K_{z_b} and K_{s_b} of 5 x 10^{-6} m^2 s^{-1}.

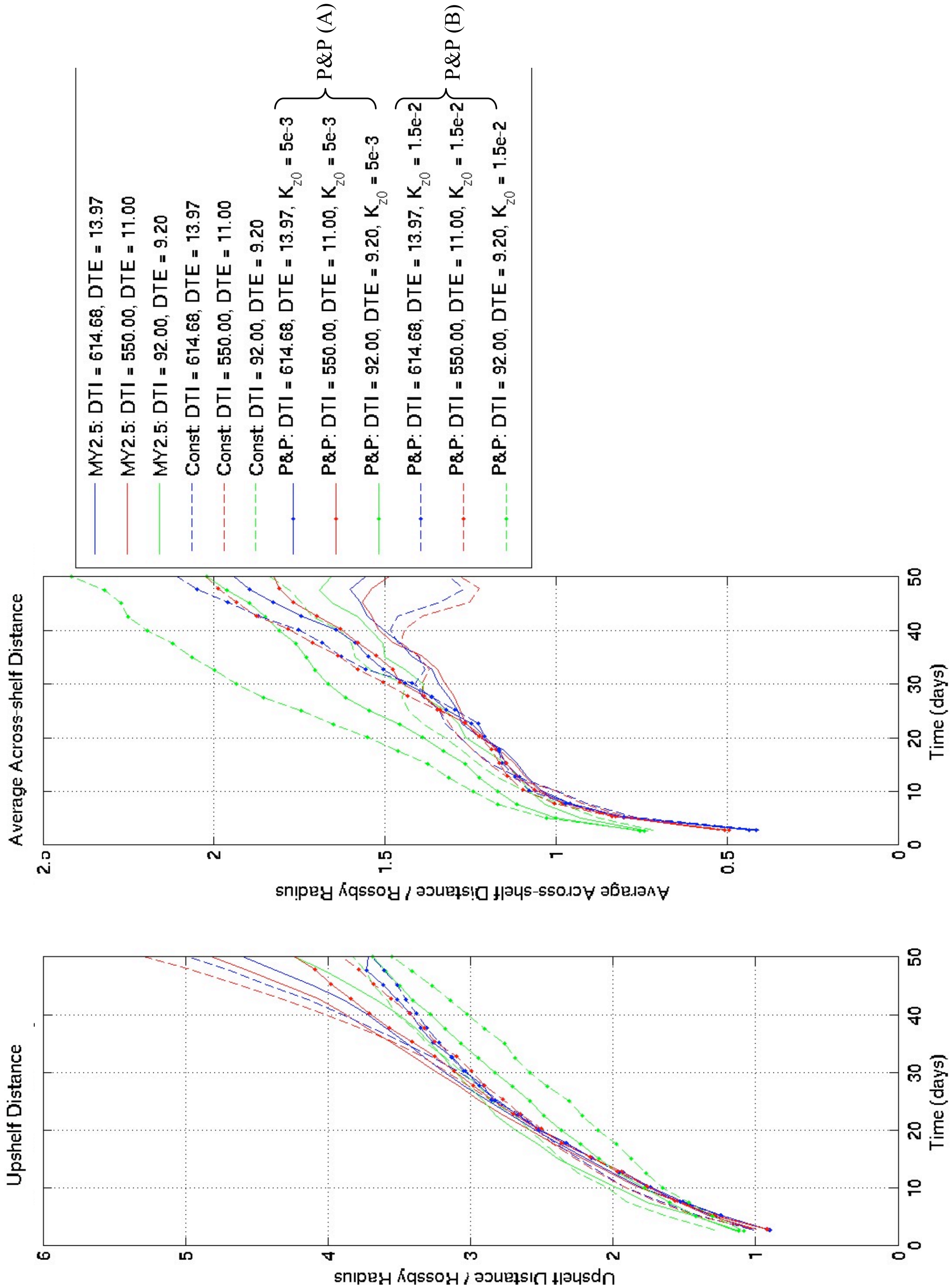

Figure 2.19: The temporal evolution for the nondimensionalized upshelf and across-shelf bulge distance for the surface-advected plume when using various timesteps for all schemes with a K_{z_b} and K_{s_b} of 5 x 10^{-6} m^2 s^{-1}.

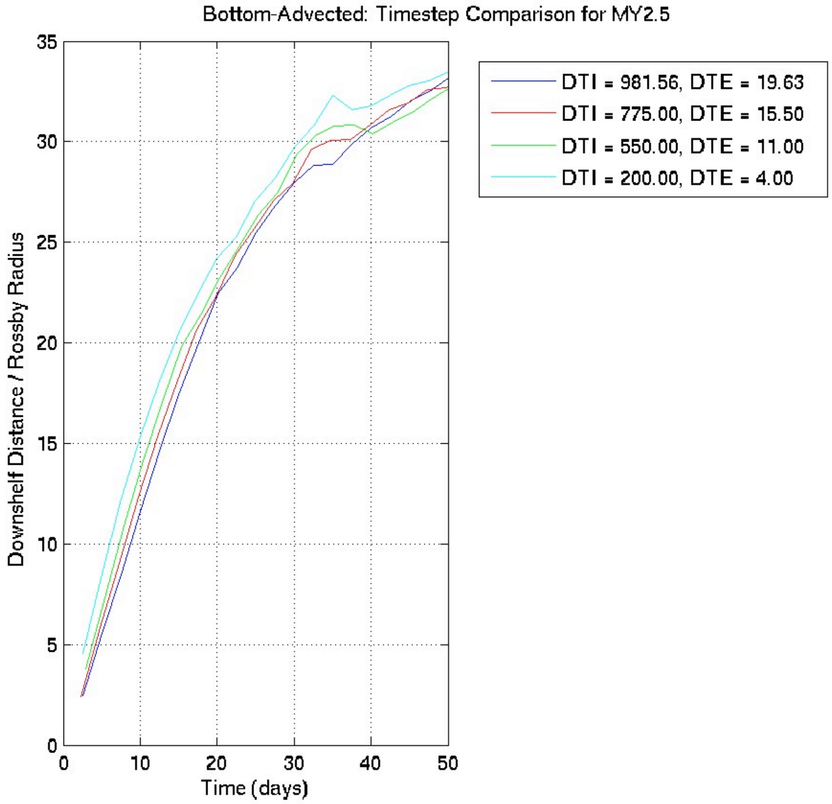

Figure 2.20: The temporal evolution for the nondimensionalized downshelf distance of the bottom-advected plume using MY2.5 for various timesteps with a K_{z_b} and K_{s_b} of 5 x 10^{-6} m^2 s^{-1}.

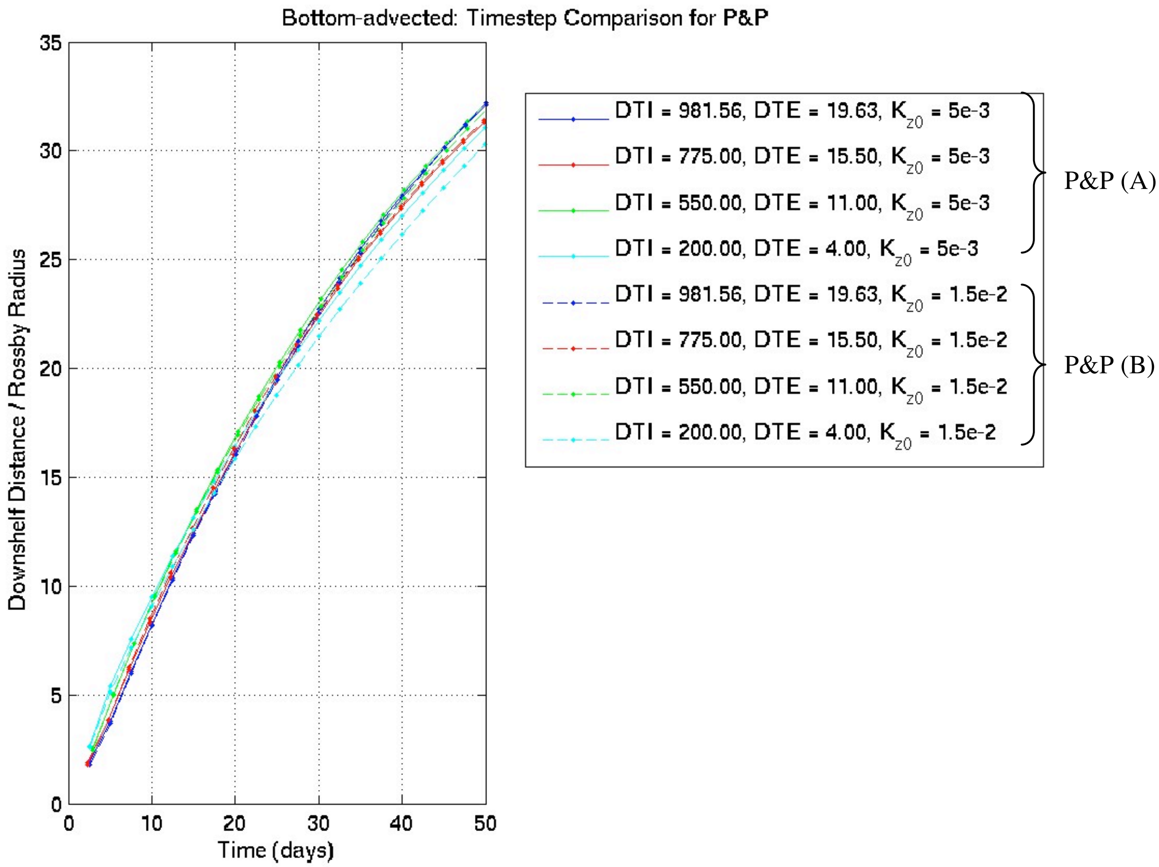

Figure 2.21: The temporal evolution of the nondimensional downshelf distance for both P&P using a K_{z_b} and K_{s_b} of 5 x 10^{-6} m^2 s^{-1} is shown using various timesteps for the bottom-advected plume.

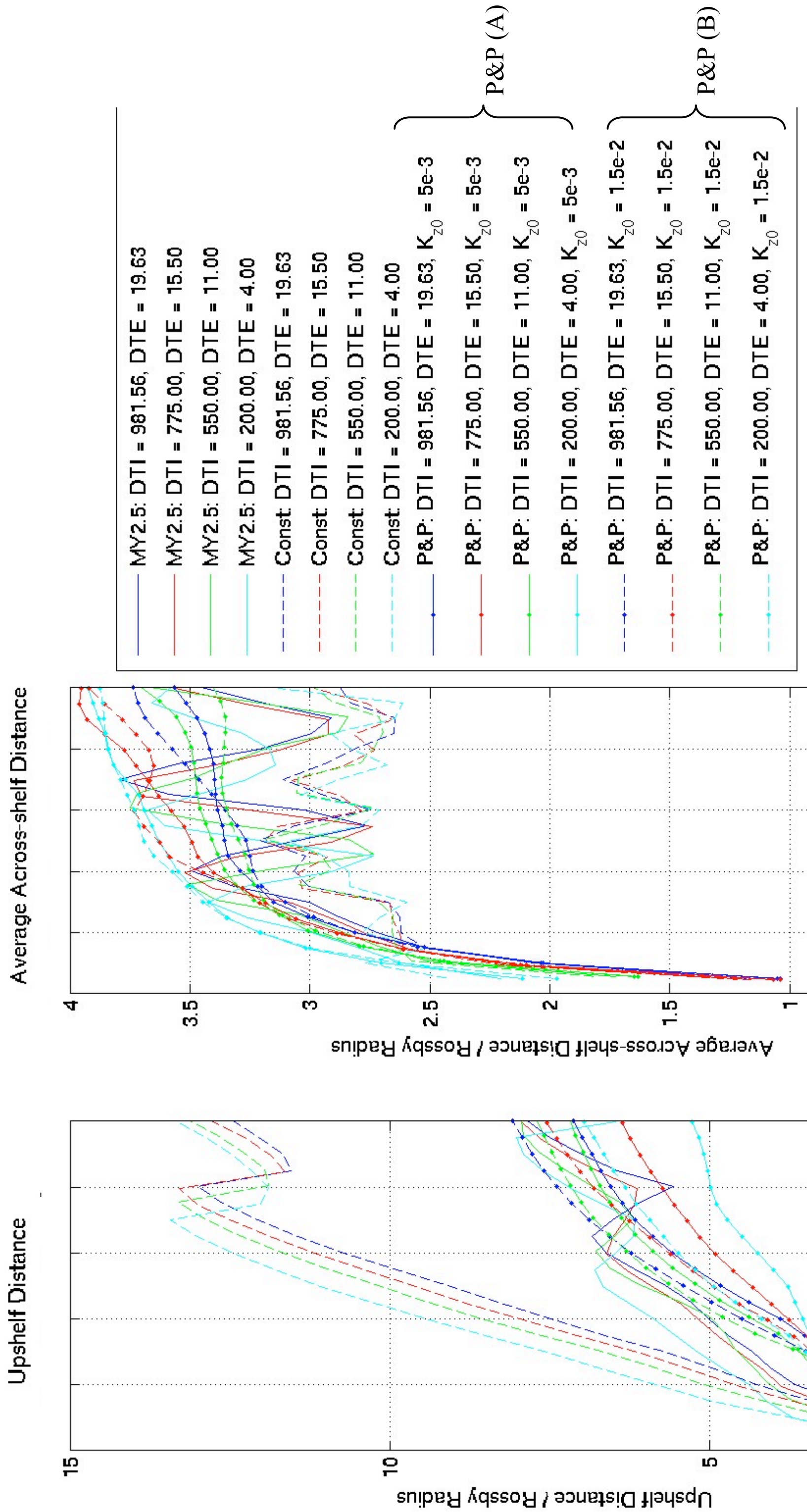

Figure 2.22: The temporal evolution for the nondimensionalized upshelf and across-shelf bulge distance of the bottom-advected plume using all schemes with a K_{z_b} and K_{s_b} of 5 x 10^{-6} m^2 s^{-1} for various timestep are shown.

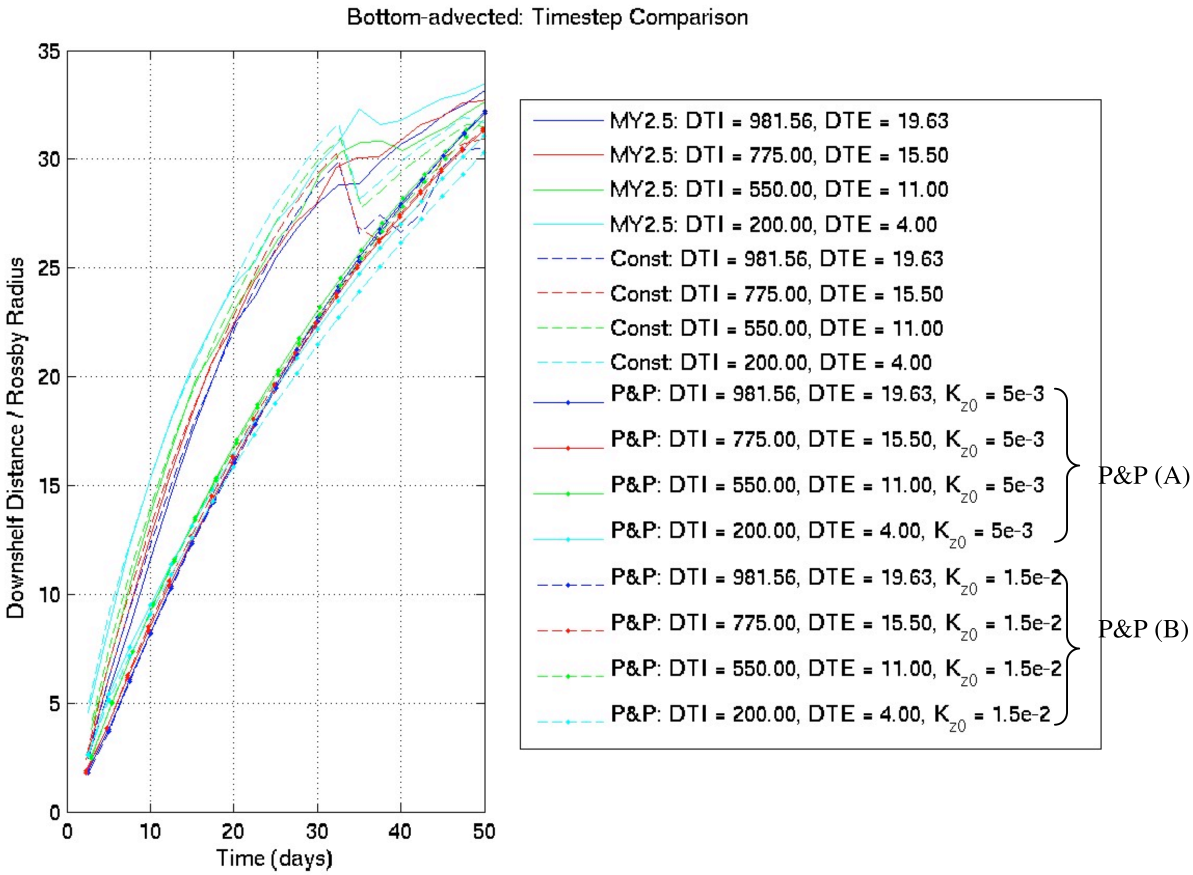

Figure 2.23: The temporal evolution for the nondimensionalized downshelf distance of the bottom-advected plume using all schemes with a K_{z_b} and K_{s_b} of 5 x 10^{-6} m^2 s^{-1} for various timestep is shown. The large jump in nondimensional extent around Day 32 for the constant scheme is due to the breakage of a downstream eddy for all the timesteps.

CHAPTER 3

RESULTS: BUOYANCY FORCING

In this chapter, the nondimensional downshelf (X_{DN}), upshelf (X_{UP}), and across-shelf (Y_{AC}) distances and horizontally integrated vertical (SF_V) and vertically integrated horizontal (SF_H) salt fluxes and background viscosity/diffusivity (K_{z_b} and K_{s_b}) will be abbreviated as shown in the parentheses. The downshelf and upshelf metrics describe the farthest downstream or upshelf point of the plume for the specified salinity anomaly contour, where the surface-advected plume used a contour of 0.10 and the bottom-advected used a contour of 0.25. The across-shelf distance is the averaged offshore extension of the specified salinity anomaly contour across 2 internal Rossby Radii downshelf of the freshwater inlet. The depth is averaged across the same Rossby Radii distance as the across-shelf in the x-direction and is taken at 80% of the averaged across-shelf distance in the offshore direction. The salt fluxes are integrated vertically or horizontally (y-direction) at one internal Rossby radius downshelf of the inlet (at 300 km for surface-advected plumes and at 297 km for bottom-advected plumes).

These metrics are then plotted with ranges (shown by the errorbar symbols) representing the location of the salinity anomaly contour that is 10% above and 10% below the contour of interest.

3.1 Evolution of the coastal plume

The evolution of both surface- and bottom-advected plumes are first examined to determine the overall features of the evolution of the plume.

3.1.1 Evolution of the surface-advected plume

Examination of the surface-advected plume at Days 2, 25, and 50 using MY2.5 with a K_{z_b} and K_{s_b} of 5 x 10^{-6} m^2 s^{-1} (Figure 3.1) reveals that the dominant direction of plume growth is in the downshelf direction, with sizable but reduced expansion in the upshelf direction and the across-shelf directions. The upshelf propagation is due to the temporal growth of the anticyclonic bulge, which develops upshelf of the freshwater inlet. The freshest pool of water collects upshelf and then circulates into the anticyclonic bulge (Yankovsky 2000). This anticyclonic bulge extends much further across-shelf than the coastal current downshelf of the freshwater inlet. The depth of the coastal current remains roughly the same throughout the run due to an increase in across-shelf distance rather than in depth; Figure 3.2 shows the cross-sectional snapshots taken at Days 2, 25, and 50 at 300 km downshelf, one internal Rossby radius downshelf of the freshwater inlet.

Examination of the temporal evolution plume parameters discussed above (Figure 3.3) reveals that the X_{DN}, X_{UP}, and Y_{AC} distances all increase with time. The SF_V slightly increases while the SF_H slightly decreases, and the depth roughly stays the same.

3.1.2 Evolution of the bottom-advected plume

The evolution of the bottom-advected plume is shown in Figures 3.4 to 3.7 using MY2.5 with K_{z_b} and K_{s_b} equal to 5 x 10^{-6} m^2 s^{-1}. This plume differs from the surface-advected plume in both initial conditions and the characteristic dynamics of the plume. As a result, the plume shape and metrics evolve differently. As in the surface-advected plume, the bottom-advected plume's dominant direction of growth is downshelf with smaller growth in the upshelf and across-shelf directions (Figure 3.4). However, there are differences between the plumes. The across-shelf extension of the anticyclonic bulge for the bottom-advected plume is comparable to the plume's subsequent coastal current. In addition, more of the freshest water accumulates immediately outside of the freshwater inlet due to the higher freshwater discharge rate, lower salinity, and a shallower bottom. A comparison of the flow and salinity fields of the surface-advected (top panel of Figure 3.5) and bottom-advected plume (bottom panel) at Day 50 reveals large differences in flow field, salinity anomaly gradients, and shape of the plumes.

Cross-sectional views of the bottom-advected plume (Figure 3.6) illustrate the across-shelf growth of the plume. Since the cross-sections are located one internal Rossby Radius downshelf (at 297 km) of the inlet, interactions between the bottom and the plume will be small (top panel Figure 3.6) and eventually increase as the plume develops (middle and bottom panels, Figure 3.6).

Note that there is no calculation for depth for the bottom-advected plume. Since the plume extends to the bottom topography, the depth parameter calculation would always be the depth of the water column.

Examination of the plume metrics (Figure 3.7) reveals that although the plume oscillates across a maximum across-shelf distance range, most likely due to low frequency meanderings in the plume, the movement across-shelf for the bulge slows in growth and roughly remains the same after Day 18. Kourafalou et al. 1996a and Garvine 1999 also noted meandering of the plume in their coastal plumes. A decrease in growth to final across-shelf distance is a sign of bottom-trapping of the plume (Chapman and Lentz 1994), where the bottom-advected plume becomes ‘trapped’ at a certain point across-shelf, as discussed earlier.

Overall, there is an increase in X_{DN}, X_{UP}, and Y_{AC} distances with time, like the evolution of the surface-advected plume. However, the Y_{AC} slows in growth after 18 days. The integrated salt fluxes, however, remain roughly the same through the 50 day run. The oscillating metrics are due to the meanderings found in the plume.

3.1.3 Plume instabilities and shedding

Plume shedding can be found in both surface- and bottom-advected plumes. The most downshelf edge, or nose, of the plume is a region where Kelvin-Helmholtz instabilities are known to develop beneath the current and along the across-shelf edge near the nose (Griffiths and Hopfinger 1983). These instabilities are not a result of the rotational forces but rather the differences in flow. With time, the nose of the plume slows due to inertial waves caused by the turbulence created vortices and waves at depth (Griffith and Hopfinger 1983). As the instabilities develop, portions of the plume may become disconnected from the plume, move downshelf or across-shelf and mix into the ambient ocean. An example of plume shedding in the bottom-advected plume (Figure 3.8, around x = 422 km) shows velocities moving towards the coast, resulting in the separation of a pocket of fresher water from the plume (same panels, x ~ 422 to 430 km). Previous studies have identified eddies, created from instabilities of the plume, shedding downshelf of coastal plumes (Whitehead and Chapman 1986). Upshelf shedding may also occur; as discussed earlier in the section on upshelf propagation, the shedding upshelf is dependent on the mixing and currents present in the flow field (Yankovsky 2000).

3.2 General dependence of plume on viscosity/diffusivity magnitudes

This section focuses on the effects of large changes in K_{z_b} and K_{s_b} magnitude on the metrics of the plume. Since density stratification tends to decrease vertical mixing in most schemes, resulting in complications in the analysis (Tilburg et al. 2007), a constant value of vertical viscosity/diffusivity is first used to simplify the analysis and examine first order responses of the plume to viscosity.

3.2.1 The surface-advected plume

Large-scale variations in the K_{z_b} and K_{s_b} values have significant effects on the plume structure. As shown with the constant scheme, an increase in the K_{z_b} and K_{s_b} magnitude leads to a decrease in the X_{DN} (top left panel in Figure 3.9) and Y_{AC} distances (middle left panel) and an increase in depth (middle right panel), where a decrease in plume size in the horizontal and increase in plume size in the vertical is expected due to the increase of vertical mixing expanding the plume in depth (Kourafalou et al 1996a and Garvine 1999). Variations in the K_{z_b} and K_{s_b} also affect the salt fluxes (bottom panels) and upshelf distance (top right panel).

The effect of variations in the K_{z_b} and K_{s_b} magnitudes is consistent for all vertical mixing schemes (Figures 3.10 through 3.15). MY2.5 and P&P, like the constant scheme, both show a decrease in X_{DN} (Figure 3.10) and Y_{AC} distances (Figure 3.11) and an increase in depth (Figure 3.12) with increase in K_{z_b} and K_{s_b}. However, the P&P schemes experience the greatest change in Y_{AC} extent across the various K_{z_b} and K_{s_b} magnitudes late in the model run. An increase in K_{z_b} and K_{s_b} magnitude leads to a decrease in SF_H during the initial development of the plume (Figure 3.13) for all schemes. Later in the run, the schemes grow similarly.

The X_{UP} distance (Figure 3.14) and SF_V (Figure 3.15) are less straightforward; the intermediate K_{z_b} and K_{s_b} of 5 x 10^{-4} m^2 s^{-1}, results in the greatest X_{UP} and SF_V. The X_{UP} pattern exists for all the schemes (Figure 3.14), but for the SF_V, the resulting behavior depends on the scheme (Figure 3.15). Both P&P schemes show an inverse correlation between SF_V and the K_{z_b} and K_{s_b} magnitude while MY2.5 and constant show somewhat of a positive correlation.

The plan and side views of the plumes simulated by the four different vertical mixing schemes with K_{z_b} and K_{s_b} magnitudes of 5 x 10^{-4} m^2 s^{-1} (Figures 3.16 and 3.17) and 5 x 10^{-6}

m^2 s^{-1} (Figures 3.19 and 3.20) reveal that order of magnitude changes in K_{z_b} and K_{s_b} have a larger effect than choice of mixing scheme. The largest K_{z_b} and K_{s_b}, 5 x 10^{-4} m^2 s^{-1}, produces schemes that are qualitatively similar in both plan (Figure 3.16) and side view (Figure 3.17, cross-section is at x = 300 km). All metrics for the surface-advected plume at this magnitude are similar, regardless of scheme (lower panels of Figures 3.10 through 3.15). Although the schemes result in some differences between the outermost contours, the inner salinity anomaly contours result in the same extents for all schemes. This is expected due to the presence of more mixing near the edges of the plume, caused by weaker density stratification and greater velocity shear (and therefore greater chance for differences in mixing), rather than in the center of the plume where the plume is highly stratified and mixing is weak.

Examination of the total diffusivity of all four schemes confirms that the formation and behavior of the plume is dominated by the K_{z_b} and K_{s_b} magnitude of 5 x 10^{-4} m^2 s^{-1} (Figure 3.18). All schemes with this magnitude result in similar plumes, where the plume is characterized by 5 x 10^{-4} m^2 s^{-1} within the plume and immediately offshore of the plume. Interestingly, MY2.5 and both P&P show larger total diffusivity present approximately 5 km away from the offshore edge of the plume, where there is little stratification and *Ri* is low.

Although both the extent and shape of individual salinity anomaly contours of the plumes at the lower K_{z_b} and K_{s_b} magnitude of 5 x 10^{-6} m^2 s^{-1} (Figures 3.19 and 3.20) are dramatically different from their increased counterparts (Figures 3.16 and 3.17), there are significant differences between schemes. The structure of the anticyclonic bulge differs among the schemes. More freshwater circulates in the plume for both P&P than for MY2.5, most likely due to more mixing in the bulge for MY2.5. Differences also exist in the downshelf and across-shelf extents. The cross-sections at 300 km downshelf of the freshwater inlet show significant variations across the schemes (Figure 3.20), where each scheme differs in salinity anomaly contours and in extent. Compared to the highest K_{z_b} and K_{s_b} magnitude, the plumes are more vertically stratified (compare Figures 3.20 and 3.17).

3.2.2 The bottom-advected plume

As in the surface-advected plume, large-scale variations in K_{z_b} and K_{s_b} have significant effects on the bottom-advected plume structure (Figure 3.21). The constant scheme shows an increase in K_{z_b} and K_{s_b} magnitude results in a decrease in X_{DN} and X_{UP} distances (top panels of Figure 3.21), and SF_V (bottom left panel). Interestingly, a magnitude of 5 x 10^{-6} m^2 s^{-1} causes the plume to shed in the downshelf (~ Day 32) and upshelf (~ Day 37) directions.

An increase in K_{z_b} and K_{s_b} also results in a decrease in Y_{AC} distance early in the development of the plume but eventually leads to an increase in Y_{AC} distance (middle panel). Again, like surface-advected plumes, the relationship between the SF_H and K_{z_b} and K_{s_b} magnitude is not straight-forward; a K_{z_b} and K_{s_b} of 5 x 10^{-6} m^2 s^{-1} shows the most SF_H while a magnitude of 5 x 10^{-5} m^2 s^{-1} has the lowest.

The effect of variations in K_{z_b} and K_{s_b} magnitudes is consistent for all vertical mixing schemes (Figures 3.22 to 3.26). All schemes show a decrease in X_{DN} distance (Figure 3.22), and a slight increase in Y_{AC} distance (Figure 3.23) with an increase in K_{z_b} and K_{s_b}. The SF_H results for all the schemes are comparable to the constant scheme for the K_{z_b} and K_{s_b} magnitudes (Figure 3.24), where 5 x 10^{-5} m^2 s^{-1} generated the least SF_H. The X_{UP} and SF_V for all schemes (Figures 3.25 and 3.26), decrease with increasing K_{z_b} and K_{s_b}. Except for the Y_{AC} metric, the schemes converge to similar plumes with larger background viscosity/diffusivity magnitudes (lower panels of Figures 3.22 through 3.26).

Examination of the plan and side (x = 297 km) views of the plumes simulated by the four different vertical mixing schemes with K_{z_b} and K_{s_b} magnitudes of 5 x 10^{-4} m^2 s^{-1} (Figures 3.27 and 3.28) and 5 x 10^{-6} m^2 s^{-1} (Figures 3.30 and 3.31) reveals that, again, the choice of K_{z_b} and K_{s_b} has a larger effect than choice of mixing scheme. Like the surface-advected plume, all schemes using the same K_{z_b} and K_{s_b} are much more similar in overall shape than the same scheme at a different viscosity, but the extent of the similarity depends on the K_{z_b} and K_{s_b} magnitude. The largest magnitude, 5 x 10^{-4} m^2 s^{-1}, produces schemes that are qualitatively similar in both views (Figures 3.27 and 3.28). Overall, the shape of the plume remains the same regardless of the vertical mixing scheme chosen. All schemes are strongly horizontally stratified. However, the P&P schemes expand slightly further across-shelf than the other two schemes; while the P&P plumes have the same diffusivity as the other schemes within the plume front, the diffusivity differs within the freshest portion of the plume and further offshore (Figure 3.29). This is due to the absence of stratification outside of the salinity anomaly contours; at these locations, the Richardson number approaches zero, causing the P&P schemes to resort to using the null viscosity and background viscosity/diffusivity, where (2.13) becomes reduced to

$$\begin{aligned} K_z &= K_{z_0} + K_{z_b} \\ K_s &= K_z + K_{s_b} \end{aligned} \tag{3.1}$$

As with the surface-advected plume, the extent and shape of individual salinity anomaly contours of the plumes at the lower K_{z_b} and K_{s_b} magnitude of 5 x 10^{-6} m^2 s^{-1} (Figures 3.30 and 3.31) are very different from their increased counterparts (Figures 3.27 and 3.28). While variations in K_{z_b} and K_{s_b} may produce large differences in the plume structure, the choice of scheme at the lower K_{z_b} and K_{s_b} can result in significant (if smaller) differences. MY2.5 and the constant scheme extend further in the upshelf and downshelf directions and contain more meanderings and instabilities compared to the P&P schemes. The constant scheme shows the most upshelf movement of the plume out of the schemes (Figure 3.30). Both P&P are characterized by more across-shelf growth for the entire plume than the other two schemes (Figure 3.31). Interestingly, the freshest water for the constant scheme does not reach the bottom of the water column like the other schemes.

3.2.3 Overall results

Overall, an increase in the K_{z_b} and K_{s_b} magnitude for the schemes results in an increase in similarity among the plumes. Therefore, like the surface-advected plume, the bottom-advected plumes show a much larger influence of the K_{z_b} and K_{s_b} when its magnitude is 5 x 10^{-6} m^2 s^{-1}.

As with the results, the constant scheme is first discussed due to the simpler characterization of vertical mixing. Both surface- and bottom-advected plumes decreased in X_{DN} growth as K_{z_b} and K_{s_b} increased for the constant scheme (Figures 3.9 and 3.21). Similarly, Garvine (1999) and Davies and Xing (1999) demonstrated a decrease in downshelf penetration and flow with increasing K_{z_b} and K_{s_b}. The decrease can be attributed to an increase in vertical mixing from increased K_{z_b} and K_{s_b} and from the horizontal velocity stratified shear at the nose of the plume, causing the plume to increase in depth and decrease in horizontal plume size. Similar to the X_{DN} extent for the constant scheme, X_{UP} propagation decreased with an increase in K_{z_b} and K_{s_b} magnitude for the bottom-advected plume (Figure 3.21); however, the surface-advected plume response differed for K_{z_b} and K_{s_b} order of magnitude variations (Figure 3.9); this will be discussed in Chapter 5.

The surface- and bottom-advected plumes differed with changes in K_{z_b} and K_{s_b} for the across-shelf expansion using the constant scheme. The surface-advected plumes narrowed in width (i.e. Y_{AC} decreased) while deepening due to more vertical mixing with increasing K_{z_b} and K_{s_b} magnitudes (Figure 3.9). Kourafalou et al (1996a), while testing the sensitivity of plumes to variable vertical eddy viscosity and diffusivity, found the same relationship between depth and across-shelf growth, where a decline in across-shelf growth corresponded to depth expansion created by an increase in K_{z_b} and K_{s_b}.

The bottom-advected plume showed a different correspondence between the Y_{AC} and the mixing coefficients, K_{z_b} and K_{s_b}, using the constant scheme (Figure 3.21). Instead, larger K_{z_b} and K_{s_b} resulted in slightly larger Y_{AC} expansion, allowing the plume to follow the bottom topography to larger depths (compare Figures 3.28 and 3.31). The plume had a shallow bottom; therefore with greater vertical mixing, the plume increased in horizontal stratification, resulting in more interaction of the plume with bottom friction and a stronger horizontal salinity anomaly gradient across-shelf, increasing the bottom offshore buoyancy flux. The combination of these changes allowed the plume to move slightly further across-shelf and in depth. These model observations are consistent with Chapman and Lentz (1994) before the 'bottom trapping' of the plume offshore. The variations shown in the salt fluxes for both types of plumes will be discussed in Chapter 5.

3.3 Effects of schemes on metrics

Schemes characterized by a K_{z_b} and K_{s_b} larger than 5 x 10^{-6} m^2 s^{-1} were dominated by the K_{z_b} and K_{s_b} value, resulting in extremely similar plumes, regardless of scheme. However, the schemes with a K_{z_b} and K_{s_b} magnitude of 5 x 10^{-6} m^2 s^{-1} demonstrated noticeable differences among the resulting plumes (Figures 3.19 and 3.20 and Figures 3.30 and 3.31). Consequently, this section will focus on comparing the evolution of the plumes using the metrics for each scheme with a K_{z_b} and K_{s_b} magnitude of 5 x 10^{-6} m^2 s^{-1}.

3.3.1 The surface-advected plume

Comparison of the evolution of the metrics reveals significant differences in the scheme (Figure 3.32). During the initial development of the plume, P&P (B) was characterized by the least amount of downshelf expansion (Figure 3.32, top left panel); the other three schemes were similar for this same period of time. At approximately Day 32, the X_{DN} expansion of the constant scheme began to decrease (10% less than P&P (A)). By Day 50, MY2.5 and both P&P schemes were characterized by very similar X_{DN} distances that were slightly greater than the constant scheme.

Larger differences among the schemes resulted for the X_{UP} distance (Figure 3.32, top right panel). The plumes behave similarly until Day 32, when larger differences appeared; the constant scheme had the largest X_{UP} extent and the P&P schemes resulted in the least expansion (20% difference).

The P&P schemes expanded the most in Y_{AC} (29% larger than the constant scheme) and in depth (45% larger than the constant scheme) by Day 50 (Figure 3.32, middle panels). Again, during the initial development of the plume, the schemes produce similar results, but by Day 40, larger differences appear. The deepening of the plume may be attributed to the large SF_V for both P&P (Figure 3.32, bottom left). Interestingly, both integrated salt fluxes (Figure 3.32, bottom panels) peak early in the simulations. The P&P schemes are characterized by dramatically increased values of SF_V values are due to very large calculated total viscosity/diffusivity coefficient values. The relationship between the SF_H and the across-shelf penetration is not as straightforward as that between the SF_V and depth; the constant scheme showed to have the least Y_{AC} movement yet the largest SF_H.

Table 3.1 summarizes the metric results in terms of the mixing scheme used. The majority of the parameters showed P&P (B) and the constant scheme to occupy the two extreme extents while MY2.5 typically resulted in metrics between the other two schemes.

Table 3.1: Ranked parameter results by mixing scheme for all parameters of interest for the surface-advected runs using a K_{z_b} and K_{s_b} magnitude of 5 x 10^{-6} m^2 s^{-1}.

SURFACE-ADVECTED	***Most*** →			→ ***Least***
Nondim. Downshelf	Mellor-Yamada Level 2.5	Pacanowski and Philander (A)	Constant	Pacanowski and Philander (B)
Nondim. Upshelf	Constant	Mellor-Yamada Level 2.5	Pacanowski and Philander (A)	Pacanowski and Philander (B)
Nondim. Across-shelf (bulge)	Pacanowski and Philander (B)	Pacanowski and Philander (A)	Mellor-Yamada Level 2.5	Constant
Depth (bulge)	Pacanowski and Philander (B)	Pacanowski and Philander (A)	Mellor-Yamada Level 2.5	Constant
Vertical Salt Flux	Pacanowski and Philander (B)	Pacanowski and Philander (A)	Mellor-Yamada Level 2.5	Constant
Horiz. Salt Flux	Constant	Mellor-Yamada Level 2.5	Pacanowski and Philander (A)	Pacanowski and Philander (B)

3.3.2 The bottom-advected plume

Comparison of the evolution of the metrics reveals that, similar to the surface-advected plume, there are noticeable differences in the schemes for the bottom-advected plume (Figure 3.33). The constant scheme and MY2.5 resulted in the largest X_{DN} expansion for the majority of the run while the two P&P schemes grow the X_{DN} distance at a slower but similar rate (Figure 3.33 top left panel). Around Day 32, the plume simulated by the constant scheme shed a pocket of fresher water downshelf, causing the downshelf extent of the plume to suddenly drop. If the plume separation were disregarded, the constant scheme would most likely continue to develop downshelf with higher growth than the other schemes. For the last ten days, the MY2.5 is 5% larger than P&P (B).

The discrepancies found in the X_{UP} direction were, again, much larger than the X_{DN}; the constant scheme was much larger (44%) than the other schemes which all had similar upshelf propagation (Figure 3.33, top right panel). The constant scheme was characterized by the least Y_{AC} expansion (Figure 3.33, middle panel). Both P&P schemes resulted with comparable Y_{AC} distances until around Day 40, where P&P (A) exceeds the other three schemes and grew an average of 22% larger than the lowest, constant scheme. Both MY2.5 and constant scheme created oscillating variability mostly likely associated with instabilities and meandering of the plume on the plume edge (also shown by Kourafalou et al. 1996a and Garvine 1999). Similar to surface-advected plumes, the bottom-advected integrated salt fluxes were strongly dependent on the choice of mixing scheme. Both P&P schemes resulted in a far greater amount of SF_V than the other schemes (Figure 3.33, bottom left panel). The large SF_V values for both P&P were the direct result of high viscosity/diffusivity coefficient values calculated, producing magnitudes as high as 10^{-2} m^2 s^{-1}. The SF_H was greatest when using the constant scheme while P&P (A) resulted in the least.

Table 3.2 summarizes the effects of the scheme on the various plume growth metrics. Similar to the surface-advected plume results, MY2.5 had the tendency to result in a plume between the constant scheme and both P&P plumes.

Table 3.2: Ranked parameter results by mixing scheme for all parameters of interest for the bottom-advected runs using a K_{z_b} and K_{s_b} magnitude of 5 x 10^{-6} m^2 s^{-1}.

BOTTOM-ADVECTED	***Most*** →			→ ***Least***
Nondim. Downshelf	Constant	Mellor-Yamada Level 2.5	Pacanowski and Philander (A)	Pacanowski and Philander (B)
Nondim. Upshelf	Constant	Mellor-Yamada Level 2.5	Pacanowski and Philander (B)	Pacanowski and Philander (A)
Nondim. Across-shelf (bulge)	Pacanowski and Philander (A)	Pacanowski and Philander (B)	Mellor-Yamada Level 2.5	Constant
Depth	N/A	N/A	N/A	N/A
Vertical Salt Flux	Pacanowski and Philander (B)	Pacanowski and Philander (A)	Constant	Mellor-Yamada Level 2.5
Horiz. Salt Flux	Constant	Mellor-Yamada Level 2.5	Pacanowski and Philander (B)	Pacanowski and Philander (A)

3.3.3 Overall results

The growth in X_{DN} differed depending on the type of plume due to differences in plume dynamics. In addition, the X_{UP} propagation was larger with lower viscosity and/or higher diffusivity for both types of plumes (Yankovsky 2000 and Garvine 2001). Both of these metric results will be further discussed in Chapter 5.

Interestingly, both P&P had the most Y_{AC} distance (29% for surface-advected and 22% for bottom-advected plumes) and depth (45% for surface-advected plumes) when compared to the other schemes (middle panels, Figures 3.32 and 3.33). This phenomenon can be explained by the geostrophic adjustment of the plume as it enters the ambient ocean. Because of the Coriolis effect, the plume turned anticyclonically as it left the estuary and formed a geostrophic current flowing downshelf. The across-shelf growth of the plume near the river inlet was directly related to the speed of the water parcel and inversely related to the Coriolis parameter (Cushman-Roisin 1994); for this study, the growth was equivalent to the initial plume relaxation, spreading one internal Rossby Radius across-shelf, and then additional across-shelf spreading was due to constant freshwater input and mixing. Since all the schemes were characterized by equal constant freshwater discharge (each type of plume) and the same Coriolis parameters, the only difference among the schemes was the vertical mixing. More vertical mixing from larger vertical mixing coefficients created a decrease in the vertical stratification and vertical salinity gradients while expanding the plume in depth. The constant scheme produced the smallest mixing coefficients, and therefore, resulted in smaller Y_{AC}, depth, and SF_V . The P&P schemes produced larger coefficients, resulting in larger Y_{AC}, depth, and SF_V .

Unlike the large changes in K_{z_b} and K_{s_b} magnitude causing the plumes to change in structure, when using only a K_{z_b} and K_{s_b} magnitude of 5 x 10^{-6} m^2 s^{-1}, the analysis of the salt fluxes was clearer and less complex. The salt fluxes showed to be interrelated, where the constant scheme resulted in the largest SF_H and lower SF_V while P&P resulted in the opposite (bottom panels, Figures 3.32 and 3.33). When the plume mixed in the vertical direction, the bottom edge of the plume expanded in depth, decreasing the vertical stratification and the localized horizontal salinity gradient at the edge of the plume; the salinity at the bottom edge increased while expanding, creating less variation in salinity with depth, and the overall increase in salinity decreased the localized horizontal salinity gradient. The horizontal viscosity/diffusivity coefficients were calculated depending on the along and across-shore horizontal gradients of velocity (Smagorinsky 1963). Therefore, the SF_H changes with modifications in the horizontal gradients were created from variations in the vertical direction. For P&P, more vertical mixing increased the depth of the plume, decreasing the horizontal salinity gradient, which in turn, lead to less SF_H. The constant scheme showed less vertical mixing, creating less of a decrease in the horizontal salinity gradient and therefore, allowed for more horizontal mixing than the P&P schemes.

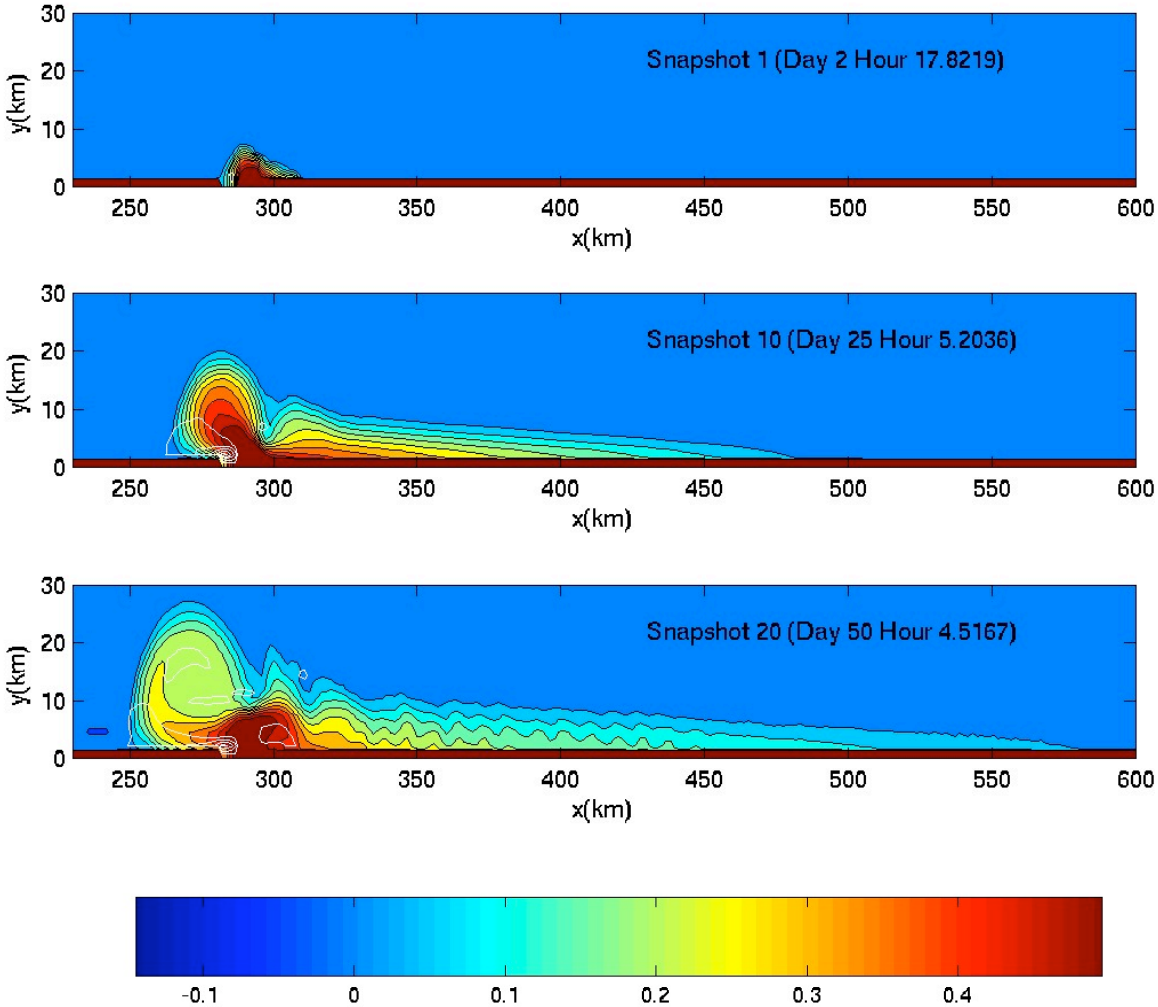

Figure 3.1: Plan view of the evolution of the surface-advected plume using MY2.5 with a K_{z_b} and K_{s_b} magnitude of 5 x 10^{-6} m^2 s^{-1}. Salinity anomaly contours are shown in color with a maximum value of 0.5 and minimum value of –0.15 with intervals of 0.05. The point-by-point horizontal salt flux is shown by the white contours with an interval of 5 x 10^{-4} m^2 s^{-1}, ranging from 0 m^2 s^{-1} to 5 x 10^{-3} m^2 s^{-1}. Note that the x- and y-directions are scaled differently.

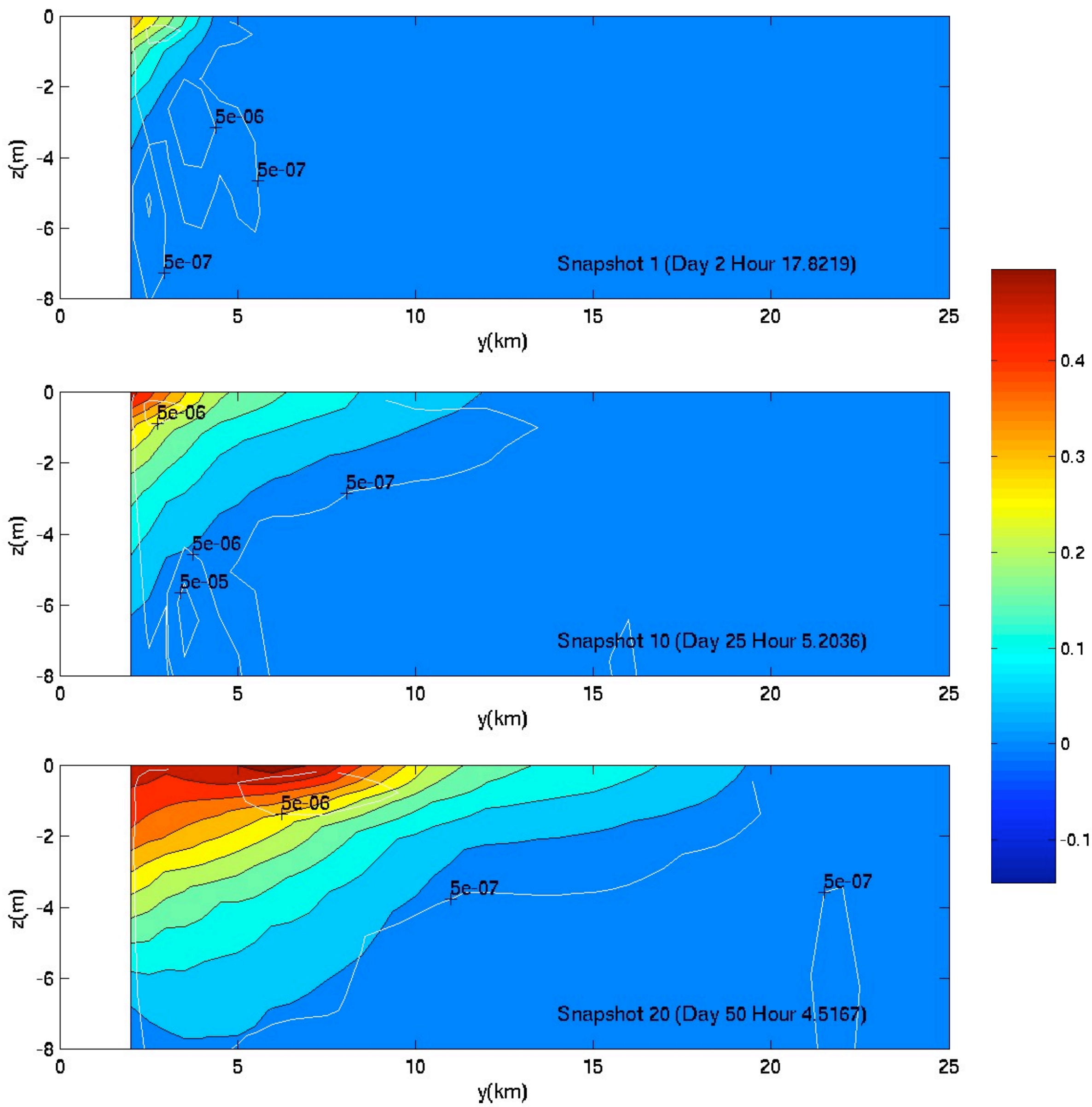

Figure 3.2: Evolution of the cross-section at one internal Rossby Radius downshelf of the inlet (x = 300 km) for the surface-advected plume using MY2.5 with a K_{z_b} and K_{s_b} value of 5 x 10^{-6} $m^2 s^{-1}$. Salinity anomaly contours are shown in color with a maximum value of 0.5 and minimum value of –0.15 with intervals of 0.05. The point-by-point vertical salt flux ($m^2 s^{-1}$) is shown by the white contours and black labels. Note that the x- and y-directions are scaled differently.

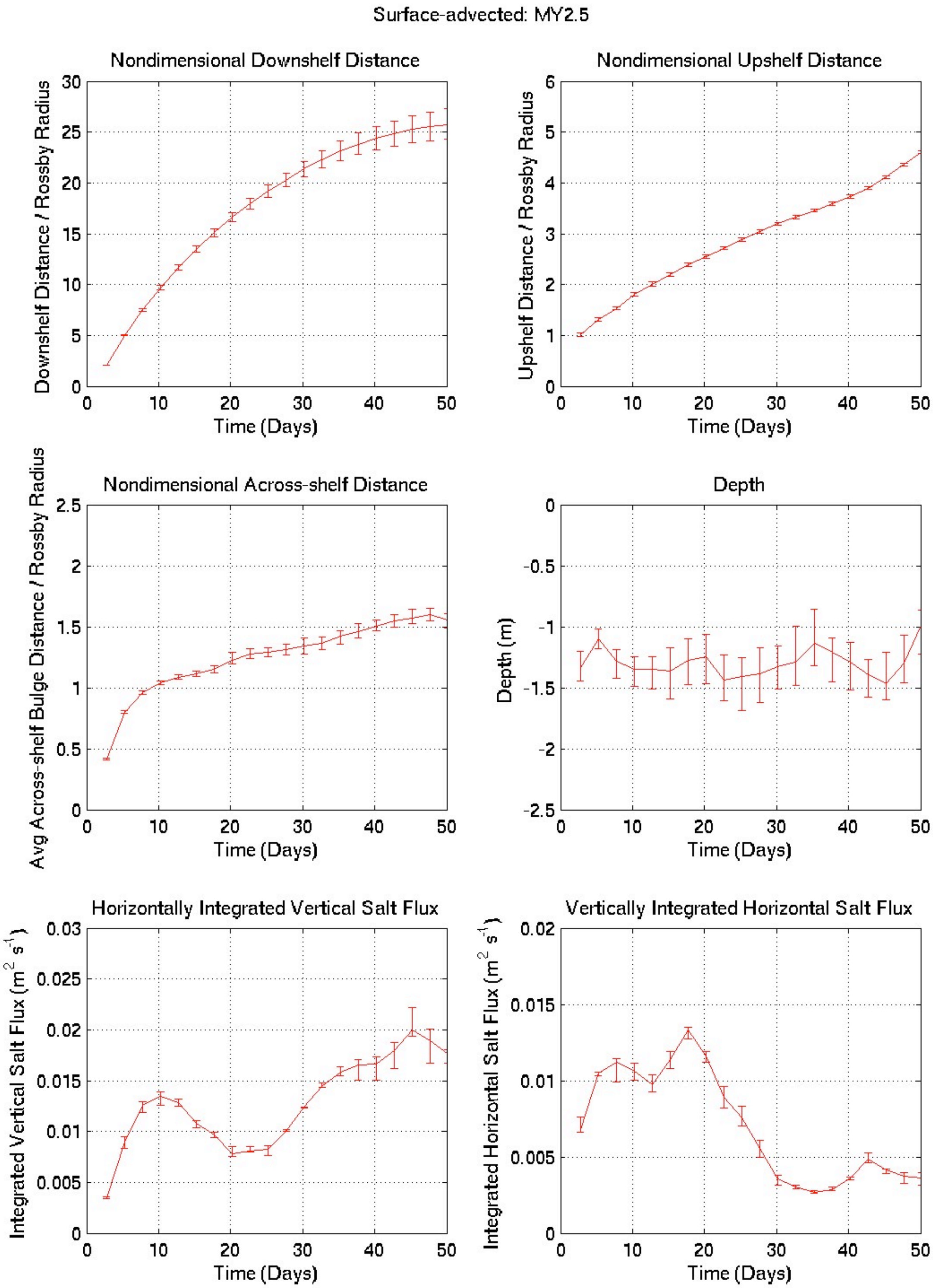

Figure 3.3: The temporal evolution of the study metrics for the surface-advected plume for MY2.5 using a K_{z_b} and K_{s_b} value of 5 x 10^{-6} m^2 s^{-1}. The results for 10% range above and below the salinity anomaly contour of interest is shown (bars) at each snapshot.

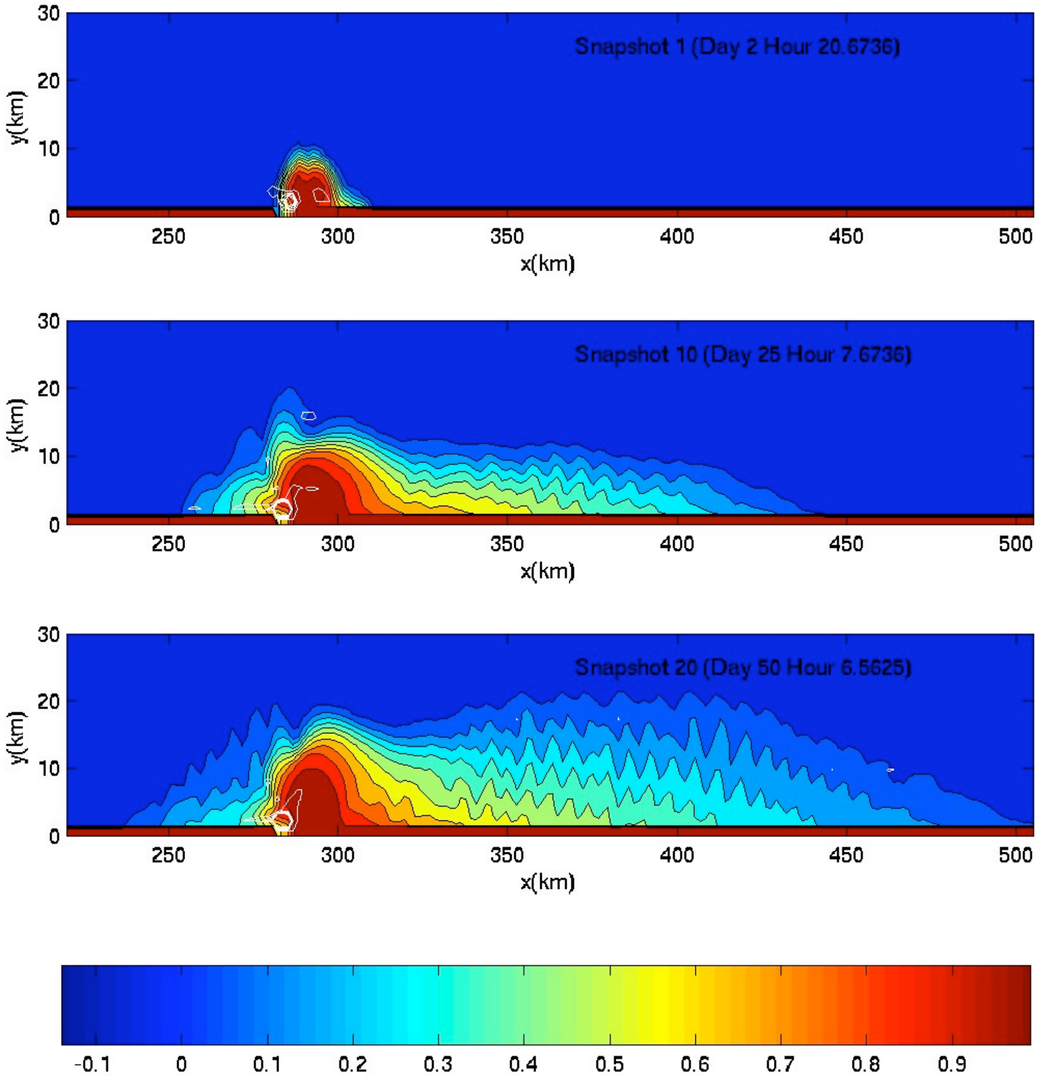

Figure 3.4: Plan view of the evolution of the bottom-advected plume using MY2.5 with a K_{z_b} and K_{s_b} of 5 x 10^{-6} m^2 s^{-1}. The salinity anomaly contours are shown in color with intervals of 0.1, ranging from –0.15 to 1. The point-by-point horizontal salt flux is shown by the white contours from with 0 m^2 s^{-1} to 5 x 10^{-3} m^2 s^{-1}, with intervals of 1 x 10^{-3} m^2 s^{-1}. Note that the x- and y-directions are scaled differently.

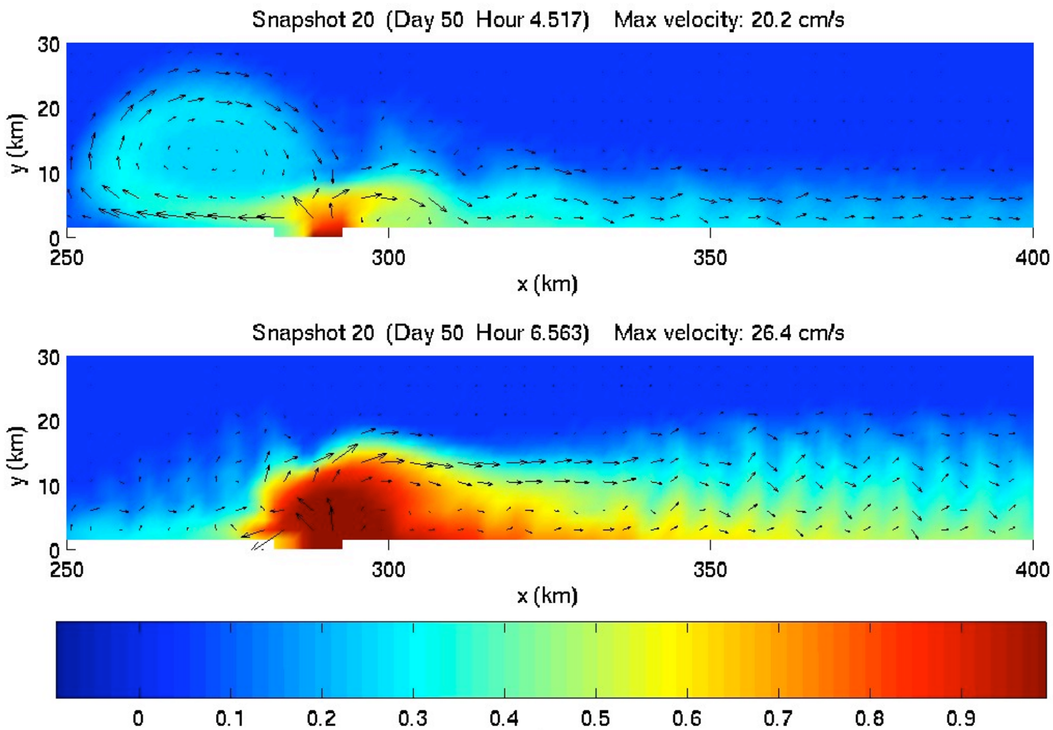

Figure 3.5: Velocity field (black arrows) over the salinity anomaly (color) field of the surface-advected plume (top) and bottom-advected plume (bottom) at Day 50 using MY2.5 with a K_{z_b} and K_{s_b} magnitude of 5 x 10^{-6} m^2 s^{-1}. Note that the x- and y-directions are scaled differently.

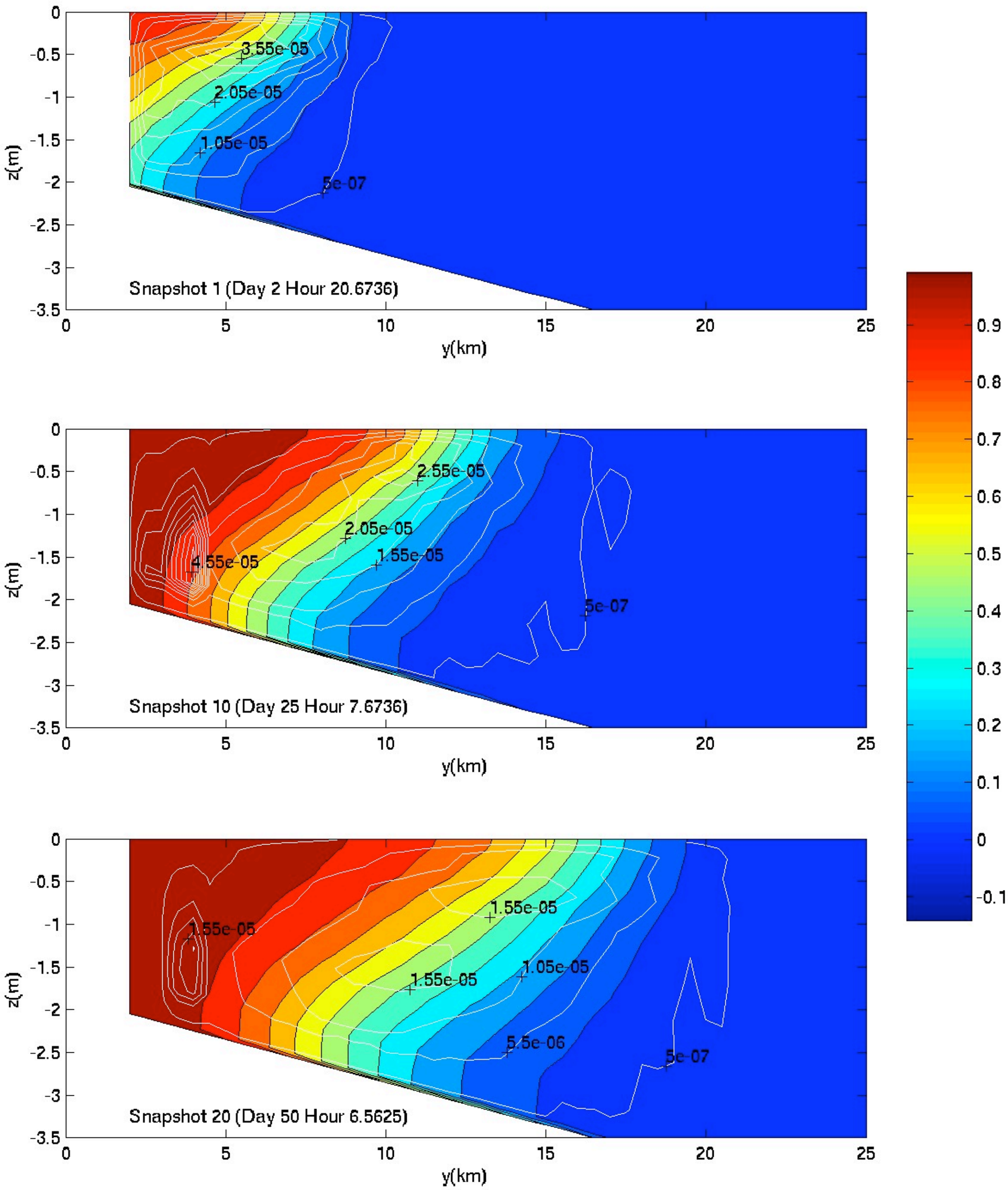

Figure 3.6: Evolution of the cross-section at one internal Rossby Radius downshelf of the inlet (x = 297 km) for the bottom-advected plume using MY2.5 with a K_{z_b} and K_{s_b} of 5 x 10^{-6} m^2 s^{-1}. The salinity anomaly contours are shown in color with intervals of 0.1, ranging from –0.15 to 1. The point-by-point vertical salt flux is shown by the white contours and black labels starting from with 5 x 10^{-7} m^2 s^{-1} with intervals of 5 x 10^{-6} m^2 s^{-1}. Note that the x- and y-directions are scaled differently.

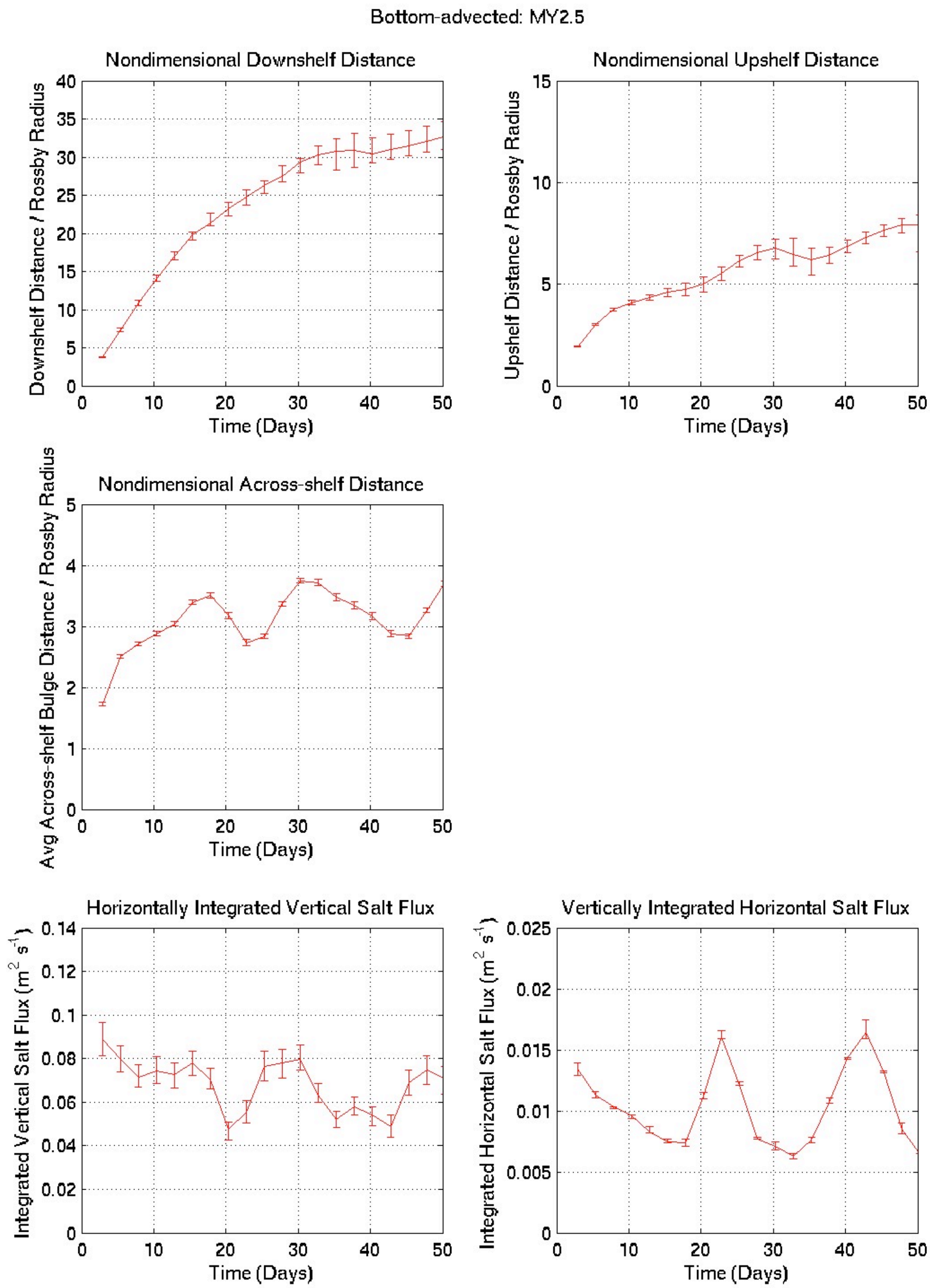

Figure 3.7: The metric evolution for the bottom-advected plume is shown for MY2.5 using a K_{z_b} and K_{s_b} of 5 x 10^{-6} m^2 s^{-1}. Note that there is no calculation for depth for the bottom-advected plume. Since the plume extends to the bottom topography, the depth parameter calculation would always be the depth of the water column. The results for 10% range above and below the salinity anomaly contour of interest is shown (bars) at each snapshot.

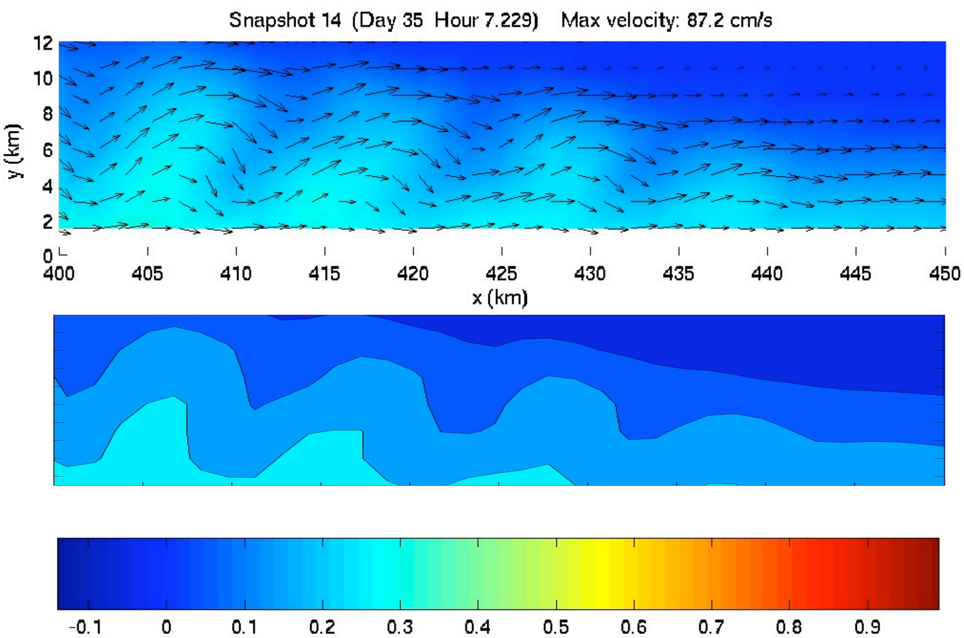

Figure 3.8: Downshelf pockets of the plume mix into the ambient ocean for the bottom-advected plume using the constant scheme with a K_{z_b} and K_{s_b} of 5 x 10^{-6} m^2 s^{-1}; the velocity field (top panel) overlain on the salinity anomaly field (color). For clarification of the location of the salinity anomaly contours, the bottom panel contours the salinity anomaly only.

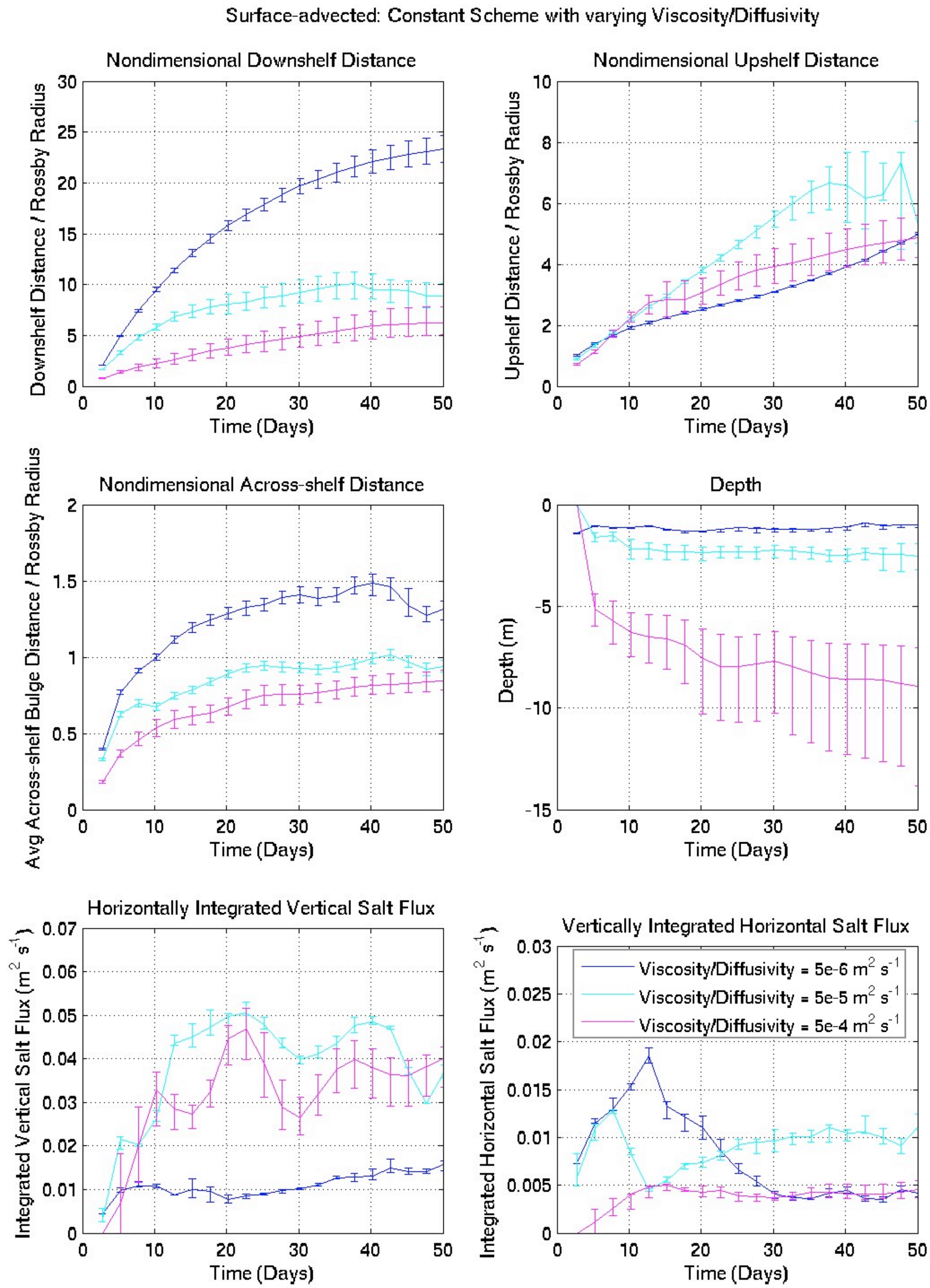

Figure 3.9: The metric developments for the surface-advected plume using the constant scheme with varying K_{z_b} and K_{s_b} magnitude are shown. The results for 10% range above and below the salinity anomaly contour of interest is shown (bars) at each snapshot.

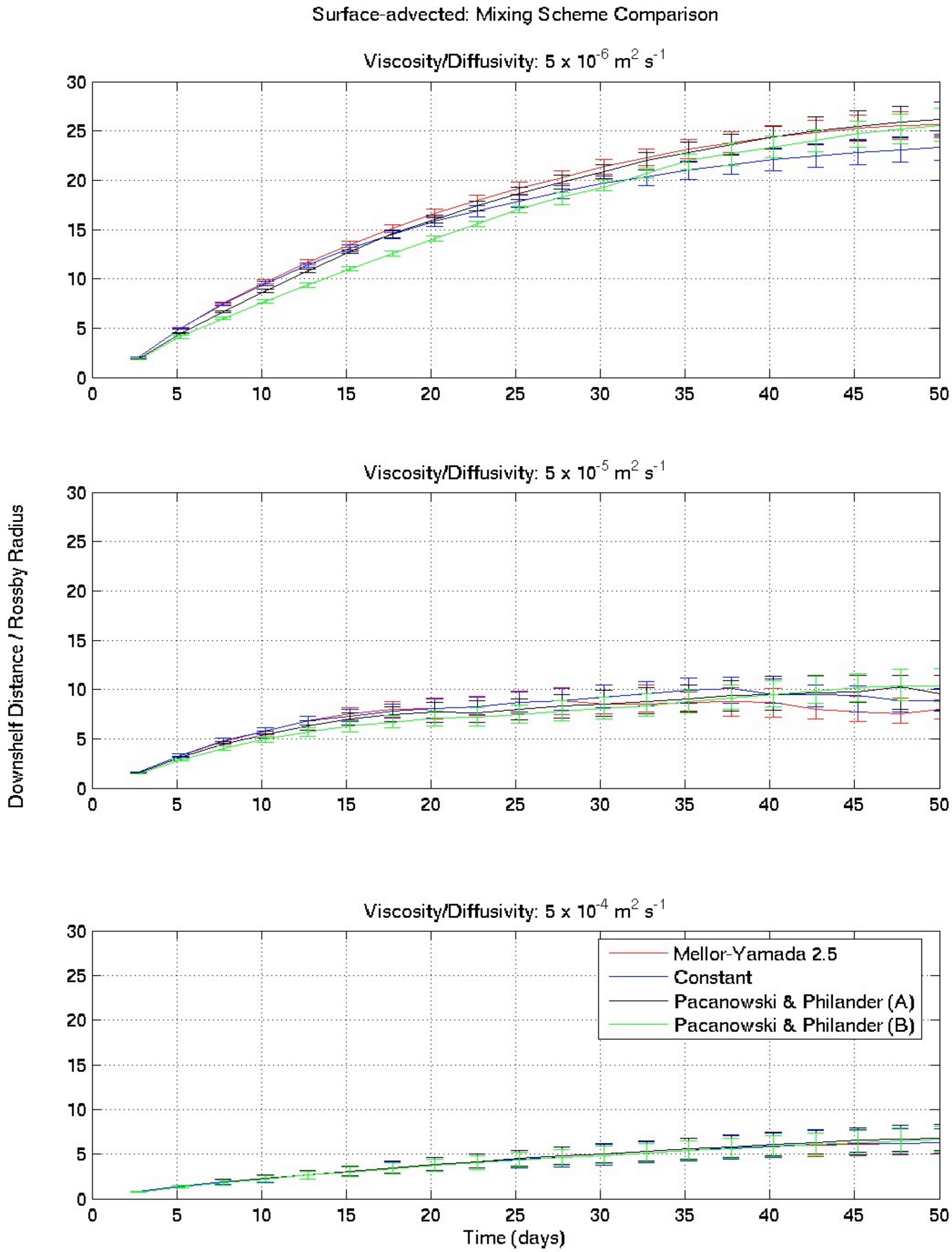

Figure 3.10: Nondimensional downshelf distance as a function of K_{z_b} and K_{s_b} magnitude and vertical mixing scheme for the surface-advected plume. The results for 10% range above and below the salinity anomaly contour of interest is shown (bars) at each snapshot.

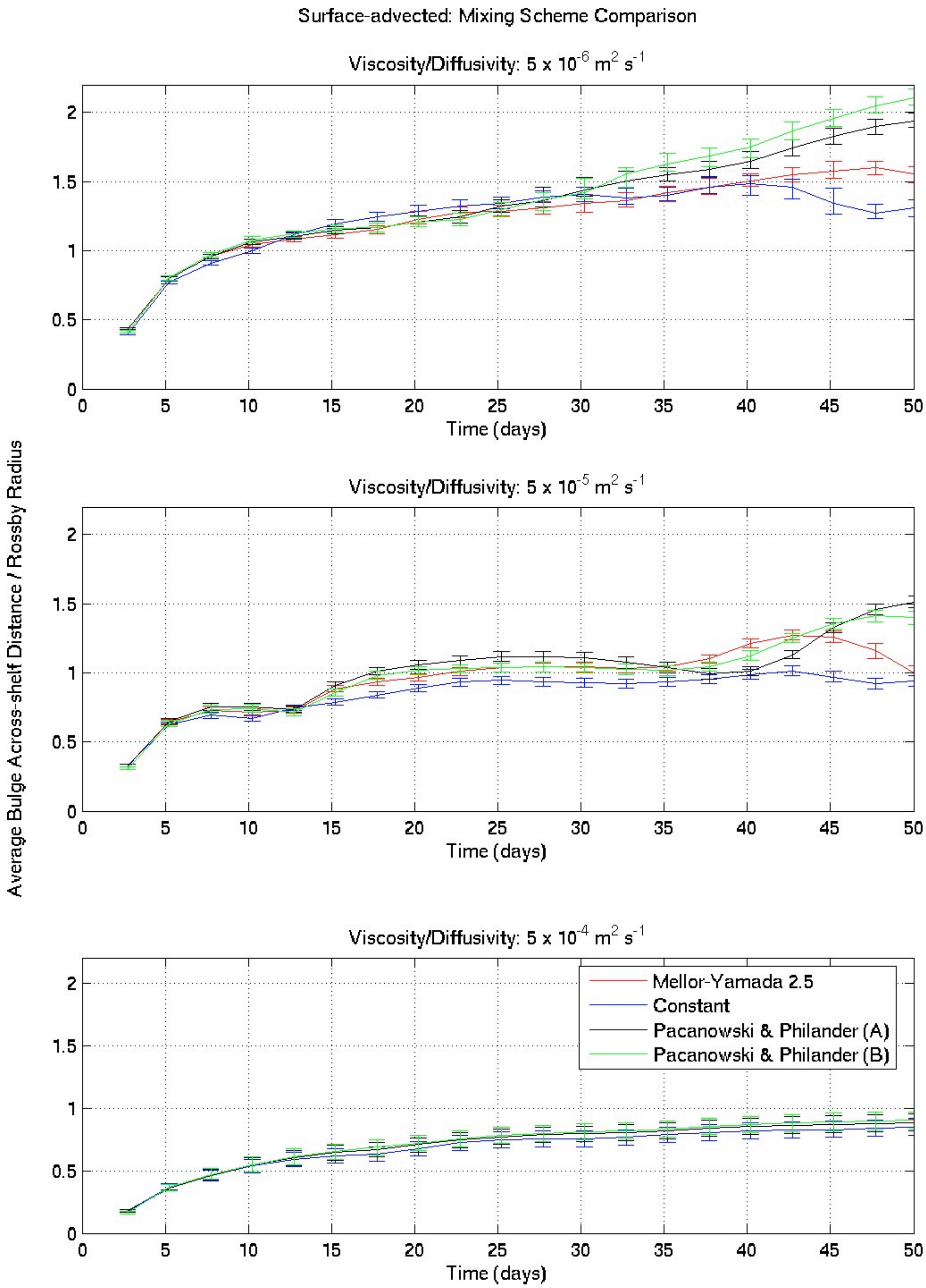

Figure 3.11: Nondimensional across-shelf bulge distance as a function of K_{z_b} and K_{s_b} magnitude and vertical mixing scheme for the surface-advected plume. The results for 10% range above and below the salinity anomaly contour of interest is shown (bars) at each snapshot.

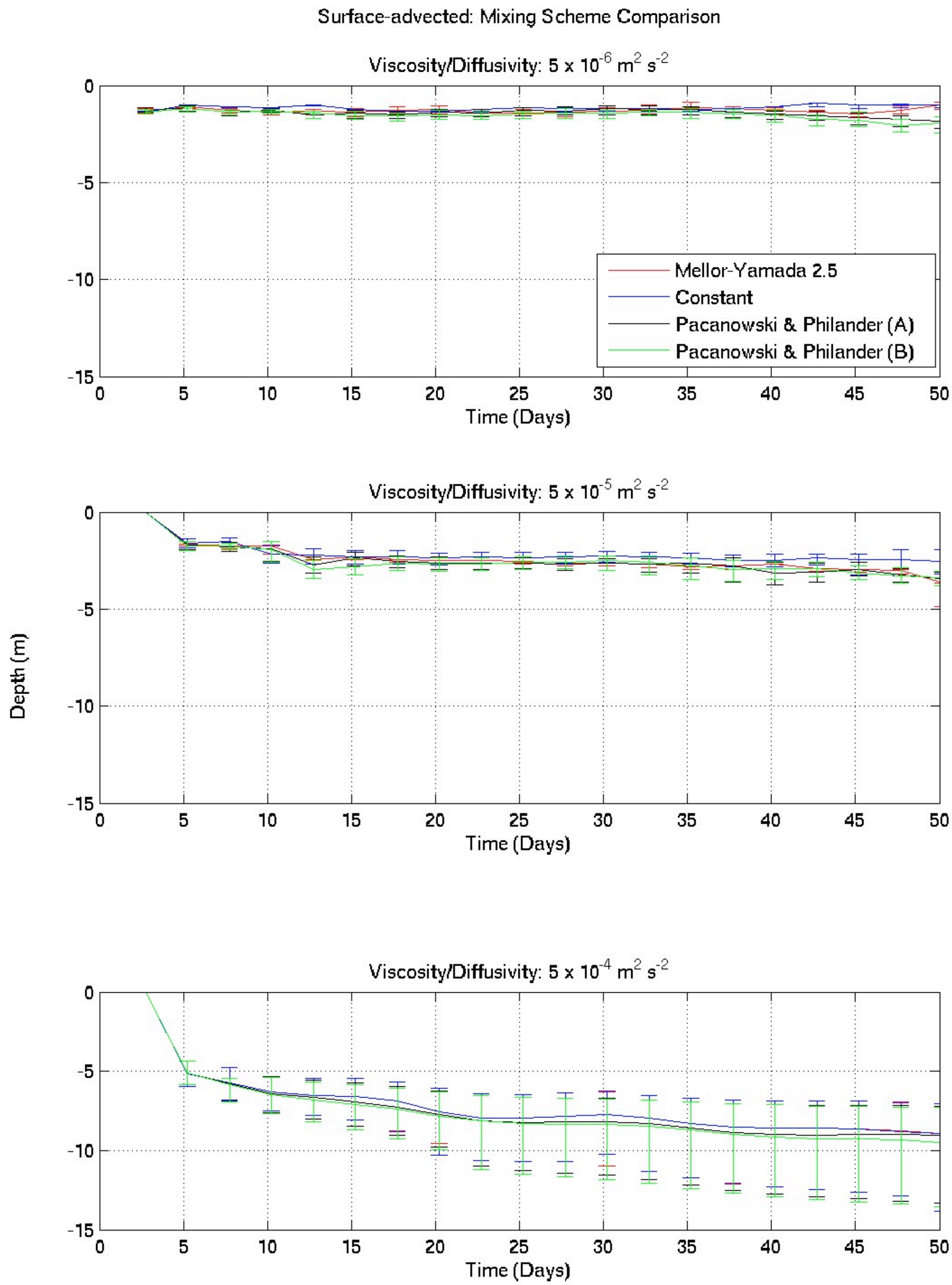

Figure 3.12: Depth as a function of K_{z_b} and K_{s_b} magnitude and vertical mixing scheme for the surface-advected plume. The results for 10% range above and below the salinity anomaly contour of interest is shown (bars) at each snapshot.

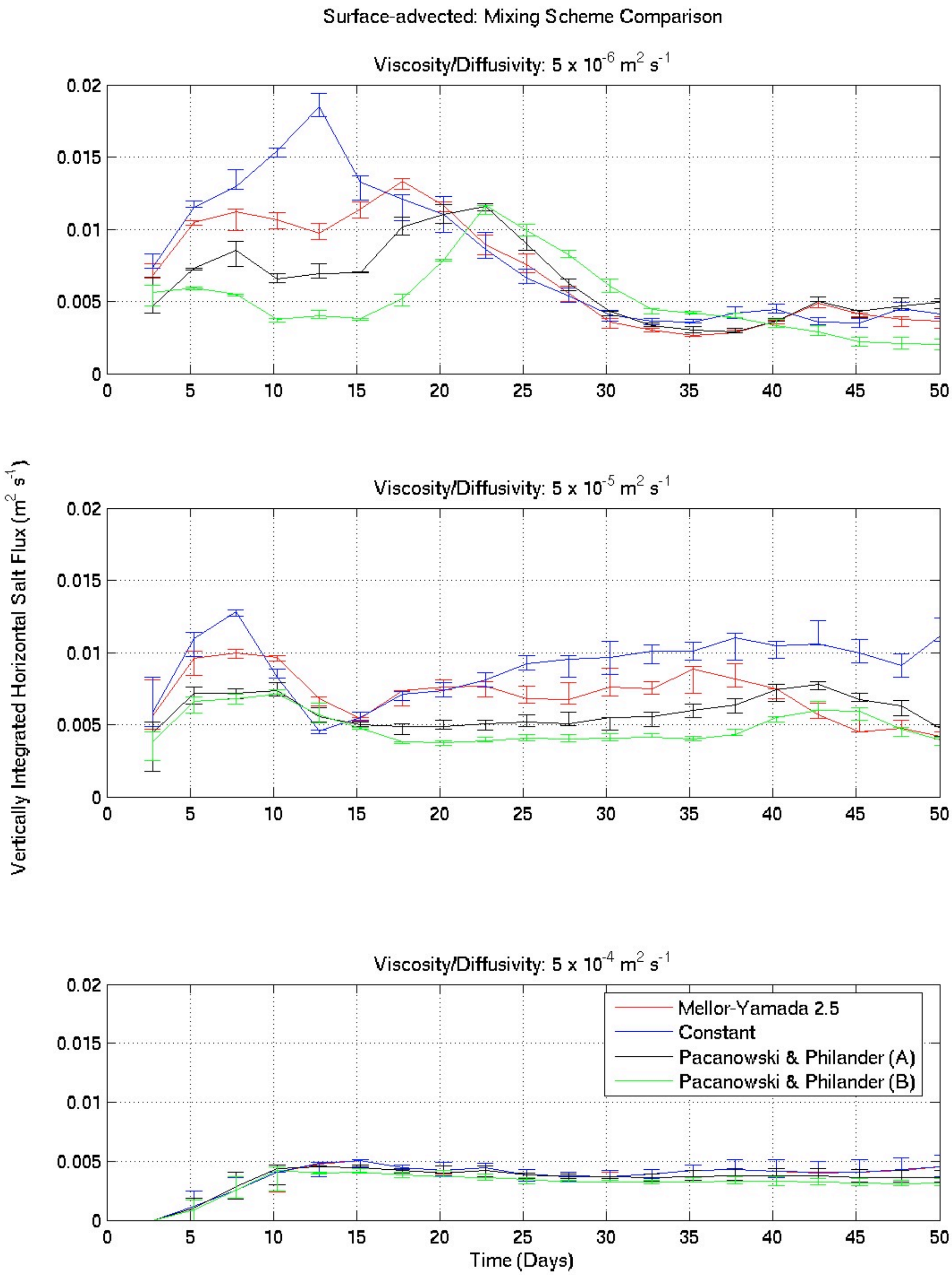

Figure 3.13: Vertically integrated horizontal salt flux as a function of K_{z_b} and K_{s_b} magnitude and vertical mixing scheme for the surface-advected plume. The results for 10% range above and below the salinity anomaly contour of interest is shown (bars) at each snapshot.

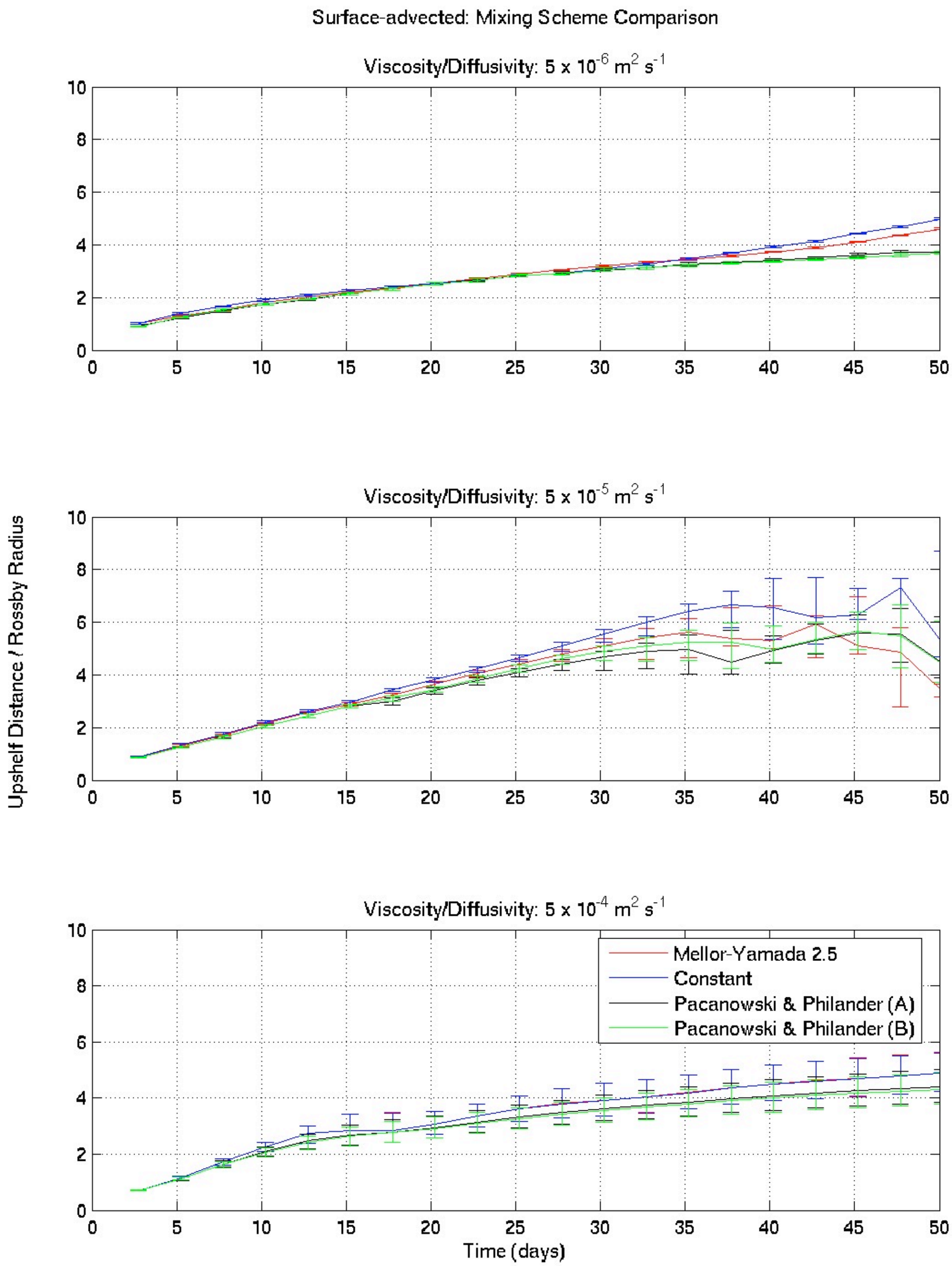

Figure 3.14: Nondimensional upshelf distances as a function of K_{z_b} and K_{s_b} magnitude and vertical mixing scheme for the surface-advected plume. The results for 10% range above and below the salinity anomaly contour of interest is shown (bars) at each snapshot.

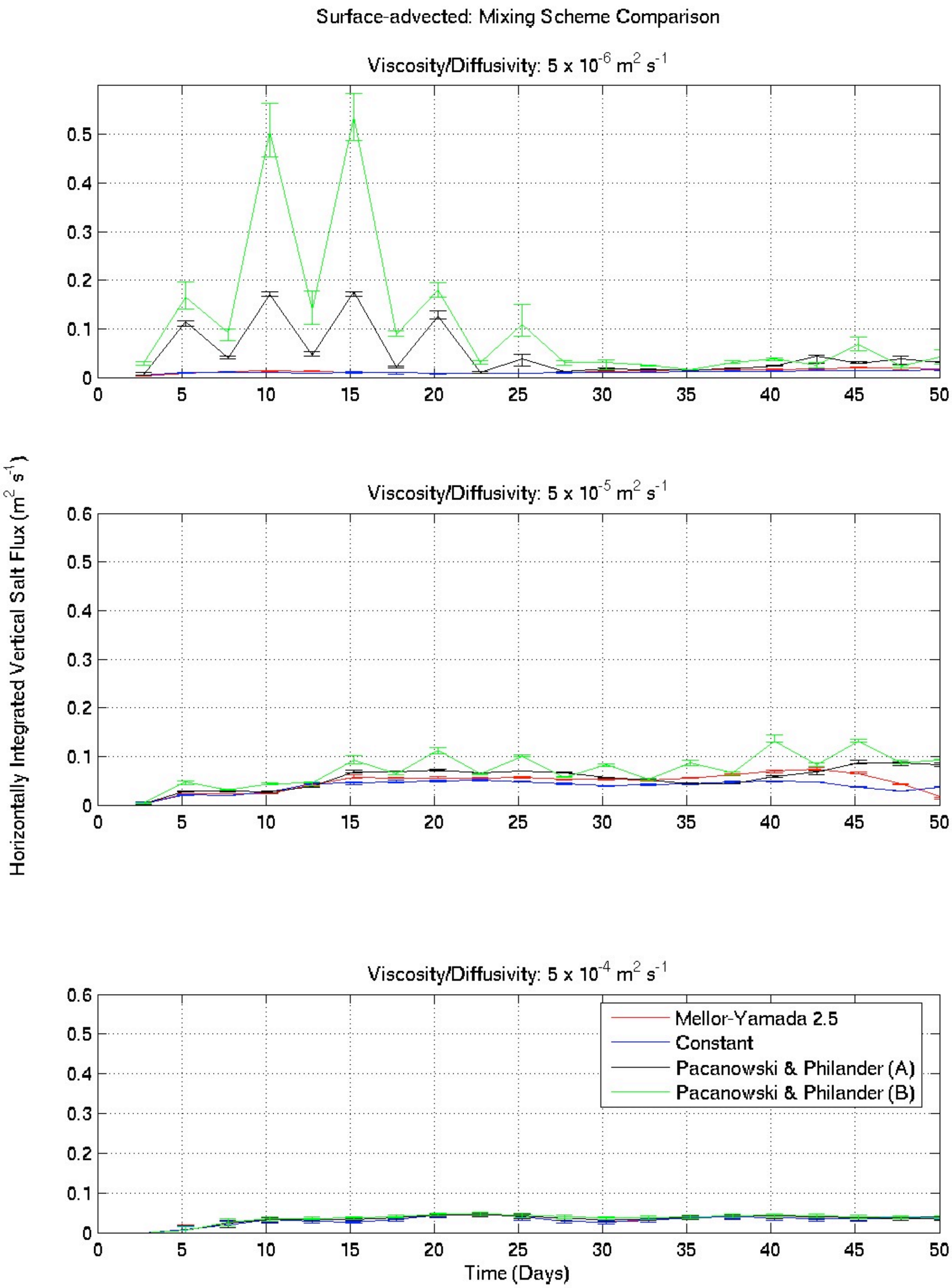

Figure 3.15: Horizontally integrated vertical salt flux as a function of K_{z_b} and K_{s_b} magnitude and vertical mixing scheme for the surface-advected plume. The results for 10% range above and below the salinity anomaly contour of interest is shown (bars) at each snapshot.

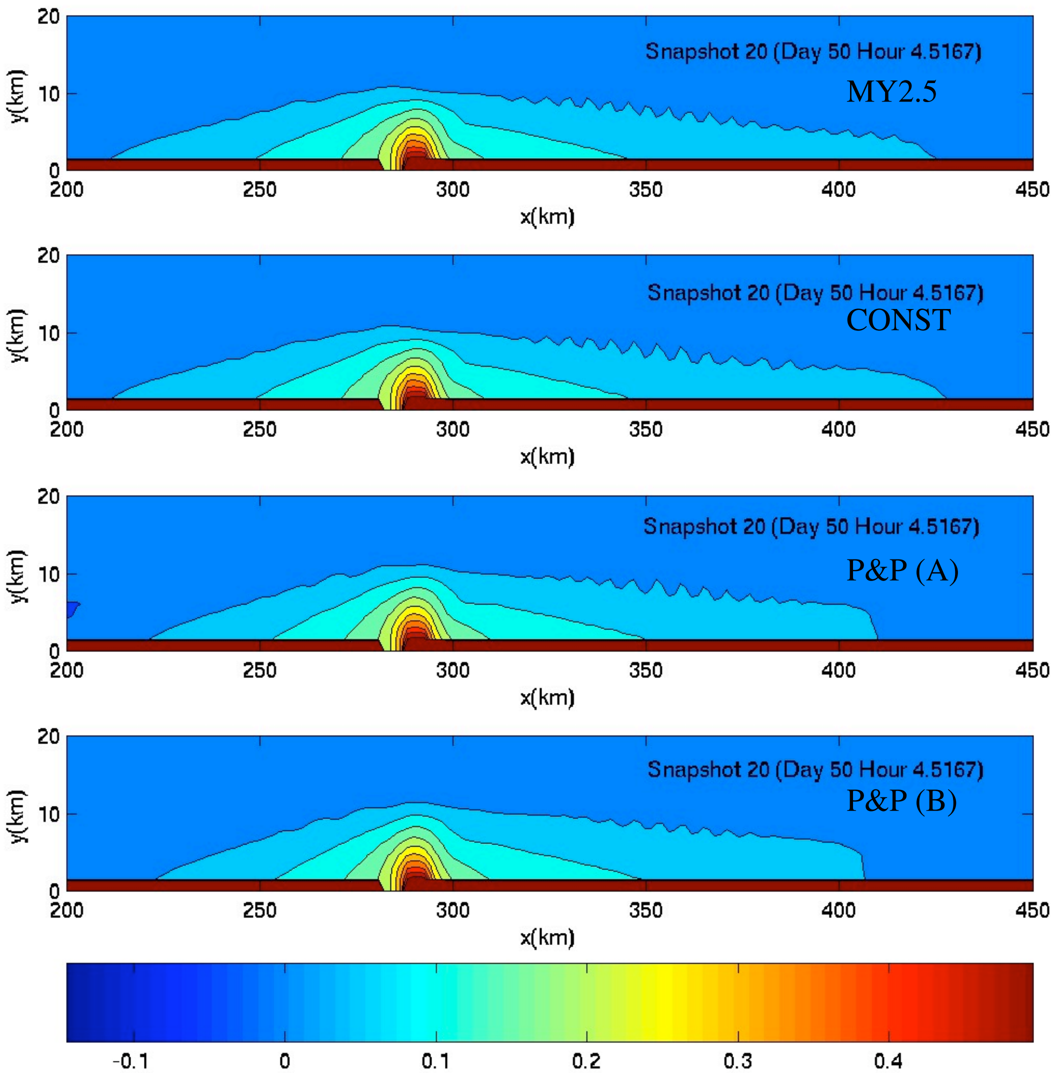

Figure 3.16: The surface-advected plume using a K_{z_b} and K_{s_b} magnitude of 5 x 10^{-4} m^2 s^{-1} on Day 50 is shown for all mixing schemes. Salinity anomaly contours are shown in color with intervals of 0.05, ranging from –0.15 to 0.5.

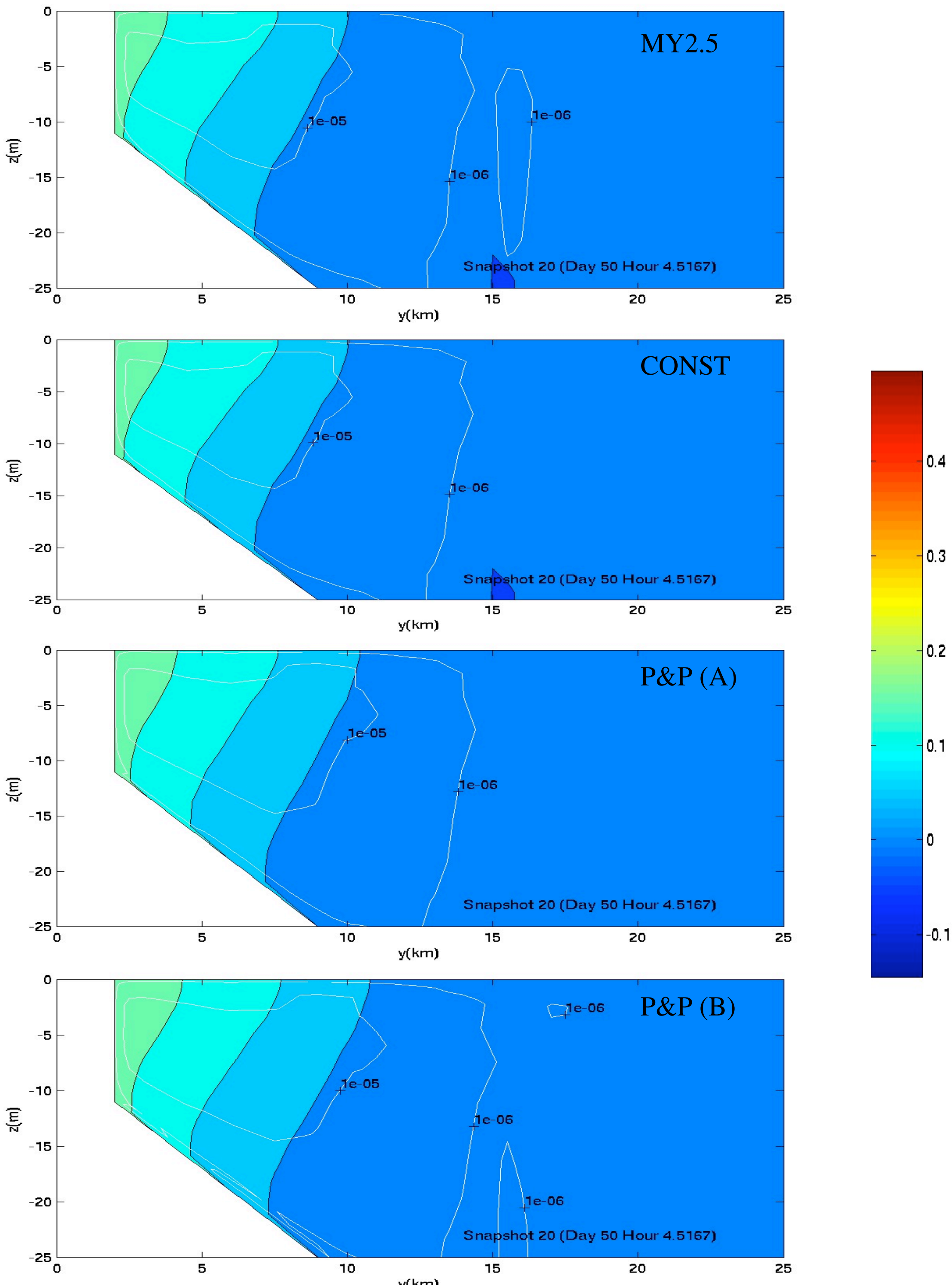

Figure 3.17: The surface-advected plume using a K_{z_b} and K_{s_b} magnitude of 5 x 10^{-4} m^2 s^{-1} on Day 50 is shown for all mixing schemes at one internal Rossby Radius downshelf of the inlet (x = 300 km). Salinity anomaly contours are in color with intervals of 0.05, ranging from –0.15 to 0.5. Point-by-point vertical salt flux (m^2 s^{-1}) contours are contoured in white and labeled in black.

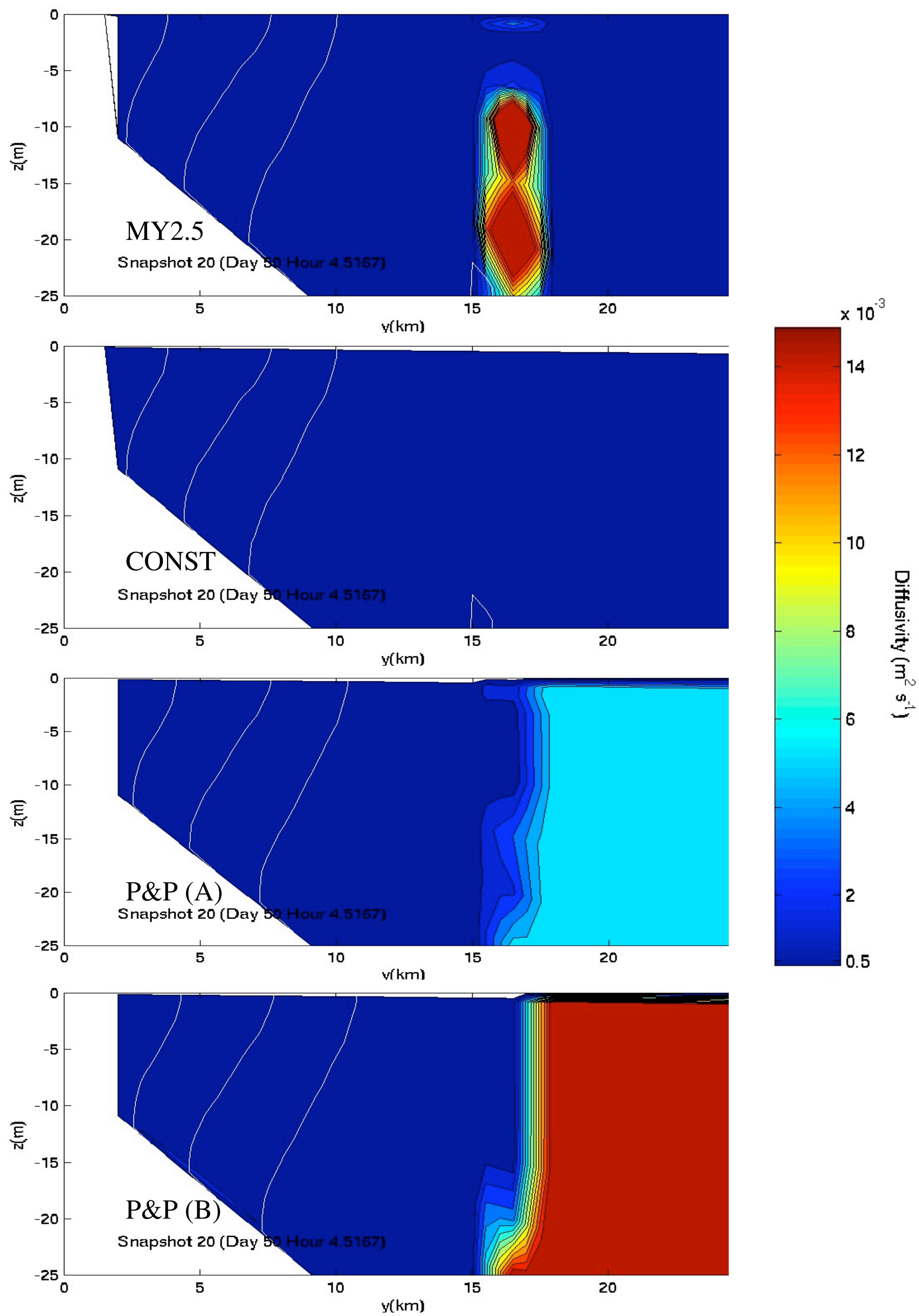

Figure 3.18: Eddy diffusivity (color) and salinity anomaly (white) contours for the surface-advected plume using a K_{z_b} and K_{s_b} magnitude of 5 x 10^{-4} m^2 s^{-1} on Day 50 at x = 300 km.

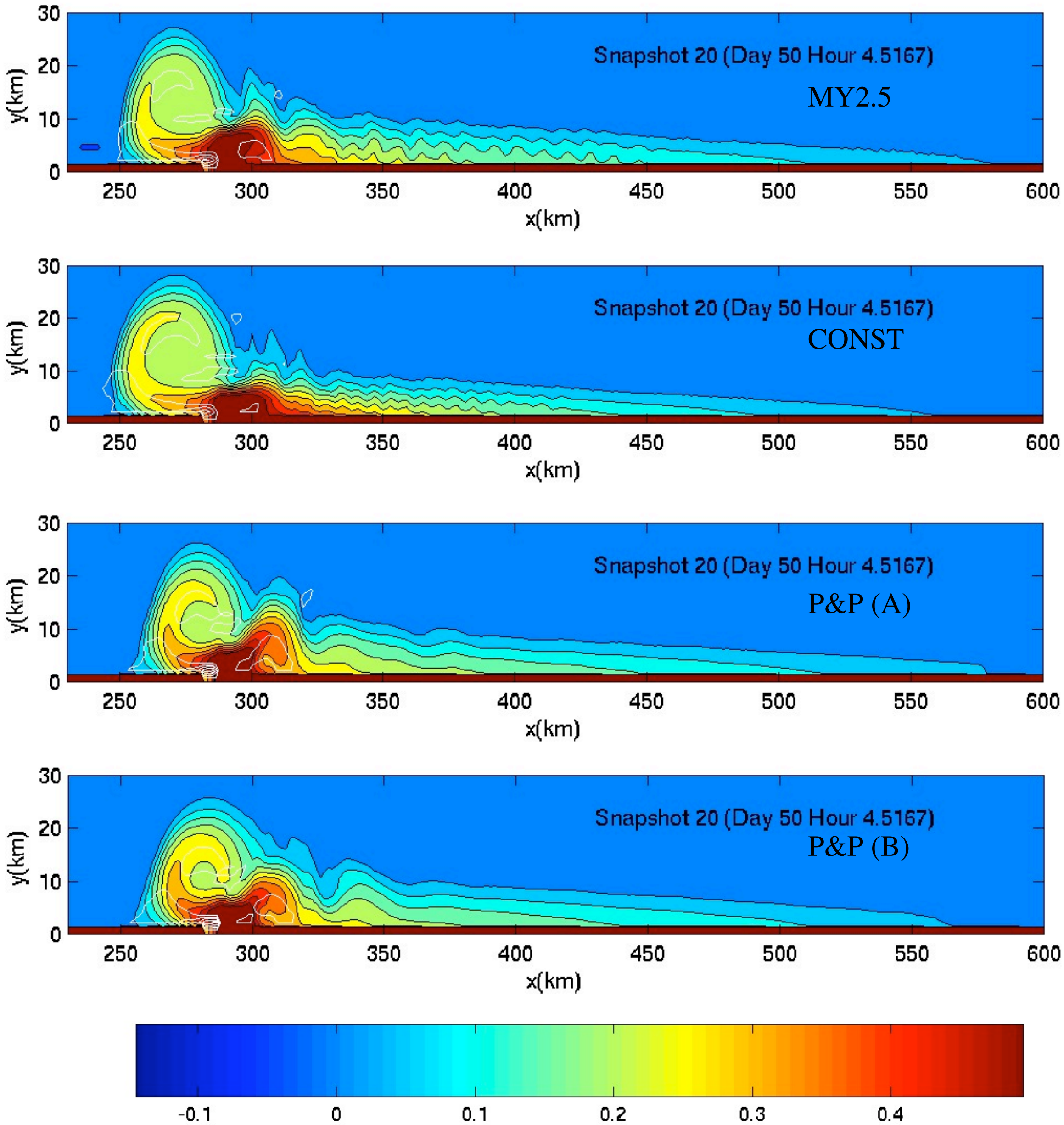

Figure 3.19: The surface-advected plume using a K_{z_b} and K_{s_b} magnitude of 5 x 10^{-6} m^2 s^{-1} at Day 50 is shown for all mixing schemes. The salinity anomaly contours are shown in color with intervals of 0.05, ranging from –0.15 to 0.5. The point-by-point vertical salt flux is shown by the white contours from with 5 x 10^{-6} m^2 s^{-1} to 5 x 10^{-3} m^2 s^{-1}, with intervals of 5 x 10^{-4} m^2 s^{-1}.

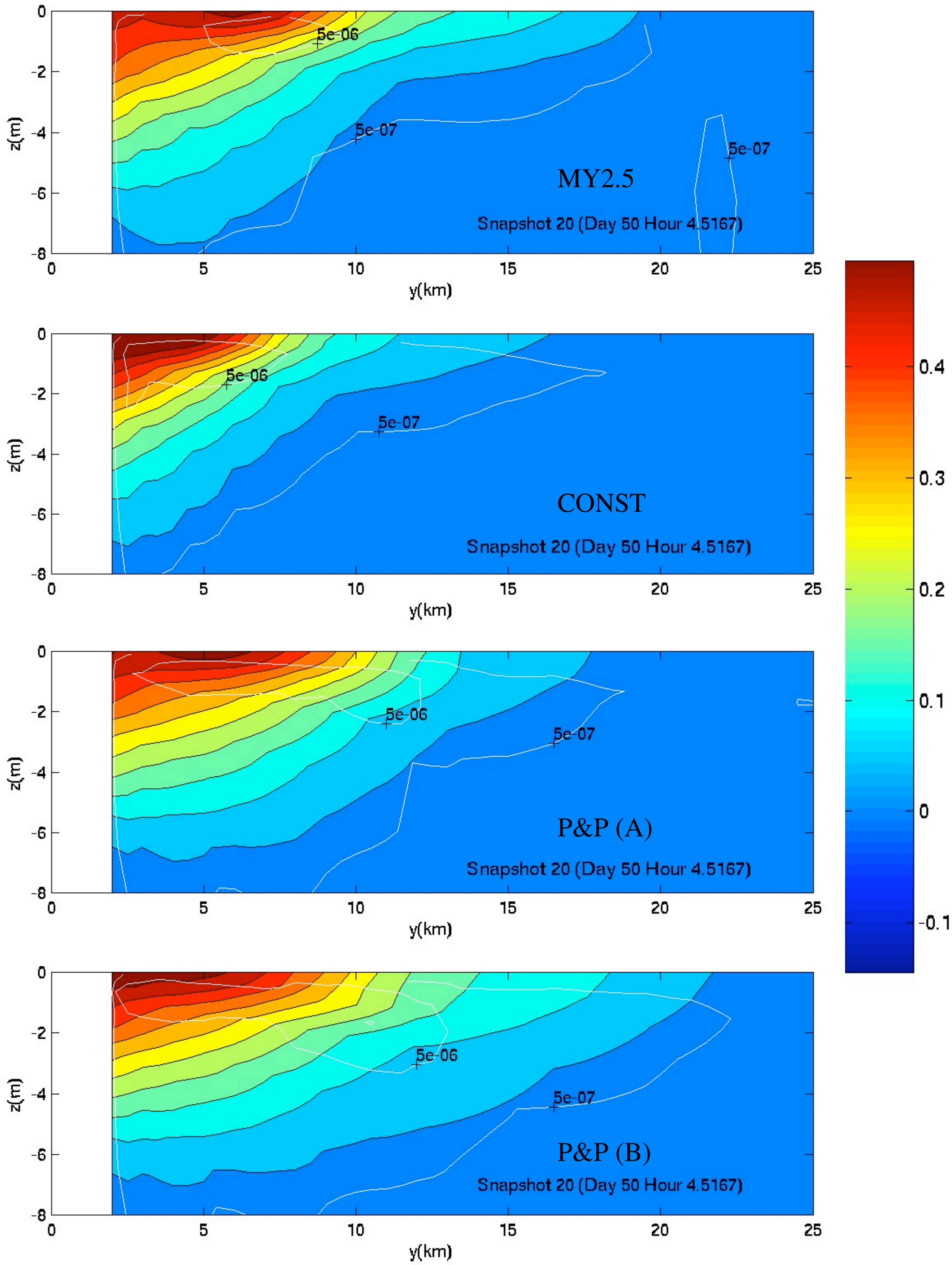

Figure 3.20: The surface-advected plume using a K_{z_b} and K_{s_b} magnitude of 5 x 10^{-6} m^2 s^{-1} on Day 50 is shown for all mixing schemes at one internal Rossby Radius downshelf of the inlet (x = 300 km). Salinity anomaly contours are shown in color with intervals of 0.05, ranging from –0.15 to 0.5. Point-by-point vertical salt flux (m^2 s^{-1}) is shown by the white contours with black labels.

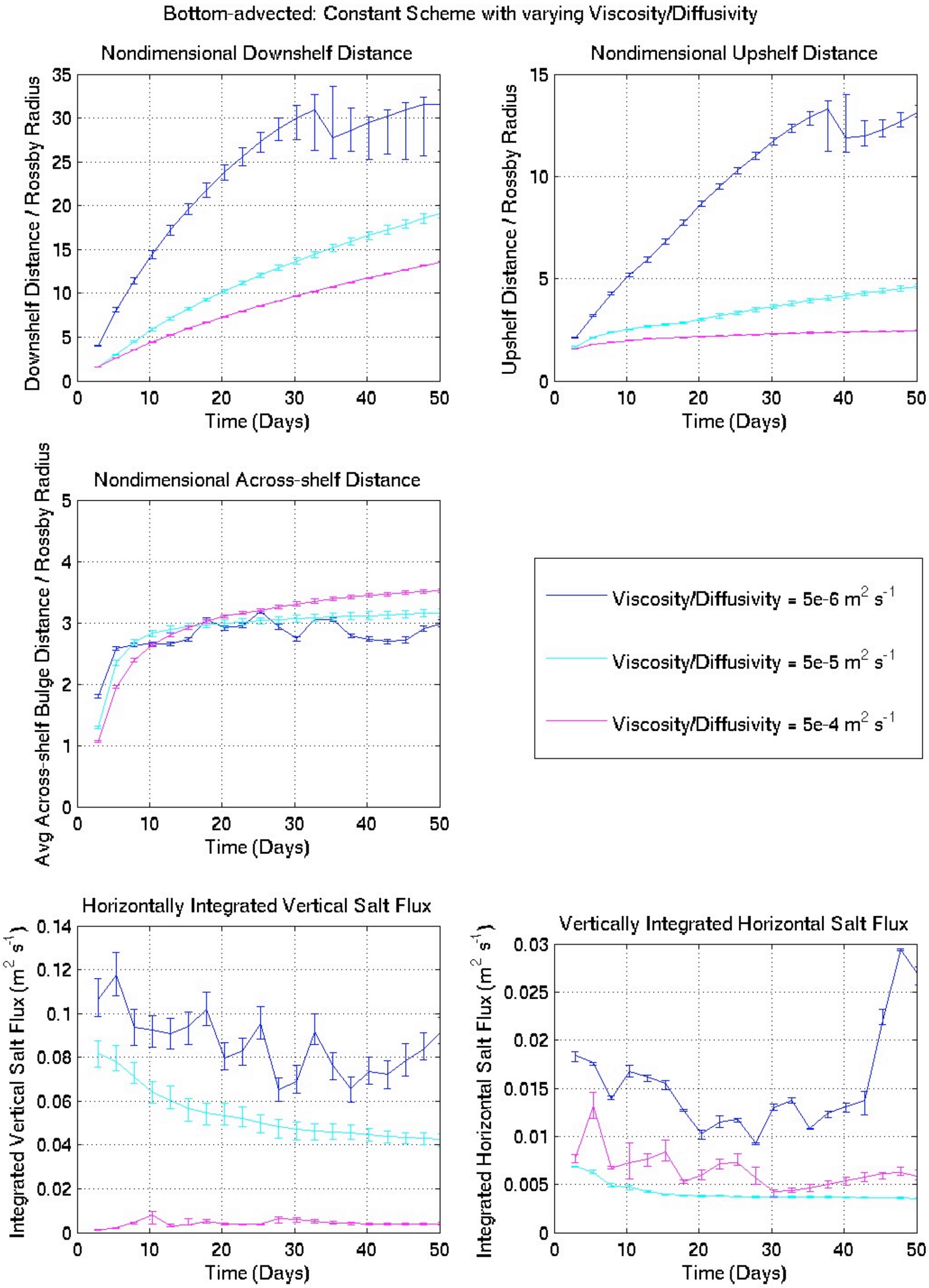

Figure 3.21: The metric developments for the bottom-advected plume using the constant scheme with varying K_{z_b} and K_{s_b} magnitude are shown. Note that the depth of the bottom-advected plume follows the bottom topography, so it was not calculated for this plume. The results for 10% range above and below the salinity anomaly contour of interest is shown (bars) at each snapshot.

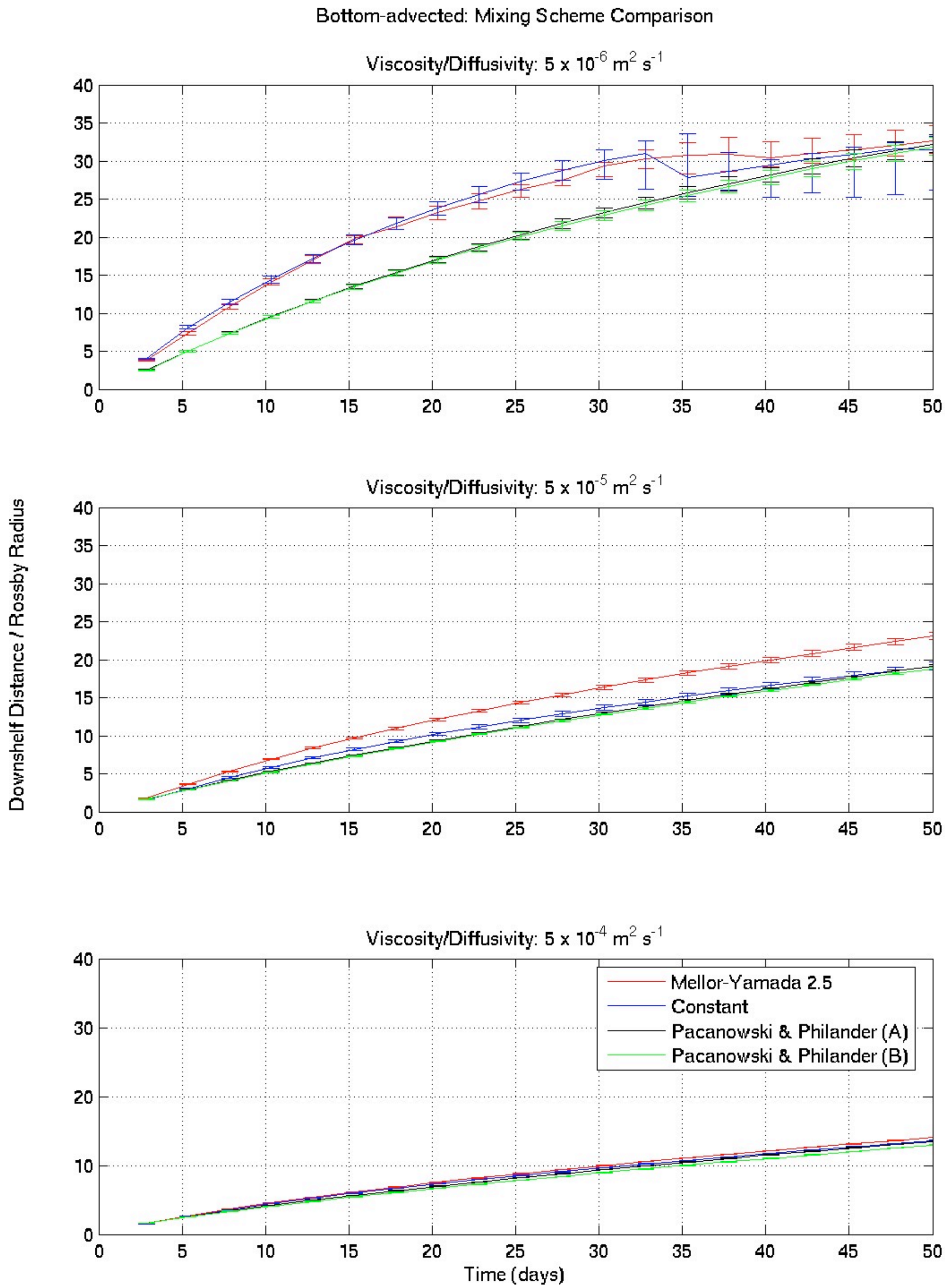

Figure 3.22: Nondimensional downshelf distance as a function of K_{z_b} and K_{s_b} magnitude and vertical mixing scheme for the bottom-advected plume. The results for 10% range above and below the salinity anomaly contour of interest is shown (bars) at each snapshot.

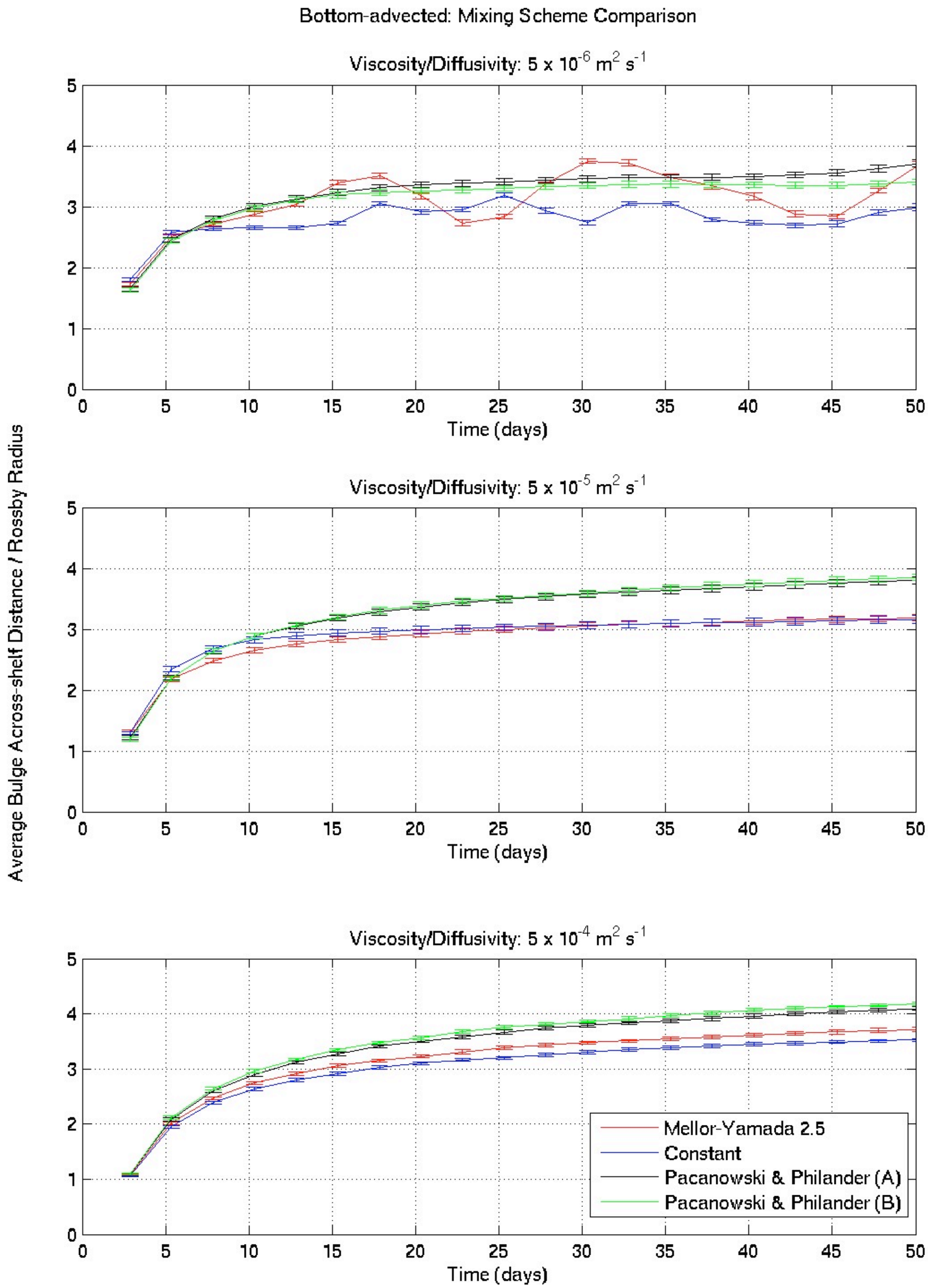

Figure 3.23: Nondimensional across-shelf bulge distance as a function of K_{z_b} and K_{s_b} magnitude and vertical mixing scheme for the bottom-advected plume. The results for 10% range above and below the salinity anomaly contour of interest is shown (bars) at each snapshot.

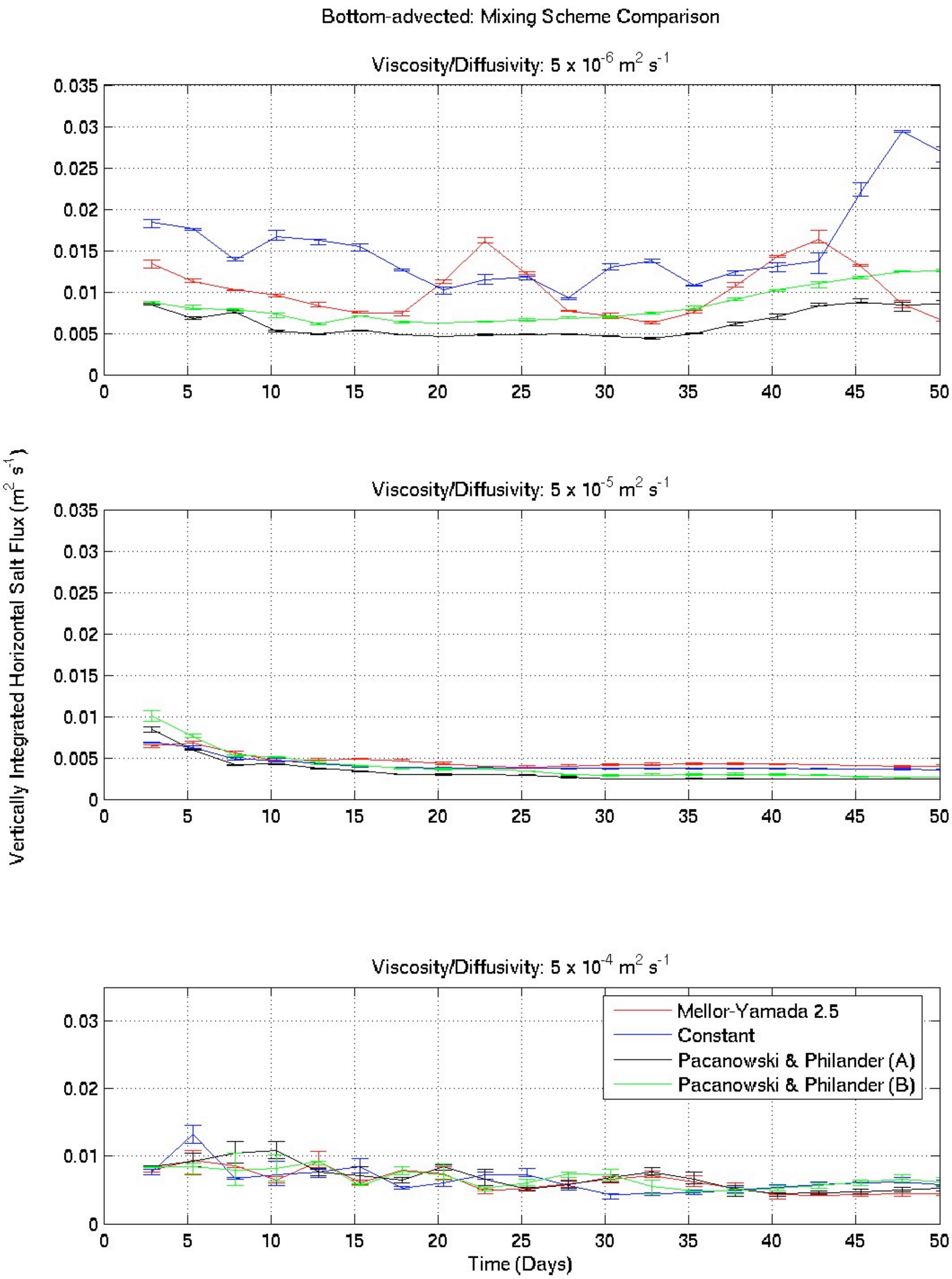

Figure 3.24: Vertically integrated horizontal salt flux as a function of K_{z_b} and K_{s_b} magnitude and vertical mixing scheme for the bottom-advected plume. The results for 10% range above and below the salinity anomaly contour of interest is shown (bars) at each snapshot.

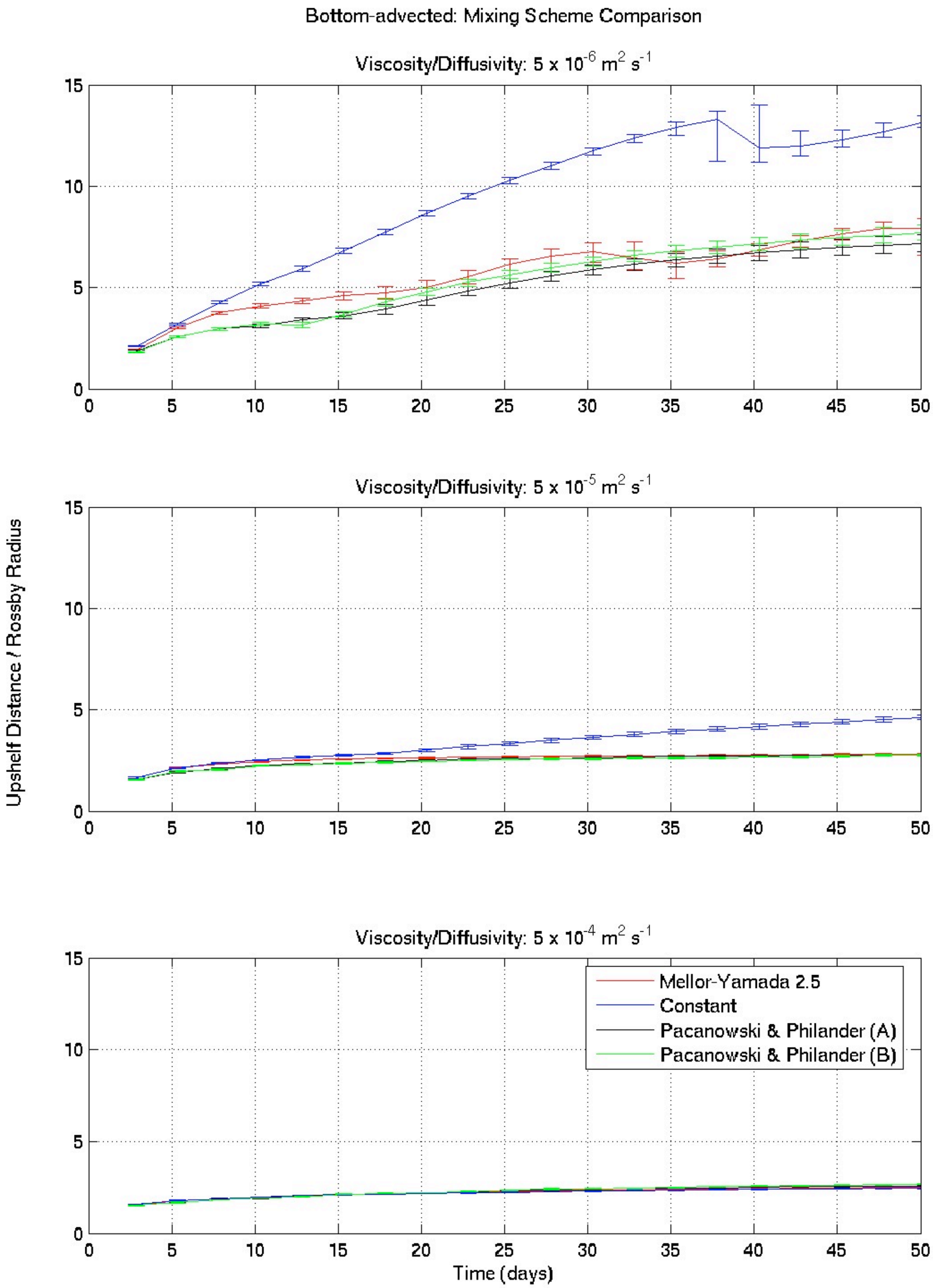

Figure 3.25: Nondimensional upshelf distance as a function of K_{z_b} and K_{s_b} magnitude and vertical mixing scheme for the bottom-advected plume. The results for 10% range above and below the salinity anomaly contour of interest is shown (bars) at each snapshot.

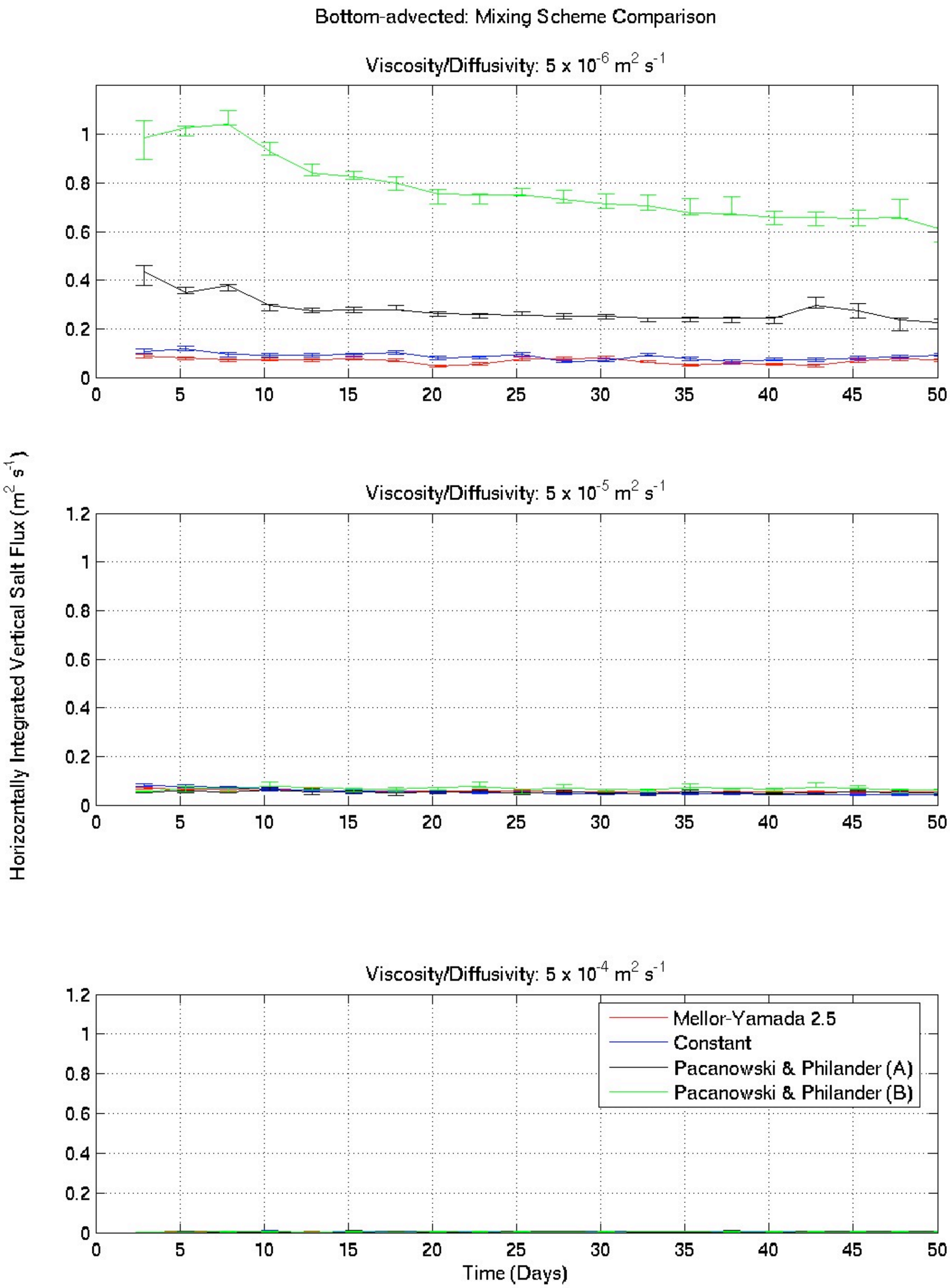

Figure 3.26: Horizontally integrated vertical salt flux as a function of K_{z_b} and K_{s_b} magnitude and vertical mixing scheme for the bottom-advected plume. The results for 10% range above and below the salinity anomaly contour of interest is shown (bars) at each snapshot.

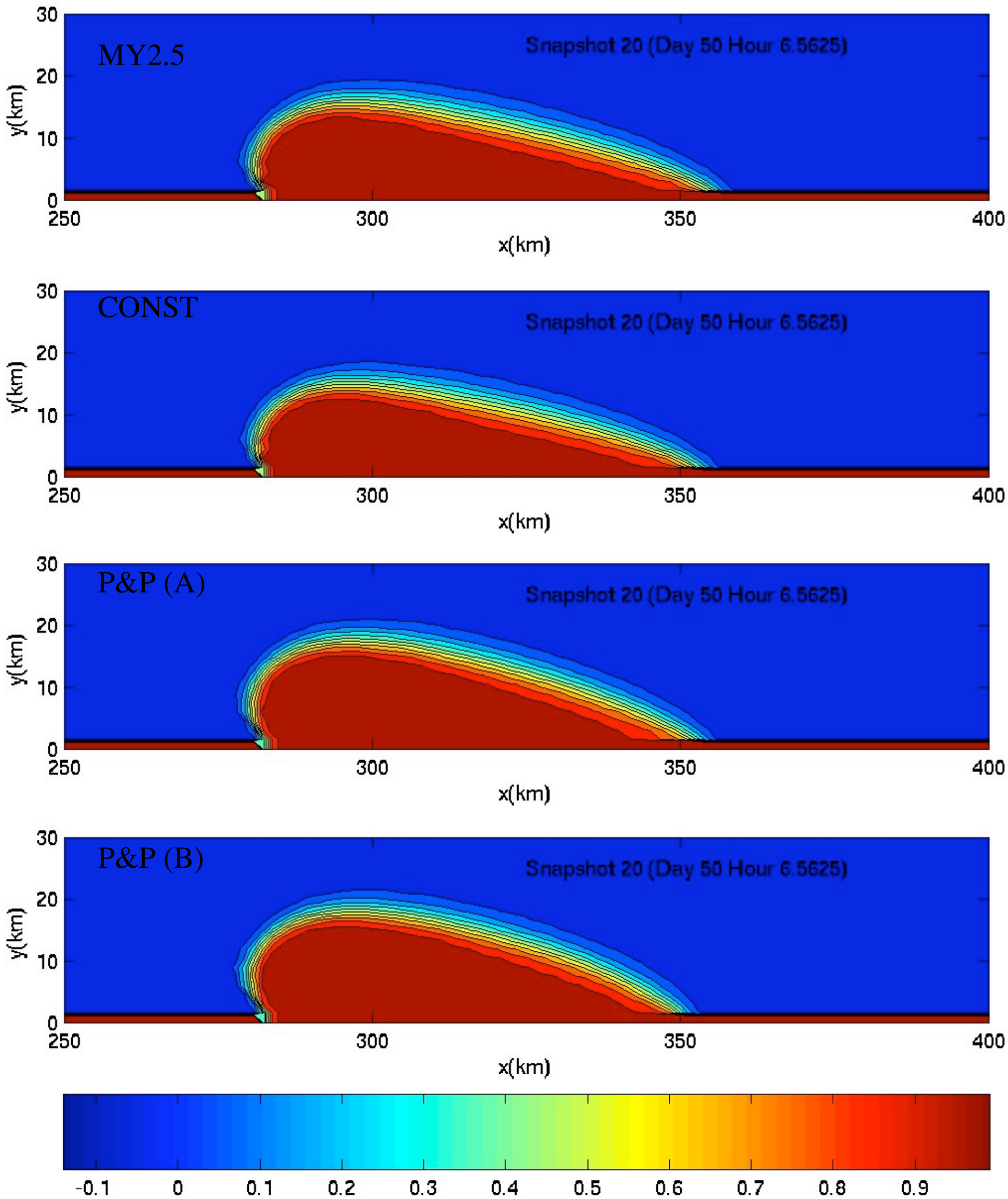

Figure 3.27: The bottom-advected plume using a K_{z_b} and K_{s_b} magnitude of 5 x 10^{-4} m^2 s^{-1} on Day 50 is shown for all mixing schemes. Salinity anomaly contours are shown in color with intervals of 0.1, ranging from –0.15 to 1.0.

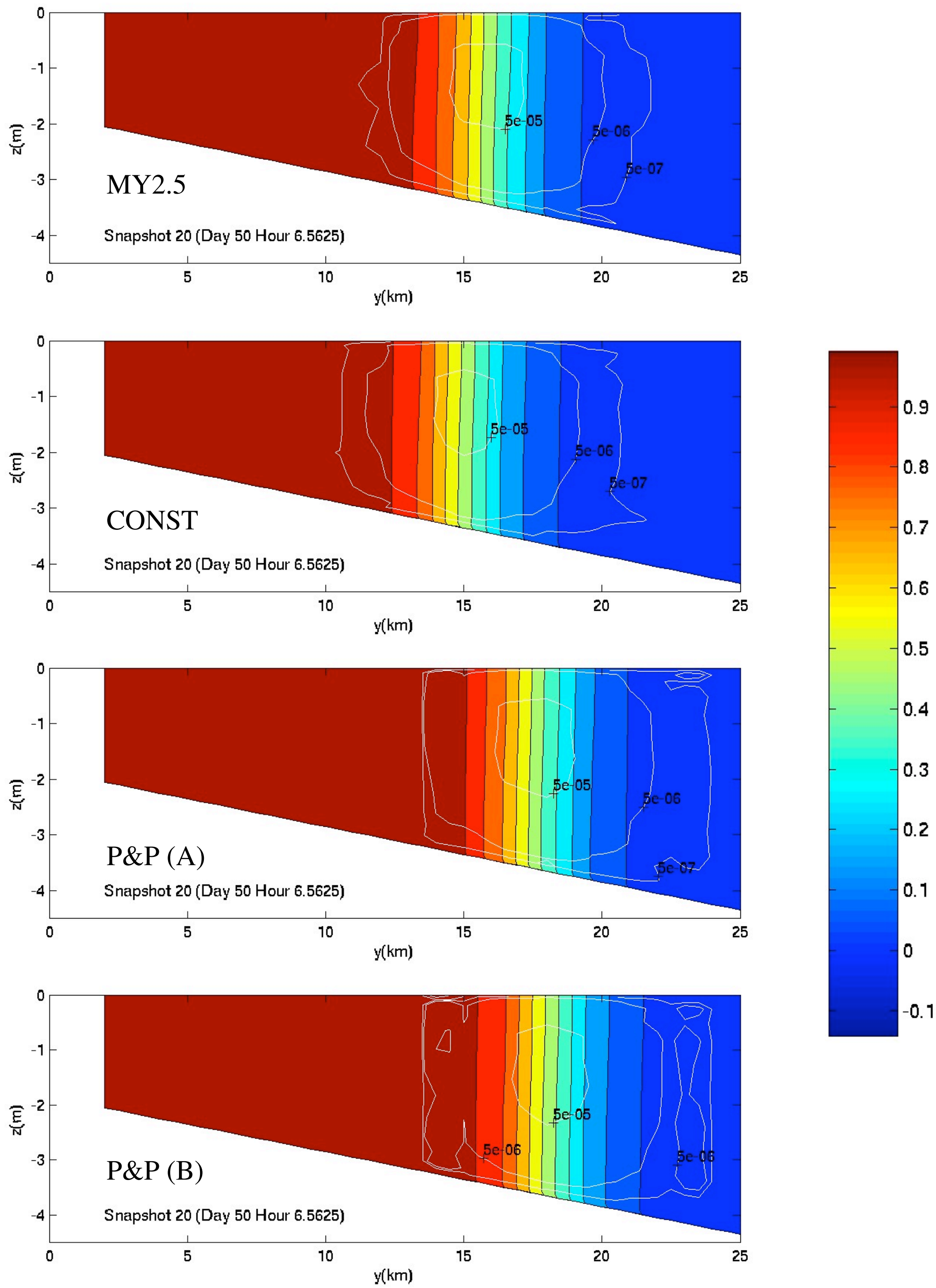

Figure 3.28: The bottom-advected schemes using a K_{z_b} and K_{s_b} magnitude of 5 x 10^{-4} m^2 s^{-1} on Day 50 is shown for all mixing schemes at one internal Rossby Radius downshelf of the inlet (x = 297 km). Salinity anomaly contours are shown in color with intervals of 0.1, ranging from –0.15 to 1.0. Point-to-point vertical salt flux (m^2 s^{-1}) is contoured in white and labeled in black.

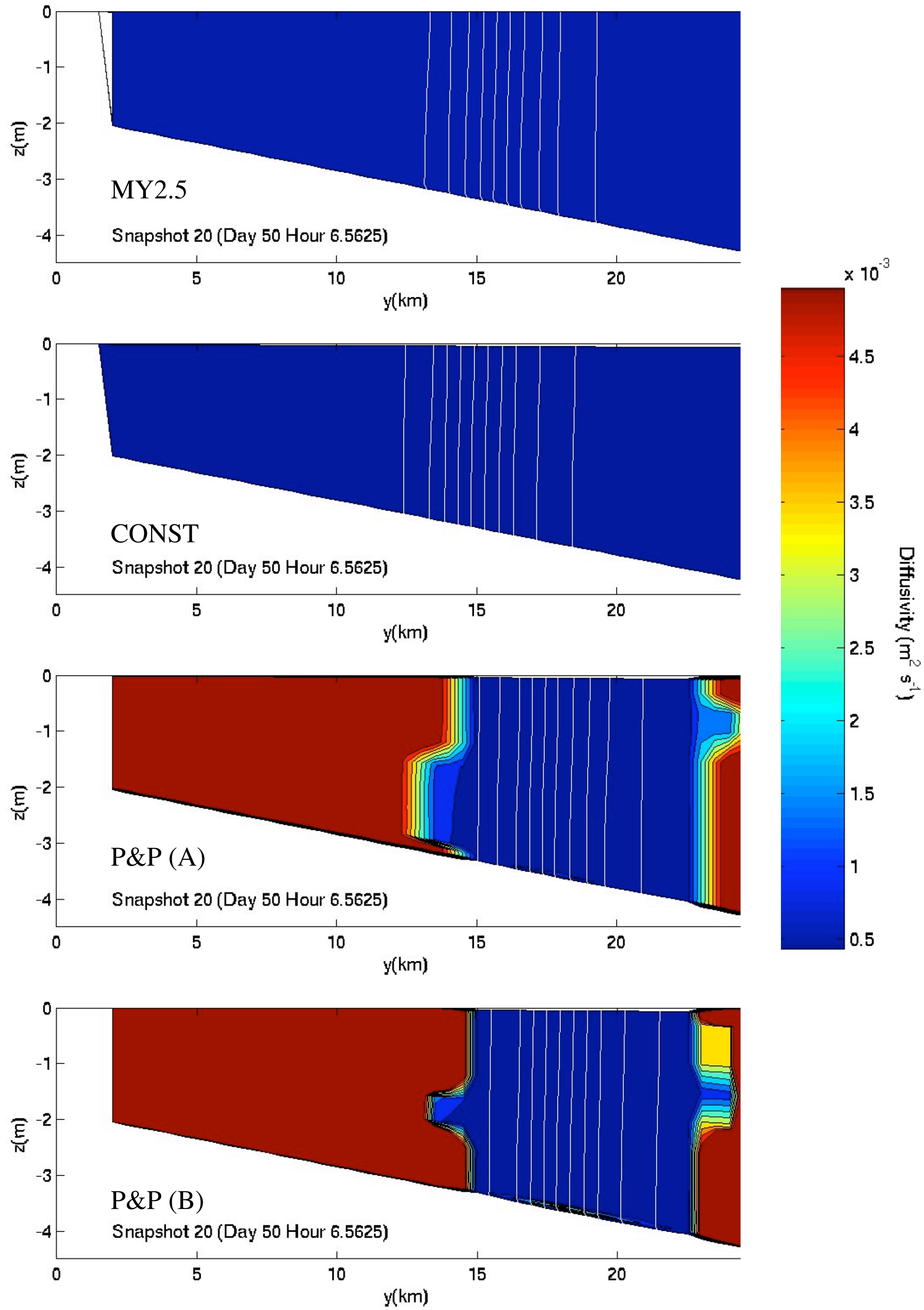

Figure 3.29: Eddy diffusivity contours (colored) overlain with salinity anomaly contours (white) for the bottom-advected plume using all schemes at Day 50 at x = 297 km. All plumes have the same diffusivity magnitude within the plume front.

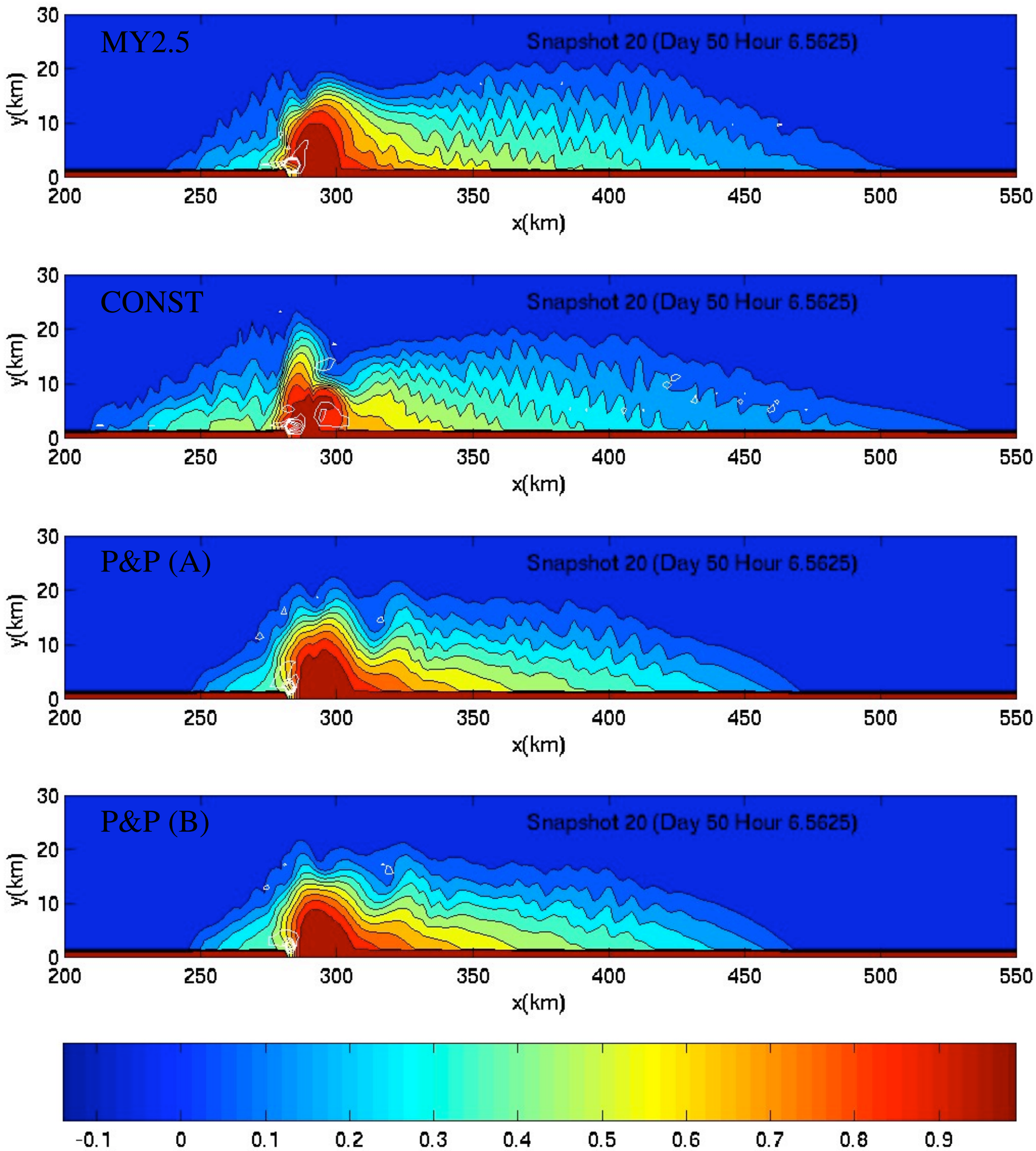

Figure 3.30: The bottom-advected plume using a K_{z_b} and K_{s_b} magnitude of 5 x 10^{-6} m^2 s^{-1} at Day 50 is shown for all mixing schemes. Salinity anomaly contours are shown in color with intervals of 0.1, ranging from –0.15 to 1.0. The point-by-point vertical salt flux is shown by the white contours from with 5 x 10^{-6} m^2 s^{-1} to 5 x 10^{-3} m^2 s^{-1}, with intervals of 1 x 10^{-3} m^2 s^{-1}.

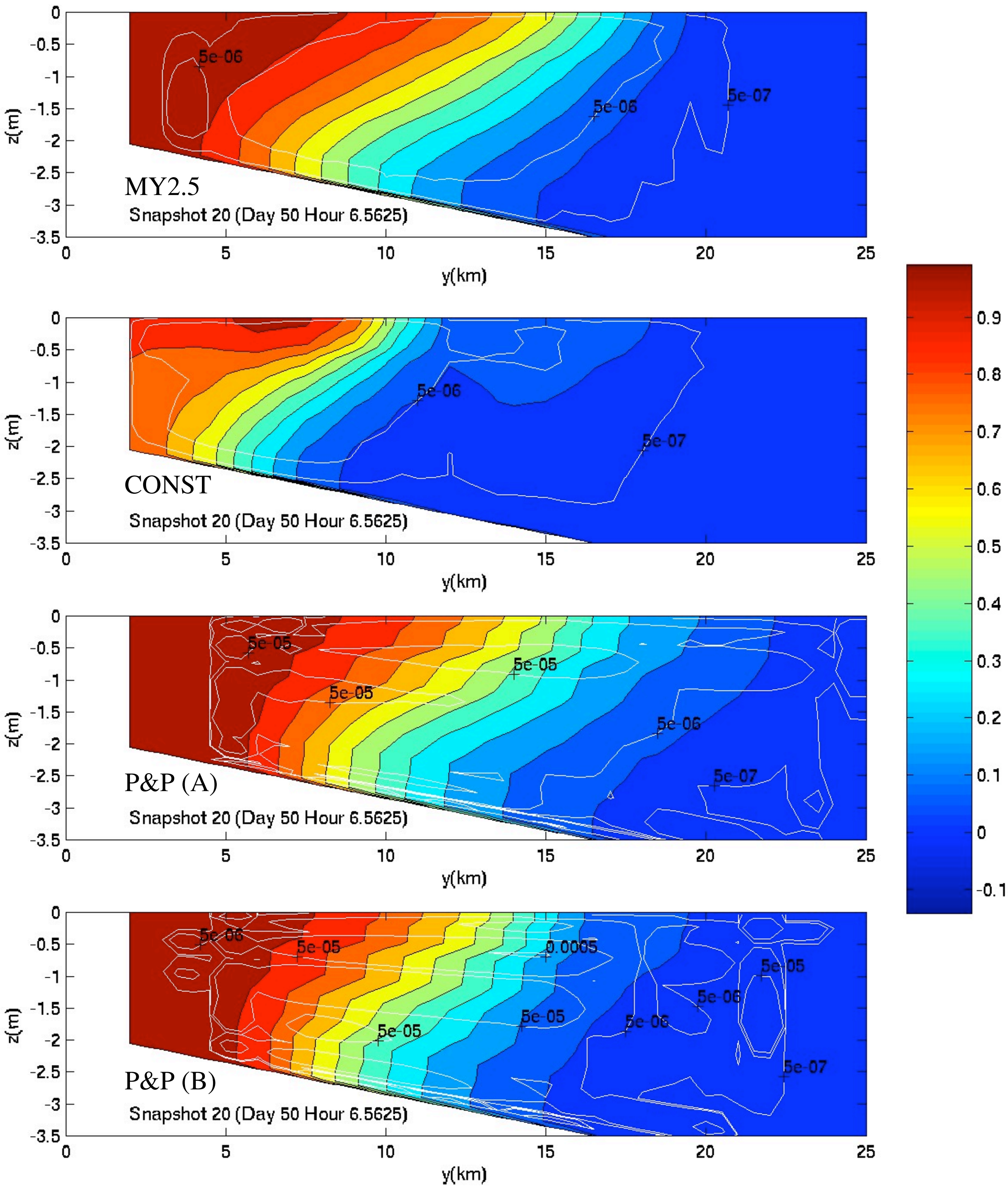

Figure 3.31: The bottom-advected plume using a K_{z_b} and K_{s_b} magnitude of 5 x 10^{-6} $m^2 s^{-1}$ on Day 50 is shown for all mixing schemes at one internal Rossby Radius downshelf of the inlet (x = 297 km). Salinity anomaly contours are shown in color with intervals of 0.1, ranging from –0.15 to 1.0. The point-by-point vertical salt flux (m^2 s^{-1}) is contoured in white and labeled in black.

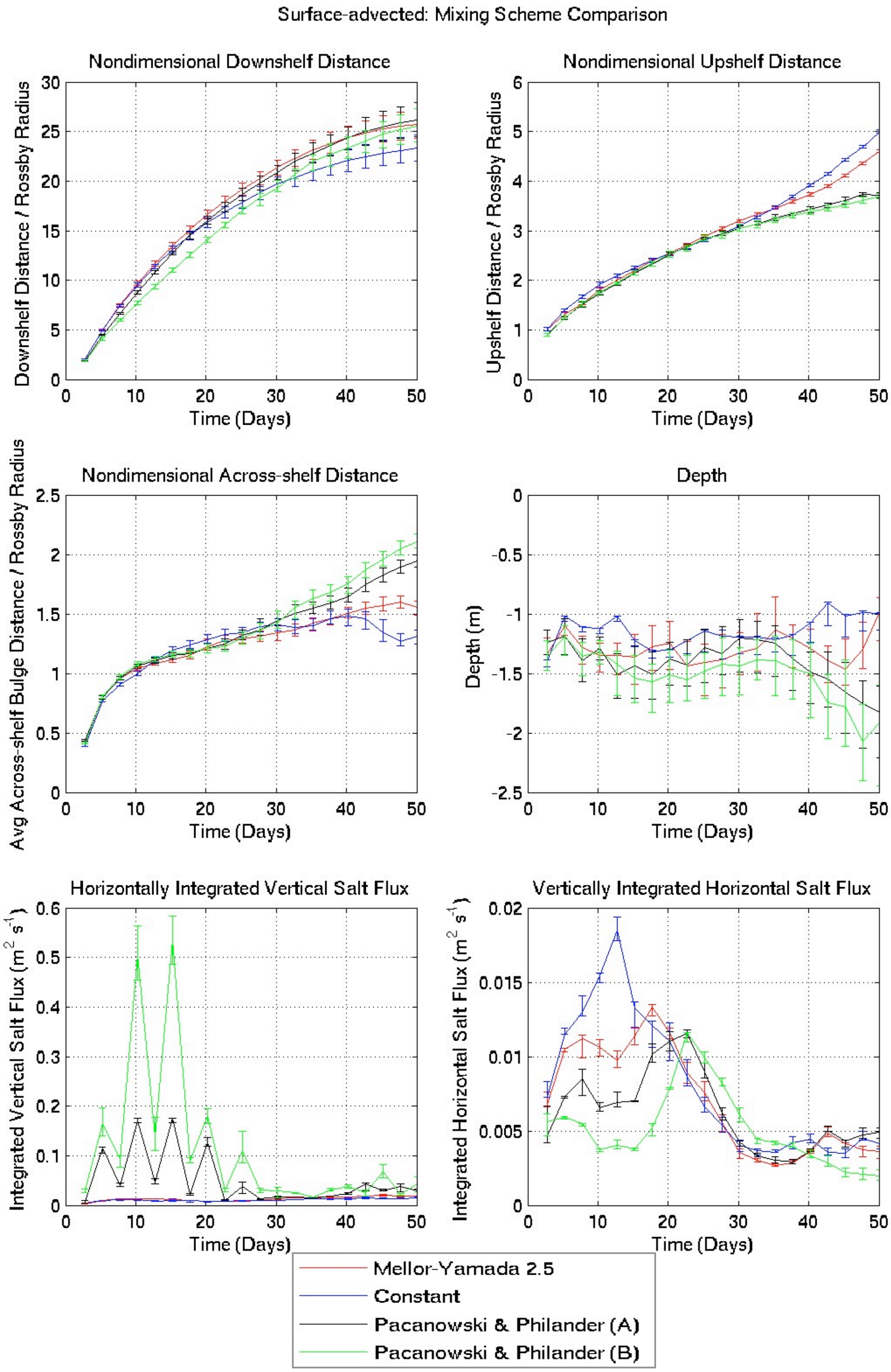

Figure 3.32: Comparison of metrics across mixing schemes for the surface-advected plume when using a K_{z_b} and K_{s_b} of 5 x 10^{-6} m^2 s^{-1}. The results for 10% range above and below the salinity anomaly contour of interest is shown (bars) at each snapshot.

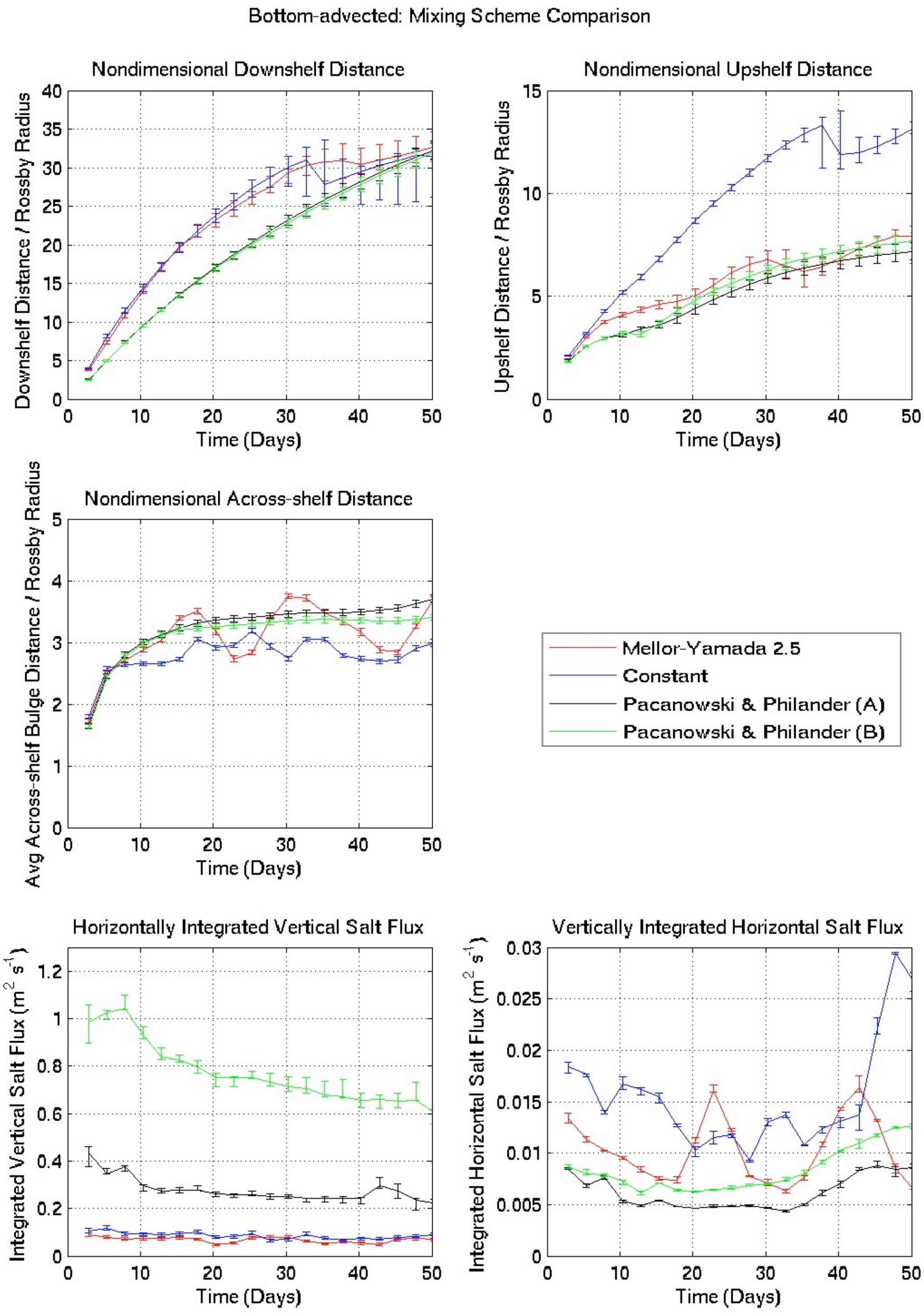

Figure 3.33: Comparison of metrics across mixing schemes for the bottom-advected plume when using a K_{z_b} and K_{s_b} of 5 x 10^{-6} m^2 s^{-1}. The bottom-advected plume follows the bottom topography, so depth is not calculated for this plume. The results for 10% range above and below the salinity anomaly contour of interest is shown (bars) at each snapshot.

CHAPTER 4

RESULTS: BUOYANCY AND TIDAL FORCING

Simulations with tidal forcing used a K_{z_b} and K_{s_b} of 5 x 10^{-4} m^2 s^{-1} in order to account for the frictional forces associated with tides. The plumes were subjected to 0.1 m, 0.2 m, and 0.5 m tidal amplitudes. However, the 0.5 m amplitude was not applied to the surface-advected plumes; the plumes would need to be run on unrealistic timesteps to satisfy the CFL condition and simulate the higher amplitude tides. Recall that surface- and bottom-advected plumes are dynamically dissimilar and run with different initial conditions, therefore it would be expected that these two plumes result in diverse outcomes using the model.

In this chapter, the nondimensional downshelf (X_{DN}), upshelf (X_{UP}), and across-shelf (Y_{AC}) distances and horizontally integrated vertical (SF_V) and vertically integrated horizontal (SF_H) salt fluxes and background viscosity/diffusivity (K_{z_b} and K_{s_b}) will be abbreviated as shown in the parentheses. The normalized downshelf ($X_{DN\text{-}NOR}$), upshelf ($X_{UP\text{-}NOR}$), and across-shelf ($Y_{AC\text{-}NOR}$) distances and horizontally integrated vertical ($SF_{V\text{-}NOR}$) and vertically integrated horizontal ($SF_{H\text{-}NOR}$) salt fluxes are abbreviated differently. The downshelf and upshelf metrics describe the farthest downstream or upstream point of the plume for the specified salinity anomaly contour, where the surface-advected plume used a contour of 0.10 and the bottom-advected used a contour of 0.25. The across-shelf distance is the averaged offshore extension of the specified salinity anomaly contour across 2 internal Rossby Radii downshelf of the freshwater inlet. The depth is averaged across the same Rossby Radii distance as the across-shelf in the x-direction and is taken at 80% of the averaged across-shelf distance in the offshore direction. The salt fluxes are integrated vertically or horizontally (y-direction) at one internal Rossby radius downshelf of the inlet (at 300 km for surface-advected plumes and at 297 km for bottom-advected plumes).

These metrics are then plotted with ranges (shown by the errorbar symbols) representing the location of the salinity anomaly contour that is 10% above and 10% below the contour of interest.

4.1 Effect of changes in tidal amplitude on mixing schemes

4.1.1 Changes in surface-advected plumes due to tidal amplitude

The structure of the surface-advected plumes shows only a slight change due to the presence of tides. Comparison of the plan view of the plume with no tides (Figure 4.1, top panel) to the plume with 0.1 m and 0.2 m tidal amplitudes (lower two panels) for MY2.5 reveals that the outer salinity anomaly contours vary only slightly in downshelf, upshelf, and across-shelf extension. Like MY2.5, only minor variations in the plumes are seen for the other schemes (Figures 4.2 through 4.4). The greater mixing accompanying the increase in tidal amplitude leads to a decrease and/or removal of the downshelf meanderings of the plume; a decrease in plume meandering due to tidal forcing has also been observed by Simpson (1997). Overall, an increase in tidal amplitude caused the plumes in decrease downshelf distance and slightly in across-shelf movement while slightly increasing in upshelf penetration.

The cross-sections at 300 km (one internal Rossby Radius downshelf of inlet) for the surface-advected plume for all mixing schemes with and without tides (Figures 4.5 through 4.8) reveal little variation in the salinity anomaly contours and in the point-to-point vertical salt flux. There is, however, a decrease in across-shelf extent and less expansion in depth with increasing tidal amplitude, which corresponds to the decrease in the size and across-shelf extent of the 1.05

x 10^{-5} m^2 s^{-1} vertical salt flux contour. Note that while all plumes touch the bottom, the maximum salinity anomaly contour that reaches the water column base is the 0.15 contour; the absolute freshest water for the model run has a salinity anomaly value of 1.00.

The metrics of each scheme for the various tidal amplitudes are shown in Figures 4.9 to 4.12. Overall, an increase in tidal amplitude limits the X_{DN} and Y_{AC} growth of the plume while at the same time increasing growth X_{UP}, however, the variations between schemes are smaller than the ranges of the different schemes (top left panels, middle left panels, top right panels), indicating minimal effects of the tides. The depth, SF_V, and SF_H also show minimal change for the tidal amplitudes (middle right panels, bottom panels).

4.1.2 Changes in bottom-advected plumes due to tidal amplitude

Bottom-advected plumes experience much larger effects due to changes in tidal amplitude. Comparison of the plan view of the plume with no tides (Figure 4.13, top panel) to 0.1 m, 0.2 m, and 0.5 m tidal amplitudes (lower panels) for MY2.5 at Day 50 demonstrates the strong relationship between the increase in tidal amplitude and changes in the plume shape. Increasing the amplitude causes the plume to develop less in the alongshelf directions (downshelf and upshelf) but grow in the across-shelf direction. The constant scheme shows much more development in the alongshelf directions, especially using 0.5 m amplitudes in the upshelf direction (Figure 4.14) while both P&P schemes behave similarly to MY2.5 (Figures 4.15 and 4.16).

The cross-sectional view of the bottom-advected plumes at 297 km (one internal Rossby Radius downshelf of inlet) for the various mixing schemes (Figures 4.17 through 4.20) reveal strong horizontal stratification and vertical salt flux, with the across-shelf salinity anomaly gradient and contoured point-to-point vertical salt flux dependent on tidal amplitude. In general, the addition of tides decreases the across-shelf salinity anomaly gradient. The location of maximum point-to-point vertical salt flux on the plume for 0 m, 0.1 m, and 0.2 m tidal amplitudes are all roughly centered on the 0.55 salinity anomaly contour, except for MY2.5 with a 0.2 m tidal amplitude where the center lies with fresher water. For 0.5 m tidal amplitudes, the location differs depending on the mixing scheme but is always within the horizontal salinity gradient.

The response of the bottom-advected plumes to tidal forcing varied dramatically across mixing schemes. Examination of the metrics of each scheme for the various tidal amplitudes (Figures 4.21 to 4.24) reveals that an increase in tidal amplitude leads to a large decrease in X_{DN} for all schemes. However, the behavior of the other metrics differs across schemes since tidal forcing alters the plume shape. MY2.5 (Figure 4.21) causes the plume to grow Y_{AC} with the presence of tides while the X_{UP} expansion depends on the tidal amplitude. The higher tidal amplitudes creates more SF_V than both, no tides and 0.1 m tidal amplitudes, and SF_H is the largest with 0.5 m tides while the lower tidal amplitudes produced less salt flux. The constant scheme (Figure 4.22) results in a large increase in X_{UP} propagation. Y_{AC} increases with increasing tidal amplitudes at small amplitudes, but at a larger amplitude (0.5 m) is dramatically smaller. The SF_V decreases as tidal amplitude increases. SF_H, like MY2.5, is largest with 0.5 m tides and much lower with lower amplitudes. Tidal forcing for both P&P (Figures 4.23 and 4.24) has very little influence on changes in the X_{UP} propagation but exerts a strong influence on the Y_{AC}. Both the temporal structure and magnitude of the salt fluxes varied with tides, with 0.5 m amplitudes typically resulting in greater fluxes.

4.1.3 Overall results

Tidal amplitudes of 0.1 and 0.2 m did not considerably alter surface-advected plumes. Variations in the plume metrics due to changes in tidal amplitude were comparable to the simulations lacking tidal forcing (Figure 4.9 to 4.12). However, similar to previous findings, the presence of tides decreased the instabilities and meanderings of the plume (Simpson 1997). While the mixing from tides was not large enough to modify much of the surface-advected plume, tidal mixing and the associated frictional influence were able to stabilize the flow and dampen the instabilities.

Because bottom-advected plumes were greatly influenced by changes in tidal amplitude due to large bottom influence (Figures 4.21 to 4.24). Increasing tidal amplitude resulted in a decrease in X_{DN} for all schemes. This result is consistent with previous studies, where tidal input created a decrease in downshelf penetration (Soares et al. 2007 and Garvine 1999). Soares et al. (2007) also demonstrated the destratification of the nose of the plume due to tidal stirring. Forcing higher tidal amplitudes, created faster velocities subjected to greater frictional forces. Thus, at the nose of the plume, where vertical stratification of horizontal velocity is large, the vertical mixing was enhanced by the addition of tidal mixing from bottom frictional forces and resulted in a decrease in X_{DN}.

Changes in the X_{UP} direction differed depending on the mixing scheme. Both P&P schemes (Figures 4.23 and 4.24) produced roughly the same X_{UP} expansion for variations in tidal amplitude as for only buoyancy forcing. The presence of 0.1 m tidal amplitudes had little effect on X_{UP} for the MY2.5 and constant schemes (Figures 4.21 and 4.22). For 0.2 m tidal amplitudes, X_{UP} decreased for MY2.5 and increased for the constant scheme. In the absence of tides, greater vertical mixing resulted in less X_{UP} expansion. Since an increase in tidal amplitude increases vertical mixing in the model, it would be expected that the P&P and MY2.5 schemes would result in similar or less upshelf propagation than no tides due to increased mixing. The constant scheme, however, increased in X_{UP} due to the averaged tidal field moving upshelf; this will be discussed in more detail later. The 0.5 m results will be discussed in Chapter 5.

Increasing amplitude from 0 m to 0.2 m resulted in more Y_{AC} growth for all the schemes (0.5 m tides will be discussed in detail later). The combination of freshwater discharge moving into the model and tidal forcing conditions in the model caused the bottom-advected plumes to grow more Y_{AC} with larger tidal amplitudes (middle panels, Figures 4.21 to 4.24). The tides in the model were forced along the offshore most boundary as a cotidal line with a 0° phase angle. Freshwater discharge and tidal forcing combined to create greater velocities and mixing during ebb tide that resulted in the across-shelf expansion of the plume. During flood tide, tidally- and buoyancy-driven velocities were in opposition. The competition between freshwater and tidal forcing has been shown in a number of previous works (Simpson 1997 and Simpson and Souza 1995), where the residual flow remains the same with tidal forcing (Stacey et al. 2001). Therefore, the plumes overall grew across-shelf due to the larger across-shelf forcing and buoyancy forcing. Again, the 0.5 m results will be discussed in Chapter 5.

The constant scheme resulted with lower tidally averaged SF_V when subjected to higher tidal amplitudes due to having larger instantaneous negative SF_V values (lower left panel, Figure 4.22). At 0.5 m, the constant scheme had a negative salt flux due to large overstraining in the plume. The other schemes considered the stratification present when calculating the mixing coefficients while the constant used 5 x 10^{-4} m^2 s^{-1} as the viscosity and diffusivity, causing the scheme to larger overstraining of the plume during flood tide compared to the other schemes. The large peak and fall in the SF_V for MY2.5 when using 0.2 and 0.5 m tides were also partially due to tidal straining fluctuations (lower left panel, Figure 4.21). P&P SF_V values (lower left panels, Figure 4.23 and 4.24) were similar with changes in amplitude for the first 30 days of the simulation; after this period of time, the changes in SF_V for the P&P schemes were dependent on the changes in the salinity gradient. Around Day 30, P&P (A) reached a peak and maintained the highest SF_V when using 0.5 m tides due to a combination of a stronger salinity gradient and calculated mixing coefficient values (bottom panels, Figure 4.19 and 4.23). The other two tidal amplitudes showed either less of a gradient or less point-to-point vertical salt flux, or both (Figure 4.19 and 4.23). The same was shown for P&P (B), where results depended on the salinity anomaly gradient and the point-to-point vertical salt flux; the largest salt flux, using no tides, had stronger stratification while the least salt flux, using 0.2 m tides, had the weakest point-to-point salt flux and weaker stratification (Figures 4.20 and 4.24).

There was no straight-forward relationship between changes in tidal amplitude and changes in SF_H (bottom right panels, Figures 4.21 to 4.24); this was most likely due to the addition of more factors, such as the effects of tidally associated velocities and changes in plume dynamics, affecting the resulting plume. The largest tidal amplitude of 0.5 m created larger SF_H compared to the other tidal amplitudes most likely caused by the higher horizontal velocities created from tidal forcing. In addition, in general, the horizontal salinity anomaly gradient for 0.1 m and 0.2 m was less than the gradient produced from no tidal forcing (Figures 4.17 to 4.20), so the two lower tidal amplitudes roughly produced lower SF_H than with no tides (Figures 4.21 to 4.24). However, overall, there was no clear relationship between tidal amplitude change and SF_H.

4.2 Effect of schemes on normalized metrics with tidal forcing

Since the structure of the plume is governed by a variety of factors, it is difficult to determine the role of each physical mechanism on the evolution of the plume and its simulated effects by the different schemes. In an attempt to isolate the effects of tidal mixing from buoyancy effects, each metric in the tidally-driven simulations is normalized by the same metric in the buoyancy only simulation, as shown in the following equation,

$$metric_{normalized} = \frac{metric_{buoyancy-tidally-forced}}{metric_{buoyancy-forced}} \tag{4.1}$$

While the effects of tides are nonlinear and a simple normalization cannot remove all effects of buoyancy from the simulation, (4.1) does allow for greater insight into the individual effects of tides. The following sections show the normalized metrics to highlight the influence of scheme on the resulting plume. The simulations with no tides are shown as a basis for comparison for scheme differences.

4.2.1 Effect of schemes on metrics for surface-advected plumes

In addition to the minor effects of tidal amplitude changes on surface-advected plumes, the various mixing schemes have minor differences among themselves, as will be discussed (Figures 4.25 to 4.27). The absence of tides (Figure 4.25) for the surface-advected plume shows small discrepancies among the mixing schemes. The differences among schemes for downshelf, across-shelf, and depth are smaller than the ranges, indicating that the different schemes produce relatively similar plumes, consistent with Section 4.1.1. The salt fluxes vary somewhat more by scheme. Examination of the normalized metrics for a tidal amplitude of 0.1 m (Figure 4.26) reveals that variations among schemes were again much smaller than the ranges, showing that the plumes are relatively similar. All the metric values are also close to a value of 1, indicating that the results are comparable to having no tides. While the $X_{DN\text{-}NOR}$ and $X_{UP\text{-}NOR}$ are extremely close to a value to of 1, there is a slight decrease in $X_{DN\text{-}NOR}$ and slight increase in $X_{UP\text{-}NOR}$. In addition, both salt fluxes somewhat show a decrease with a 0.1 m tidal amplitude (Figure 4.26, bottom panels). Note that the large salt flux ranges at the beginning of the run are not unusual since integrated salt flux can change depending as the plume evolves with time.

The plumes subjected to a 0.2 m tidal amplitude demonstrate larger discrepancies among the ranges for the mixing schemes (Figure 4.27). While all the metrics for the schemes are alike, the $X_{DN\text{-}NOR}$ and $Y_{AC\text{-}NOR}$ extents of the plumes show a greater spread in results, where the largest (P&P (B)) and smallest (constant) metric ranges extend much farther than the other schemes. In general, compared to no tides and 0.1 m tides, a decrease in $X_{DN\text{-}NOR}$, $Y_{AC\text{-}NOR}$, and depth extents and an increase in $X_{UP\text{-}NOR}$ distance resulted. The salt fluxes produce values that oscillates around a value slightly smaller than 1.

The results for all the tidal amplitudes for the surface-advected plumes demonstrate that the differences among the schemes are relatively minor, and the choice of scheme for the surface-advected plume with 0.1 or 0.2 m tides is not of great consequence for this study (shown by Figures 4.26 and 4.27).

4.2.2 Effect of schemes on metrics for bottom-advected plumes

Discrepancies among schemes are more apparent for the bottom-advected plumes. The absence of tides (Figure 4.28) shows that the range of the salt flux values is comparable to the difference among the schemes. However, a difference for the downshelf and upshelf penetrations, and across-shelf extent exists. For these three metrics, the relative percentage difference, averaged across the last 10 days between the largest scheme metric and smallest scheme, are respectively, 6%, 7%, and 15%. The choice of scheme is even more important for the 0.1 m normalized tidal amplitude results (Figure 4.29), where P&P and the constant schemes differ in the $Y_{AC\text{-}NOR}$ expansion (19% difference), $X_{DN\text{-}NOR}$ (12% difference) and $X_{UP\text{-}NOR}$ directions (7% difference). Overall, the constant scheme (P&P schemes) results in the most (least) $X_{UP\text{-}NOR}$ propagation and the least (most) $Y_{AC\text{-}NOR}$ expansion. The salt fluxes shows differences in scheme midway through the simulations. Like with buoyancy forcing only, the MY2.5 scheme results in a plume between the plumes created from the other two schemes.

The bottom-advected plumes subjected to 0.2 m tidal amplitudes (Figure 4.30) show a larger difference among the schemes. The variations among schemes are much larger than the ranges, showing the importance of scheme choice. The difference in $X_{DN\text{-}NOR}$ is 14% between the largest (constant) and smallest (MY2.5) schemes. The $X_{UP\text{-}NOR}$ propagation results are roughly the same for P&P and MY2.5, but the constant scheme creates larger $X_{UP\text{-}NOR}$ movement (20% larger). The largest differences among schemes are present in the $Y_{AC\text{-}NOR}$, a 34% difference, and $SF_{V\text{-}NOR}$ metrics, where the largest (least) $Y_{AC\text{-}NOR}$ and $SF_{V\text{-}NOR}$ growth is created by MY2.5 (the constant scheme). The $SF_{V\text{-}NOR}$ for the schemes varies up until around Day 35 where the differences in the $SF_{V\text{-}NOR}$ values decrease while the differences in $SF_{H\text{-}NOR}$ increase.

The largest discrepancies among the schemes for all metrics are shown when using 0.5 m tidal amplitudes (Figure 4.31), where the metrics are significantly different from the plumes without tidal forcing. For a tidal amplitude of 0.5 m, the constant scheme results with the least $X_{DN\text{-}NOR}$ (47% lower) and $Y_{AC\text{-}NOR}$ distances (49% lower) and $SF_{V\text{-}NOR}$, but the scheme has the greatest $X_{UP\text{-}NOR}$ propagation (62% larger) and $SF_{H\text{-}NOR}$. Therefore, when compared to the other amplitudes, applying larger tidal amplitude results in larger differences among the mixing schemes.

Differences among the schemes increase with increasing tidal amplitude. Generally, with increasing tidal forcing, $X_{DN\text{-}NOR}$ distance decreases while the $Y_{AC\text{-}NOR}$ distance increases. The behavior of the $X_{UP\text{-}NOR}$ depends on the mixing scheme, where the constant scheme increases $X_{UP\text{-}NOR}$ penetration with increasing amplitude. The salt fluxes show larger changes in the values with tides. The results for all tidal amplitudes for the bottom-advected plumes are summarized in Table 4.1, where all the metrics are presented for each of the tidal amplitudes. The scheme with the largest metric is shown in the first row of every metric, followed by decreasing metrics produced from the other schemes. The shaded boxes highlight the results that are the same as the results in buoyancy only forcing. The table contains empty spaces for the metric results that were unclear.

4.2.3 Overall results

The surface-advected plumes lacked differentiation across mixing schemes for the metrics with various tidal amplitudes (Figures 4.26 and 4.27). However, for bottom-advected plumes, importance of scheme choice increased with increasing tidal amplitude, seen in the increase in spread of the metrics and shift away from a normalized value of 1 (Figures 4.29 to 4.31). Differences across schemes increased in $X_{DN\text{-}NOR}$ distance with increasing tidal amplitude for the bottom-advected plumes. For an amplitude of 0.1 m (0.2 m), the constant scheme was 12% (14%) larger than P&P (B) (MY2.5). The $X_{DN\text{-}NOR}$ growth for the schemes diverged using a tidal amplitude of 0.5 m (top left panel, Figure 4.31); P&P (B) was 47% larger than the constant.

Larger tidal amplitudes increased $X_{UP\text{-}NOR}$ movement for the constant scheme, from a 7% difference with a 0.1 m tidal amplitudes to a 62% difference for the schemes with a 0.5 m tidal amplitude. Similar to buoyancy only forcing, the constant scheme resulted in the highest $X_{UP\text{-}NOR}$ propagation compared to the other mixing schemes.

The constant scheme had the least $Y_{AC\text{-}NOR}$ development while the scheme with the largest growth depended on the tidal amplitude. P&P schemes had the most expansion for the 0.1 m tidal amplitude (19% larger than constant scheme), and MY2.5 (34% and 49% larger than constant scheme) resulted with the largest for the higher amplitudes (middle panel, Figures 4.29

to 4.31). Again, the choice of scheme proved to have a major influence on the shape of the plume. Changes in the largest across-shelf expansion was most likely related to changes in the downshelf expansion for MY2.5 and both P&P; with 0.1 m tides, MY2.5 had higher downshelf and lower across-shelf extents than both P&P, but at higher amplitudes, the MY2.5 had lower downshelf and higher across-shelf extents than both P&P. The expansion of the plume was interrelated, as demonstrated by the connection between freshwater transport in the bulge and coastal current (Fong and Geyer 2002), where more freshwater in the bulge resulted in less freshwater transported in the current (and visa versa).

The relationship between the salt fluxes was not as clear as with buoyancy forcing using a K_{z_b} and K_{s_b} of 5 x 10^{-6} m^2 s^{-1} (bottom panels, Figures 4.29 to 4.31). However, the constant scheme, like with buoyancy only forcing, had the tendency to create less $SF_{V\text{-}NOR}$ and more $SF_{H\text{-}NOR}$ for the various tidal amplitudes during the simulations. More mixing created by tides produced different plumes for the constant scheme (Figure 4.14 and 4.22), yet the $SF_{H\text{-}NOR}$ for 0, 0.1, and 0.2 m tidal amplitudes were similar, also shown in MY2.5 (Figure 4.13 and 4.21). This could be an indication that for these schemes, the $SF_{H\text{-}NOR}$ played much less of a role in the resulting plume except when subjected to larger tidal amplitudes.

BOTTOM-ADVECTED		***0.1 m tides***	***0.2 m tides***	***0.5 m tides***
Normalized Downshelf	***most***	_______	Pacanowski and Philander (B)	Pacanowski and Philander (B)
		_______	_______	Pacanowski and Philander (A)
		_______	_______	Mellor-Yamada Level 2.5
	least	_______	Mellor-Yamada Level 2.5	Constant
Normalized Upshelf		Constant	Constant	Constant
		Mellor-Yamada Level 2.5	Pacanowski and Philander (B)	Mellor-Yamada Level 2.5
		Pacanowski and Philander (B)	Mellor-Yamada Level 2.5	Pacanowski and Philander (B)
		Pacanowski and Philander (A)	Pacanowski and Philander (A)	Pacanowski and Philander (A)
Normalized Across-shelf (bulge)		Pacanowski and Philander (A)	Mellor-Yamada Level 2.5	Mellor-Yamada Level 2.5
		Pacanowski and Philander (B)	Pacanowski and Philander (A)	Pacanowski and Philander (A)
		Mellor-Yamada Level 2.5	Pacanowski and Philander (B)	Pacanowski and Philander (B)
		Constant	Constant	Constant
Normalized Vertical Salt Flux		Pacanowski and Philander (B)	Mellor-Yamada Level 2.5	Pacanowski and Philander (A)
		Mellor-Yamada Level 2.5	Pacanowski and Philander (B)	Pacanowski and Philander (B)
		Pacanowski and Philander (A)	Pacanowski and Philander (A)	Mellor-Yamada Level 2.5
		Constant	Constant	Constant
Normalized Horizontal Salt Flux		*Constant	_______	Constant
		*Mellor-Yamada Level 2.5	_______	Mellor-Yamada Level 2.5
		*Pacanowski and Philander (B)	_______	Pacanowski and Philander (B)
		*Pacanowski and Philander (A)	_______	Pacanowski and Philander (A)

Table 4.1: The results for the bottom-advected plumes with 0.1 m, 0.2 m, and 0.5 m tidal amplitudes are summarized in the table above. Note that some boxes remain empty due to ambiguous results. The shaded boxes show the scheme ordering results that match the results when only buoyancy forcing is present. The starred schemes could be interpreted differently.

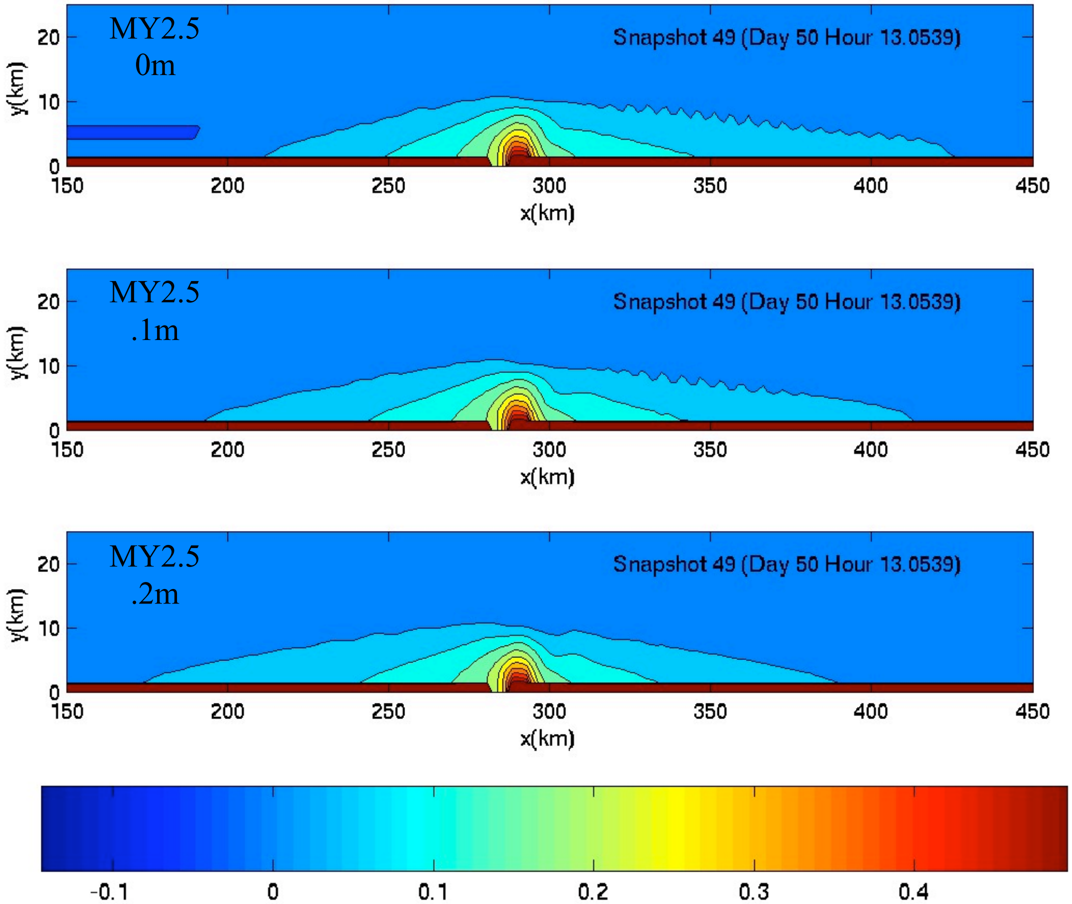

Figure 4.1: The surface-advected plume subjected to 0 m (no tides), 0.1 m, and 0.2 m tidal amplitudes using MY2.5 on Day 50 are shown above. Salinity anomaly contours range from –0.15 to 0.50, with intervals of 0.05. Note that x- and y-directions are scaled differently.

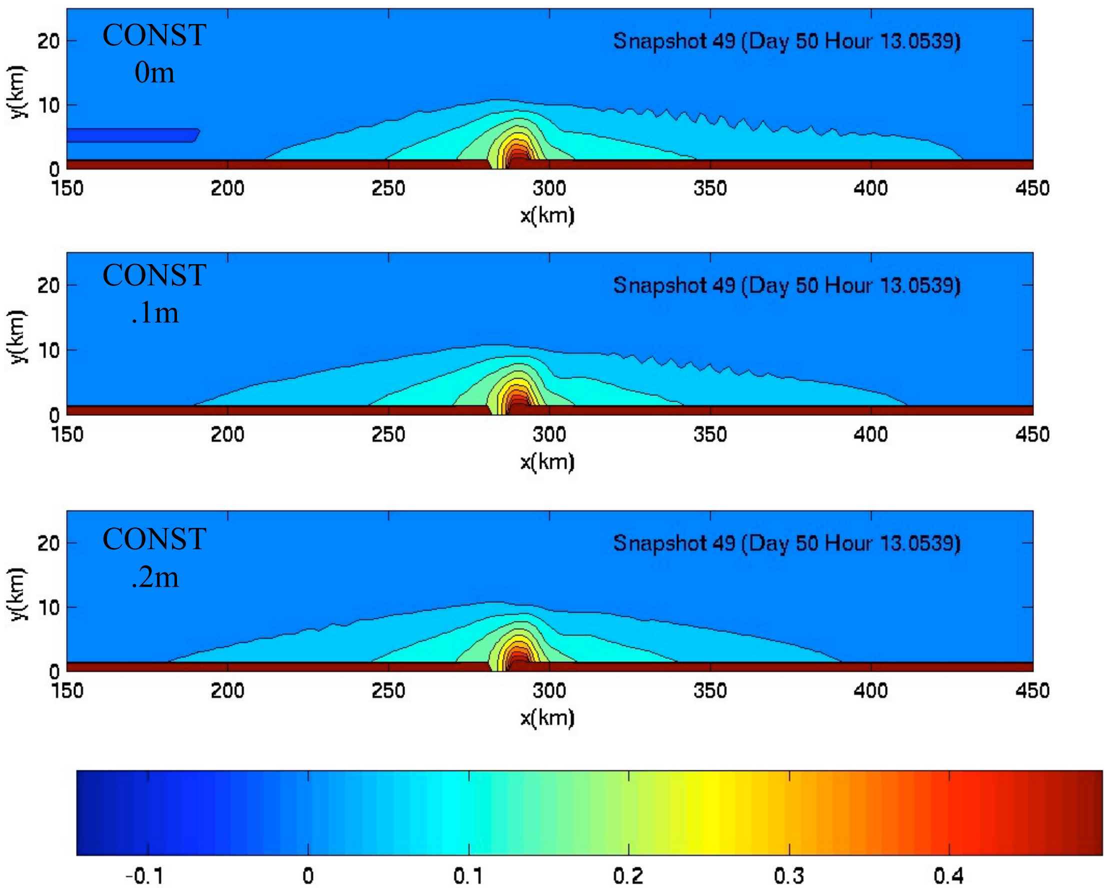

Figure 4.2: The surface-advected plume subjected to 0 m (no tides), 0.1 m, and 0.2 m tidal amplitudes using the constant scheme on Day 50 are shown above. Salinity anomaly contours range from –0.15 to 0.50, with intervals of 0.05. Note that x- and y-directions are scaled differently.

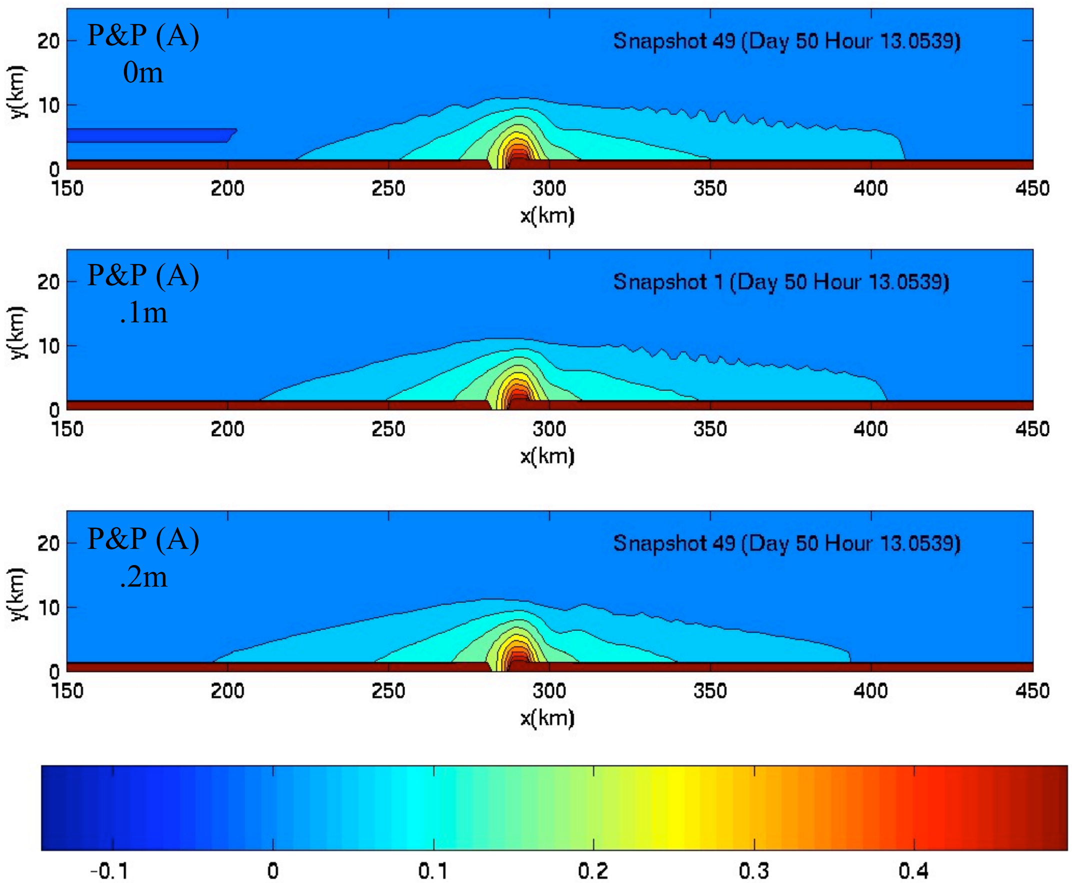

Figure 4.3: The surface-advected plume subjected to 0 m (no tides), 0.1 m, and 0.2 m tidal amplitudes using P&P (A) on Day 50 are shown above. Salinity anomaly contours range from –0.15 to 0.50, with intervals of 0.05. Note that x- and y-directions are scaled differently.

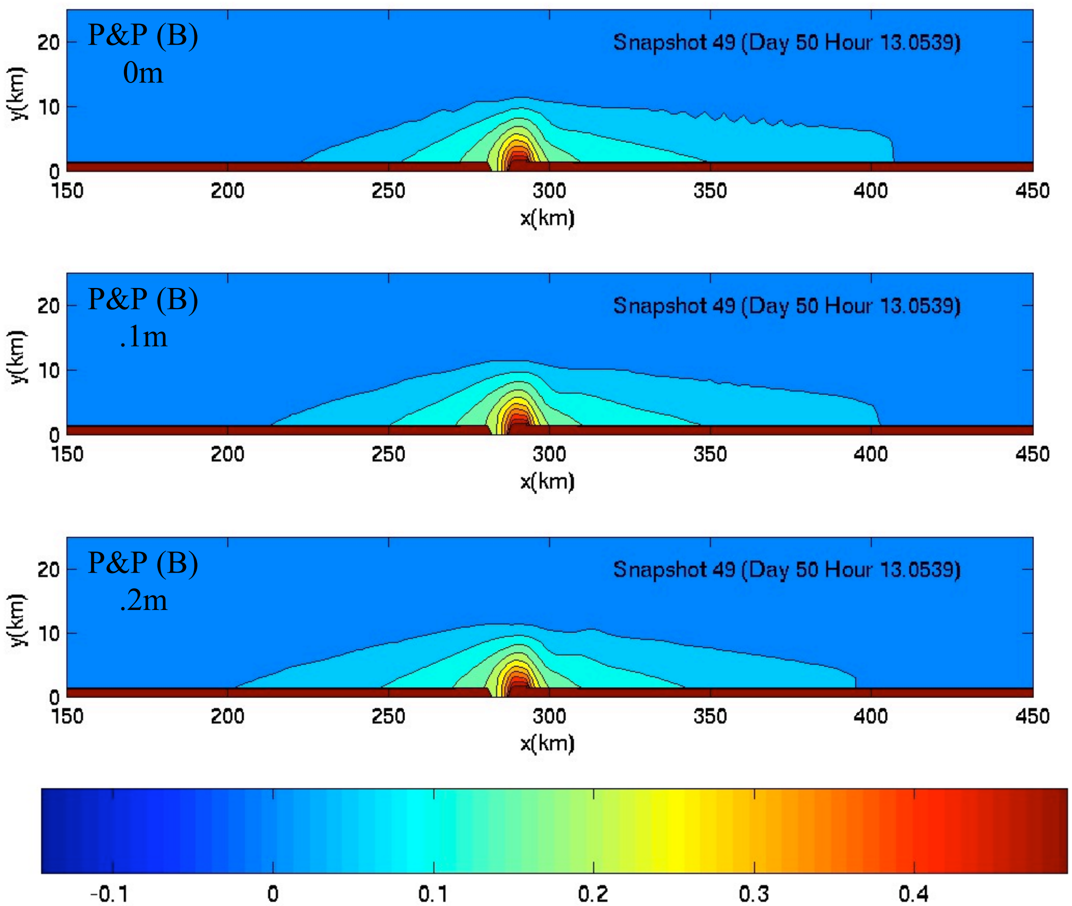

Figure 4.4: The surface-advected plume subjected to 0 m (no tides), 0.1 m, and 0.2 m tidal amplitudes using P&P (B) on Day 50 are shown above. Salinity anomaly contours range from –0.15 to 0.50, with intervals of 0.05. Note that x- and y-directions are scaled differently.

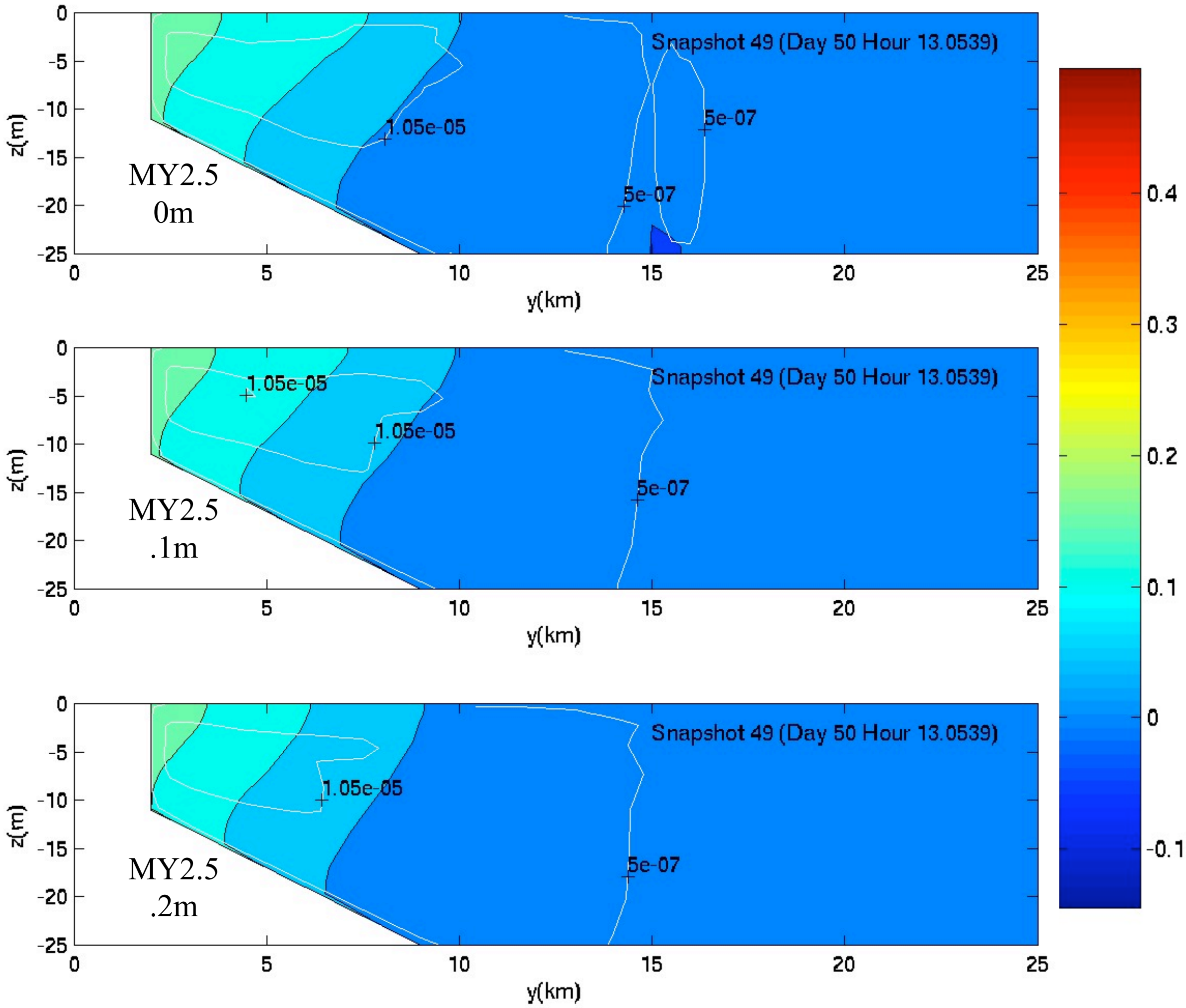

Figure 4.5: Cross-sections of the surface-advected plume subjected to 0 m (no tides), 0.1 m, and 0.2 m tidal amplitudes using MY2.5 on Day 50 at 300 km are shown above. Salinity anomaly contours (colored contours) range from –0.15 to 0.50, with intervals of 0.05, and the point-to-point vertical salt flux (white contours, black labels) range from 5 x 10^{-7} to 10^{-4} m^2 s^{-1}, with intervals of 1 x 10^{-5} m^2 s^{-1}. Note that x- and y-directions are scaled differently.

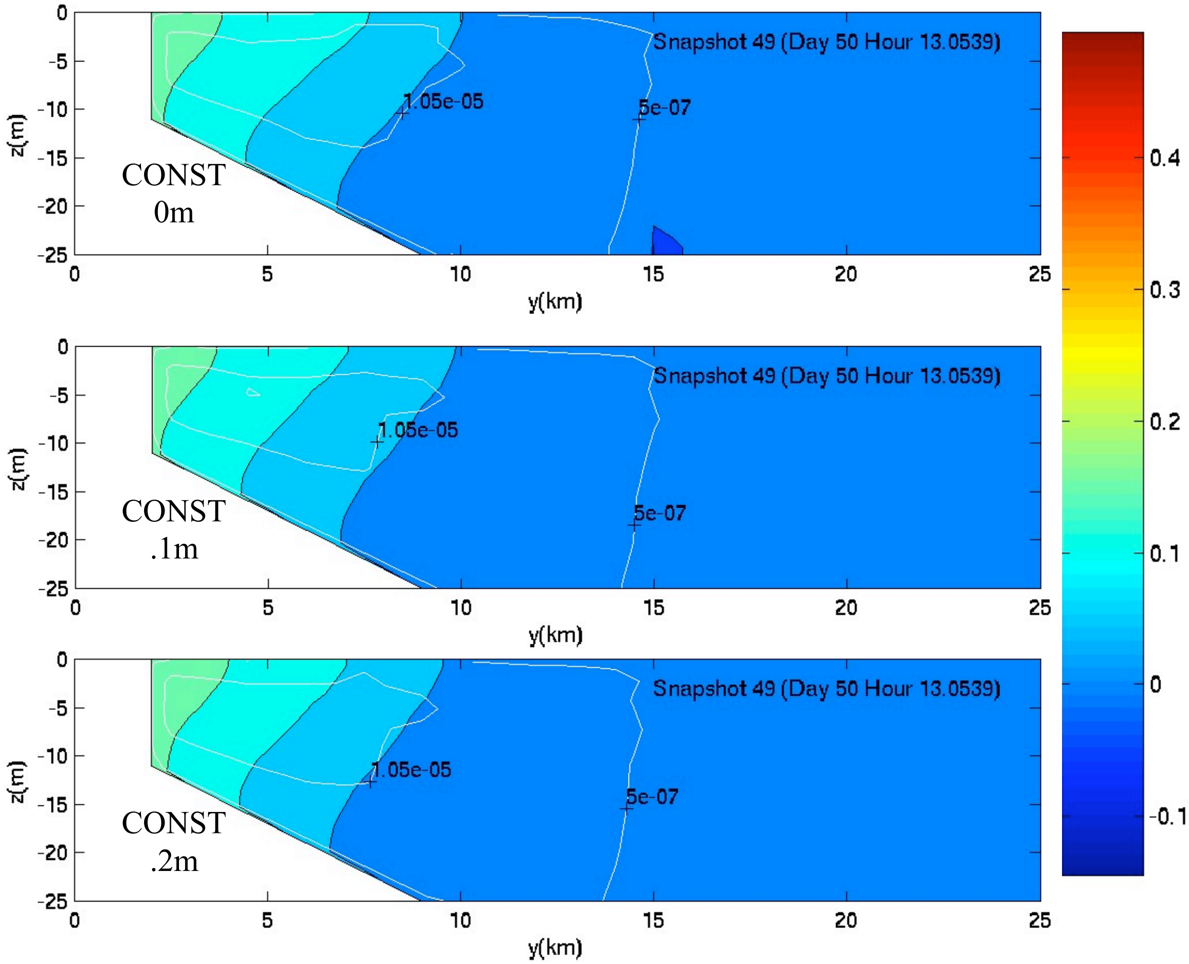

Figure 4.6: Cross-sections of the surface-advected plume subjected to 0 m (no tides), 0.1 m, and 0.2 m tidal amplitudes using the constant scheme on Day 50 at 300 km are shown above. Salinity anomaly contours (colored contours) range from –0.15 to 0.50, with intervals of 0.05, and the point-to-point vertical salt flux (white contours, black labels) range from 5 x 10^{-7} to 10^{-4} m^2 s^{-1}, with intervals of 1 x 10^{-5} m^2 s^{-1}. Note that x- and y-directions are scaled differently.

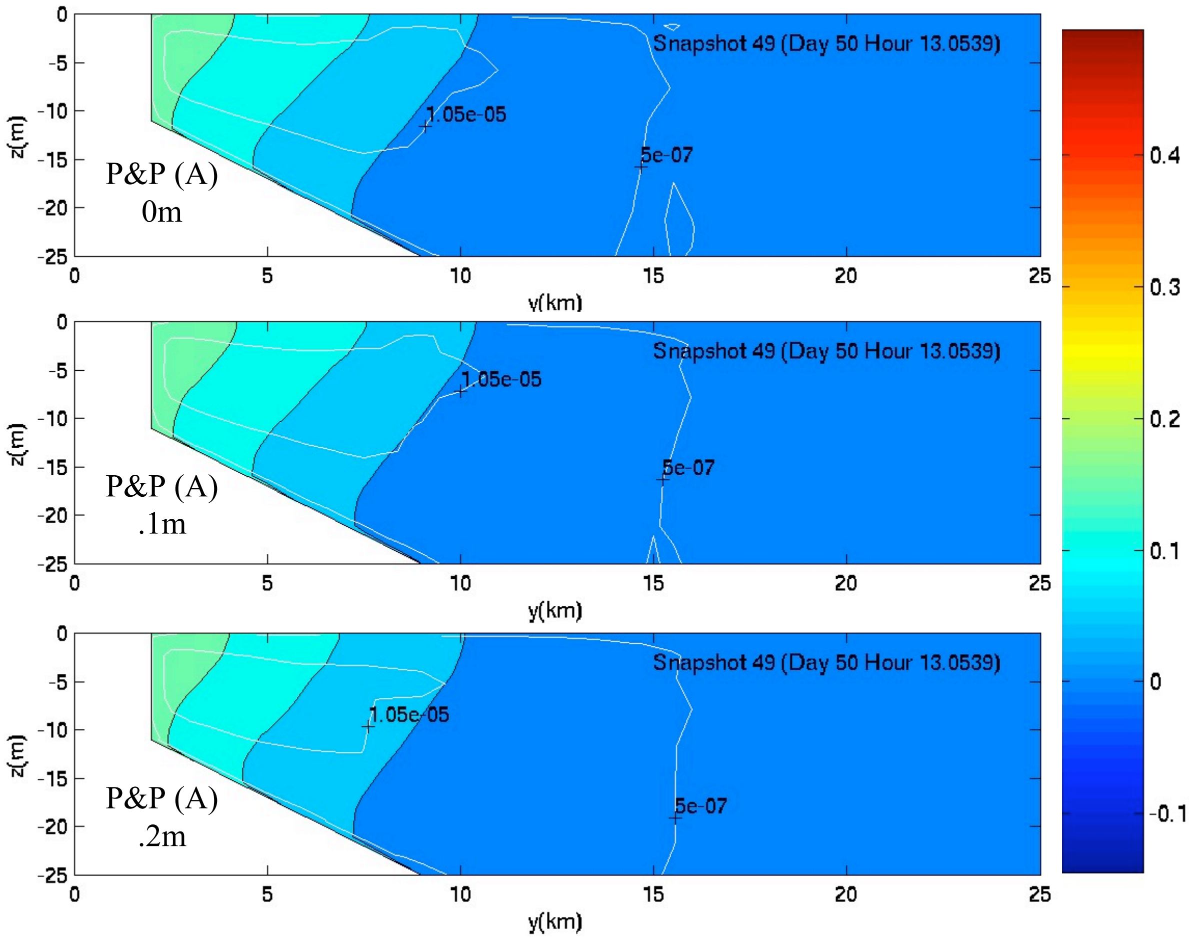

Figure 4.7: Cross-sections of the surface-advected plume subjected to 0 m (no tides), 0.1 m, and 0.2 m tidal amplitudes using P&P (A) on Day 50 at 300 km are shown above. Salinity anomaly contours (colored contours) range from –0.15 to 0.50, with intervals of 0.05, and the point-to-point vertical salt flux (white contours, black labels) range from 5 x 10^{-7} to 10^{-4} m^2 s^{-1}, with intervals of 1 x 10^{-5} m^2 s^{-1}. Note that x- and y-directions are scaled differently.

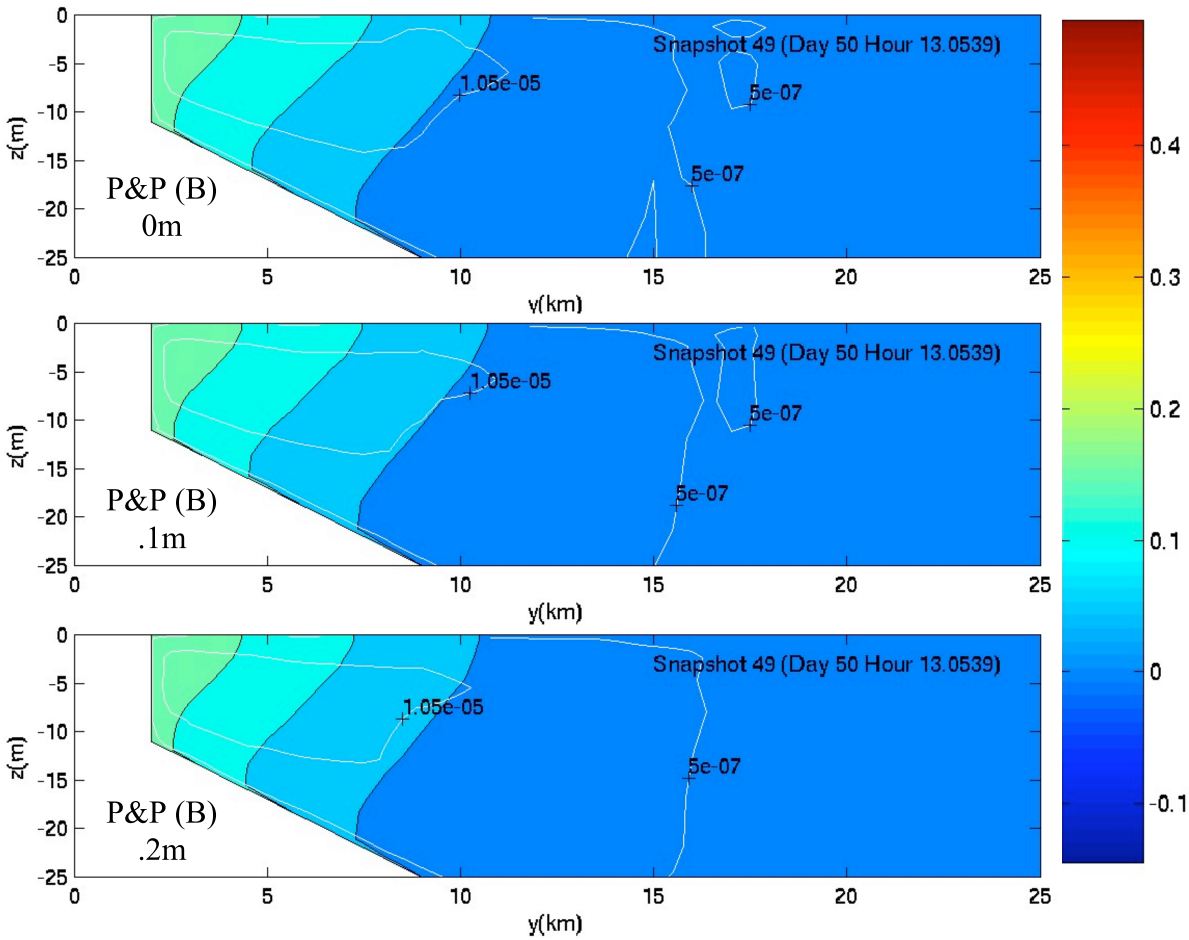

Figure 4.8: Cross-sections of the surface-advected plume subjected to 0 m (no tides), 0.1 m, and 0.2 m tidal amplitudes using P&P (B) on Day 50 at 300 km are shown above. Salinity anomaly contours (colored contours) range from –0.15 to 0.50, with intervals of 0.05, and the point-to-point vertical salt flux (white contours, black labels) range from 5 x 10^{-7} to 10^{-4} m^2 s^{-1}, with intervals of 1 x 10^{-5} m^2 s^{-1}. Note that x- and y-directions are scaled differently.

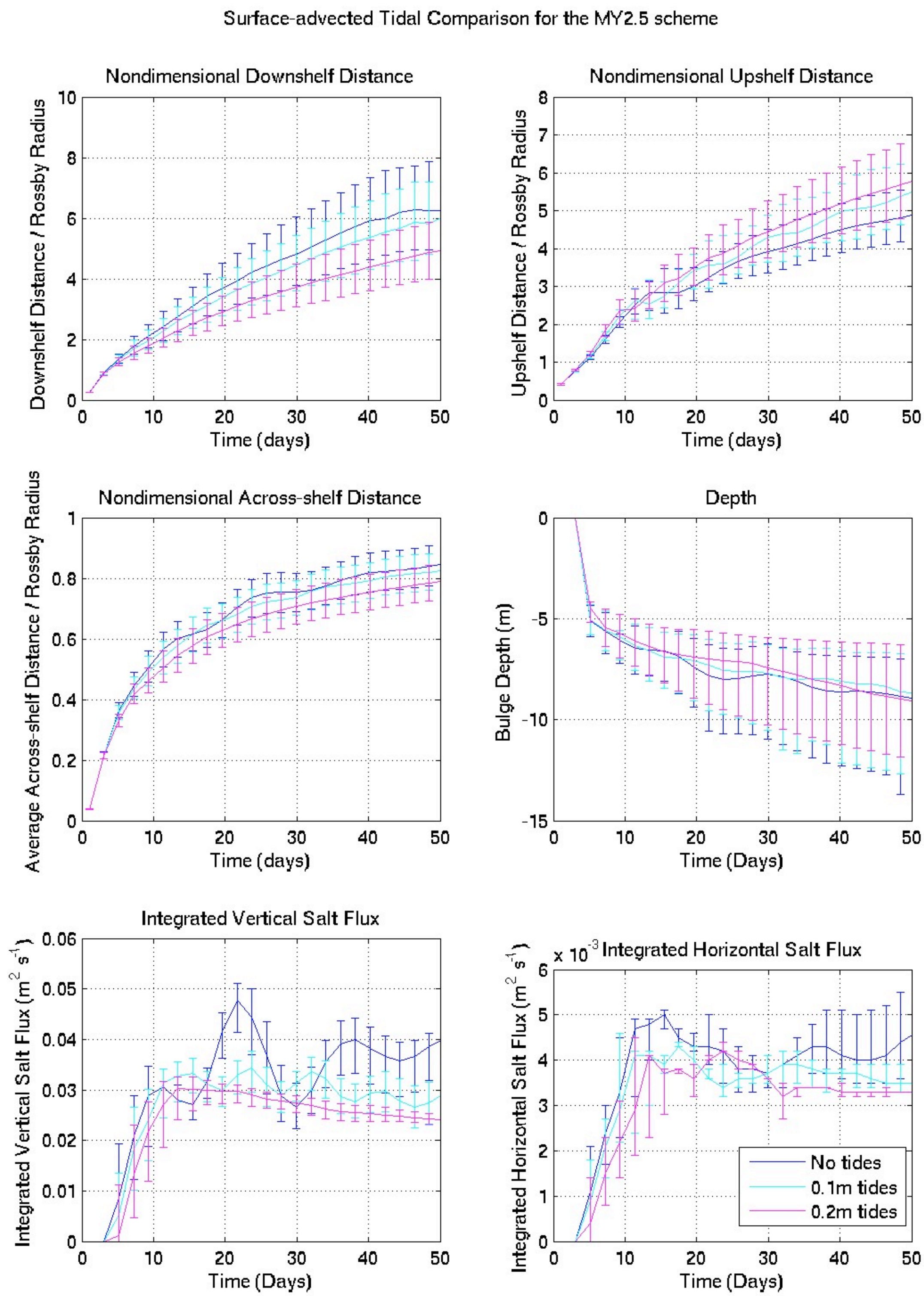

Figure 4.9: Comparison of metrics across various tidal amplitudes for the surface-advected plume using MY2.5.

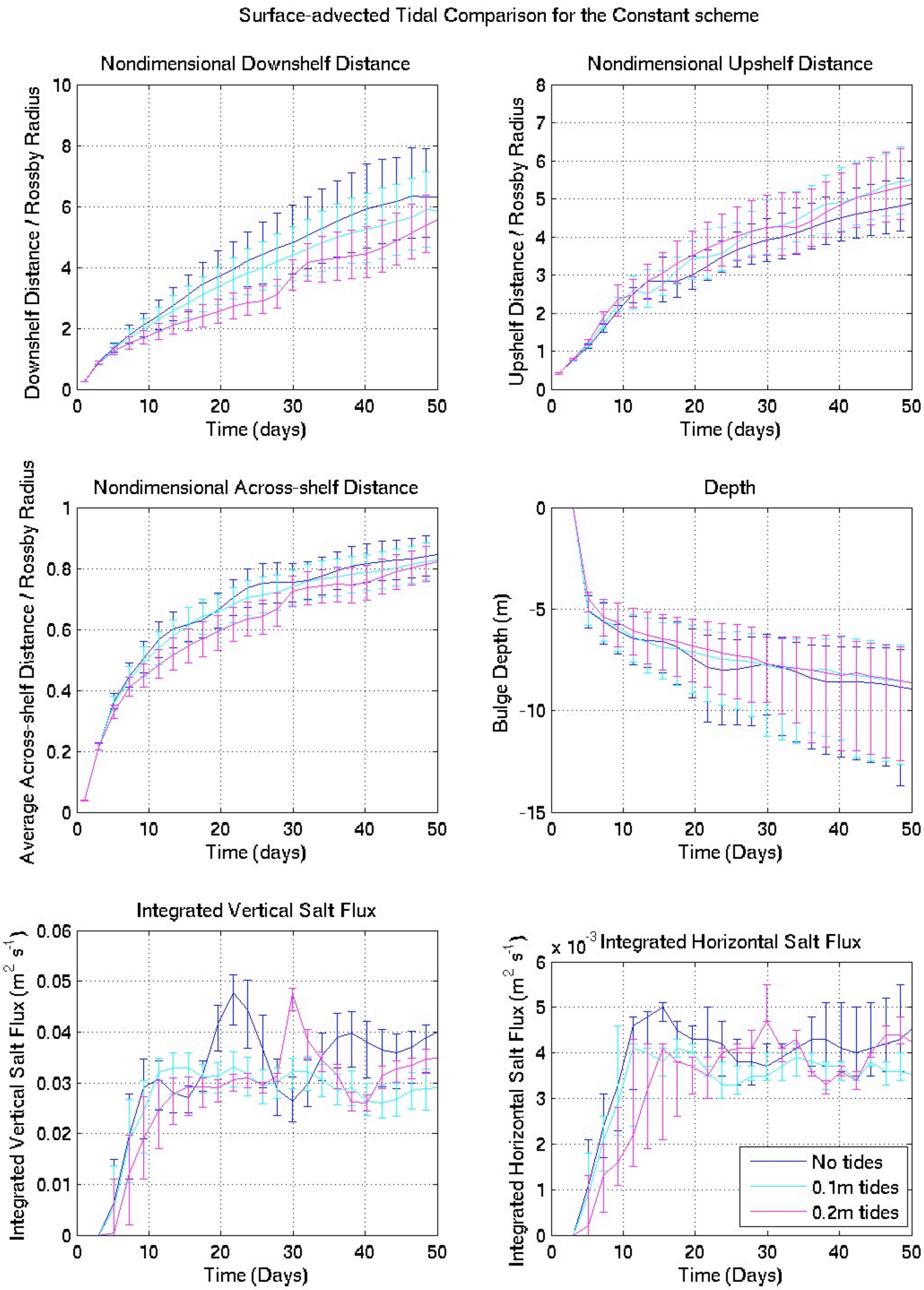

Figure 4.10: Comparison of metrics across various tidal amplitudes for the surface-advected plume using the constant scheme.

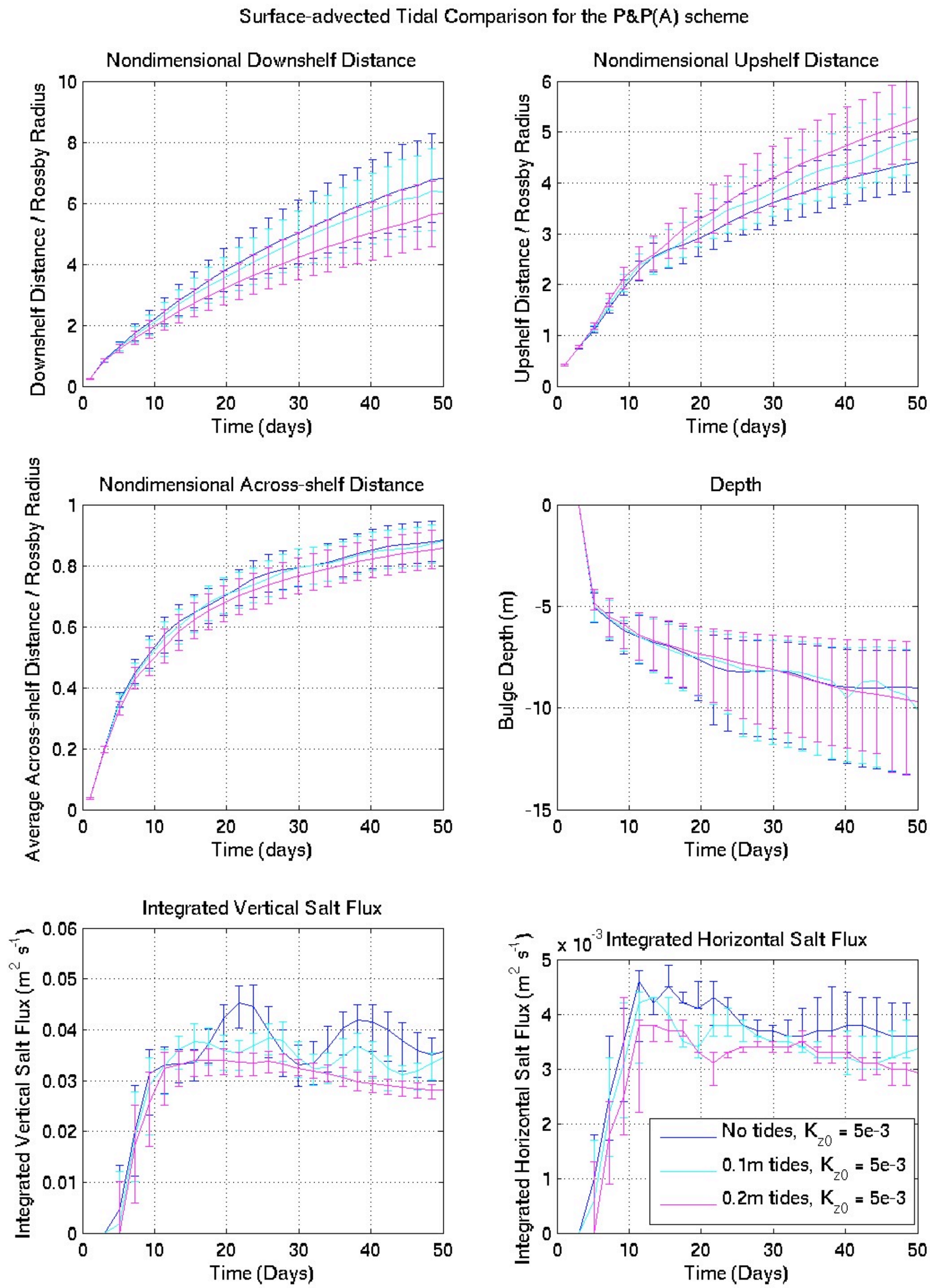

Figure 4.11: Comparison of metrics across various tidal amplitudes for the surface-advected plume using P&P (A).

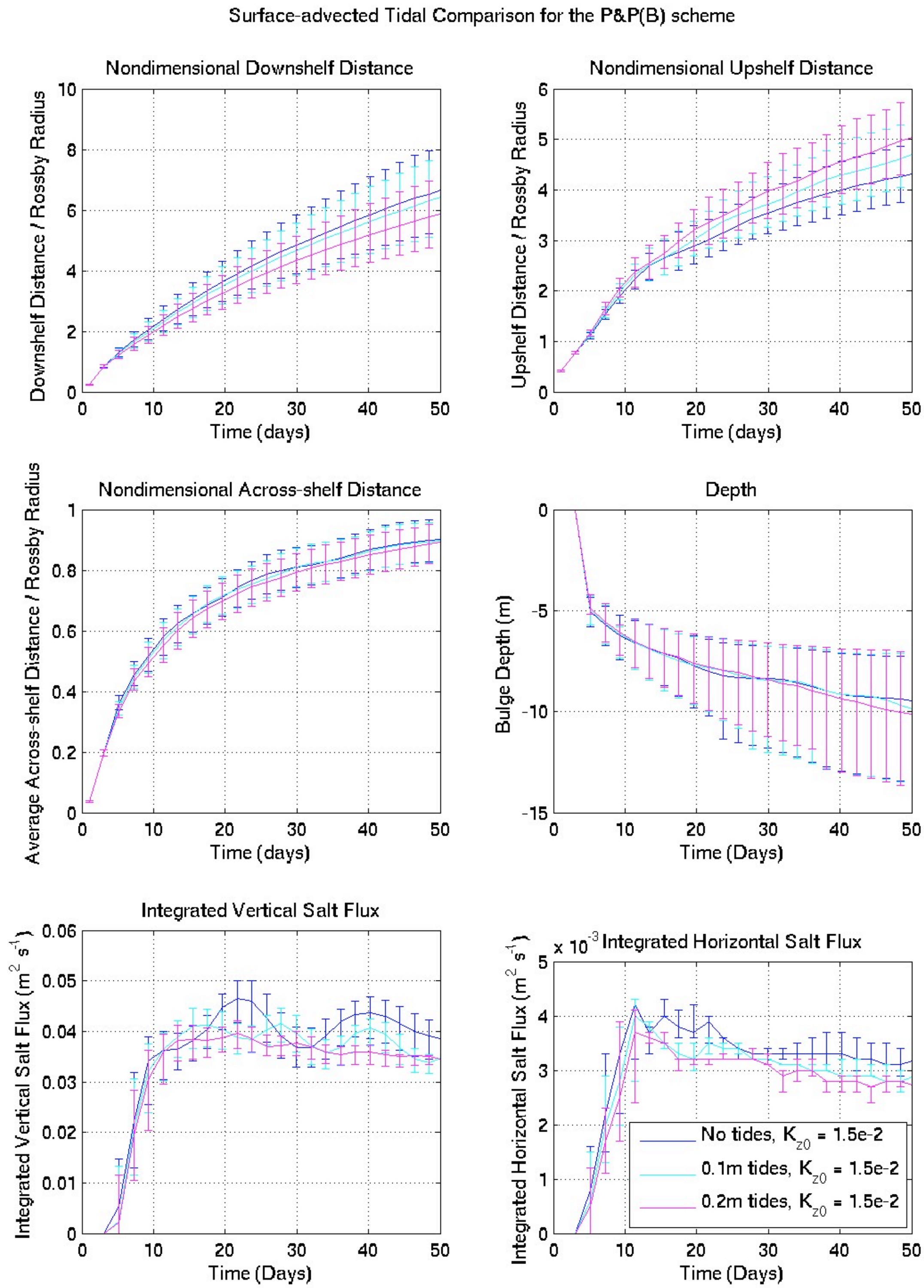

Figure 4.12: Comparison of metrics across various tidal amplitudes for the surface-advected plume using P&P (B).

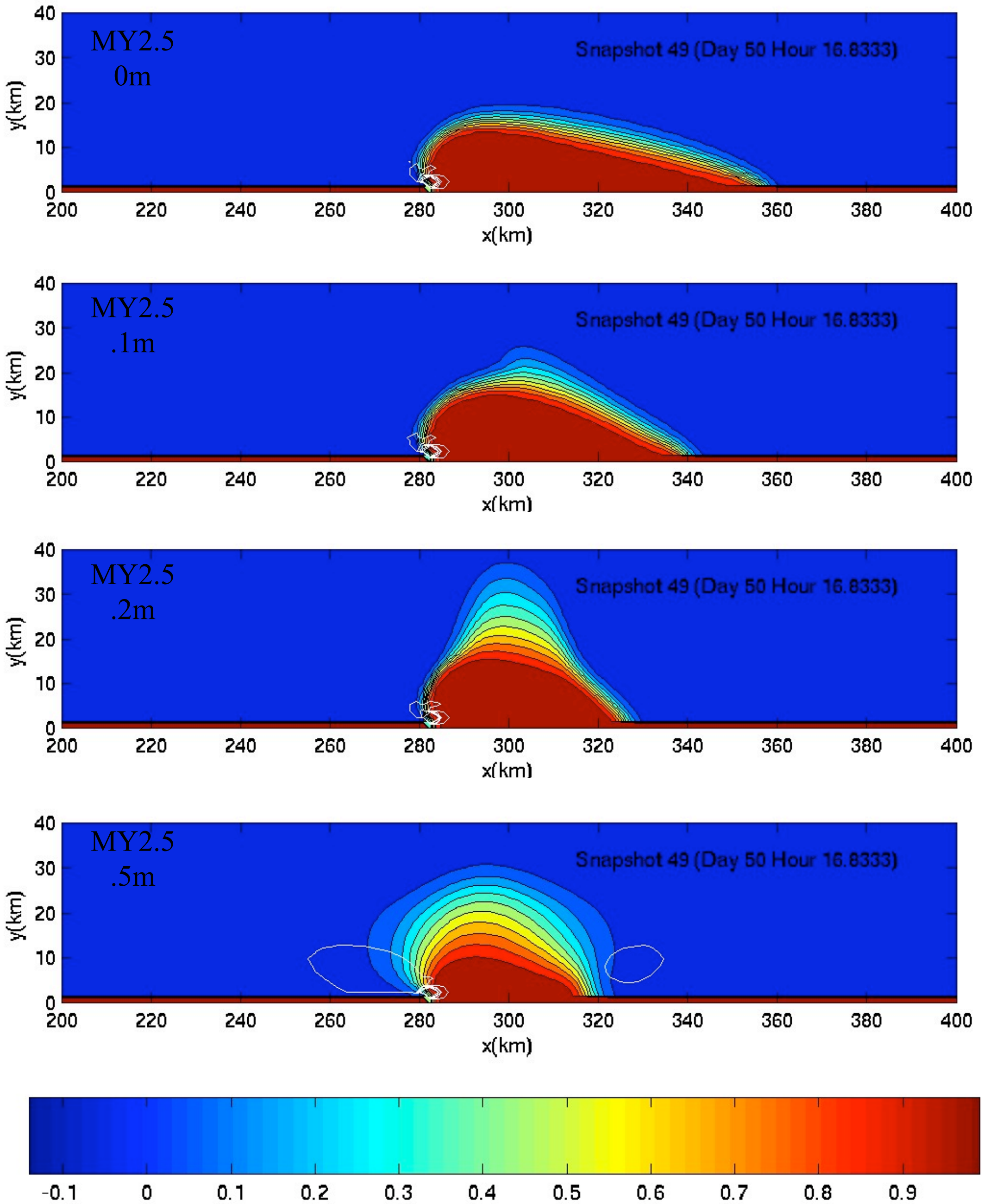

Figure 4.13: The bottom-advected plume subjected to 0 m (no tides), 0.1 m, 0.2 m, and 0.5 m tidal amplitudes using MY2.5 at Day 50 are shown above. Salinity anomaly contours range from –0.15 to 1.00, with intervals of 0.10. The point-to-point horizontal salt flux (white contours) range from 5 x 10^{-6} to 10^{-3} m^2 s^{-1}, with intervals of 1 x 10^{-3}. Note that x- and y-directions are scaled differently.

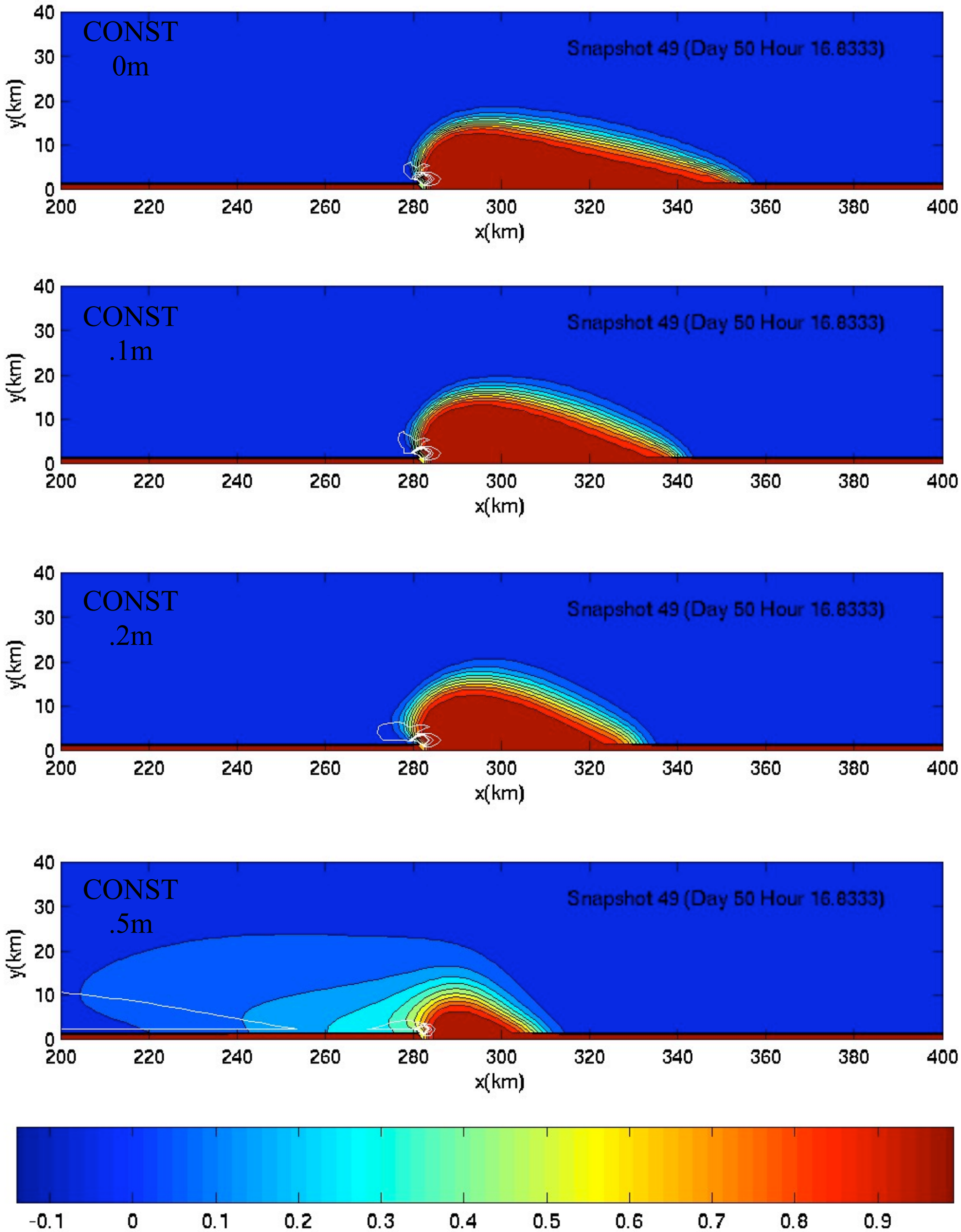

Figure 4.14: The bottom-advected plume subjected to 0 m (no tides), 0.1 m, 0.2 m, and 0.5 m tidal amplitudes using the constant scheme at Day 50 are shown above. Salinity anomaly contours range from –0.15 to 1.00, with intervals of 0.10. The point-to-point horizontal salt flux (white contours) range from 5 x 10^{-6} to 10^{-3} m^2 s^{-1}, with intervals of 1 x 10^{-3}. Note that x- and y-directions are scaled differently.

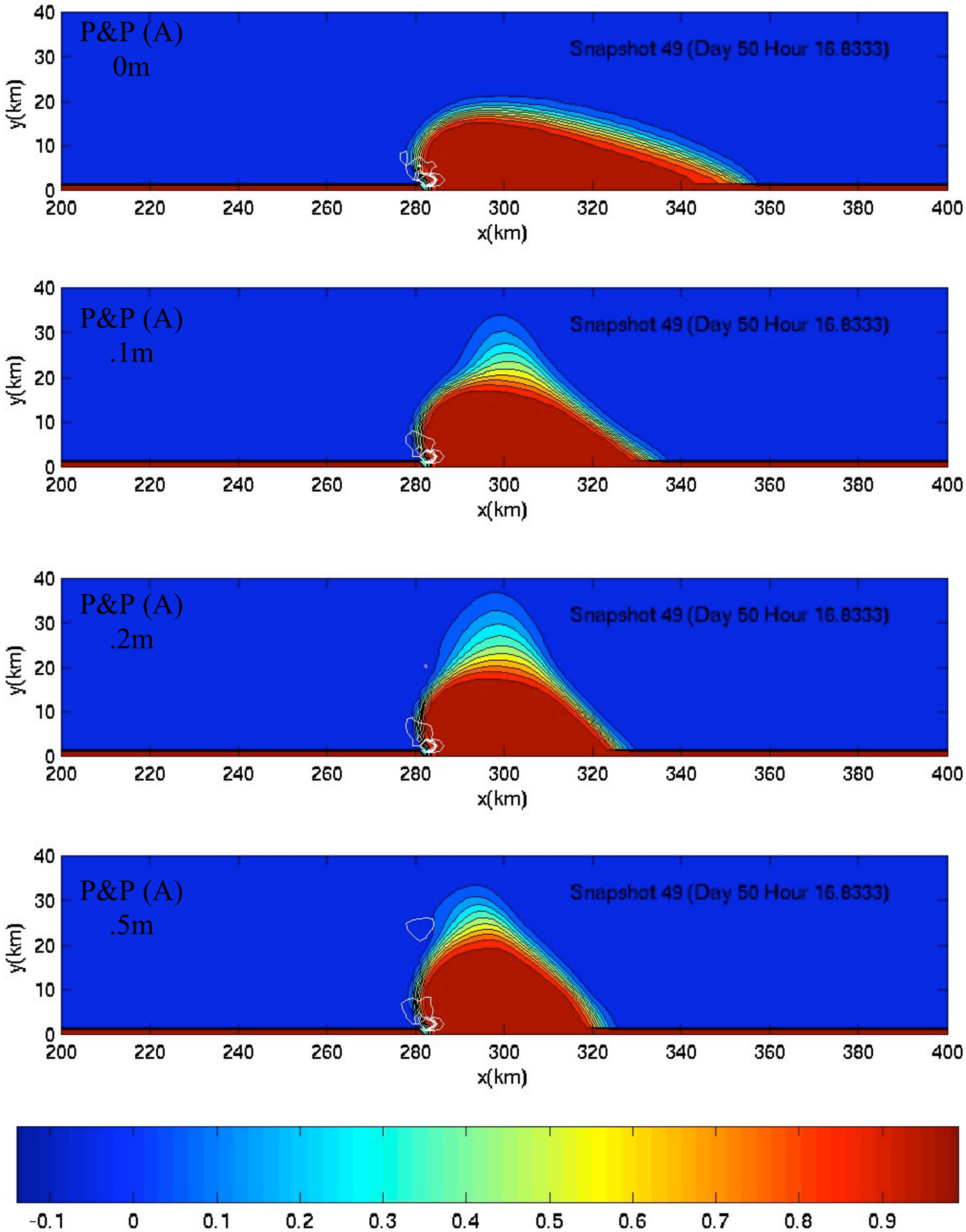

Figure 4.15: The bottom-advected plume subjected to 0 m (no tides), 0.1 m, 0.2 m, and 0.5 m tidal amplitudes using P&P (A) at Day 50 are shown above. Salinity anomaly contours range from –0.15 to 1.00, with intervals of 0.10. The point-to-point horizontal salt flux (white contours) range from 5 x 10^{-6} to 10^{-3} m^2 s^{-1}, with intervals of 1 x 10^{-3}. Note that x- and y-directions are scaled differently.

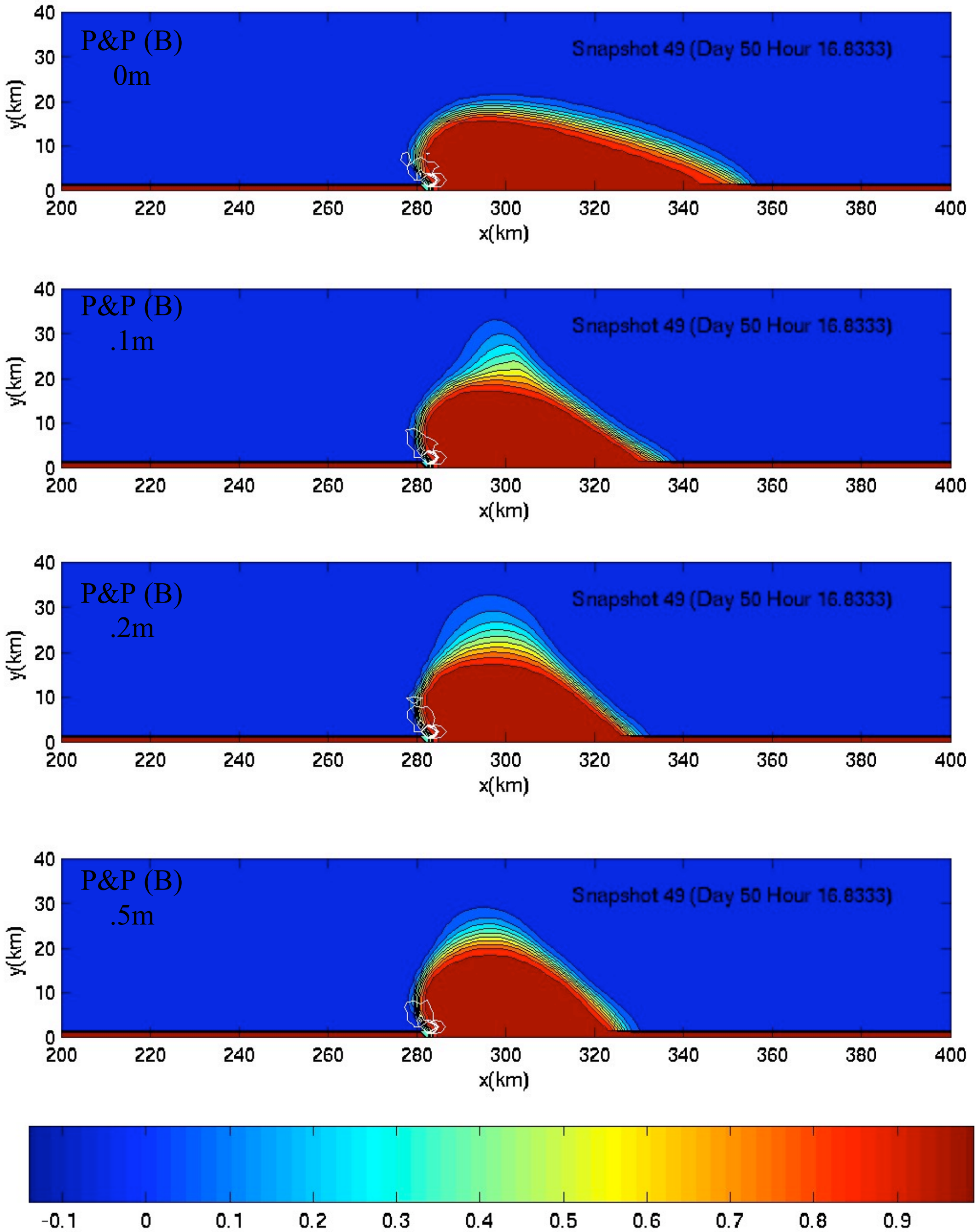

Figure 4.16: The bottom-advected plume subjected to 0 m (no tides), 0.1 m, 0.2 m, and 0.5 m tidal amplitudes using P&P (B) at Day 50 are shown above. Salinity anomaly contours range from –0.15 to 1.00, with intervals of 0.10. The point-to-point horizontal salt flux (white contours) range from 5 x 10^{-6} to 10^{-3} m^2 s^{-1}, with intervals of 1 x 10^{-3}. Note that x- and y-directions are scaled differently.

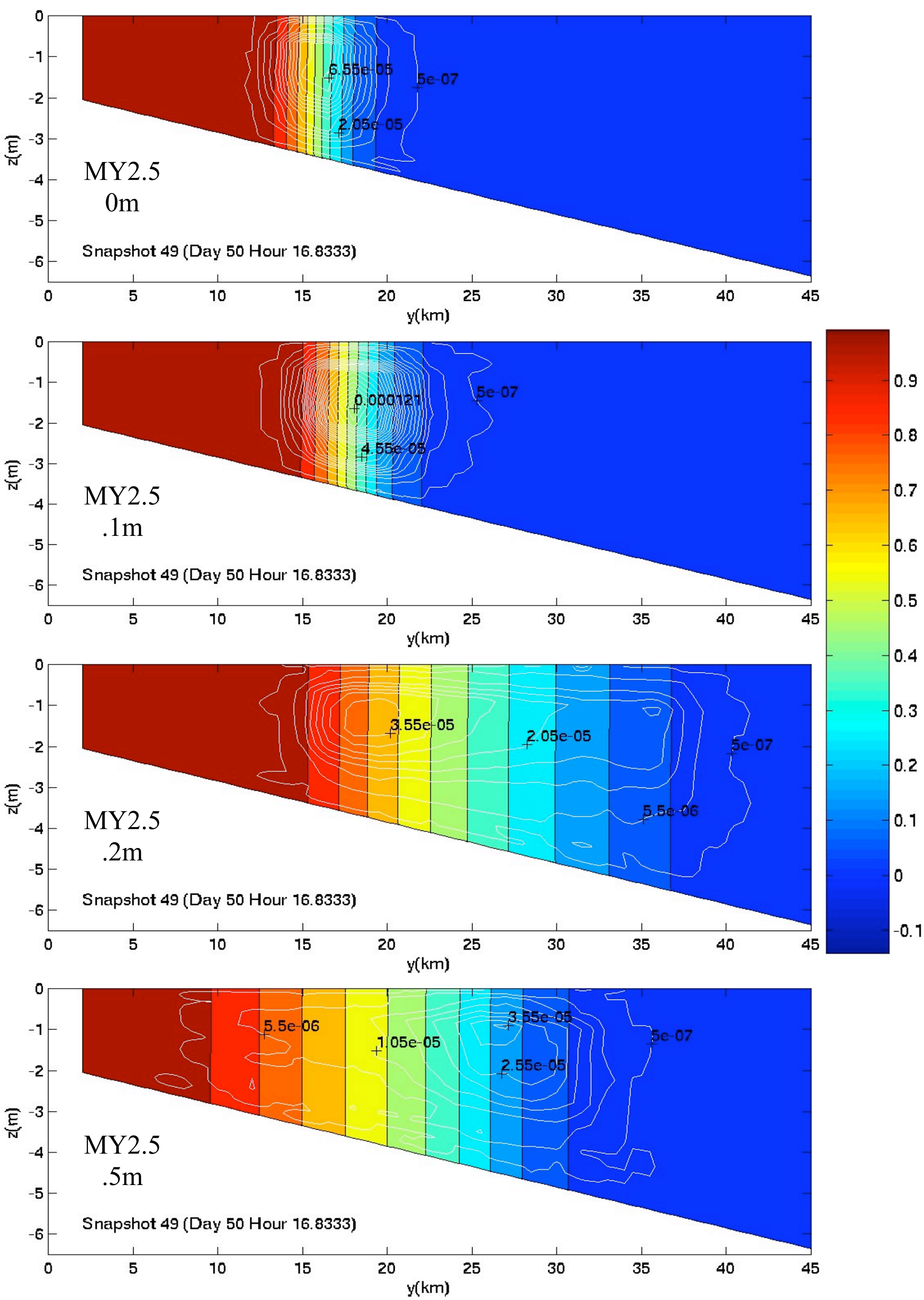

Figure 4.17: Cross-sections of the bottom-advected plume subjected to 0 m (no tides), 0.1 m, 0.2 m, and 0.5 m tidal amplitudes using MY2.5 on Day 50 at 297 km are shown above. Salinity anomaly contours range from –0.15 to 1.00, with intervals of 0.10, and the point-to-point vertical salt flux (white contours, black labels) range from 5 x 10^{-7} to 10^{-4} m^2 s^{-1}, with intervals of 5 x 10^{-6} m^2 s^{-1}. Note that x- and y-directions are scaled differently.

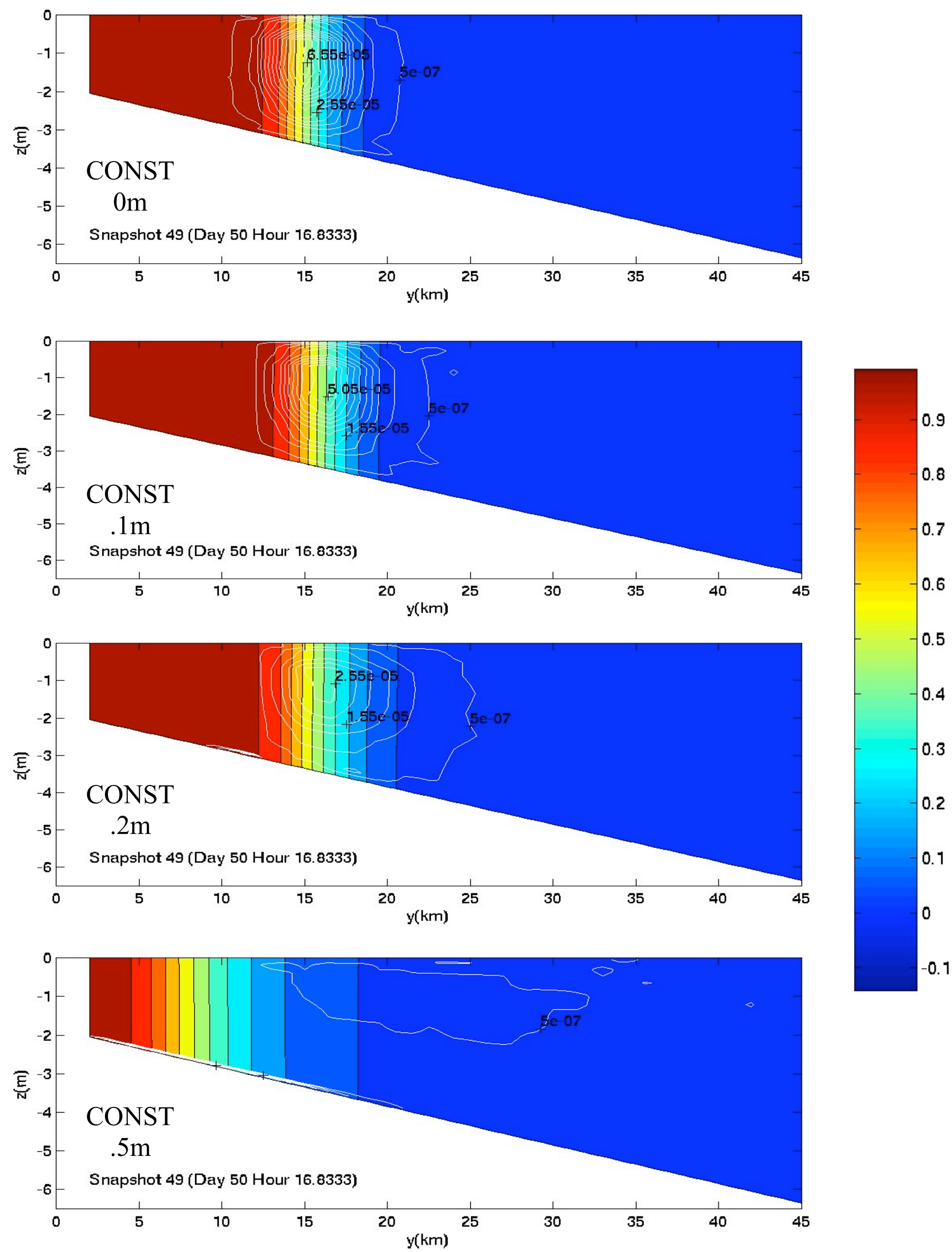

Figure 4.18: Cross-sections of the bottom-advected plume subjected to 0 m (no tides), 0.1 m, 0.2 m, and 0.5 m tidal amplitudes using the constant scheme on Day 50 at 297 km are shown above. Salinity anomaly contours range from –0.15 to 1.00, with intervals of 0.10, and the point-to-point vertical salt flux (white contours, black labels) range from 5 x 10^{-7} to 10^{-4} m^2 s^{-1}, with intervals of 5 x 10^{-6} m^2 s^{-1}. Note that x- and y-directions are scaled differently.

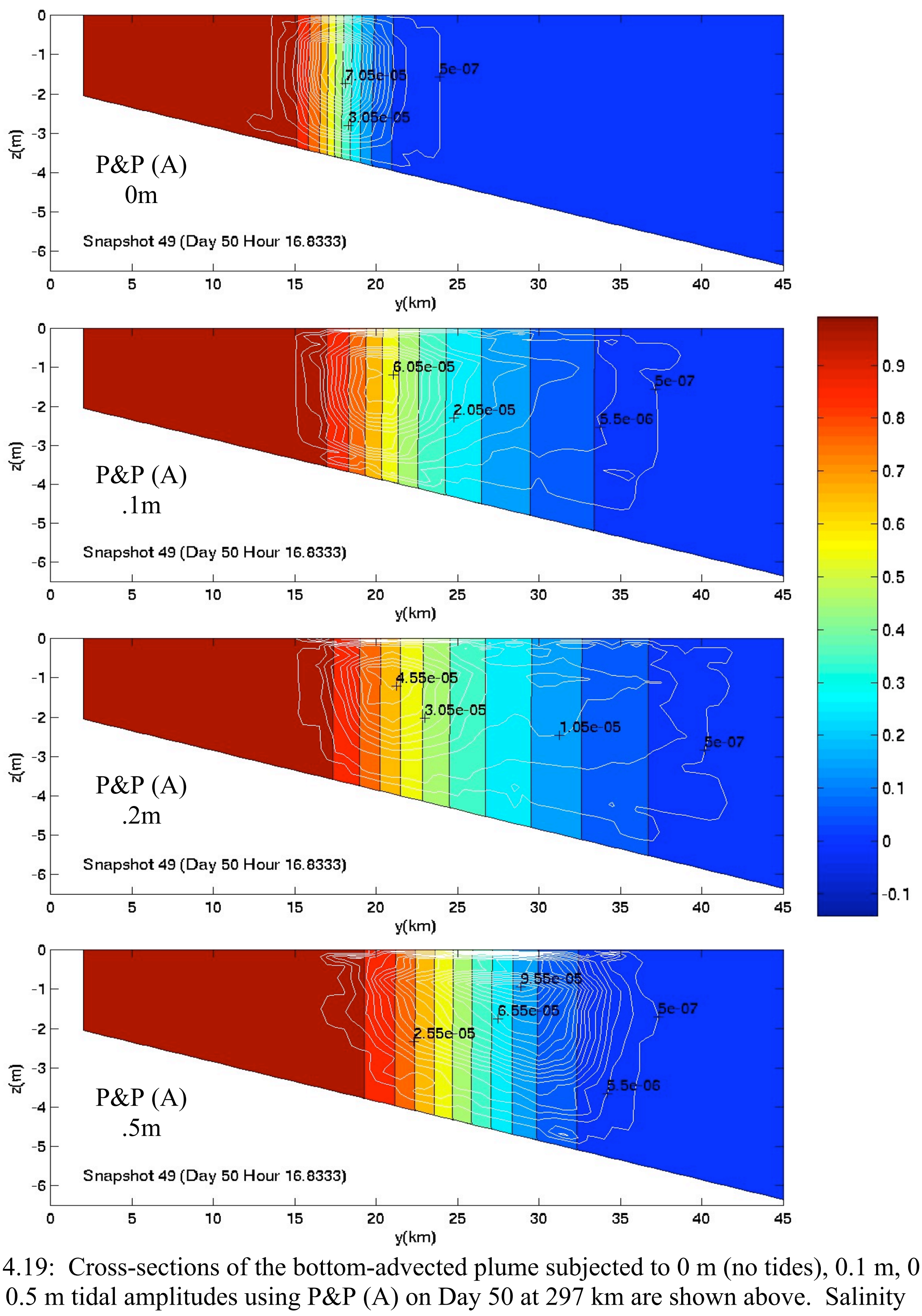

Figure 4.19: Cross-sections of the bottom-advected plume subjected to 0 m (no tides), 0.1 m, 0.2 m, and 0.5 m tidal amplitudes using P&P (A) on Day 50 at 297 km are shown above. Salinity anomaly contours range from –0.15 to 1.00, with intervals of 0.10, and the point-to-point vertical salt flux (white contours, black labels) range from 5 x 10^{-7} to 10^{-4} m^2 s^{-1}, with intervals of 5 x 10^{-6} m^2 s^{-1}. Note that x- and y-directions are scaled differently.

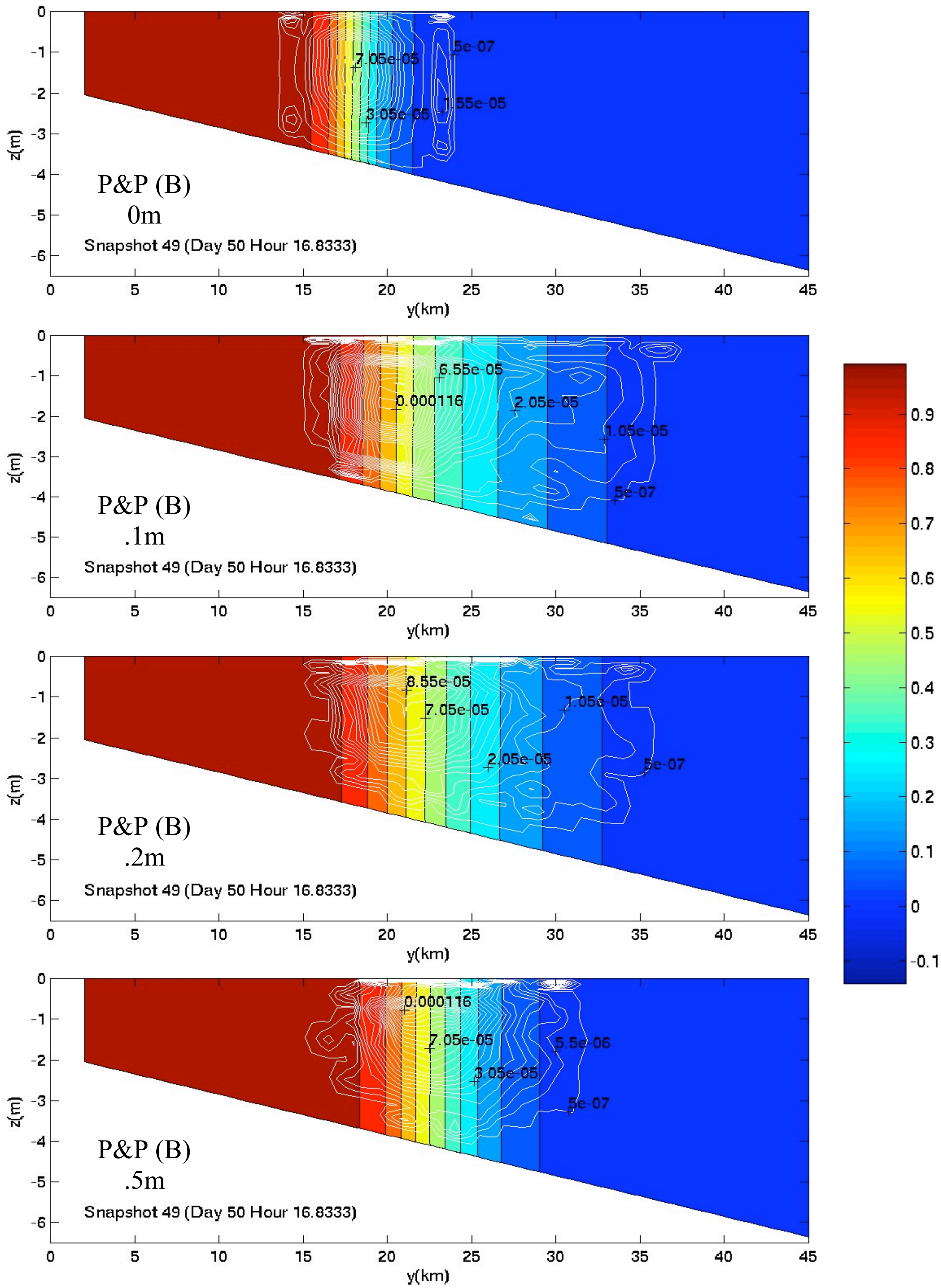

Figure 4.20: Cross-sections of the bottom-advected plume subjected to 0 m (no tides), 0.1 m, 0.2 m, and 0.5 m tidal amplitudes using P&P (B) on Day 50 at 297 km are shown above. Salinity anomaly contours range from –0.15 to 1.00, with intervals of 0.10, and the point-to-point vertical salt flux (white contours, black labels) range from 5 x 10^{-7} to 10^{-4} m^2 s^{-1}, with intervals of 5 x 10^{-6} m^2 s^{-1}. Note that x- and y-directions are scaled differently.

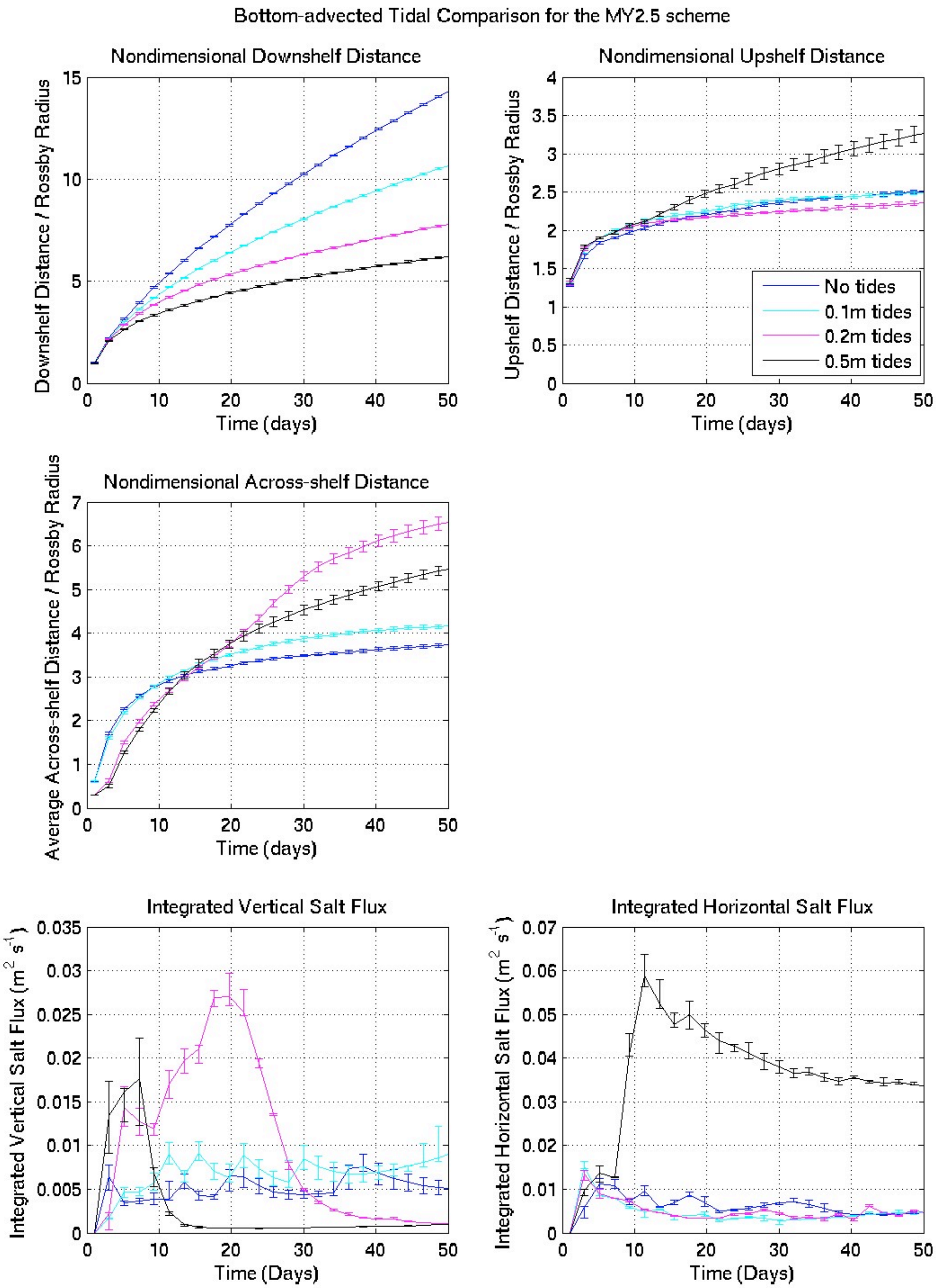

Figure 4.21: Comparison of metrics across various tidal amplitudes for the bottom-advected plume using MY2.5. Depth calculations are absent because bottom-advected plumes follow the bottom topography.

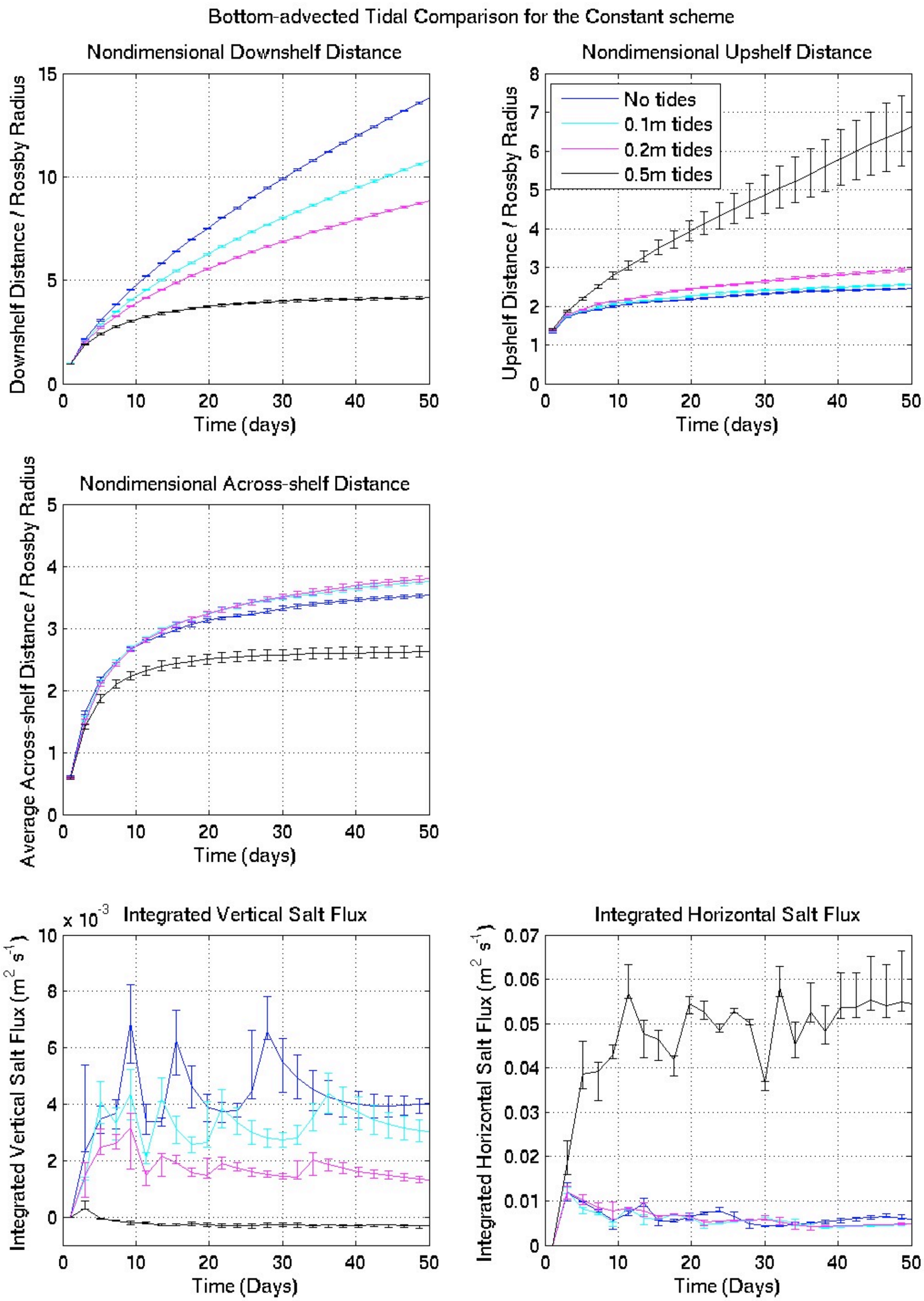

Figure 4.22: Comparison of metrics across various tidal amplitudes for the bottom-advected plume using the constant scheme. Depth calculations are absent because bottom-advected plumes follow the bottom topography.

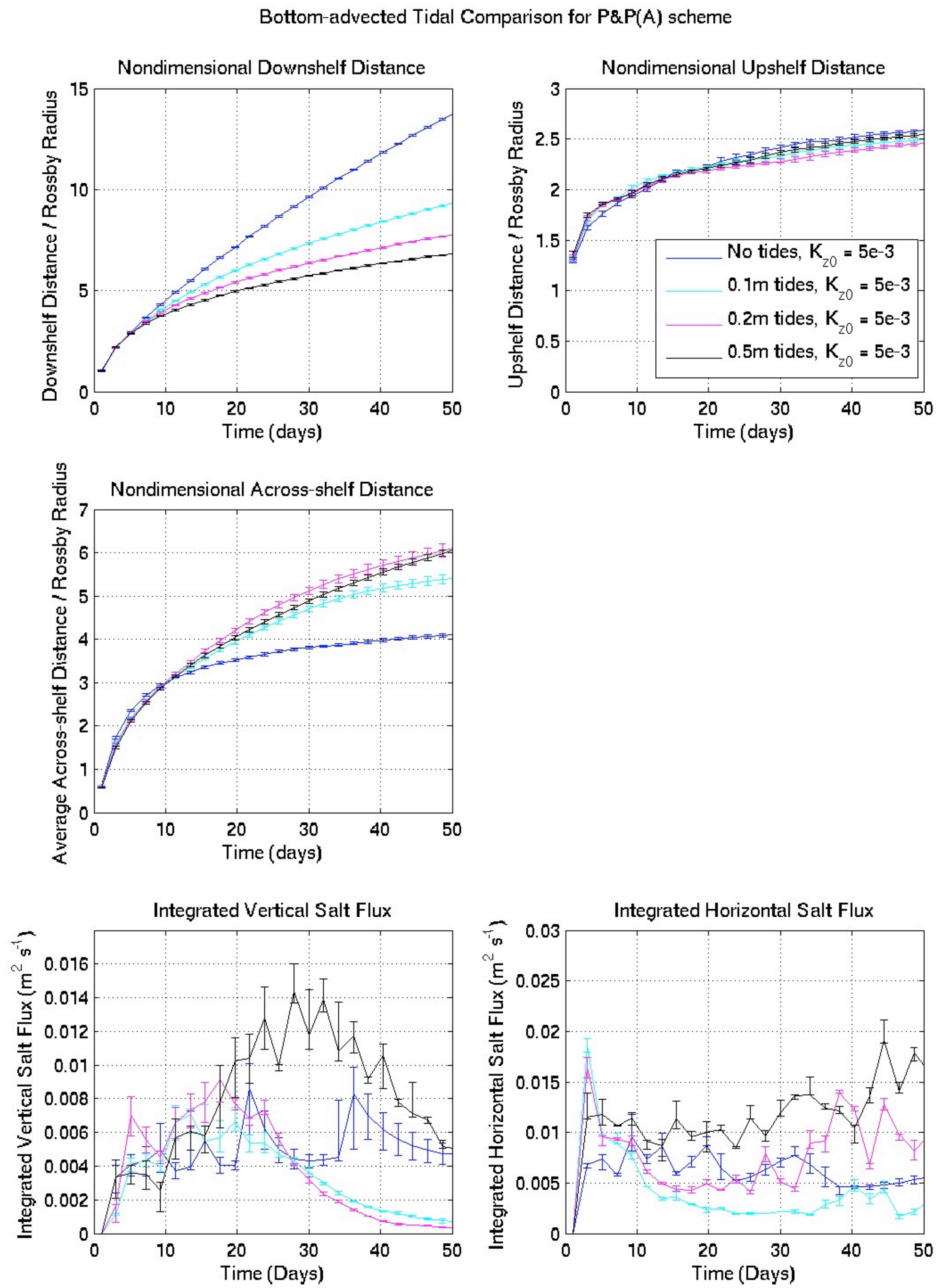

Figure 4.23: Comparison of metrics across various tidal amplitudes for the bottom-advected plume using P&P (A). Depth calculations are absent because bottom-advected plumes follow the bottom topography.

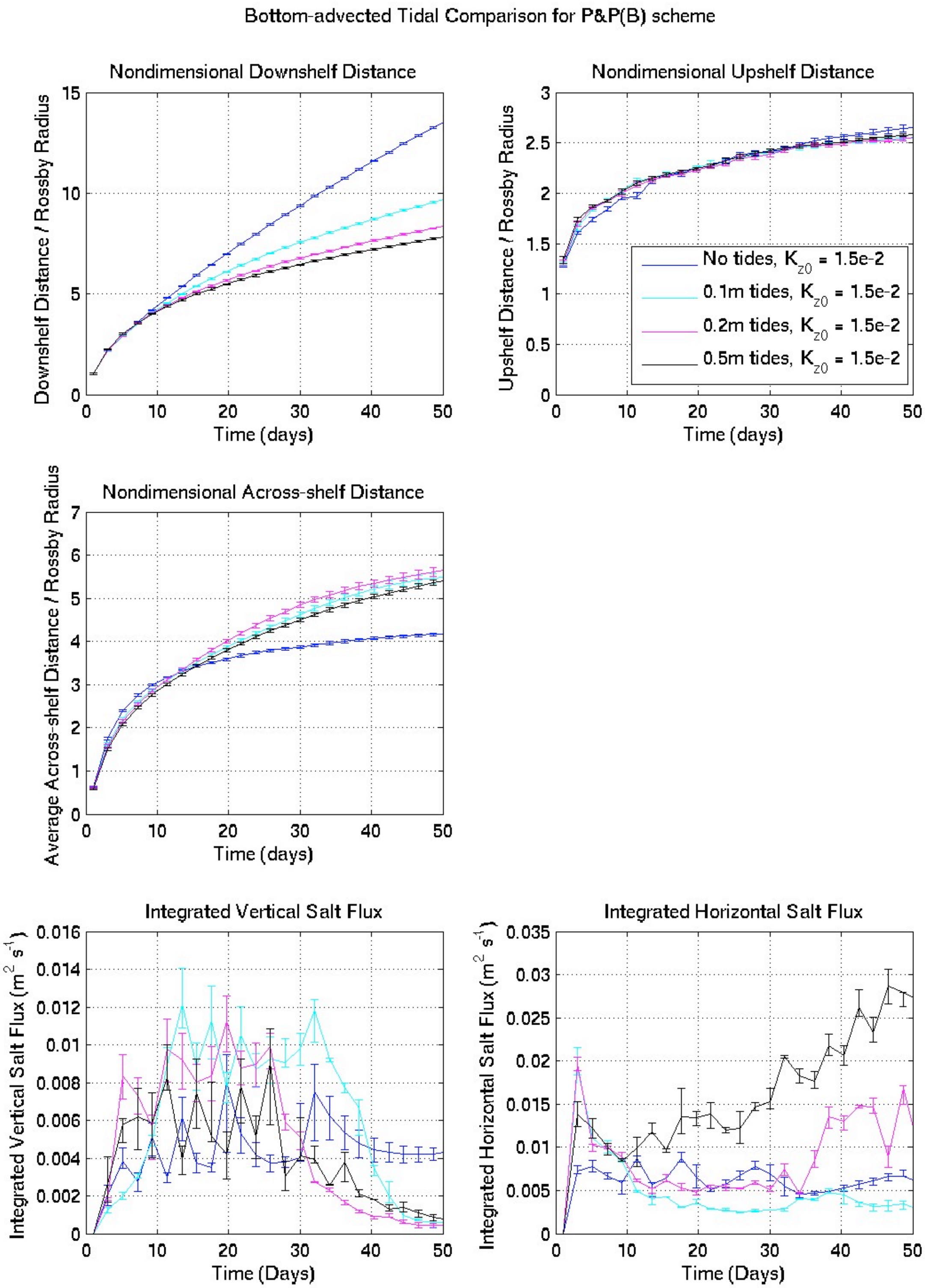

Figure 4.24: Comparison of metrics across various tidal amplitudes for the bottom-advected plume using P&P (B). Depth calculations are absent because bottom-advected plumes follow the bottom topography.

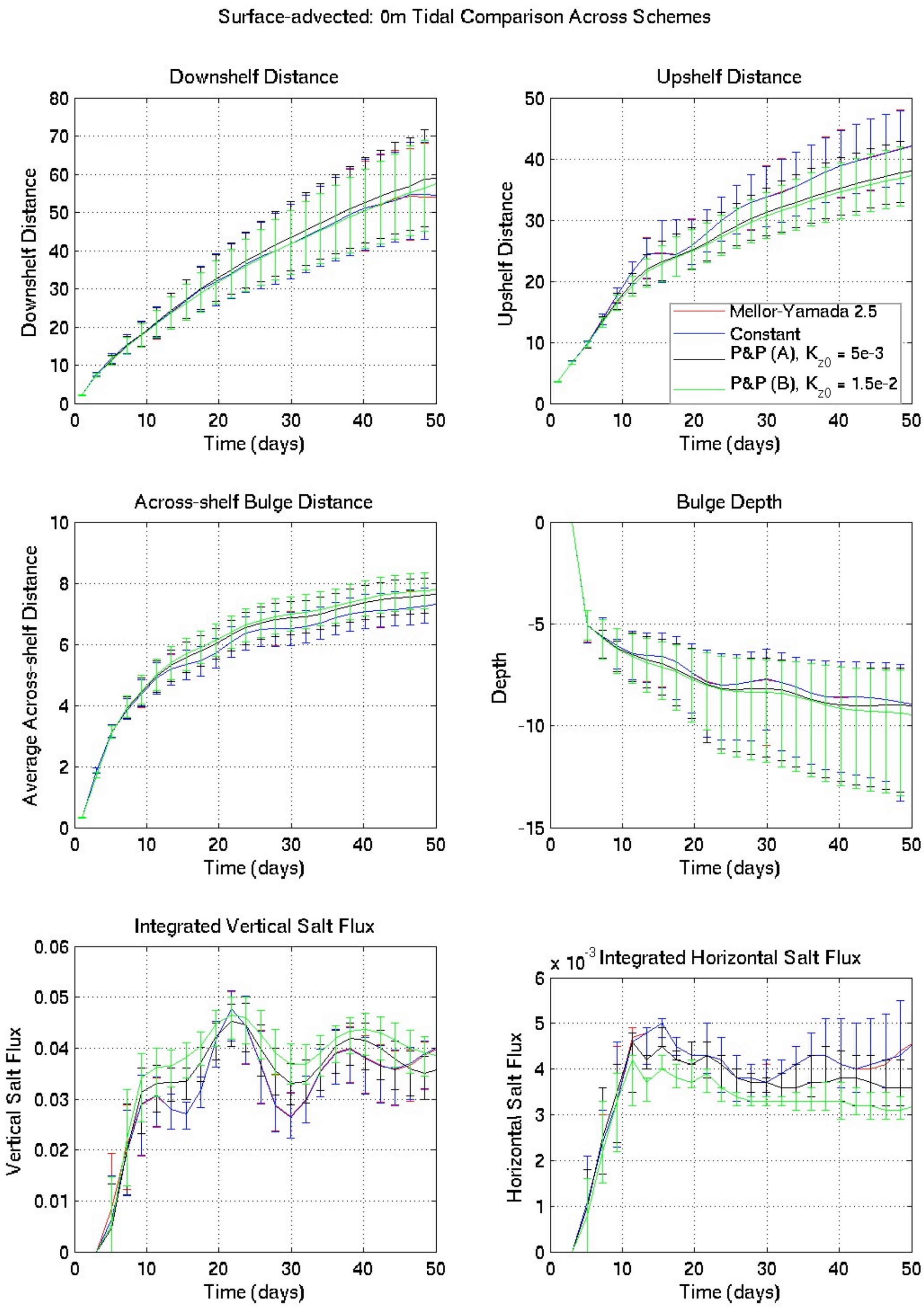

Figure 4.25: Comparison of metrics across mixing schemes for the surface-advected plume with no tidal amplitude.

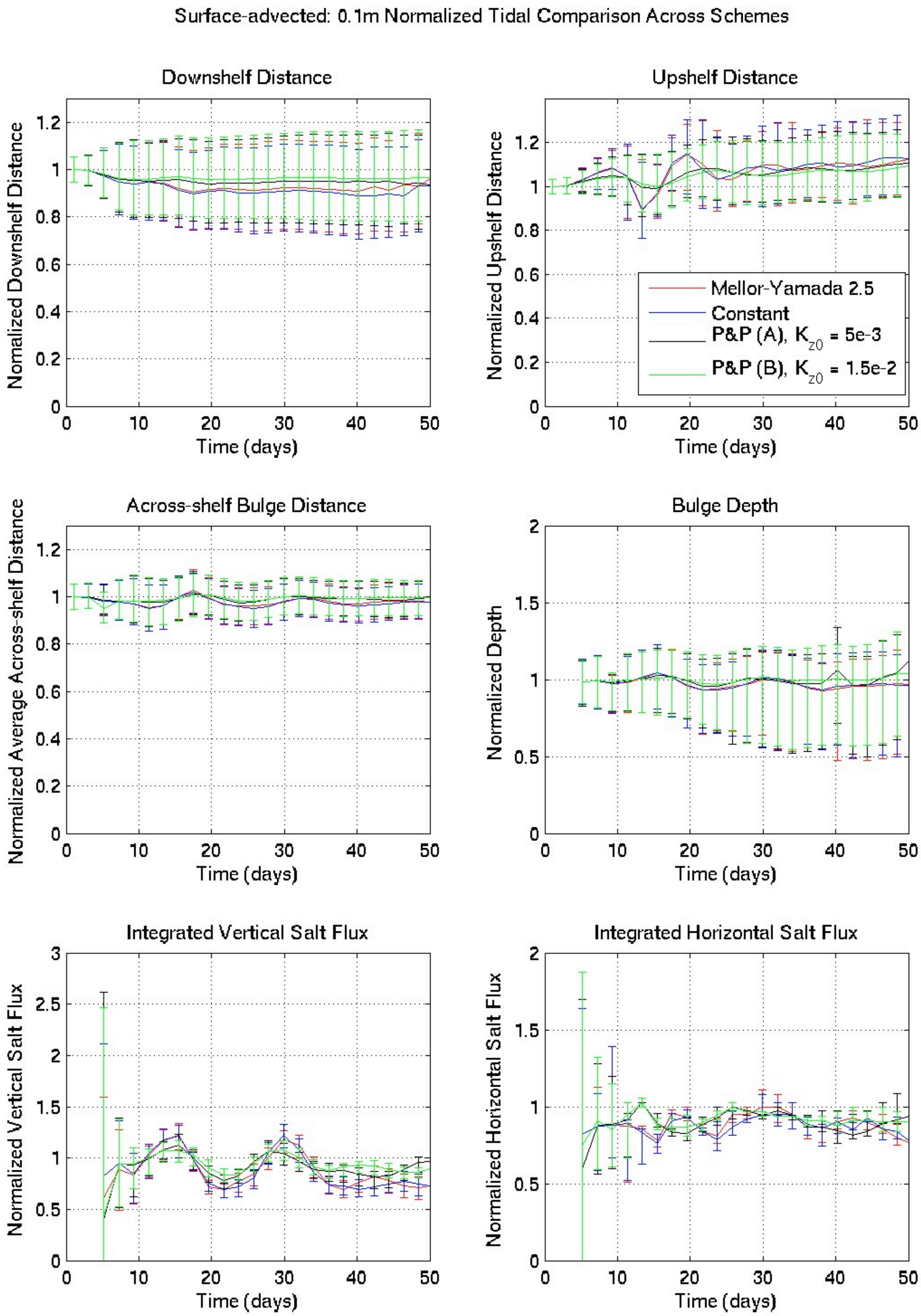

Figure 4.26: Comparison of normalized metrics across mixing schemes for the surface-advected plume with 0.1 m tidal amplitudes.

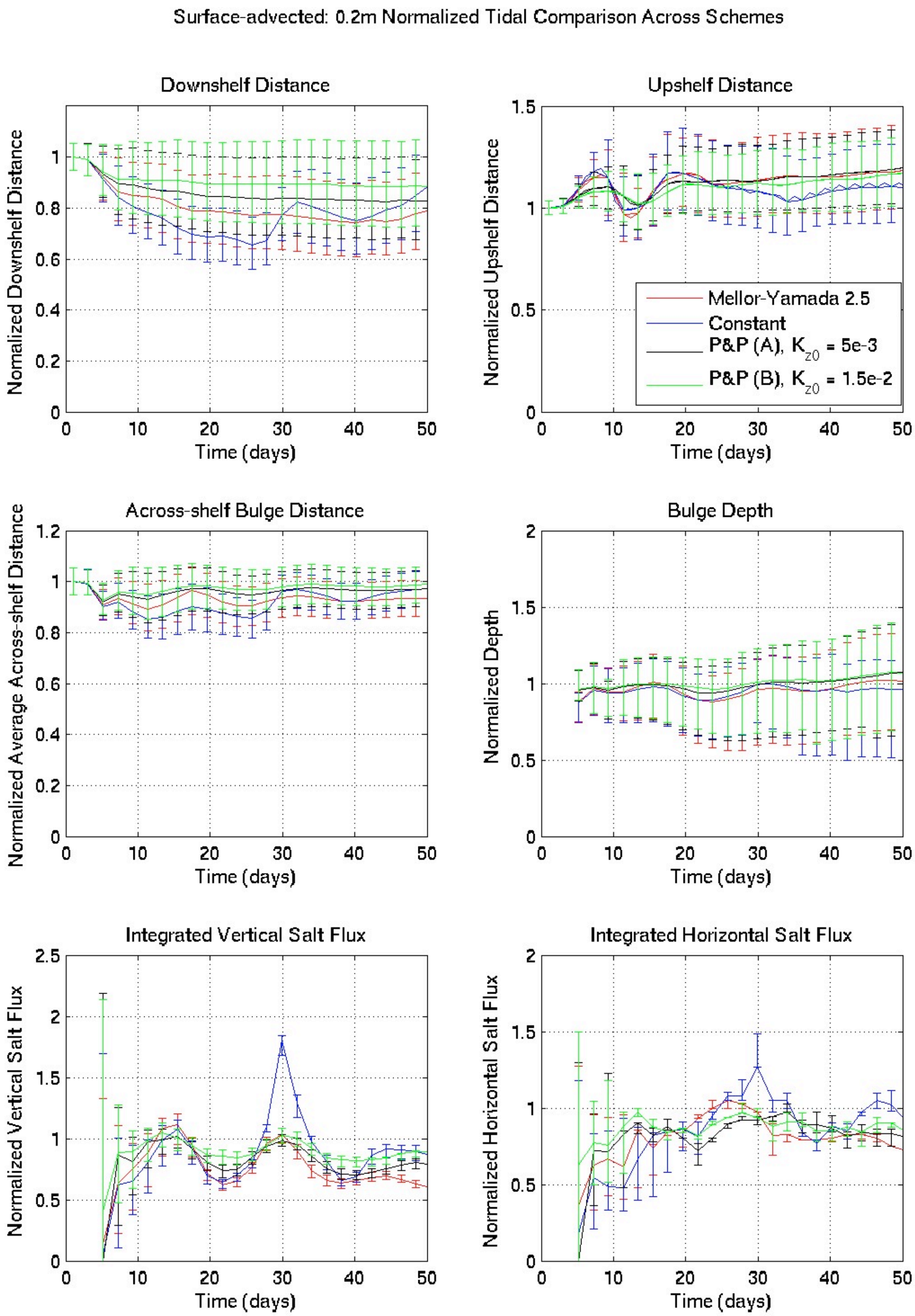

Figure 4.27: Comparison of normalized metrics across mixing schemes for the surface-advected plume with 0.2 m tidal amplitudes.

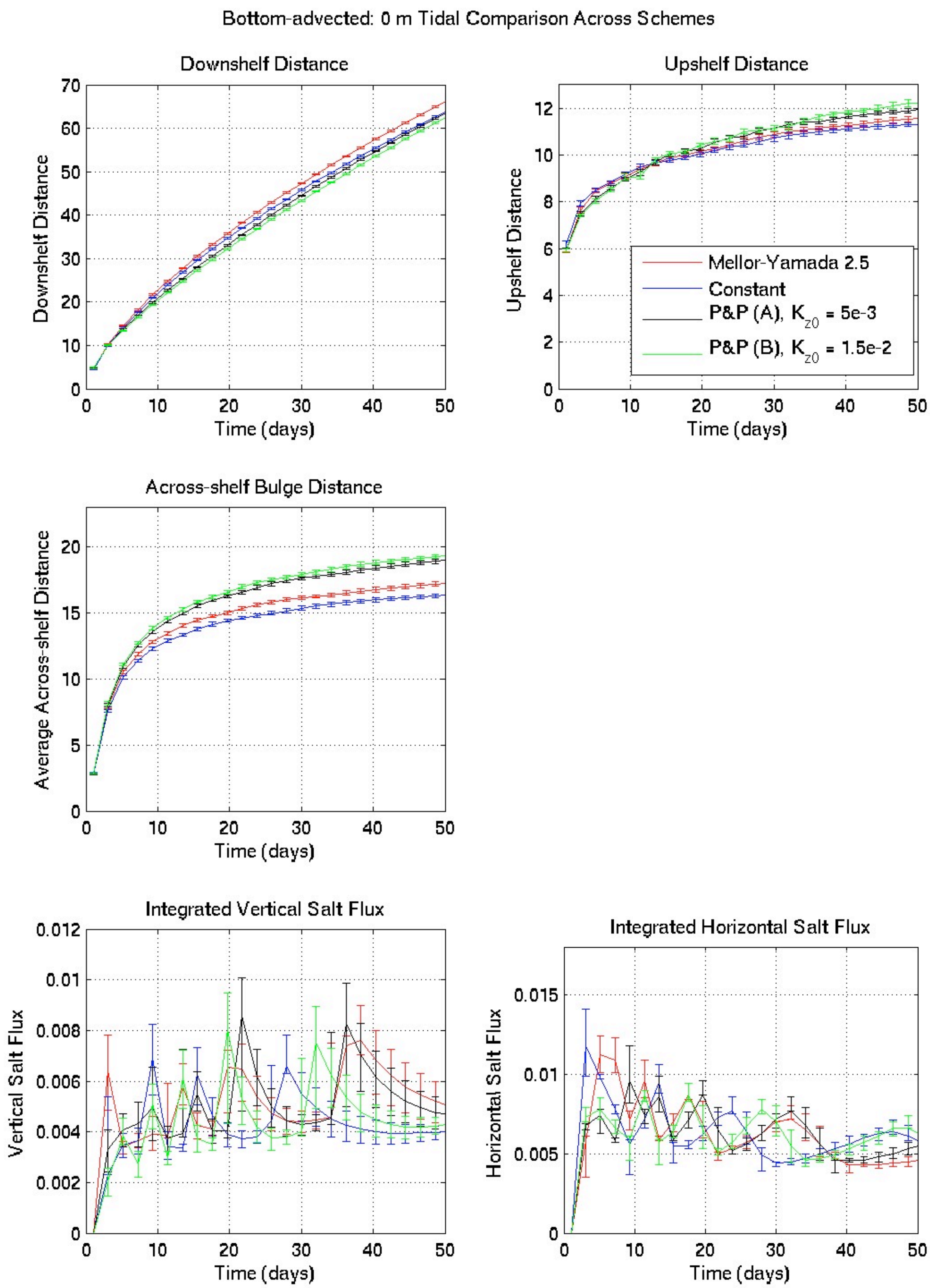

Figure 4.28: Comparison of metrics across mixing schemes for the bottom-advected plume with no tidal amplitude. Depth calculations are absent because bottom-advected plumes follow the bottom topography.

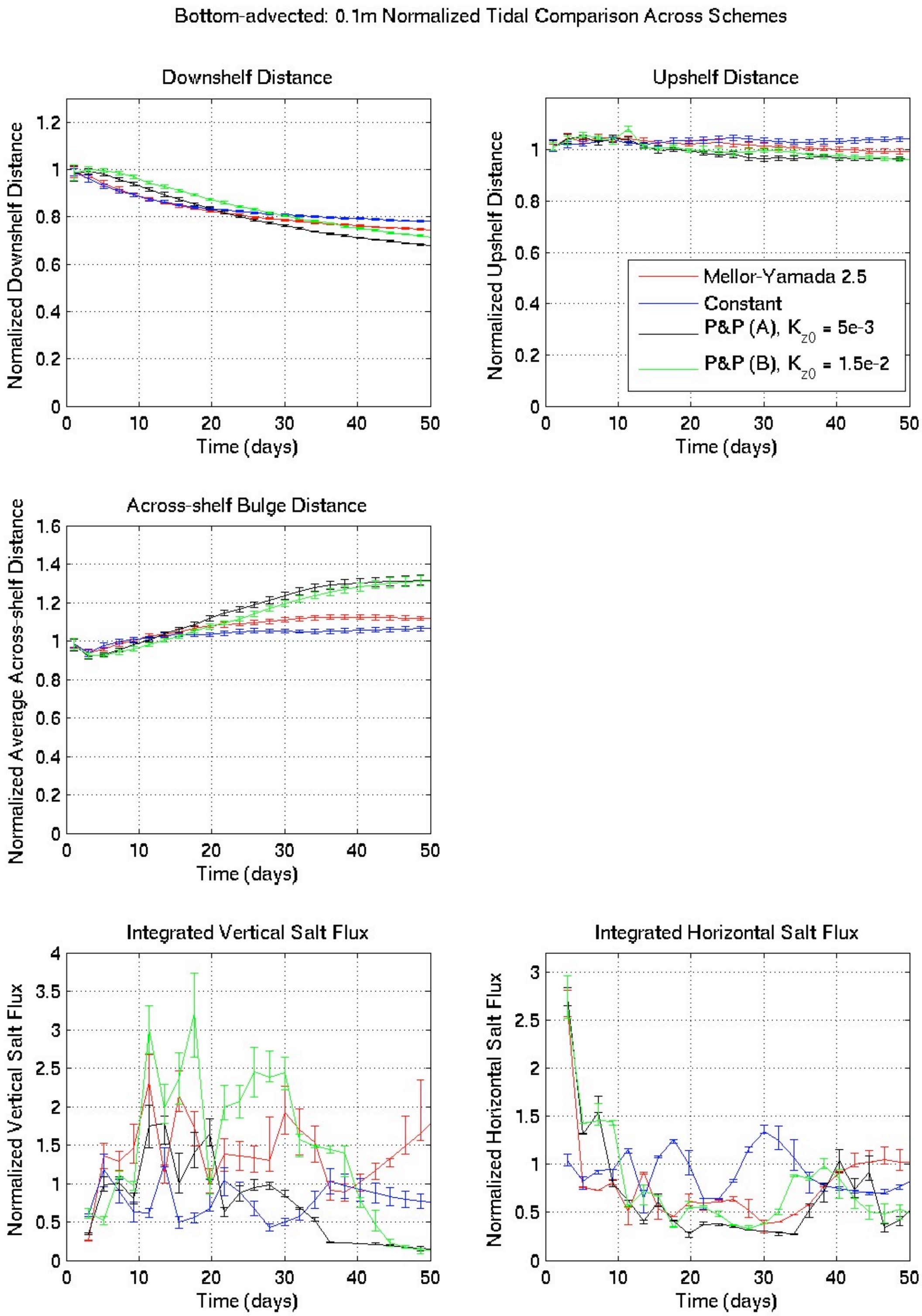

Figure 4.29: Comparison of normalized metrics across mixing schemes for the bottom-advected plume with 0.1 m tidal amplitudes. Depth calculations are absent because bottom-advected plumes follow the bottom topography.

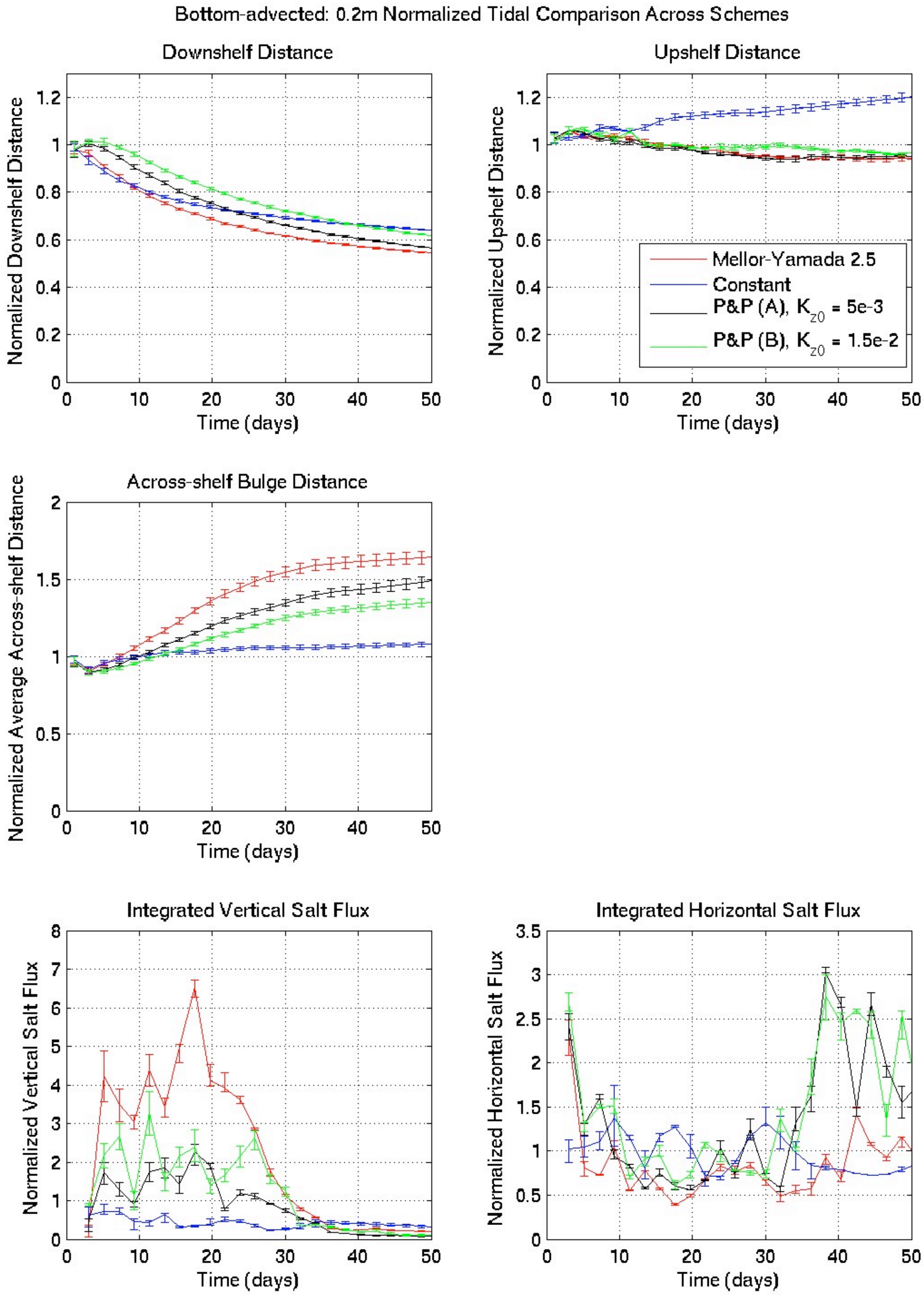

Figure 4.30: Comparison of normalized metrics across mixing schemes for the bottom-advected plume with 0.2 m tidal amplitudes. Depth calculations are absent because bottom-advected plumes follow the bottom topography.

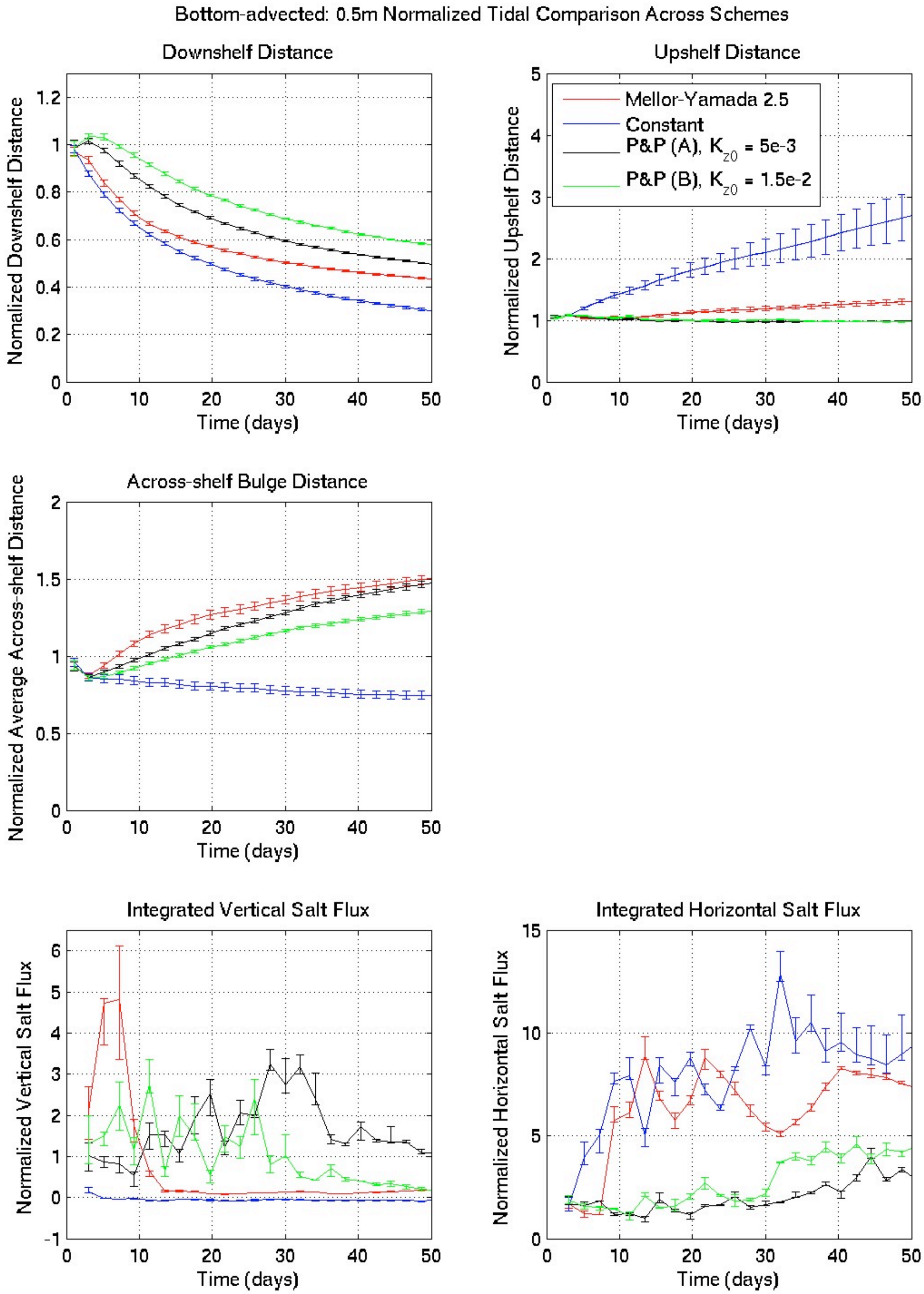

Figure 4.31: Comparison of normalized metrics across mixing schemes for the bottom-advected plume with 0.5 m tidal amplitudes. Depth calculations are absent because bottom-advected plumes follow the bottom topography.

CHAPTER 5

DISCUSSION

This study is consistent with a number of others (e.g. Chapman 2002, Hetland 2005, Nunes Vaz and Simpson 1994, and Durski et al. 1994) in that the choice of mixing scheme does have an effect on the resulting freshwater coastal current system when modeling the coastal environment. The extent of influence depends on various factors: the magnitude of K_{z_b} and K_{s_b}, the type of plume, and the tidal amplitude applied in the model. This section will discuss the results in the order in which they were presented in earlier sections.

5.1 Buoyancy Forcing

5.1.1 General dependence of viscosity/diffusivity

Overall, comparison simulations using various K_{z_b} and K_{s_b} magnitudes demonstrated a general dependence of scheme on the selected magnitude. A K_{z_b} and K_{s_b} magnitude of 5×10^{-5} m^2 s^{-1} and higher decreased the differences among the schemes. At a magnitude of 5×10^{-4} m^2 s^{-1}, the plumes were extremely similar for surface- and bottom-advected plumes, shown in Chapter 3. The background magnitude dominated the total viscosity/diffusivity for all the schemes with larger K_{z_b} and K_{s_b} magnitudes, resulting in similar plumes for all schemes at the highest K_{z_b} and K_{s_b} magnitude. This finding is consistent with Li et al. (2005), where the sensitivity of vertical stratification to the background diffusivity was tested; they concluded that background diffusivity affected stratification with a value larger or equal than 5×10^{-5} m^2 s^{-1}.

Order of magnitude changes in K_{z_b} and K_{s_b} also demonstrated the reliance of plume development on the mixing present. With the two larger magnitudes, the structure and shapes of all the plumes changed similarly across schemes, where more vertical mixing expanded the plumes in depth and decreased the vertical stratification $\left(\frac{dS}{dz}\right)$ of the plumes. A decrease in vertical stratification with increasing vertical viscosity magnitudes has previously been shown to occur for the constant scheme (Garvine 1999). The increase in vertical viscosity increases the viscous stress on the salinity gradient and creates more vertical mixing, allowing for the plumes to expand in depth and decrease in vertical stratification. Li et al. (2005) found a reduction of the vertical stratification with increasing diffusivity when testing various background diffusivities for the Chesapeake Bay.

As mentioned in the results section, the upshelf propagation and salt fluxes results for the plumes needed further explanation. Differing from previous studies, a magnitude of 5 x 10^{-6} m^2 s^{-1} for the surface-advected plume resulted in the least X_{UP} growth; however, this result was due to the presence of a large anticyclonic bulge limiting the upshelf growth. The plumes produced by the two higher magnitudes were characterized by smaller anticyclonic bulges with larger alongshelf dimensions than in the across-shelf, leading to greater expansion upshelf (Figure 6.1). Yankovsky (2000) and Garvine (2001) found that the relationship between vertical mixing of momentum and density governs the upshelf movement of the plume. As the Prandtl number ($\Pr = K_{z_b} / K_{s_b}$) decreased, the upshelf movement increased. While simulations in this study use a Pr = 1, simulations of both surface- and bottom-advected plumes subjected to various Prandtl numbers, holding the viscosity value at 5 x 10^{-6} m^2 s^{-1}, were run (Figures 5.2 and 5.3). This upshelf movement was inherently unstable. One of the surface-advected plumes (Pr = 0.1) and a number of bottom-advected plumes ($0.1 < \Pr < 1$) experienced abrupt changes in X_{UP} due to an upshelf pocket of freshwater disconnecting from the plume and moving upshelf. In general, these findings were in agreement with previous research.

Variations in SF_V were created by the structural changes from increasing K_{z_b} and K_{s_b} magnitude for the surface-advected plume (Figure 3.9 and Figure 5.4). SF_V did not monotonically increase with K_{s_b}, indicating that increasing K_{s_b} decreased the vertical salinity gradient (Figure 5.4). The intermediate and highest magnitudes of K_{s_b} (Figure 3.9) produced relatively similar SF_V values, illustrating that the offsetting changes in vertical salinity gradient and K_{s_b} resulted in little change for SF_V. Tilburg et al. (2007) performed similar salt flux calculations and also found only minor differences in salt flux resulting from simultaneously increasing diffusivity and decreasing vertical stratification. Similarly, in this study, the intermediate K_{s_b} was able to produce the largest SF_V with intermediate K_{z_b} and K_{s_b} and a large vertical salinity anomaly.

Increasing K_{z_b} and K_{s_b} also decreased the vertical stratification in the bottom-advected plumes (Figure 5.5). However, unlike the surface-advected plumes, the effects of decreased stratification dominated over the changes in K_{s_b}, resulting in dramatically lowering the vertical salt flux (Figure 3.21). Because the water column became increasingly homogenous with increased K_{z_b} and K_{s_b}, it was expected that while mixing was present, less vertical salt flux occurred due to similarities in salinity.

The resulting SF_H with various K_{z_b} and K_{s_b} magnitudes created slightly different results for the two types of plumes using the constant scheme (Figures 3.9 and 3.21). Since the horizontal diffusivity was calculated from the Smagorinsky (1963) formula (2.3), and not directly specified by the user, the response of the plume to changes in K_{z_b} and K_{s_b} was not straight-forward. Therefore, changes in the calculated SF_H could be due to changes in structure and dynamics caused by the large magnitude changes in K_{z_b} and K_{s_b} rather than the influence of the vertical mixing scheme. With increasing vertical K_{z_b} and K_{s_b}, the vertical stratification decreased for the surface-advected plumes (Figure 5.4) while for the bottom-advected plumes, a combination of a decrease in vertical stratification and increase in horizontal salinity anomaly gradient resulted (Figure 5.5). Therefore, it would be expected that increasing K_{z_b} and K_{s_b} caused variations in SF_H for surface-advected plumes due to a change in plume structure (Figure 3.9). An overall decrease in SF_H was shown for the surface-advected plumes for roughly the first half of the simulations; for the rest of the run, the intermediate magnitude increased SF_H while 5 x 10^{-6} m^2 s^{-1} produced a similar SF_H as 5 x 10^{-4} m^2 s^{-1}. The increase in SF_H for a magnitude of 5 x 10^{-5} m^2 s^{-1} was the result of larger calculated horizontal diffusivity; Figure 5.1 (second panel) showed the flow field for the surface-advected plume, where at 300 km, the velocities showed larger divergence at this location than the other two magnitudes. Therefore, since the diffusivity was calculated from the velocities and divergence, the larger calculated diffusivity created a larger SF_H for the latter half of the runs.

For bottom-advected plumes using the constant scheme (Figure 3.21), a magnitude of 5 x 10^{-4} m^2 s^{-1} created larger SF_H than the intermediate magnitude. While the lowest magnitude, 5 x 10^{-6} m^2 s^{-1}, resulted in the largest SF_H with larger calculated horizontal diffusivity. The 5 x 10^{-4} m^2 s^{-1} magnitude resulted in the second highest SF_H due to the strong horizontal salinity anomaly gradient. Therefore, the relationships between SF_H and K_{z_b} and K_{s_b} magnitude changes were equally dependent on the calculated horizontal mixing terms and the horizontal salinity anomaly gradient.

Because of the structural changes in the plumes with changes in K_{z_b} and K_{s_b} magnitude, the SF_V and SF_H for both plumes showed different results. Therefore, variations in K_{z_b} and K_{s_b} did significantly alter the plumes in not only structure but also in dynamics.

The responses of the other schemes, MY2.5 and both P&P, to order of magnitude changes in K_{z_b} and K_{s_b} were similar to the response of the constant scheme for surface-advected plumes (Figures 3.10 to 3.15) and bottom-advected plumes (Figures 3.22 to 3.26) with the exception of SF_V in the surface-advected plume. During the initial development of the plume, Ri was small and both P&P schemes produced very high mixing coefficients and therefore, vertical salt fluxes (Figure 3.15). However, once the plume had developed, the schemes produced similar SF_V values.

5.1.2 Effects of scheme on metrics

A K_{z_b} and K_{s_b} magnitude of 5 x 10^{-6} m^2 s^{-1} for both surface-advected and bottom-advected plumes created the largest differences among the schemes with the least influence of K_{z_b} and K_{s_b}. Therefore, the mixing scheme comparison was conducted at this magnitude. While the other metrics are presented in detail in Chapter 3, the X_{DN} and X_{UP} metrics are discussed in more detail here.

The growth in X_{DN} differed depending on the type of plume due to differences in plume dynamics. The surface-advected plume typically had two distinguishing features, an anticyclonic bulge and a coastal current moving downshelf. These two features were interconnected, where freshwater discharges into the anticyclonic bulge and eventually is transported by the coastal current (Isobe 2005, Fong and Geyer 2002); therefore, the total transport of the freshwater was divided between the two features, where the size of the bulge determined the transport of freshwater in the current. Larger bulges tend to maintain more of the freshwater and less transport downshelf (Fong and Geyer 2002). The constant scheme produced the largest freshwater bulge compared to the other schemes (Figure 5.6); therefore, less downshelf transport resulted.

Because the bottom-advected plume lacked differentiation between the anticyclonic bulge and coastal current, the growth in X_{DN} distance was dependent on the mixing within the coastal current. The nose of the plume was characterized by strong vertical stratification of density velocities. Larger mixing coefficients and more mixing reduced the distance downshelf. The constant scheme, known to mix the least with the use of K_{z_b} and K_{s_b}, created the largest downshelf expansion. MY2.5 resulted in a comparable X_{DN} extent as the constant scheme. In areas of high stratification (where $Ri > 0.25$), MY2.5 resorts to applying K_{z_b} and K_{s_b} as the mixing coefficients. Since the coastal current contains relatively larger vertical salinity gradients, the vertical coefficients for MY2.5 and constant schemes are similar; Figure 5.8 (top panels) shows similar point-by-point vertical salt flux (white contours) for MY2.5 and constant scheme near the nose of the plume (434 km) . Both P&P schemes produced larger mixing coefficients than the constant scheme, where the viscosity and diffusivity terms were first calculated and then added to K_{z_b} and K_{s_b}; therefore, larger vertical salt flux was created (bottom panels, Figure 5.7). Therefore, the downshelf edge of the plume mixed more, resulting in less downshelf development.

Similar to previous studies, the X_{UP} propagation was larger with lower viscosity and/or higher diffusivity for both types of plumes (Yankovsky 2000 and Garvine 2001). Movement of water upshelf had less resistance of flow with lower viscosity, creating less viscous shear and the associated mixing, and more movement upshelf with higher diffusivity of the salinity gradient; recall that as the plume moved out of the inlet, water turned and moved downshelf, creating a strong salinity gradient near the upshelf edge of the plume. The constant scheme, which had the least total viscosity, resulted in the largest X_{UP} propagation (20% larger for surface-advected and 44% larger for bottom-advected plumes) of all schemes (top right panels, Figures 3.32 and 3.33).

The constant scheme tended to produce the least total viscosity and diffusivity for both types of plumes and the least amount of vertical salt flux upshelf of the inlet (white contours, Figures 5.6 and 5.8). Since upshelf propagation resulted from smaller mixing, the constant scheme, resulted in the most upshelf movement.

5.2 Buoyancy and Tidal Forcing

5.2.1 Changes in tidal amplitude

Tidal forcing promotes mixing by creating larger vertical shear from bottom friction. Since tides are barotropic, the tidal velocities are directly related to the height of the tidal amplitude, where a greater wave height creates a larger pressure gradient and faster velocities. Since tides are shallow water waves, the associated velocities extend to the bottom and are subjected to frictional bottom forces. As a result, an increase in vertical eddy viscosity may be found near the bottom (Garvine 1999 and Guo and Valle-Levinson 2007), where the bottom friction increases the shear in the water column, creating a bottom mixing layer in the model. Because of the importance of bottom frictional forces on tidal mixing, the influence of tidal forcing on surface- and bottom-advected plumes differ.

Simulations incorporating tidal forcing used a background viscosity/diffusivity of 5 x 10^{-4} m^2 s^{-1} in order to account for the frictional forces associated with tides; runs with smaller K_{z_b} and K_{s_b} were not possible most likely due to restrictions of the CFL condition. Other reasons for failure are unknown and should be investigated in future research; since buoyancy only forcing showed the largest differences among the schemes using much lower K_{z_b} and K_{s_b}, larger variations due to tides could possibly be analyzed. In addition, while the bottom-advected plumes were subjected to all the tidal amplitudes, the 0.5 m amplitude was not applied to the surface-advected plumes. The plumes had to be run on unrealistic timesteps to satisfy the CFL condition and simulate the higher amplitude tides.

Tidal amplitudes of 0.1 and 0.2 m did not considerably alter surface-advected plumes. Variations in the plume metrics due to changes in tidal amplitude were smaller than the +/- 10% range of the metric values and were comparable to the simulations lacking tidal forcing (Figure 4.9 to 4.12). These plumes showed only minor changes in the outer most salinity anomaly contours subjected to bottom influences (Figure 4.1 to 4.8). However, the freshest water for the surface-advected plumes remained near the inlet and free from influence of bottom friction and thus, from tidal mixing (Figure 5.9). The surface-advected plumes changed slightly with variations in tidal amplitude. This is consistent with Yankovsky et al. (2001), where tidal fluctuations, created from pulsing variable freshwater discharge, produced only minor effects on the surface-advected plume. However, if 0.5 m tidal amplitudes were possible for surface-advected plumes, there could be more influence of tidal forcing on this type of plume.

Because bottom-advected plumes are largely influenced by bottom friction (Figure 5.10), they were greatly influenced by changes in tidal amplitude (Figures 4.21 to 4.24). Large tidal influence was evident in the presence of large variations in vertical salt flux and tidal straining for all bottom-advected plumes. To clearly demonstrate the presence of tidal straining, the instantaneous snapshots of large positive and negative variations in vertical salt flux are shown. Figure 5.11 shows the SF_V for the bottom-advected plume using MY2.5 with 0.2 m tides as a function of time (upper panel) and two different instantaneous snapshots of cross-sections at two separate times (lower panels). Since the SF_V was calculated approximately every 2 days, the expected tidal sinusoidal signature with a period of 12.42 hours is aliased. However the tidal straining is still evident in the time series, indicated by the positive and negative values of SF_V.

Day 17 (middle panel, Figure 5.11) showed slight overstraining within the freshwater plume (at locations ~14 km, 17 km, and 20 km), where denser water was pushed over lighter water creating an unstable condition with negative vertical salt flux. At Day 22 (bottom panel, Figure 5.11), the flood current caused fresher water at the surface to move farther across-shelf than near the bottom due to bottom friction. Here, the vertical salt flux was positive, indicating the return of the freshwater plume to a buoyancy forced stratified flow enhanced by the flood tide.

The hourly horizontal Richardson parameter for the MY2.5 with 0.2 m tidal amplitude simulation was calculated near the freshwater inlet for Days 2 to 4 (Figure 5.12). Stacey et al. (2001) determined a threshold value of ~ 3, where greater values on ebb tide indicated the interaction and amplification of stratifying and shear flow effects for the system. Values below this threshold indicated the destratification of the plume due to tidal mixing; evidence of tidal straining was shown in the large variation in the horizontal Richardson parameter, with calculated values above and below the threshold for the two day period (Figure 5.12).

Bottom-advected plumes subjected to 0.5 m tidal amplitudes behaved differently from the trend of 0 m, 0.1 m, and 0.2 m tides for Y_{AC} and the salt fluxes; this was also apparent in the large change in plume shape with this tidal amplitude (bottom panels, Figures 4.13 to 4.16). With higher tidal amplitude, the barotropic forcing created higher velocities by the pressure gradient, changing the competition between the constant freshwater discharge and tidal forcing and altering the overall plume shape. Each scheme produced different results for the 0.5 m tidal amplitude due to the variations in the tidally averaged velocity field across the schemes (Figure 5.13). Examination of vertical mixing coefficients near the bottom (Figure 5.14) revealed large differences between the schemes, as expected. Therefore, as the velocity field rotated with the effects of Coriolis, the mixing created by vertical shear induced from bottom friction differed, causing an overall difference in the direction of tidally averaged flow and in shape of the tidal ellipse. Greater mixing near the bottom resulted in slower velocities on the surface. The constant scheme produced the least viscosity and resulted in the largest tidal velocities and largest tidal ellipse while P&P (B) produced the largest viscosity values, creating the smallest tidal velocities and tidal ellipse (Figure 5.15).

Examination of the tidal ellipse (Figure 5.15) produced by the constant scheme shows a net upshelf flow, where -*u* velocities are larger than +*u* velocities. A plan view of the tidally-averaged velocity field confirms the presence of a roughly homogeneous flow field moving upshelf, causing the plume to also move upshelf (second panels, Figures 5.13).

For a tidal amplitude of 0.5 m, MY2.5 was subjected to mixing in all directions and a decrease in the horizontal salinity gradient (top panel, Figure 5.13). Since the viscosity field near the bottom increased with distance across-shelf (top panel, Figure 5.14), less mixing was possible near the coast than at the across-shelf edge of the model domain. Therefore, the plume expanded the most in the across-shelf direction and less closer near the coast.

Both P&P schemes produced the least behavioral changes of the plumes using the highest tidal amplitude; the schemes maintained strong stratification for the plume in the alongshelf directions but expanded in the across-shelf direction (bottom two panels, Figure 5.13). The tidal velocities for the P&P schemes had larger *v* than *u* velocities, allowing for more across-shelf expansion of the plumes to result (Figure 5.15). The P&P scheme were based on the Richardson number and the lack of stratification resulted in a Richardson number of zero; the scheme then used the null viscosity (P&P (A) = 5 x 10^{-3} m^2 s^{-1}, P&P (B) = 1.5 x 10^{-2} m^2 s^{-1}) plus the K_{z_b} to calculate the total viscosity. Most of the model had no changes in vertical stratification, causing the majority of the model domain to use the same value for viscosity; the salinity anomaly front was the only region of stratification for these plumes (bottom panels, Figure 5.14). Therefore, only changes within the plume front resulted.

5.2.2 Effect of schemes on normalized metrics

The combination of tidal- and buoyancy-forcing complicated the analysis of the tidal effects on the buoyant plume. Therefore, tidal simulations were normalized, by dividing by the results from no tides, in attempt to eliminate the buoyancy forcing effects and focus on the modifications of the plume created from tidal forcing and mixing scheme.

The surface-advected plumes compared across the various mixing parameterizations lacked differentiation for the metrics (Figures 4.26 and 4.27). These plumes, unlike bottom-advected plumes, had minimal influence from bottom topography, creating less tidally induced variations among the schemes. Therefore, the resulting surface-advected plumes were similar to those created with only buoyancy forcing; all normalized metrics for tidal amplitudes of 0.1 and 0.2 m were in the vicinity of a normalized value of 1, giving evidence of similar plumes (Figures 4.26 and 4.27).

The importance of choice of scheme increased with increasing tidal amplitudes for the bottom-advected plumes, seen in the increase in spread of the metrics and shift away from a normalized value of 1 (Figures 4.29 to 4.31). Since tidal amplitude determined the amount of mixing in the water column, increasing tidal amplitudes metric variations across mixing schemes. The normalized tidal metric results had many similarities to the buoyancy forcing results. The $X_{DN\text{-}NOR}$ and $X_{UP\text{-}NOR}$ metrics are discussed in more detail than in Chapter 4.

$X_{DN\text{-}NOR}$ disparities across scheme increased with increasing tidal amplitude for the bottom-advected plumes, indicating that greater mixing increased the importance of choice of vertical mixing scheme in the $X_{DN\text{-}NOR}$ direction. The constant scheme developed the most downshelf for both 0.1 m and 0.2 m tidal amplitudes, where the scheme produced the least mixing (Figure 5.7), causing the nose of the plume to mix less than the other schemes and develop further downshelf. The X_{DN-NOR} growth for the schemes diverged using a tidal amplitude of 0.5 m (top left panel, Figure 4.31); P&P (B) was 47% larger than the constant. The increase in scheme difference resulted from larger influence of tidal forcing and the tidal ellipse, causing the constant scheme to produce the least X_{DN-NOR}, as a consequence of large X_{UP-NOR} growth.

Larger tidal amplitudes increased X_{UP-NOR} movement for the constant scheme. The combination of lower viscosity (Yankovsky 2000 and Garvine 2001) and the velocity field created from tidal mixing (second panel, Figure 5.13) promoted the extensive growth in the upshelf direction. Tidal currents have been shown to constrain upshelf movement when using MY2.5 (Garvine 1999 and Guo and Valle-Levinson 2007); in this study, MY2.5 and both P&P demonstrated this behavior with higher calculated mixing terms. The P&P schemes upshelf growth maintained roughly the same with and without tides while MY2.5 had similar X_{UP-NOR} results for 0, 0.1, and 0.2 m tides (top right, Figures 4.28 to 4.31). However, at 0.5 m, MY2.5 increased movement X_{UP-NOR} due to the overall plume expansion from larger tidal forcing.

5.3 Model Runtime

In computational modeling, the runtime and the accuracy of a model is of great importance. Therefore, the runtimes in user real time of the plumes with and without tides were recorded for a period ~1.29 simulation days to determine which vertical mixing parameterizations perform at faster speeds. Table 5.1 demonstrates that for all plumes and situations, MY2.5 by far has the longest runtime (1 to 3 minutes slower than the other schemes) while the constant or P&P (B) schemes run faster. Since MY2.5 calculates the viscosity/diffusivity coefficients using a series of complex equations, it would be expected for this scheme to have the longest running time. The differences between the runtimes vary depending on the situation and the type of plume. Therefore, since time is a valuable resource, the knowledge of the runtime is important when determining the submodel for use; especially if the simulation period is over longer periods. For example, a 100 day simulation for the surface-advected with no tides using MY2.5 would ~ 1200 minutes while the constant scheme would ~ 1000 minutes; there is an approximately 3 hour runtime difference.

Table 5.1: Shows the model runtime in real time (minutes:seconds) for the plumes with and without tidal forcing over a period of ~ 1.29 days. Bottom-advected plumes have a longer runtime than surface-advected plumes due to using a smaller timestep.

NO TIDES	*MY2.5*	*Constant*	*P&P (A)*	*P&P (B)*
Surface-advected	12:25.79	10:17.01	10:21.22	10:17.44
Bottom-advected	28:31.04	25:57.46	26:32.06	26:23.67

WITH TIDES	*MY2.5*	*Constant*	*P&P (A)*	*P&P (B)*
Surface-advected (0.2 m amplitude)	7:20.07	6:18.02	6:25.93	6:36.90
Bottom-advected (0.5 m amplitude)	30:53.17	26:33.46	27:05.50	26:23.83

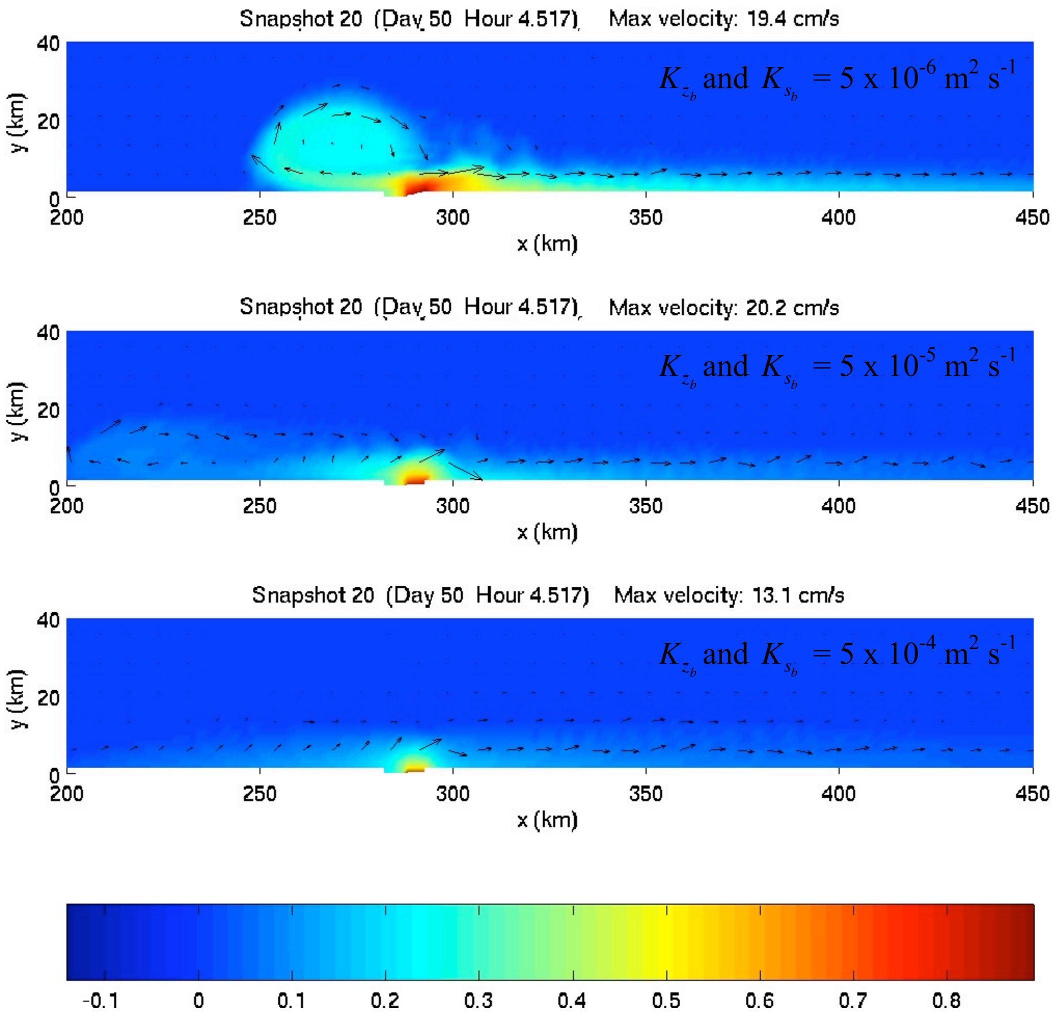

Figure 5.1: The surface-advected velocity (black arrows) and salinity anomaly (color) fields are shown for the constant scheme using various K_{z_b} and K_{s_b} magnitudes.

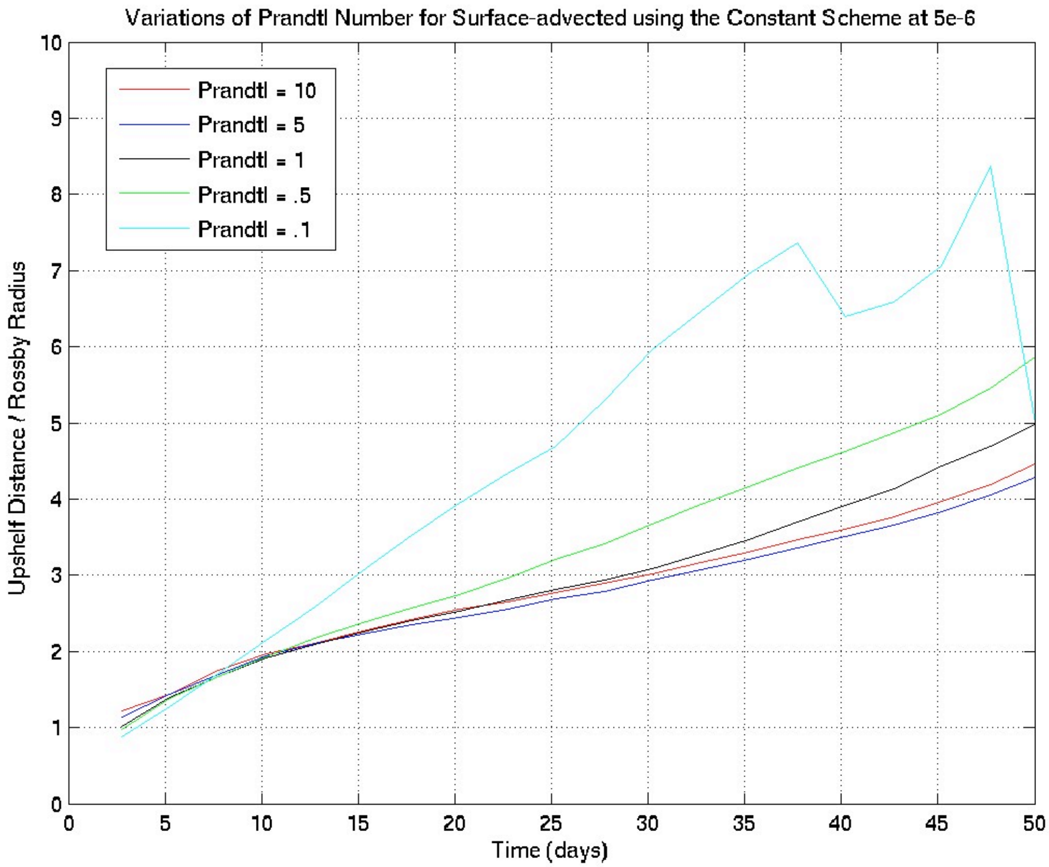

Figure 5.2: This graph shows the changes in the nondimensional upshelf movement with various diffusivity values for the surface-advected plume. The Prandtl number is changed while holding the viscosity value at 5 x 10^{-6} m^2 s^{-1}.

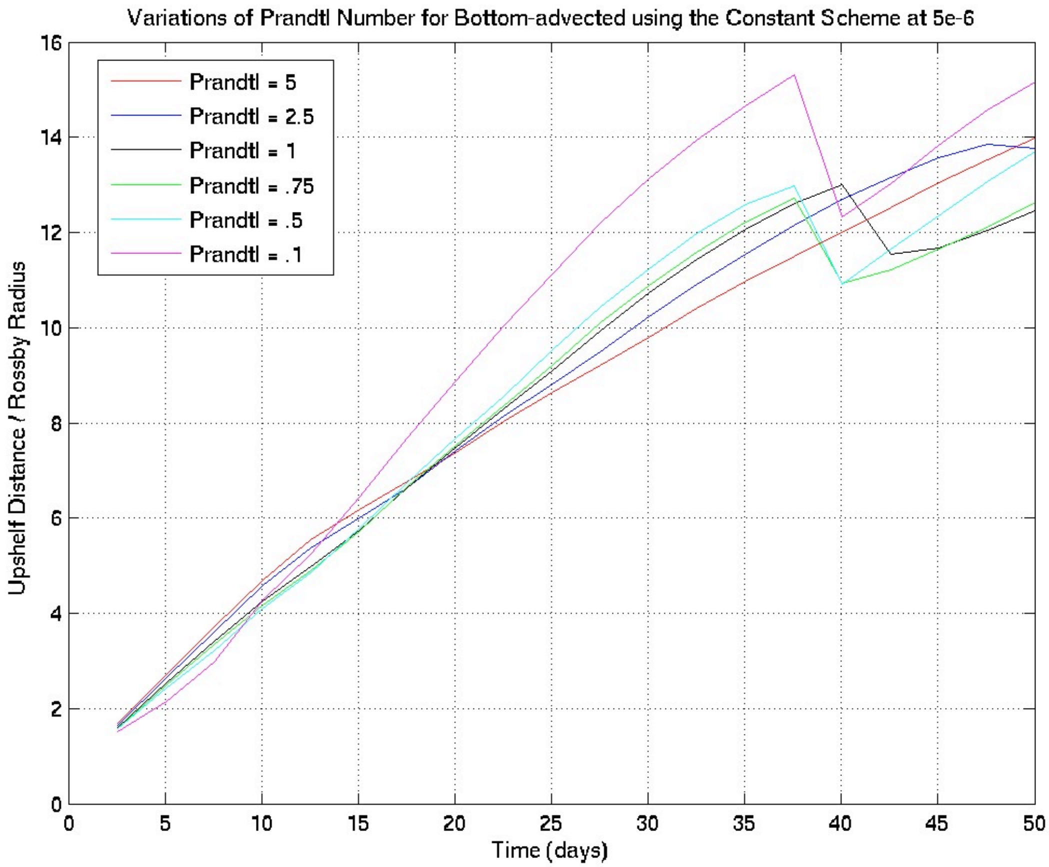

Figure 5.3: This graph shows the changes in the nondimensional upshelf movement with various diffusivity values for the bottom-advected plume. The Prandtl number is changed while holding the viscosity value at 5 x 10^{-6} m^2 s^{-1}.

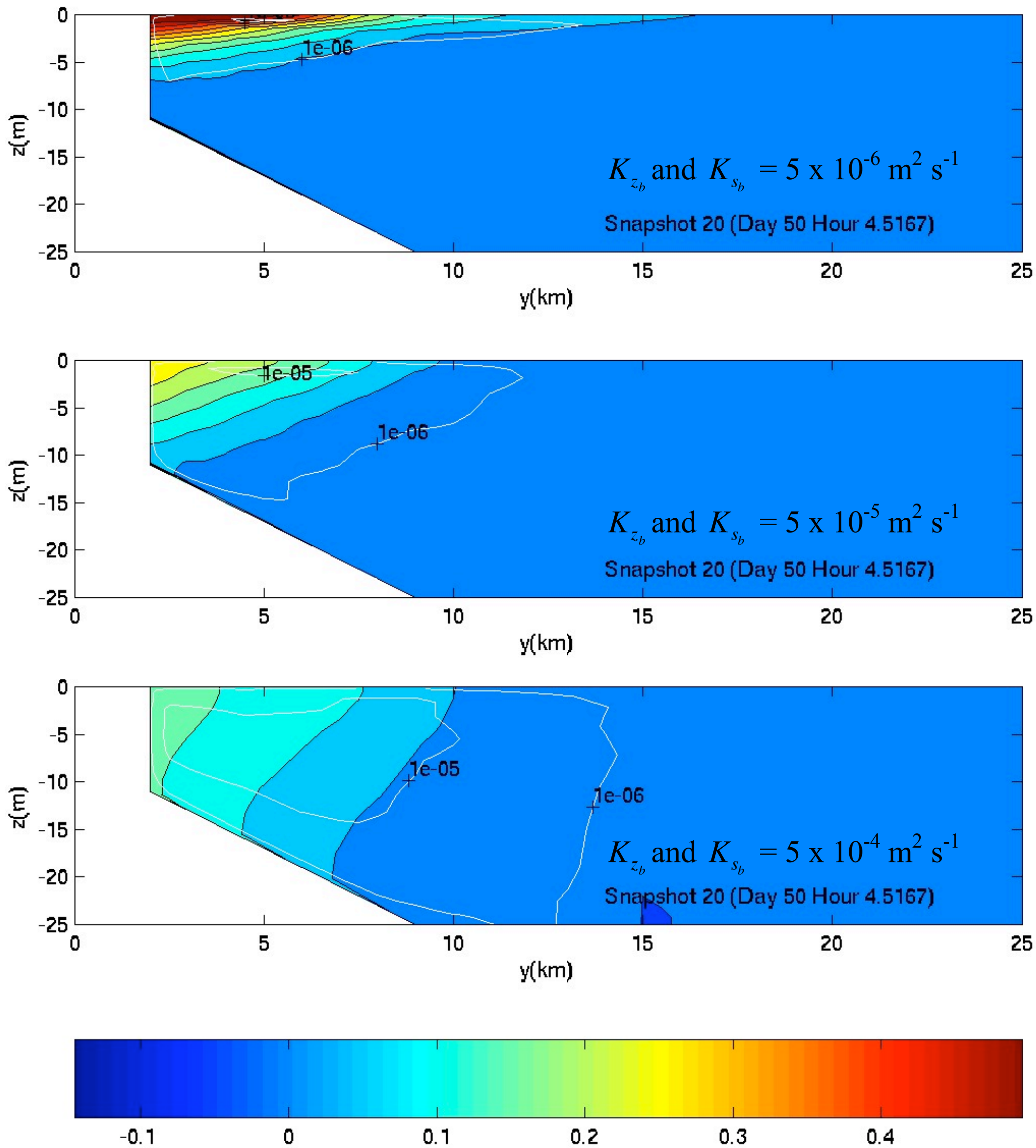

Figure 5.4: Cross-sectional view of the surface-advected plume at 300 km downshelf of inlet for the various K_{z_b} and K_{s_b} magnitudes when using the constant scheme. The salinity anomaly contours (color) and point-to-point vertical salt flux (white contours) are presented in this figure.

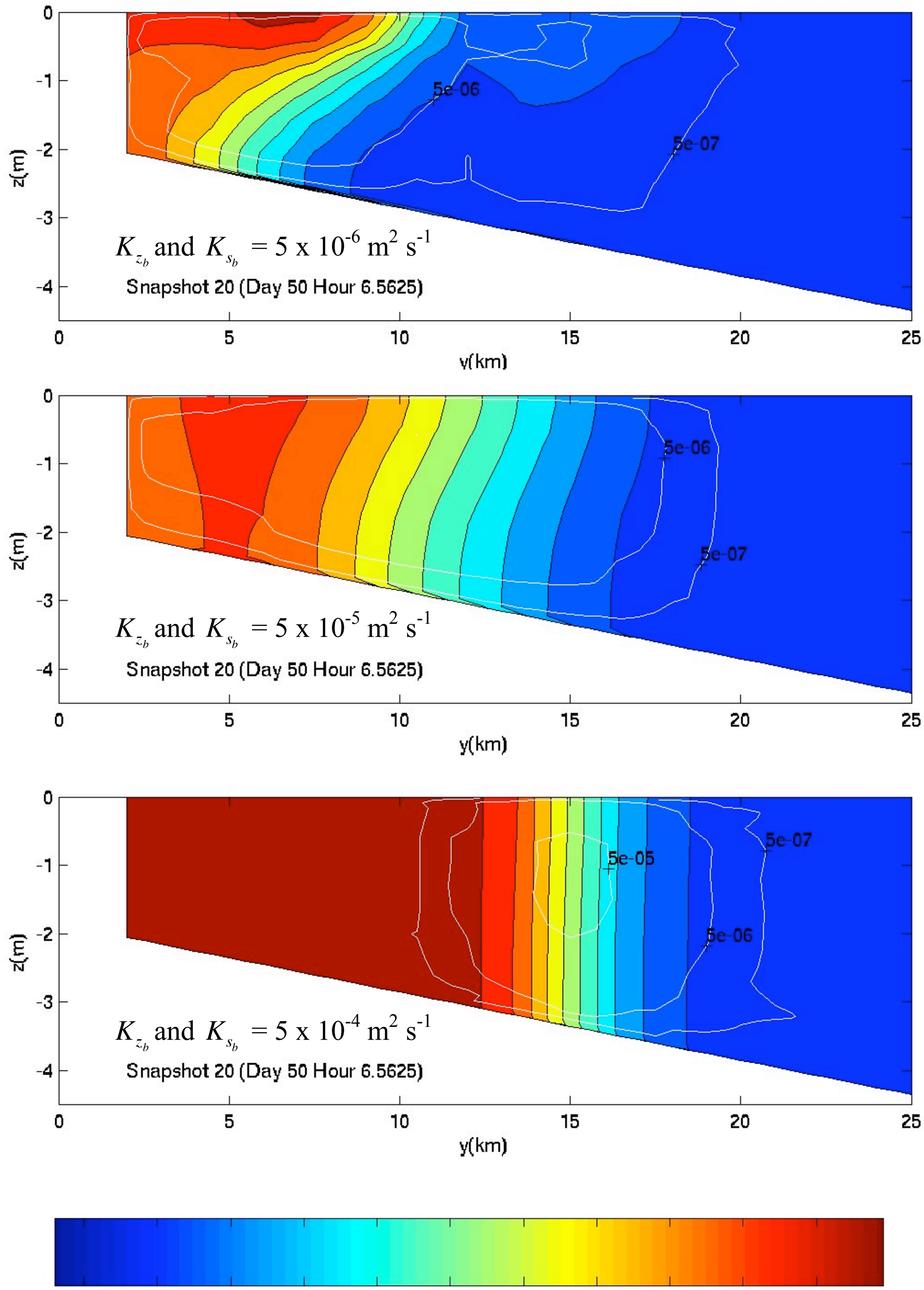

Figure 5.5: Cross-sectional view of the bottom-advected plume at 297 km downshelf of inlet for the various K_{z_b} and K_{s_b} magnitudes when using the constant scheme. The salinity anomaly contours (color) and point-to-point vertical salt flux (m^2 s^{-1}, white contours) are presented in this figure.

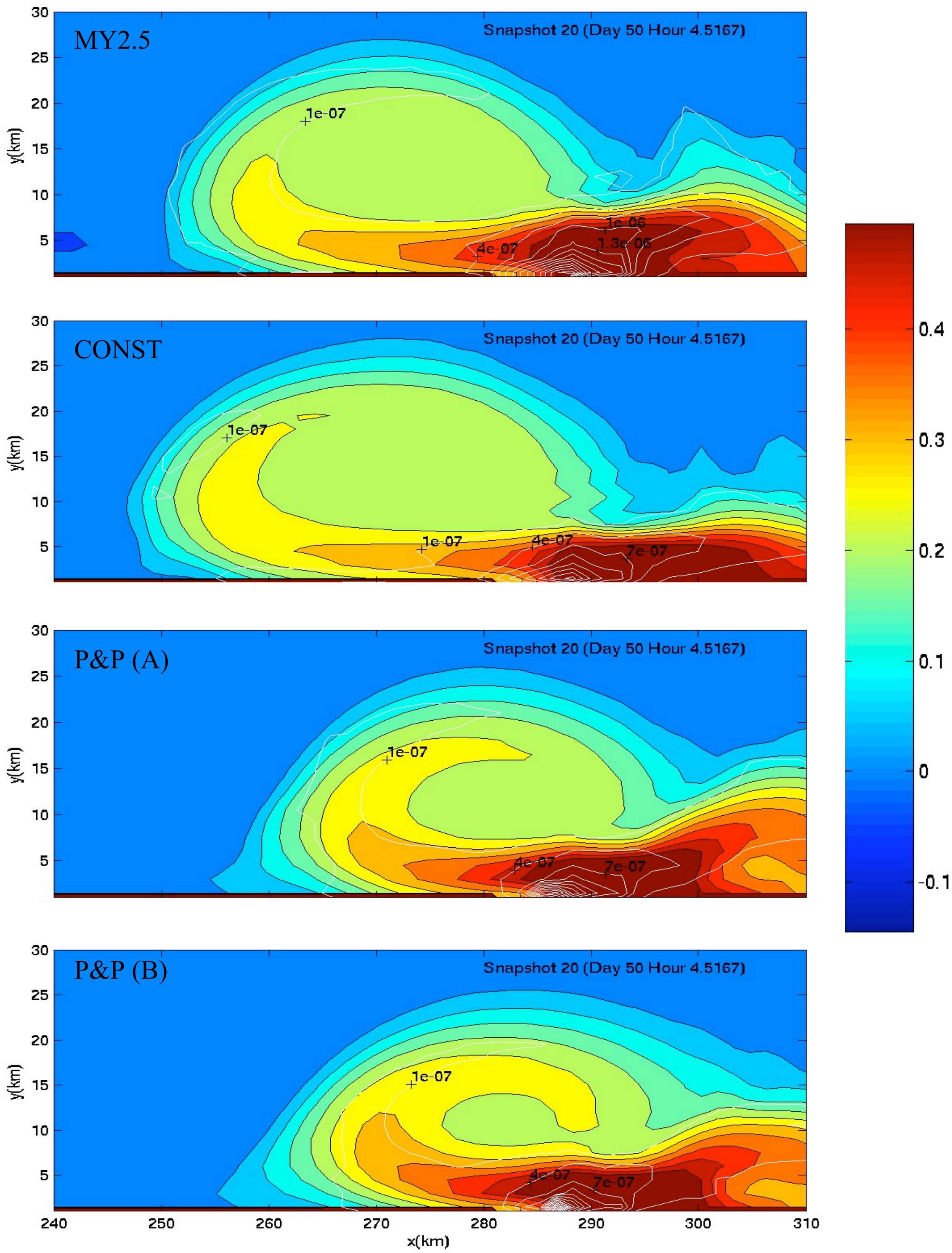

Figure 5.6: The point-to-point vertical salinity salt flux ($m^2\ s^{-1}$, white contours) and salinity anomaly (colored contours) using the first two sigma levels for the surface-advected plume when K_{z_b} and K_{s_b} is set to $5 \times 10^{-6}\ m^2\ s^{-1}$.

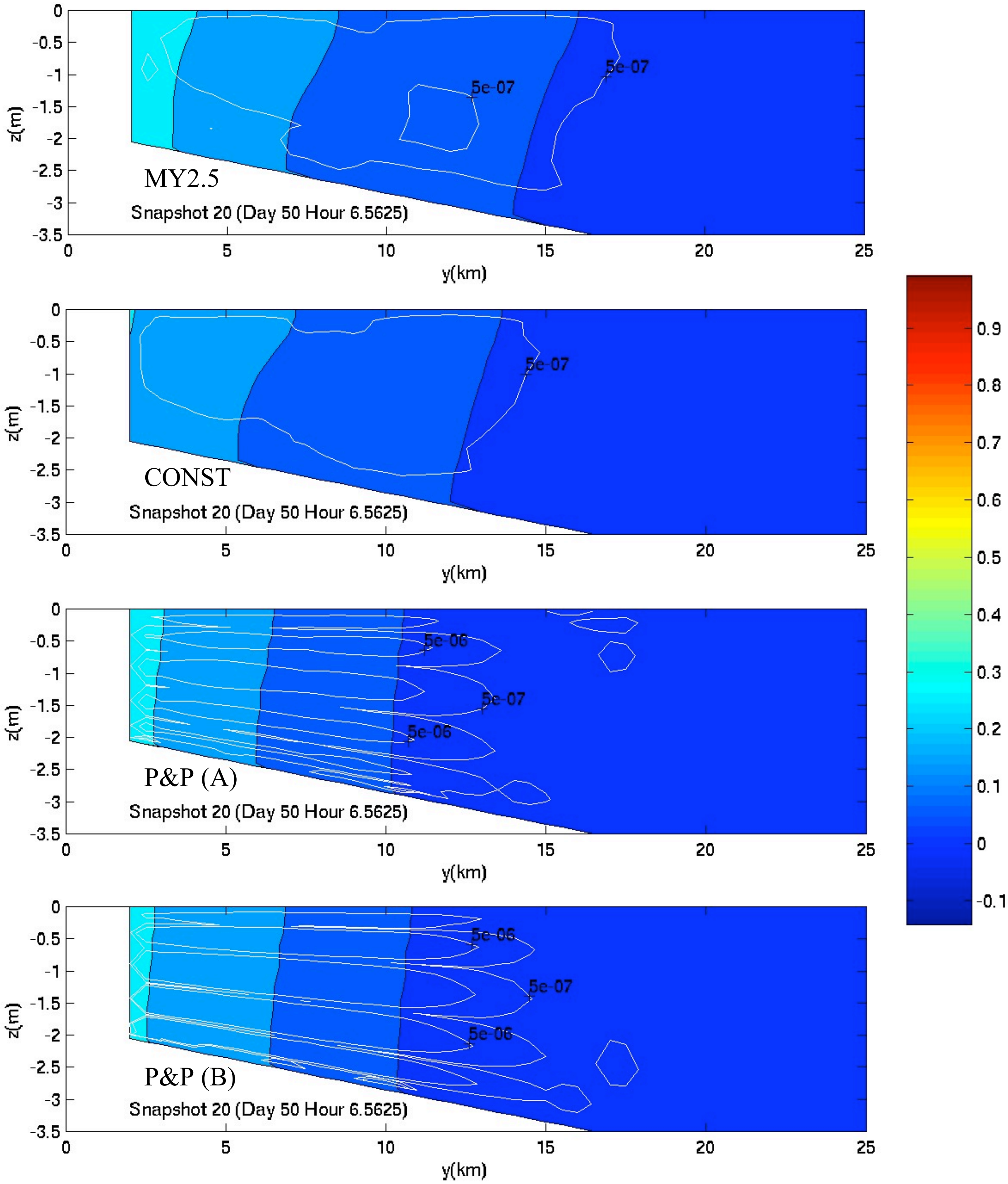

Figure 5.7: The cross-sectional view, at 434 km, of the downshelf nose of the bottom-advected plume using the K_{z_b} and K_{s_b} as 5 x 10^{-6} m^2 s^{-1}. The point-to-point vertical salinity salt flux (m^2 s^{-1}) is contoured in white, and salinity anomaly contoured in color.

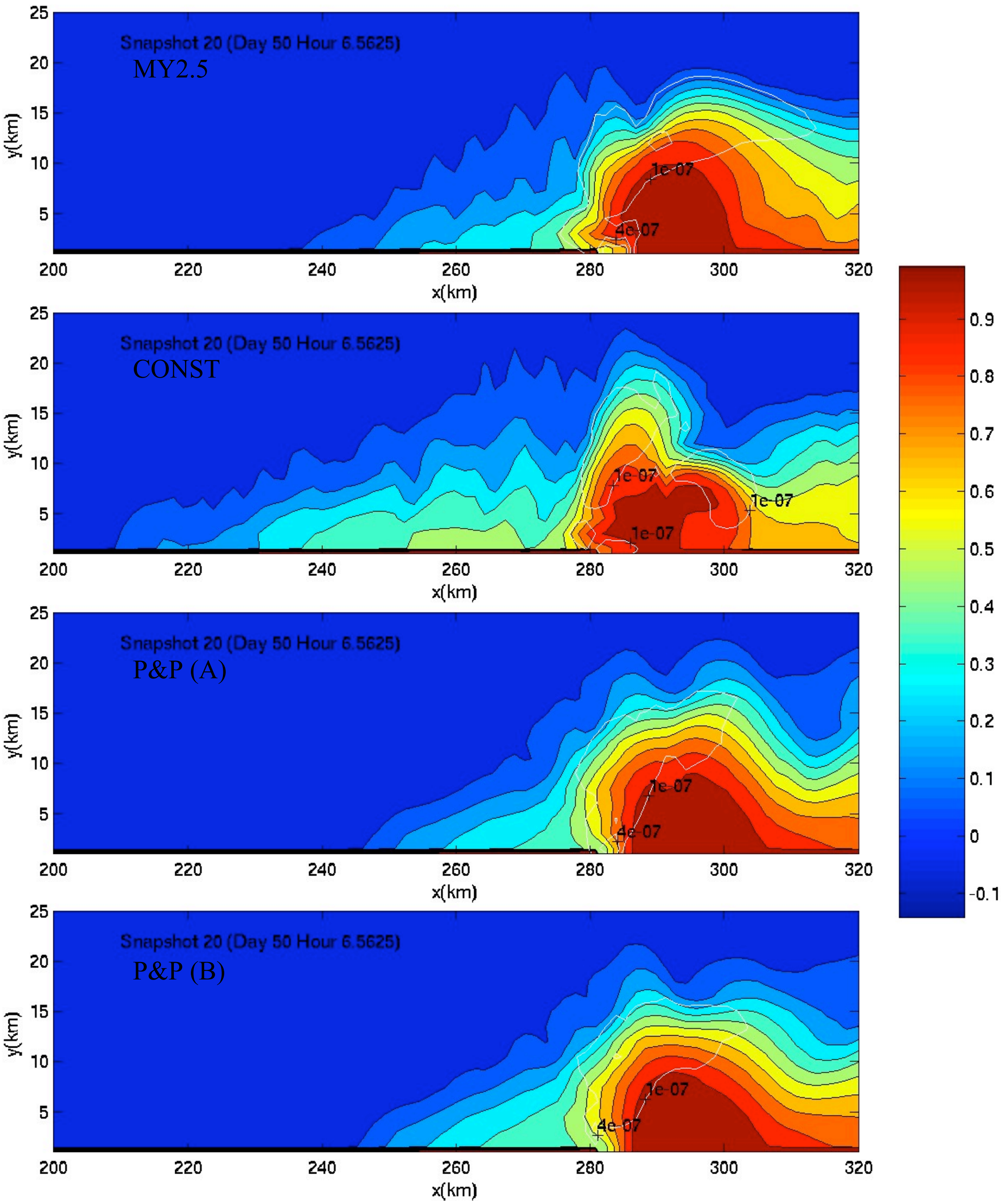

Figure 5.8: The point-to-point vertical salinity salt flux (m^2 s^{-1},white contours) and salinity anomaly (colored contours) using the first two sigma levels for the bottom-advected plume when K_{z_b} and K_{s_b} is set to 5 x 10^{-6} m^2 s^{-1}.

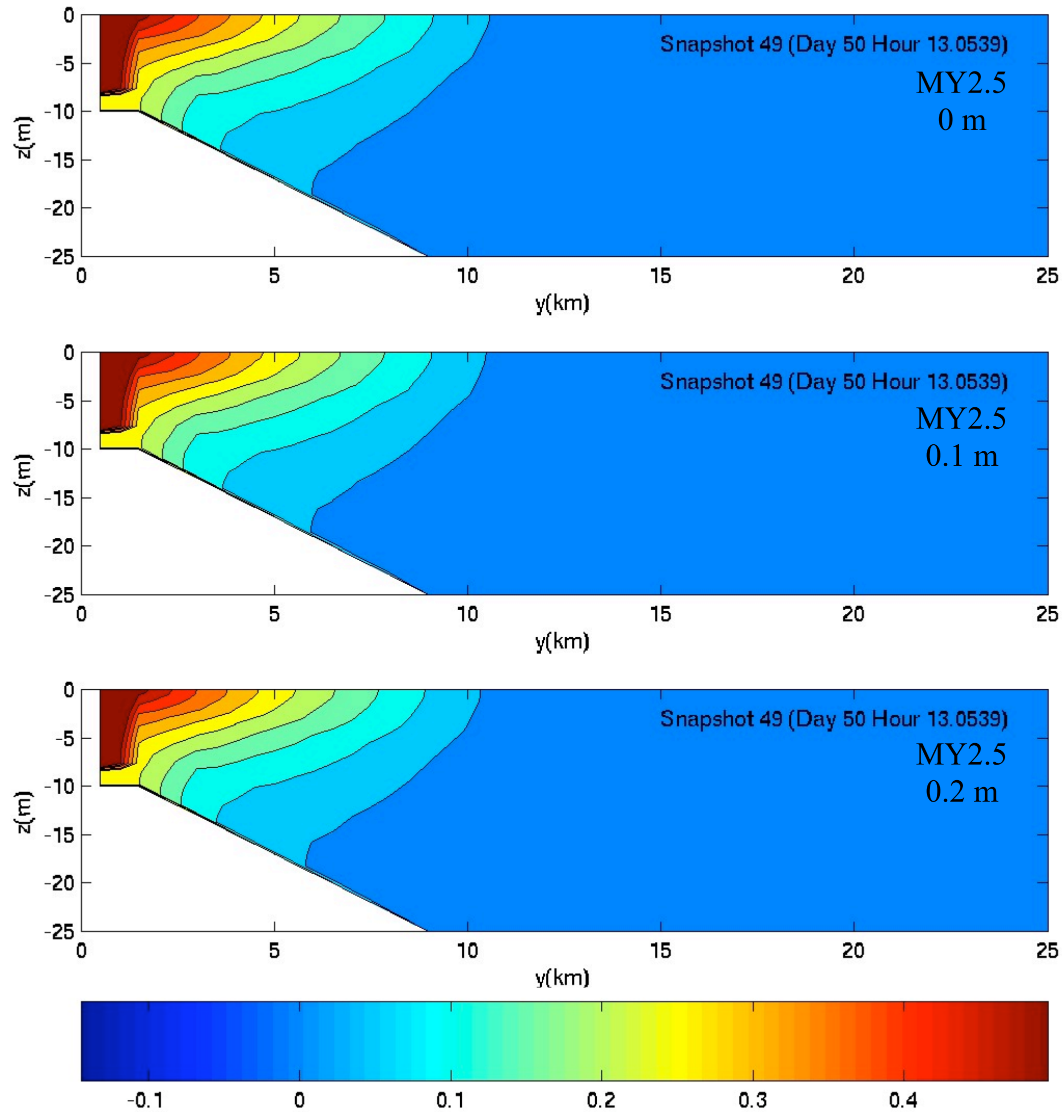

Figure 5.9: The surface-advected plume using MY2.5 for no tides (top), 0.1 m (middle), and 0.2 m (bottom) tidal amplitudes at the freshwater inlet (290 km).

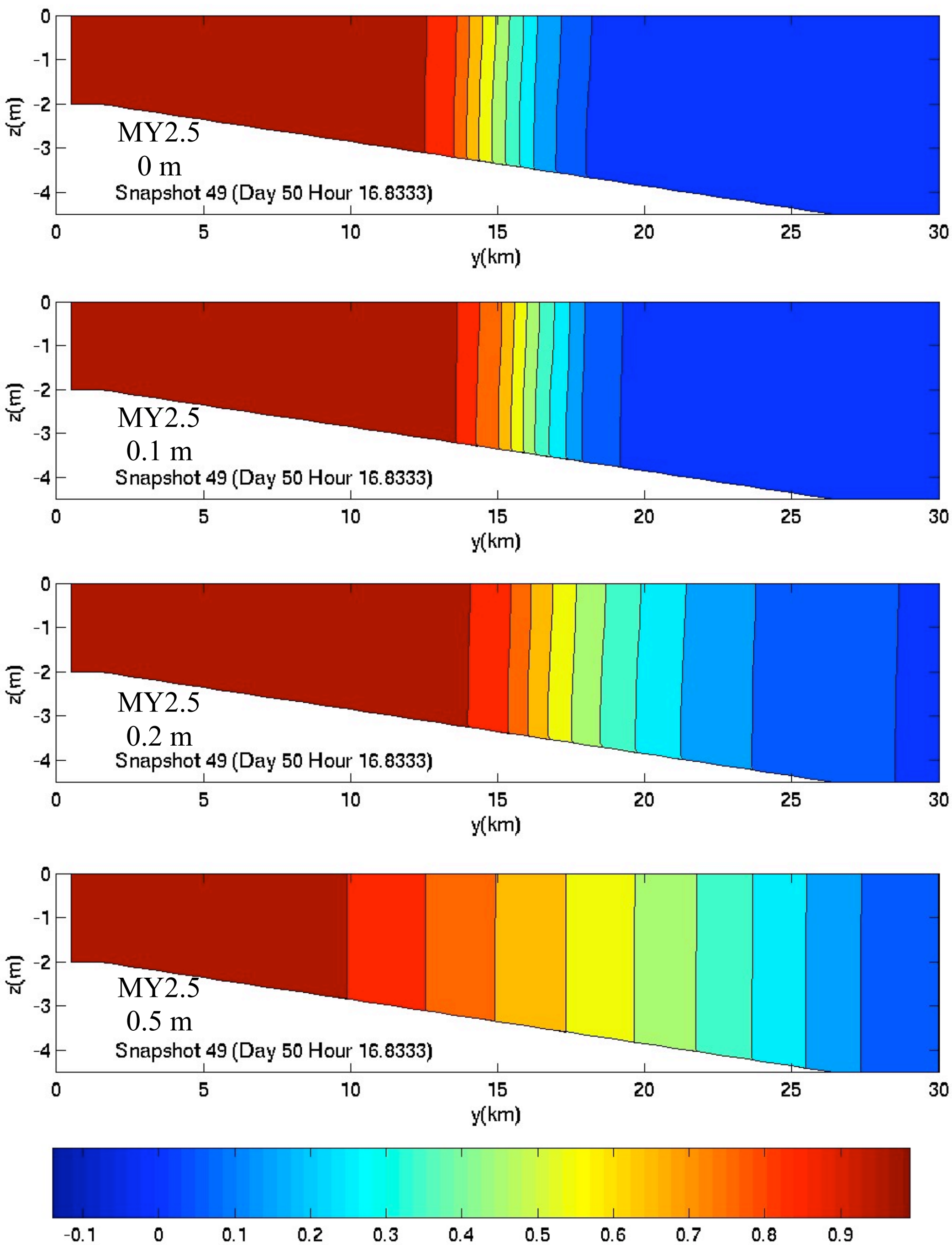

Figure 5.10: The bottom-advected plume using MY2.5 for no tides (top), 0.1 m (second), 0.2 m (third), and 0.5 m (bottom) tidal amplitudes at the freshwater inlet (290 km).

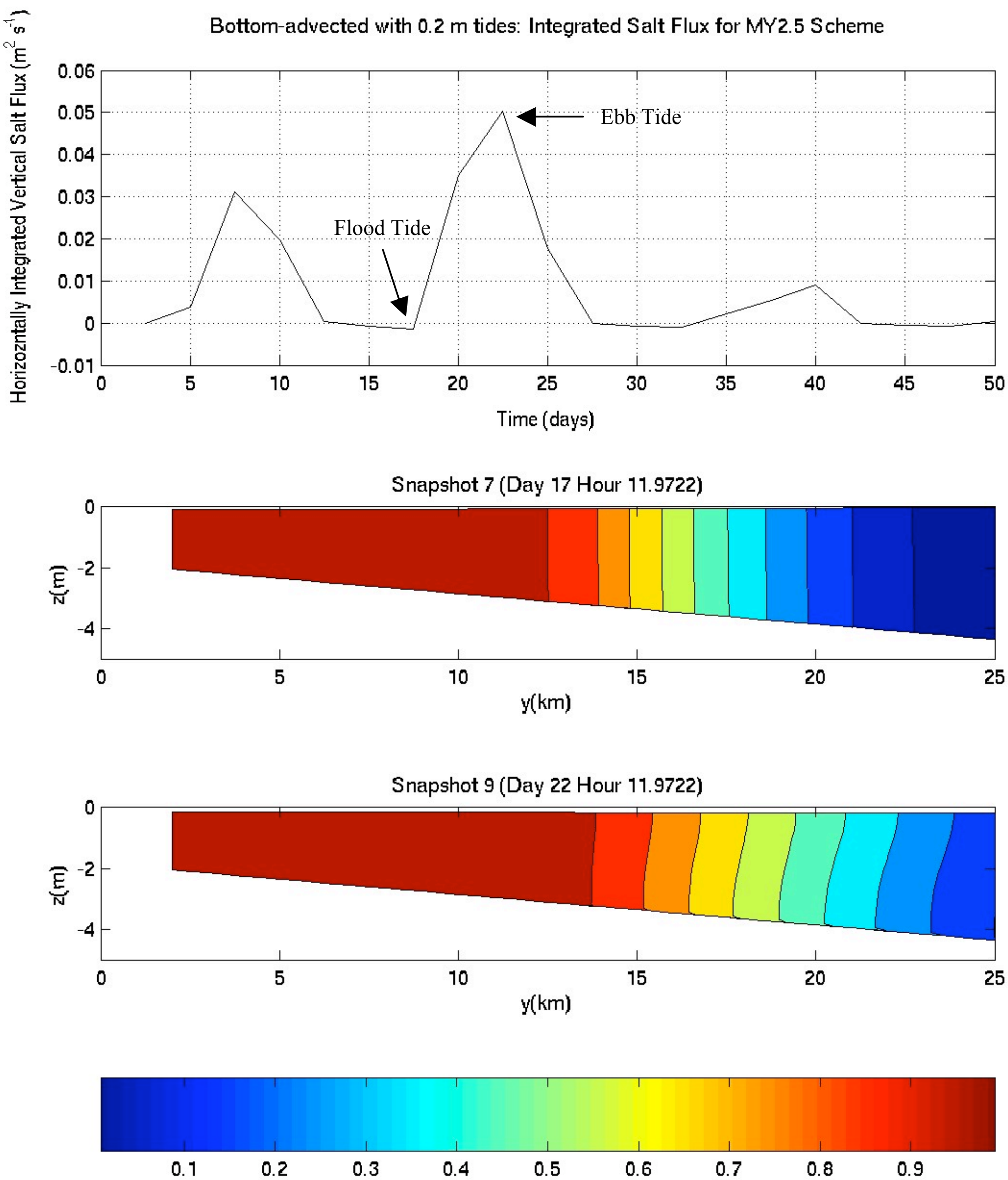

Figure 5.11: The effect of tidal forcing is shown in the integrated vertical salt flux (top), overstraining of the salinity anomaly gradient during flood current (middle), and the return of normal freshwater outflow during ebb current (bottom) for the bottom-advected plume using MY2.5 with 0.2 m tides. Note that these figures are runs with snapshots every ~ 2 days, recording instantaneous data.

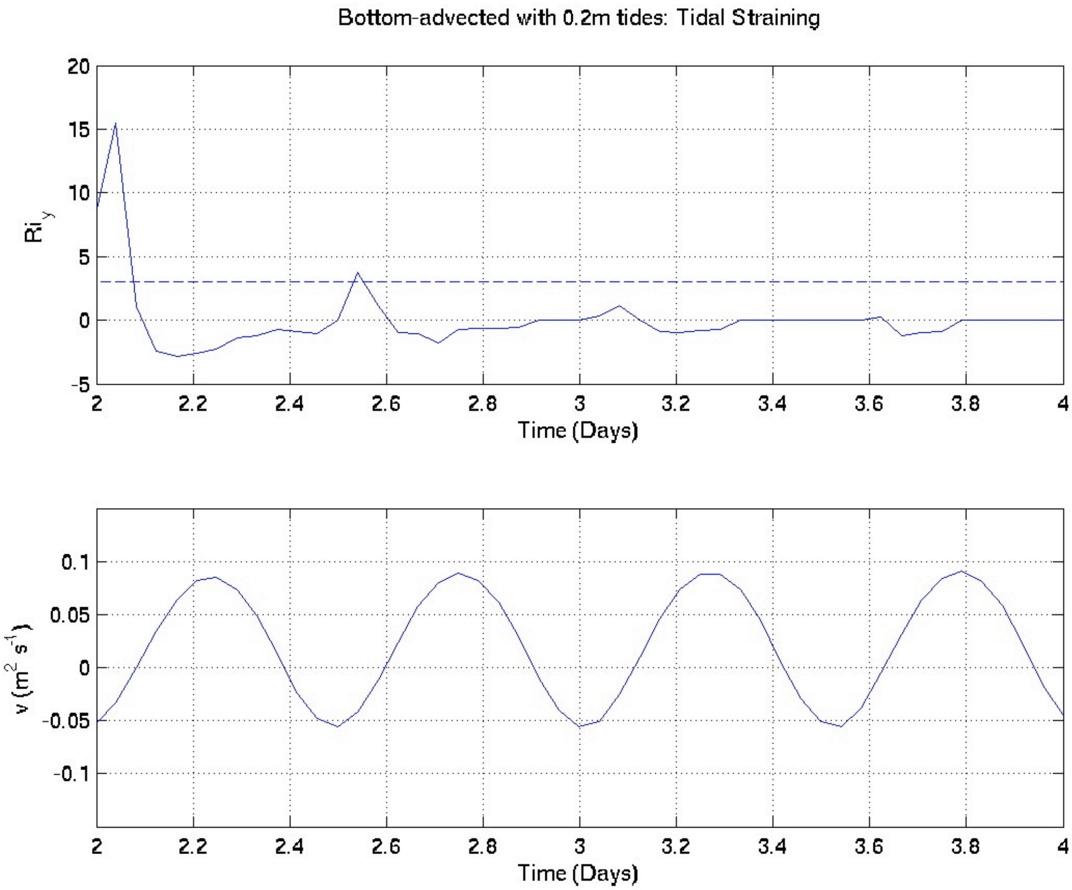

Figure 5.12: The instantaneous hourly horizontal Richardson number (top panel) and *v* velocity (bottom panel) for two days, or four tidal periods, at 290 km downshelf, 2 km across-shelf, and roughly 1 m in depth. The dotted line on the top panel represents the threshold value of 3 on ebb tides, where stratification and shear flow are amplified. Values under the dotted line represents the destratification of the system due to tidal mixing (Stacey et al. 2001).

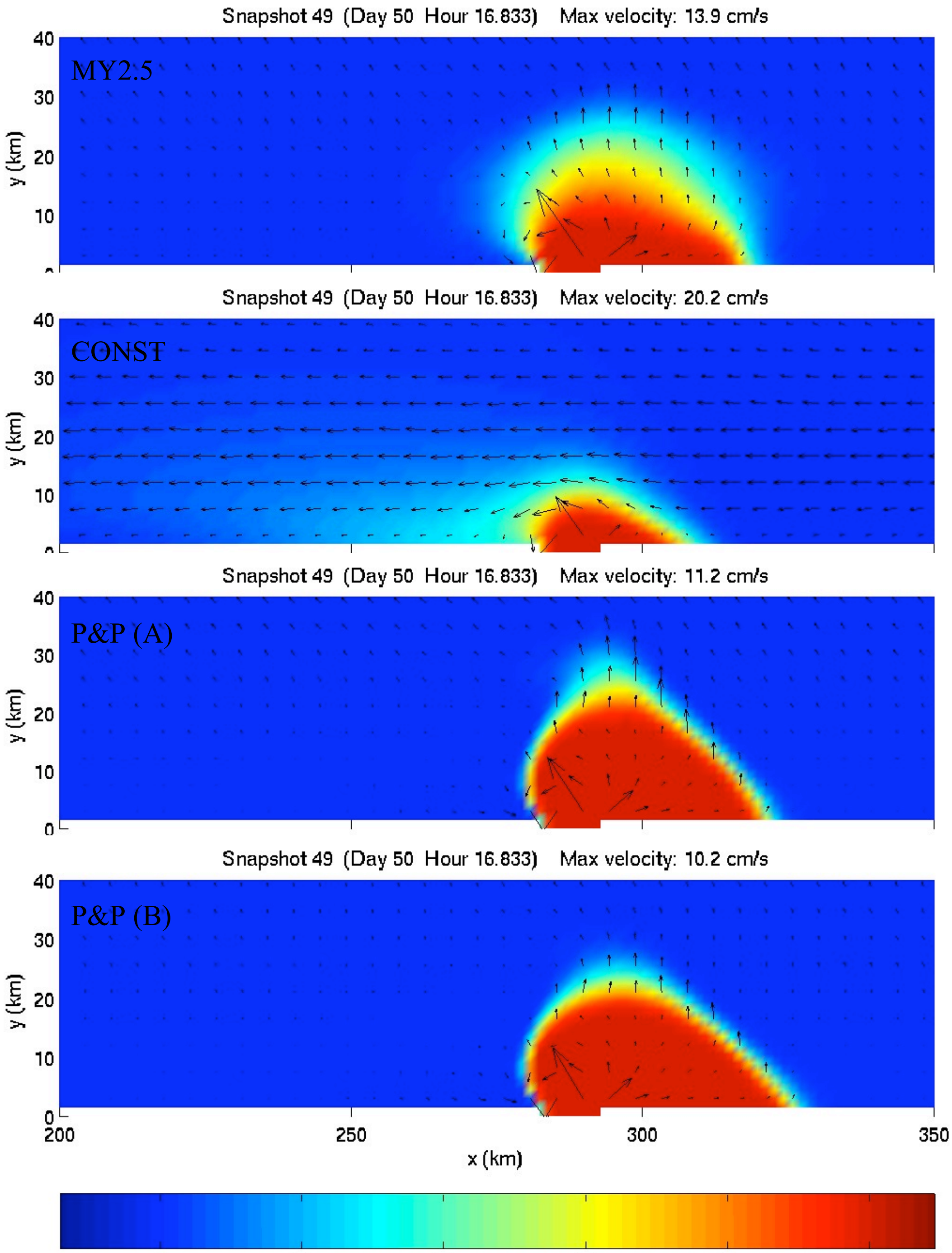

Figure 5.13: Tidally averaged velocity field (black arrows) and salinity anomaly field (shading) for bottom-advected plumes using 0.5 m amplitudes at the surface for all schemes.

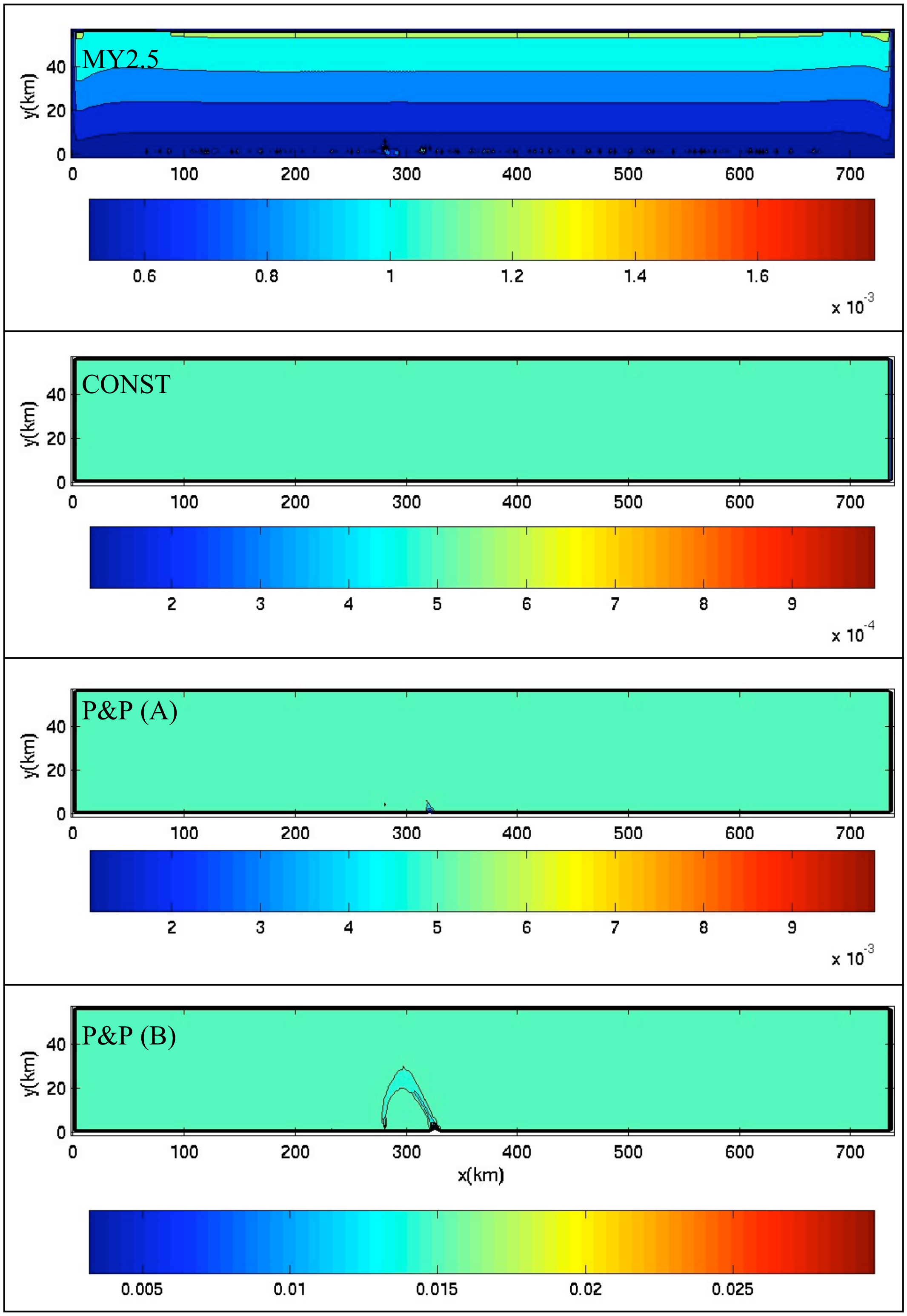

Figure 5.14: The tidally averaged viscosity ($m^2 s^{-1}$) near the bottom (sigma level 14 out of 15) for all schemes at Day 50 when using a tidal amplitude of 0.5 m for the bottom-advected plume.

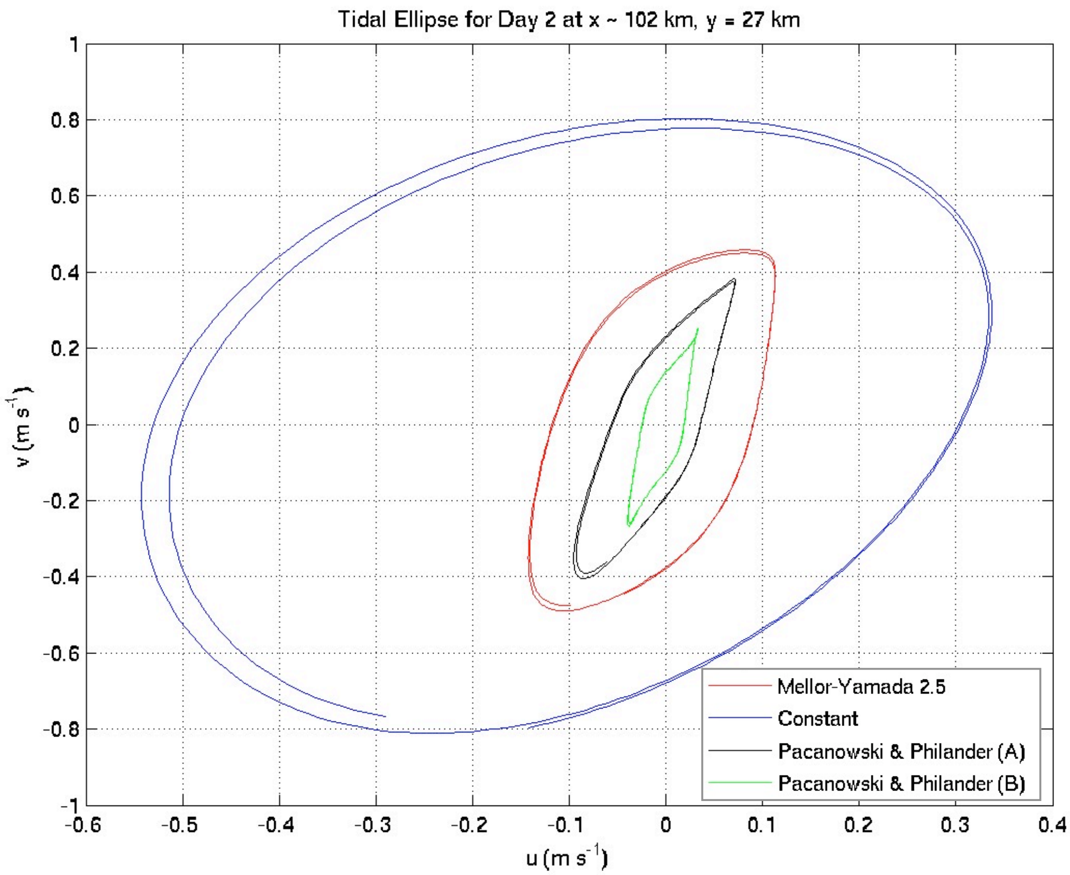

Figure 5.15: The tidal ellipse for the various schemes on Day 2, at 102 km downshelf and 27 km across-shelf, for the bottom-advected plume using a tidal amplitude of 0.5 m. The velocity points were recorded instantaneously with time (one day; a complete semi-diurnal cycle).

CHAPTER 6

CONCLUSIONS/FUTURE WORK

6.1 Conclusions

The sensitivity of an idealized coastal environment to three vertical mixing schemes, the constant scheme, Mellor-Yamada Level 2.5, and the Pacanowski and Philander scheme, was investigated first, using various background viscosity/diffusivity magnitudes with only buoyancy forcing and then, using a set background viscosity/diffusivity magnitude with the same buoyancy forcing and various tidal amplitudes.

The schemes were compared using specified dimensional parameters, the downshelf, upshelf, and across-shelf distances, the depth, and the integrated horizontal and vertical salt fluxes. The growth of the plume is intimately related to the efficiency of mixing, where the plume continually grows through time with constant freshwater discharge, and the edge of the plume is simultaneously mixed into the ambient ocean. Along the edges, the mixing is dominated by vertical shear, where vertical gradients of horizontal velocity are the strongest; this region of higher mixing has also been observed in previous research (Wright and Coleman 1971, Hetland 2005, and Tilburg et al. 2007). Therefore, the metrics were analyzed on the plume edge.

6.1.1 Timestep sensitivity analysis

Although changes in timestep were not present among the runs for each of the plumes, a timestep sensitivity analysis was performed on the model. These tests showed that changes among the mixing schemes had a larger effect on the plumes than changes in model timestep.

6.1.2 Buoyancy forcing

This investigation showed that higher vertical background viscosity/diffusivity increased the mixing of the coastal plumes and thus, decreased the vertical stratification while increasing the influence of bottom friction. At a magnitude of 5 x 10^{-4} m^2 s^{-1}, all the schemes resulted in the same plume for surface-advected plumes and similar plumes for the bottom-advected plumes, as shown by the metrics. Larger background viscosities/diffusivities, 5 x 10^{-5} m^2 s^{-1} and higher, dominated the total viscosity/diffusivity coefficients, creating similar values used for each scheme. This result was consistent with the Mellor-Yamada 2.5 study by Li et al. (2005). Therefore, the importance of scheme choice with higher background magnitudes decreased. When using a background magnitude of 5 x 10^{-6} m^2 s^{-1}, however, larger differences were found among the schemes for the metrics and so, the importance in selecting the vertical mixing scheme increased.

6.1.3 Tidal forcing

The influence of tidal forcing on the plumes depended on the full presence of bottom friction. To initiate frictional influences, a background vertical viscosity/diffusivity of 5 x 10^{-4} m^2 s^{-1} was used for both plumes to simulate tides. In addition, using a background of 5 x 10^{-6} m^2 s^{-1} was not possible in ECOM3d due to larger velocities from tides breaking the CFL criterion. Therefore, for future studies, this should be further investigated.

Surface-advected plumes resulted in the same plume with no tides and with tidal amplitudes of 0.1 and 0.2 m, where the freshest water was free from bottom influence, so tidal forcing did not alter the plumes. Therefore, no differentiation existed among the schemes for the surface-advected plumes with tides. For the bottom-advected plumes, large tidal effects were shown by the presence of tidal straining. The plumes interacted heavily with the bottom, subjecting the plumes to tidally induced shear and mixing. As a result, changes in plume shape with variations in tidal amplitude were shown. The buoyancy forcing, tidal forcing, and velocity field controlled the plume shape, where at higher tidal amplitudes, tidal forcing was more influential and determined the resulting plume shape. Therefore, differences among the schemes increased with increasing tidal amplitudes and vertical mixing, indicating that the choice of scheme is more important with larger tidal amplitudes and higher mixing for the bottom-advected plumes.

6.1.4 Overall mixing scheme conclusions

For both buoyancy and tidal forcing, certain schemes typically had the highest or lowest individual metric; these findings may be applied to future research when choosing the mixing scheme based on the type of plume and forcings present. Note that from this point onwards, the tidal forcing results only apply to the bottom-advected plumes since the surface-advected plumes showed no difference from tidal forcing.

The constant scheme had the tendency to create the largest upshelf movement, more integrated horizontal salt flux, and less integrated vertical salt flux for both forcings. This scheme used the user specified background vertical viscosity/diffusivity as the mixing coefficients in the model, so compared to the other schemes, the constant scheme produced the least viscosity/diffusivity and the least mixing. Therefore, larger upshelf propagation and lower vertical salt flux resulted, where more vertical mixing leads to a decrease in the horizontal salinity gradient and decrease in horizontal salt flux. With lower vertical salt flux and a stronger horizontal salinity gradient, the constant scheme also resulted with higher horizontal salt flux.

Although the constant scheme is extremely simple in implementation and analysis, it overall performed reasonably against the other, more complicated schemes. In addition, the scheme typically had the shortest computational run time. Therefore, if computational resources and time were limited, the constant scheme would be acceptable for use. However, the main concern for the constant scheme was the larger numerical upshelf propagation created. If the model were to use large diffusivity or small viscosity, the constant scheme would be unsuitable in that the numerical upshelf behavior would increase; this was shown clearly in the results of this investigation as well as in previous research (Yankovsky 2000 and Garvine 2001). In addition, the scheme does not realistically account for large variations in stratification, present in coastal regions. Therefore, one would need to be careful when using the scheme in these situations.

The Pacanowski and Philander schemes typically developed plumes with larger across-shelf and depth reach as well as larger integrated vertical salt flux. Larger total viscosity/diffusivity values were frequently calculated from smaller Richardson numbers with higher vertical shear. The higher viscosity/diffusivity coefficients from the scheme directly resulted in larger vertical mixing, leading to larger changes in across-shelf, depth and integrated vertical salt flux compared to the other schemes. Even with changes in the null viscosity, the Pacanowski and Philander plumes had greater similarity with different null viscosities compared to the Mellor-Yamada and constant schemes. This scheme proved to be different from the other schemes, and sometimes even different against variations in the null viscosity. Although the study used null viscosities recommended by the authors (Pacanowski and Philander 1981), testing the changes created from various null viscosities would be beneficial before using the scheme to model the coastal plume.

The Pacanowski and Philander is useful for investigations focusing on the shear and buoyancy of coastal plumes in that it is a simple empirical method based on the Richardson number to approximate the vertical mixing coefficients. In addition, the scheme has a straight-forward implementation, is simpler in analysis, and has a shorter run time than Mellor-Yamada 2.5. However, as shown in this study, there is the potential for this scheme to create large viscosity/diffusivity coefficient values when the Richardson number is very small, so there could be a possibility of overestimating the vertical shear and vertical mixing present. However, this can only be verified by comparing the scheme's plume to observations. In addition, in areas of no stratification with vertical shear, such as when tidal forcing is present, the scheme uses the null viscosity as the viscosity mixing coefficient; areas with stratification are calculated using the empirical equations. Thus, the interaction between areas with no stratification and areas with stratification may then be inaccurate.

The most complex scheme, the Mellor-Yamada Level 2.5 scheme, resulted in plumes with the parameters lying between the other schemes for buoyancy forcing only. Therefore, with lesser background viscosity/diffusivity, the Mellor-Yamada scheme seems to be a good 'middle of the road' scheme, which would support its frequent use in coastal plume investigations. As mentioned in previous chapters, the Mellor-Yamada Level 2.5 scheme uses only the constant scheme in areas with a high Richardson number, but in areas with a low Richardson number, the mixing coefficient is first calculated with a series of equations and then added onto the user specified background viscosity/diffusivity value. In this study, the Mellor-Yamada scheme usually resulted in a plume more similar to the constant scheme than the Pacanowski and Philander schemes. Therefore, the constant scheme would be a good replacement if the Mellor-Yamada was unavailable for simulations with only buoyancy forcing, or there is limited runtime and computational resources. However, the constant scheme is only a good replacement if the vertical mixing is not the study's primary focus due to its tendency of creating the numerical upshelf growth as well as its limitations in using a constant coefficient in areas of large shear.

The addition of tidal forcing and more mixing allowed for Mellor-Yamada Level 2.5 to produce higher across-shelf extents and vertical salt flux, and the plume became individualistic with increased tidal amplitude for the bottom-advected plume. Since this scheme bases viscosity/diffusivity calculations on a large number of equations and assumptions, it would be expected that larger changes in the plume would occur with larger mixing available and the input of tidal waves. However, due to the complexity of its calculation, the analysis of the scheme is quite complicated, and the scheme uses longer computational and run time. While Mellor-Yamada Level 2.5 is more realistic than the other two schemes, drawbacks still exist.

Therefore, depending on the coastal scenario, certain schemes are much more suitable than others. These ideas may be applied in future research when determining the specific mixing scheme for use. Because larvae, nutrients, and pollutants are dependent on the movement and behavior of the coastal current system, knowing the tendency for certain schemes to produce larger mixing coefficients and possibly larger mixing into the ambient ocean would be important for modeling the transport of these materials. Therefore, choosing the appropriate vertical mixing parameterization in the model would greatly impact the modeled material dispersion into the ocean.

6.2 Future work

The results were analyzed specifically to determine how variations in the magnitude of viscosity/diffusivity cause differences among the three mixing schemes. Since a large amount of model output was produced from this study, the model data could also be analyzed with a different focus as well. Tracking the flow of potential energy and kinetic energy and then, comparing the energy flow across mixing schemes would be an appropriate direction for this investigation. Because of the close relationship between energy and mixing, this type of study would be beneficial in determining the prime areas of mixing and the strength of mixing. It could have the potential to add great support to this study's conclusions. In addition, by showing the energy structure of the plumes, more of the dynamics associated with different types of plumes could be further investigated.

Further investigating the vertical and horizontal salt fluxes would also be beneficial. The method in which these two metrics were calculated was useful for this study, however, some of the results were influenced by other factors in the plume, causing difficulty in interpretation. Therefore, additional salt flux calculations, such as bulk salt flux calculations, could either support or refute these results.

As shown in Figures 3.18 and 3.29, while the plumes using different mixing schemes all appear to be the same, the across-shelf diffusivity varied in the ambient ocean. Therefore, it would be interesting to examine the circulation structures that the different mixing schemes create in their simulations and how changes in viscosity/diffusivity magnitudes affect these structures.

A potential area of future work is to further investigate the affect of changing the null viscosity for the Pacanowski and Philander scheme. As this study showed, the two null viscosities used had the potential to differ greatly. Therefore focusing on the structure of the plume while comparing more than two null viscosities would help improve on the usage of the Pacanowski and Philander scheme.

Comparing this study's results to observations of various surface-advected and bottom-advected systems would be the most beneficial direction of investigation. While an idealized model is appropriate to generalize trends in modeling, comparing the results to observed coastal systems would help to improve on the overall modeling and mixing of the plumes.

REFERENCES

Avicola, G., and P. Huq (2002). "Scaling analysis for the interaction between a buoyant coastal current and the continental shelf: Experiments and observations." J. Phys. Oceanogr. **32**: 3233 - 3248.

Battisti, D. S., and A.J. Clarke (1982). "A Simple Method for Estimating Barotropic Tidal Currents on Continental Margins with Specific Applicastion to the M2 Tide off the Atlantic and Pacific Coasts of the United States." J. Phys. Oceanogr. **12**: 8 - 16.

Beardsley, R. C., R. Limeburner, H. Yu, and G.A. Cannon (1985). "Discharge of the Changjiang (Yangtze River) into the East China Sea." Cont. Shelf Res. **4**: 57 - 76.

Blumberg, A. F. (1995). A Primer for ECOM. New Jersey, HydroQual, Inc.**:** 1 - 84.

Burchard, H., and O. Petersen (1999). "Models of turbulence in the marine environment - a comparative study of two-equation turbulence models." J. Mar. Syst. **21**: 29 - 53.

Burchard, H., O. Petersen, and T.P. Rippeth (1998). "Comparing the performance of the Mellor-Yamada and the k-_ two-equation turbulence models." J. Geophys. Res. **103**(C5): 10,543 - 10,554.

Chapman, D. C. (1985). "Numerical treatment of cross-shelf open boundaries in a barotropic coastal ocean model." J. Phys. Oceanogr. **15**: 1060 - 1075.

Chapman, D. C., and S.J. Lentz (1994). "Trapping of a coastal density front by the bottom boundary layer." J. Phys. Oceanogr. **24**: 1464 - 1479.

Chapman, D. C. (2002). "Sensitivity of a model shelfbreak front to the parameterization of vertical mixing." J. Phys. Oceanogr. **32**: 3291 - 3298.

Childs, C. R., N.N. Rabalais, R.E. Turner, and L.M. Proctor (2002). "Sediment denitrification in the Gulf of Mexico zone of hypoxia." Mar. Ecol. Prog. Ser. **240**: 285 - 290.

Colling, A. (2001). Ocean Circulation. Milton Keynes, England, Butterworth/Heinemann with The Open University.

Courant, R., K. Friedrichs, and H. Lewy (1967). "On the Partial Difference Equations of Mathematical Physics." IBM Journal(March 1967): 215 - 234.

Cushman-Roisin, B. (1994). Introduction to Geophysical Fluid Dynamics. Englewood Cliffs, New Jersey, Prentice Hall.

Davies, A. M. a. J. X. (1999). "Sensitivity of Plume Dynamics to the Parameterization of Vertical Mixing." *International Journal for Numerical Methods in Fluids* **30**: 357 - 405.

Durski, S. M., S.M. Glenn, and D.B. Haidvogel (2004). "Vertical mixing schemes in the coastal ocean: Comparison of the level 2.5 Mellor-Yamada scheme with an enhanced version of the K profile parameterization." *J. Geophys. Res.* **109**(C01015): doi:10.1029/2002JC001702.

Dyer, K. R. (1997). Estuaries: A Physical Introduction. Chichester, John Wiley & Sons.

Epifanio, C. E., and R.W. Garvine (2001). "Larval transport on the Atlantic Continental Shelf of North America: A review." *Estua., Coast., and Shelf Sci.* **52**: 51 - 77.

Ferber, D. (2001). "Keeping the Stygian Waters at Bay." *Science* **291**(*Feb. 9*): 968 - 973.

Fong, D. A., and W.R. Geyer (2001). "Response of a river plume during an upwelling favorable wind event." *J. Geophys. Res.* **106**(C1): 1067 - 1084.

Fong, D. A., and W.R. Geyer (2002). "The alongshore transport of freshwater in a surface-trapped river plume." *J. Phys. Oceanogr.* **32**: 957 - 972.

Galperin, B., L.H. Kantha, S. Hassid, and A. Rosati (1988). "A quasi-equilibrium turbulent energy model for geophysical flows." *J. Atmos. Sci.* **45**(1): 55 - 62.

Garvine, R. W. (1995). "A dynamical system for classifying buoyant coastal discharges." *Cont. Shelf Res.* **15**(13): 1585 - 1596.

Garvine, R. W. (1999). "Penetration of buoyant coastal discharge onto the continental shelf: A numerical model experiment." *J. Phys. Oceanogr.* **29**: 1892 - 1909.

Garvine, R. W. (2001). "The impact of model configuration in studies of buoyant coastal discharge." *J. Mar. Res.* **59**: 193 - 225.

Griffiths, R. W., and E.J. Hopfinger (1983). "Gravity currents moving along a lateral boundary in a rotating fluid." *J. Fluid Mech.* **134**: 357 - 399.

Guo, X., and A. Valle-Levinson (2007). "Tidal effects on estuarine circulation and outflow plume in the Chesapeake Bay." *Cont. Shelf Res.* **27**: 20 - 42.

Harms, I. H., M.J. Karcher, and D. Dethleff (2000). "Modelling Siberian river runoff - implications for contaminant transport in the Arctic Ocean." *J. Mar. Syst.* **27**: 95 - 115.

Hetland, R. D. (2005). "Relating River Plume Structure to Vertical Mixing." *J. Phys. Oceanogr.* **35**: 1667 - 1688.

Houghton, R. W., C.E. Tilburg, R.W. Garvine, and A. Fong (2004). "Delaware River plume response to a strong upwelling-favorable wind event." Geophys. Res. Lett. **31**(L07302): doi:10.1029/2003GL018988.

Isobe, A. (2005). "Ballooning of river-plume bulge and it's stabilization by tidal currents." J. Phys. Oceanogr. **35**: 2337 - 2351.

Jones, J. H. (1973). "Vertical mixing in the Equatorial Undercurrent." J. Phys. Oceanogr. **3**: 286 - 296.

Kantha, L. H., and C.A. Clayson (2000). Numerical Models of Oceans and Oceanic Processes. San Diego, Academic Press.

Kourafalou, V. H., L.Y. Oey, J.D. Wang, and T.N. Lee (1996a). "The fate of river discharge on the continental shelf: 1. Modeling the river plume and the inner shelf coastal current." J. Geophys. Res. **101**(C2): 3415 - 3434.

Large, W. G., and P.R. Gent (1999). "Validation of vertical mixing in an Equatorial Ocean Model using Large Eddy Simulations and observations." J. Phys. Oceanogr. **29**: 449 - 464.

Large, W. G., J.C. McWilliams, and S.C. Doney (1994). "Oceanic vertical mixing: A review and a model with a nonlocal boundary layer parameterization." Reviews of Geophysics **32**(4): 363 - 403.

Li, M., L. Zhong, and W.C. Boicourt (2005). "Simulations of Chesapeake Bay estuary: Sensitivity to turbulence mixing parameterizations and comparison with observations." J. Geophys. Res. **110**(C12004): doi:10.1029/2004JC002585.

Libes, S. M. (1992). An Introduction to Marine Biogeochemistry, John Wiley & Sons, Inc.

Mellor, G. L. (1973). "Analytic prediction of the properties of stratified planetary surface layers." J. Atmos. Sci. **30**: 1061 - 1069.

Mellor, G. L. (1998). Users Guide for a Three-Dimnesional, Primitive Equation, Numerical Ocean Model. New Jersey, Princeton University**:** 1 - 41.

Mellor, G. L., and T. Yamada (1974). "A hierarchy of turbulence closure models for planetary boundary layers " J. Atmos. Sci. **31**: 1791 - 1806.

Mellor, G. L., and T. Yamada (1982). "Development of a turbulence closure model for geophysical fluid problems." Reviews of Geophysics and Space Physics **20** (4): 851 - 875.

Münchow, A., and R.W. Garvine (1993). "Dynamical properties of a buoyancy-driven coastal current." J. Geophys. Res. **98**(C11): 20,063 - 20,077.

NASA/GSFC (2003). The Mississippi Satellite: Terra. MODIS Rapid Response System. Mississippi.A2003004.1655.1km.jpg.

Nunes Vaz, R. A., and J.H. Simpson (1994). "Turbulence closure modeling of estuarine stratification." *J. Geophys. Res.* **99**(C8): 16,143 - 16,160.

Pacanowski, R. C., and S.G.H. Philander (1981). "Parameterization of vertical mixing in numerical models of tropical oceans." *J. Phys. Oceanogr.* **11**: 1443 - 1451.

Robinson, A. R. (1966). "An investigation into the wind as the cause of Equatorial Undercurrent." *J. Mar. Res.* **24**: 179 - 204.

Sanders, T. M., and R.W. Garvine (1996). "Frontal observations of the Delaware Coastal Current source region." *Cont. Shelf Res.* **16**(8): 1009 - 1021.

Sanders, T. M., and R.W. Garvine (2001). "Fresh water delivery to the continental shelf and subsequent mixing: An observational study." *J. Geophys. Res.* **106**(C11): 27,087 - 27,101.

Simpson, J. H. (1997). "Physical processes in the ROFI regime." *J. Mar. Syst.* **12**: 3 - 15.

Simpson, J. H., and A.J. Souza (1995). "Semidiurnal switching of stratification in the region of freshwater influence of the Rhine." *J. Geophys. Res.* **100**(C4): 7037 - 7044.

Simpson, J. H., and J. Brown, J. Matthews, and G. Allen (1990). "Tidal Straining, Density Currents, and Stirring in the Control of Estuarine Stratification." *Estuaries* **13**(2): 125 - 132.

Simpson, J. H., E. Williams, L.H. Brasseur, and J.M. Brubaker (2005). "The impact of tial straining on the cycle of turbulence in a partially stratified estuary." *Cont. Shelf Res.* **25**: 51 - 64.

Smagorinsky, J. (1963). "General circulation experiments with the primitive equations, I." *Mon. Wea. Rev.* **91**(3): 99 - 164.

Smolarkiewicz, P. K. (1984). "A Fully Multidimensional Positive Definite Advection Transport Algorithm with Small Implicit Diffusion." *J. Comput. Phys.* **54**: 325 - 362.

Smolarkiewicz, P. K., and T.L. Clark (1986). "The Multidimensional Positive Definite Advection Transport algoritym: Further Development and applications." *J. Comput. Phys.* **67**: 396 - 438.

Soares, I. D., V. Kourafalou, and T.N. Lee (2007). "Circulation on the western South Atlantic continental shelf: 1. Numerical processs studies on buoyancy." *J. Geophys. Res.* **112**(C04002): doi:10.1029/2006JC003618.

Stacey, M. T., J.R. Burau, and S.G. Monismith (2001). "Creation of residual flows in a partially stratified estuary." *J. Geophys. Res.* **106**(C8): 17013 - 17037.

Stacey, M. T., S.G. Monismith, and J.R. Burau (1999). "Observations of Turbulence in a partially stratified estuary." *J. Phys. Oceanogr.* **29**: 1950 - 1970.

Tennekes, H., and J.L. Lumley (1972). A First Course in Turbulence. Cambridge, The MIT Press.

Tilburg, C. E. (2003). "Across-shelf transport on a continental shelf: Do across-shelf winds matter?" *J. Phys. Oceanogr.* **33**: 2675 - 2688.

Tilburg, C. E., R.W. Houghton, and R.W. Garvine (2007). "Mixing of a dye tracer in the Delaware plume: Comparison of observations and simulations." *J. Geophys. Res.* **112**(C12004): doi:10.1029/2006JC003928.

Tilburg, C. E., L.T. Houser, C.N. Steppe, R.W. Garvine, and C.E. Epifanio (2006). "Effects of coastal transport on larval patches: Models and observations." *Estua., Coast., and Shelf Sci.* **67**: 145-160.

Umlauf, L., and H. Burchard (2005). "Second-order turbulence closure models for geophysical boundary layers. A review of recent work." *Cont. Shelf Res.* **25**: 795 - 827.

Whitehead, J. A., and D.C. Chapman (1986). "Laboratory observations of a gravity current on a sloping bottom: the generation of shelf waves." *J. Fluid Mech.* **172**(373 - 399).

Whitney, M. M. (2003). Simulating the Delaware Coastal Current. University of Delaware. *PhD thesis:* 284.

Whitney, M. M., and R.W. Garvine (2005). "Wind influence on a coastal buoyant outflow." *J. Geophys. Res.* **110**(C03014): doi:10.1029/2003JC002261.

Whitney, M. M., and R.W. Garvine (2006). "Simulating the Delaware Bay buoyant outflow: Comparison with observations." *J. Phys. Oceanogr.* **36**: 3 - 21.

Wijesekera, H. W. (2007). *Personal Communication.*

Wijesekera, H. W., J.S. Allen, and P.A. Newberger (2003). "Modeling study of turbulent mixing over the continental shelf: Comparison of turbulent closure schemes." *J. Geophys. Res.* **108(**C3 3103): doi:10.1029/2001JC001234.

Wright, L. D., and J.M. Coleman (1971). "Effluent Expansion and Interfacial Mixing in the Presence of a Salt Wedge, Mississippi River Delta." *J. Geophys. Res.* **76**(36): 8649 - 8661.

Yankovsky, A. E. (2000). "The cyclonic turning and propagation of buoyant coastal discharge along the shelf." *J. Mar. Res.* **58**: 585 - 607.

Yankovsky, A. E., and D.C. Chapman (1997). "A simple theory for the fate of buoyant coastal discharges." *J. Phys. Oceanogr.* **27**: 1386 - 1401.

Yankovsky, A. E., B.M. Hickey, and A.K. Münchow (2001). "Impact of variable inflow on the dynamics of a coastal buoyant plume." *J. Geophys. Res.* **106**(C9): 19,809 - 19,824.

APPENDIX A

MELLOR-YAMADA LEVEL 2.5

Mellor-Yamada Level 2.5 is a second moment method utilizing statistical methods to model turbulence (Mellor and Yamada 1982, Galperin 1988). This scheme is originally derived from the Navier-Stokes equation, (2.7) to (2.9), and after several assumptions, the Mellor-Yamada Level 4 closure scheme is formed. With each descending Mellor-Yamada Level, different assumptions are made for the scaling of the terms, and terms with a specified order of magnitude of anisotropy, or directional dependence, are neglected. The significance of this is that turbulence by nature, has anisotropic features, where all three dimensional directions change characteristics.

This section will follow through, in more detail, the derivations and assumptions leading to the creation of the Mellor-Yamada Level 2.5 closure scheme used in ECOM3d, based on Mellor and Yamada 1974 and 1982. The scheme is originally derived from (2.7) to (2.9) to form the foundation of the Mellor-Yamada scheme, the three equations below,

$$\frac{\partial \overline{u_i u_j}}{\partial t} + U_k \frac{\partial \overline{u_i u_j}}{\partial x_k} + \overline{u_j u_k}\frac{\partial U_i}{\partial x_k} + \overline{u_i u_k}\frac{\partial U_j}{\partial x_k} + \frac{\partial \overline{u_i u_j u_k}}{\partial x_k} + f_k(\varepsilon_{jkl}\overline{u_l u_i} + \varepsilon_{ikl}\overline{u_l u_j})$$
$$= -\frac{1}{\rho_o}\frac{\partial \overline{p u_j}}{\partial x_i} - \frac{1}{\rho_o}\frac{\partial \overline{p u_i}}{\partial x_j} + \overline{\frac{p}{\rho_o}\frac{\partial u_j}{\partial x_i}} + \overline{\frac{p}{\rho_o}\frac{\partial u_i}{\partial x_j}} - \frac{g_i}{\rho_o}\overline{u_j \rho'} - \frac{g_j}{\rho_o}\overline{u_i \rho'} + \nu\frac{\partial}{\partial x_k}\left(\frac{\partial \overline{u_i u_j}}{\partial x_k}\right) - 2\nu\overline{\frac{\partial u_i}{\partial x_k}\frac{\partial u_j}{\partial x_k}} \tag{A.1}$$

$$\frac{\partial \overline{u_i s}}{\partial t} + U_k \frac{\partial \overline{u_i s}}{\partial x_k} + \overline{u_k s}\frac{\partial U_i}{\partial x_k} + \overline{u_i u_k}\frac{\partial S}{\partial x_k} + \frac{\partial \overline{u_i u_k s}}{\partial x_k} + \varepsilon_{ikl} f_k \overline{u_l s}$$
$$= \frac{1}{\rho_o}\frac{\partial \overline{ps}}{\partial x_i} + \overline{\frac{p}{\rho_o}\frac{\partial s}{\partial x_i}} - \frac{g_i}{\rho_o}\overline{s\rho'} + \gamma\frac{\partial}{\partial x_k}\left(\overline{u_i\frac{\partial s}{\partial x_k}}\right) - \gamma\overline{\frac{\partial u_i}{\partial x_k}\frac{\partial s}{\partial x_k}} + \nu\frac{\partial}{\partial x_k}\left(\overline{s\frac{\partial u_i}{\partial x_k}}\right) - \nu\overline{\frac{\partial u_i}{\partial x_k}\frac{\partial s}{\partial x_k}} \tag{A.2}$$

$$\frac{\partial \overline{s^2}}{\partial t} + U_k \frac{\partial \overline{s^2}}{\partial x_k} + 2\overline{u_k s}\frac{\partial S}{\partial x_k} + \frac{\partial \overline{u_k s^2}}{\partial t} = \gamma \frac{\partial}{\partial x_k}\left(\frac{\partial \overline{s^2}}{\partial x_k}\right) - 2\gamma \overline{\frac{\partial s}{\partial x_k}\frac{\partial s}{\partial x_k}} \tag{A.3}$$

where $\rho' = (\partial \rho / \partial S) * s$ (based on Mellor and Yamada 1974). These three equations, (A.1) to (A.3), are then subjected to a number of assumptions.

One assumption is the Rotta hypothesis, a method to approximate the process in which energy is redistributed among various energy components to define 'energy distribution terms' which are assumed to be a function of some Reynolds stress and some mean shear (Mellor and Herring 1973). The approximations for the pressure terms are expressed as,

$$\overline{\frac{p}{\rho_0}\left(\frac{\partial u_i}{\partial x_j} + \frac{\partial u_j}{\partial x_i}\right)} = -\frac{q}{3l_1}\left(\overline{u_i u_j} - \frac{\delta_{ij}}{3}q^2\right) + C_1 q^2\left(\frac{\partial U_i}{\partial x_j} + \frac{\partial U_j}{\partial x_i}\right) \tag{A.4}$$

$$\overline{\frac{p}{\rho_0}\frac{\partial s}{\partial x_i}} = -\frac{q}{3l_2}\overline{u_i s} \tag{A.5}$$

where p is the pressure, q^2 is the turbulent kinetic energy where $\frac{1}{2}q^2 = \frac{1}{2}\overline{u_k^{\,2}}$, δ_{ij} is the Kronecker symbol, C_1 is a constant, and l_1 and l_2 are length scales (Mellor and Yamada 1982).

The pressure diffusion terms are assumed to be small and are equal to,

$$\overline{pu_i} = \overline{ps} = 0 \tag{A.6}$$

(Mellor 1973).

Kolmogorov's hypothesis of local isotropy is used to close the dissipation for the small scales, as turbulence is dissipated into heat. This hypothesis is based on the fact that if the Reynolds number is large, then the dissipation can be assumed to be independent of viscosity, and so, one of the viscosity or diffusivity terms disappear on the right hand side of (A.1) and (A.3) (Mellor and Herring 1973). The resulting dissipation terms can then be approximated by,

$$2\nu\overline{\frac{\partial u_i}{\partial x_k}\frac{\partial u_j}{\partial x_k}} = \frac{2}{3}\frac{q^3}{\Lambda_1}\delta_{ij} \tag{A.7}$$

$$2\gamma\overline{\frac{\partial s}{\partial x_k}\frac{\partial s}{\partial x_k}} = 2\frac{q}{\Lambda_2}\overline{s^2} \tag{A.8}$$

where Λ_1 and Λ_2 are length scales (Mellor and Yamada 1982). Mellor (1973) also assumes the following, for (A.2),

$$(\gamma+\nu)\overline{\frac{\partial u_i}{\partial x_k}\frac{\partial s}{\partial x_k}} = 0 \tag{A.9}$$

One of the major assumptions in the Mellor-Yamada closure schemes is that all length scales are set to be proportional for simplicity, shown below as,

$$(l_1,\Lambda_1,l_2,\Lambda_2) = (A_1,B_1,A_2,B_2)l \tag{A.10}$$

where the variables on the left hand side of the equation are various length scales used in the various Mellor-Yamada equations, and the variables on the right hand side, except for the master length scale, l, are constants measured from data (Mellor and Yamada 1982). This assumption greatly simplifies the need to individually calculate each length scale; however, it then results in the dependence of all length scales on one master length scale and previously measured data. Mellor and Yamada have pointed out this assumption to be the 'weakest link' in their scheme (Mellor and Yamada 1982).

The master length scale, l, is derived by taking the integral of a correlation function and can be calculated from the equation below,

$$\frac{D}{Dt}\left(q^2 l\right) - \frac{\partial}{\partial z}\left[qlS_l\frac{\partial}{\partial z}\left(q^2 l\right)\right] = lE_1\left[P_s + P_b\right] - \frac{q^3}{B_1}\left\{1 + E_2\left(\frac{l}{\kappa L}\right)^2\right\} \tag{A.11}$$

where S_q is a dimensionless number, B_1, S_l, E_1, and E_2 are empirical constants, κ is the von Kármán constant, and L is a measure of the distance away from the bottom (Mellor and Yamada 1982).

Due to the difficulty in determining and measuring triple correlation terms, the turbulent velocity diffusion terms are approximated accordingly,

$$\overline{u_i u_j u_k} = \frac{3}{5} lqS_q \left(\frac{\partial \overline{u_i u_j}}{\partial x_k} + \frac{\partial \overline{u_i u_k}}{\partial x_j} + \frac{\partial \overline{u_j u_k}}{\partial x_i} \right) \tag{A.12}$$

$$\overline{u_i u_k s} = -lqS_{us} \left(\frac{\partial \overline{u_k s}}{\partial x_i} + \frac{\partial \overline{u_i s}}{\partial x_k} \right) \tag{A.13}$$

$$\overline{u_k s^2} = -lqS_s \frac{\partial \overline{s^2}}{\partial x_k} \tag{A.14}$$

S_q, S_{us}, and S_s are dimensionless numbers that are identical values representing different absolute constants or unchanging function parameters and s is the fluctuating salinity. The formation and reasoning behind these formulas have been discussed in Mellor and Herring (1973) and Mellor (1973). Mellor (1973) state that these diffusional terms are not ‘overly important’ terms in their scheme, so these approximations hold very well for its level of importance in the scheme.

The above assumptions are applied to (A.1) to (A.3) to create the three equations below that form the Mellor-Yamada Level 4 closure scheme (based on Mellor and Yamada 1982):

$$\begin{aligned} &\frac{D\overline{u_i u_j}}{Dt} - \frac{\partial}{\partial x_k}\left[\frac{3}{5} lqS_q \left(\frac{\partial \overline{u_i u_j}}{\partial x_k} + \frac{\partial \overline{u_i u_k}}{\partial x_j} + \frac{\partial \overline{u_j u_k}}{\partial x_i} \right) \right] \\ &= -\frac{q}{3l_1}\left(\overline{u_i u_j} - \frac{\delta_{ij}}{3} q^2 \right) + C_1 q^2 \left(\frac{\partial U_i}{\partial x_j} + \frac{\partial U_j}{\partial x_i} \right) - \frac{2}{3}\frac{q^3}{\Lambda_1}\delta_{ij} \\ &- \overline{u_j u_k}\frac{\partial U_i}{\partial x_k} - \overline{u_i u_k}\frac{\partial U_j}{\partial x_k} - \frac{g_i}{\rho_o}\overline{u_j \rho'} - \frac{g_j}{\rho_o}\overline{u_i \rho'} - f_k(\varepsilon_{jkl}\overline{u_l u_i} + \varepsilon_{ikl}\overline{u_l u_j}) \end{aligned} \tag{A.15}$$

$$\frac{D\overline{u_i s}}{Dt} - \frac{\partial}{\partial x_k}\left[lqS_{us}\left(\frac{\partial \overline{u_k s}}{\partial x_i} + \frac{\partial \overline{u_i s}}{\partial x_k}\right)\right] = -\overline{u_k s}\frac{\partial U_i}{\partial x_k} - \overline{u_i u_k}\frac{\partial S}{\partial x_k} - \frac{g_i}{\rho_o}\overline{s\rho'} - \frac{q}{3l_2}\overline{u_i s} - \varepsilon_{ikl} f_k \overline{u_l s} \tag{A.16}$$

$$\frac{D\overline{s^2}}{Dt} - \frac{\partial}{\partial x_k}\left[lqS_s \frac{\partial \overline{s^2}}{\partial x_k}\right] = -2\overline{u_k s}\frac{\partial S}{\partial x_k} - 2\frac{q}{\Lambda_2}\overline{s^2} \tag{A.17}$$

where $D()/Dt = U_k \partial()/\partial x_k + \partial()/\partial t$.

From Mellor-Yamada Level 4, (A.15) is broken into its isotropic and anisotropic parts. The isotropic equation is created by contracting (A.15) to create a turbulent transport equation, where $i = j$. The anisotropic equation is conceived from the difference of (A.15), multiplied by $\delta_{ij}/3$, and the turbulent transport equation. The four equations, the turbulent transport or the isotropic (A.15), the anisotropic (A.15), (A.16), and (A.17), are then subjected scaling. Mellor and Yamada (1982) assume, during all scaling, that,

$$\begin{aligned} \overline{u_i u_j} &= \left(\frac{\delta_{ij}}{3} + a_{ij}\right)q^2 \\ a_{ii} &= 0 \\ \overline{u_i s} &= b_i q\sqrt{\overline{s^2}} \end{aligned} \tag{A.18}$$

whereas the *a* and *b* variables represent the level of anisotropy or the departure from isotropy (Mellor and Yamada 1974). To create the Mellor-Yamada Level 3 equations, Mellor and Yamada continue to assume that,

$$\frac{Uq^2}{L} = \frac{aq^3}{\Lambda} \tag{A.19}$$

whereas U and L are velocity and length scales, and terms an order of a^2 are eliminated. The Mellor-Yamada Level 3 Equations, with the addition of (A.17), are shown below as,

$$\frac{Dq^2}{Dt} - \frac{\partial}{\partial x_k}\left[lqS_q \frac{\partial q^2}{\partial x_k}\right] = 2(P_s + P_b - \varepsilon) \tag{A.20}$$

$$\overline{u_i u_j} = \frac{\delta_{ij}}{3} q^2 - \frac{3l_1}{q} \left[\begin{array}{l} \overline{u_k u_i} \dfrac{\partial U_j}{\partial x_k} + \overline{u_k u_j} \dfrac{\partial U_i}{\partial x_k} + \dfrac{2}{3} \delta_{ij} P_s - C_1 q^2 \left(\dfrac{\partial U_j}{\partial x_i} + \dfrac{\partial U_i}{\partial x_j} \right) \\ + \dfrac{g_j}{\rho_0} \overline{u_i \rho'} + \dfrac{g_i}{\rho_0} \overline{u_j \rho'} + \dfrac{2}{3} \delta_{ij} P_b + f_k \left(\varepsilon_{jkl} \overline{u_l u_i} + \varepsilon_{ikl} \overline{u_l u_j} \right) \end{array} \right] \quad \text{(A.21)}$$

$$\overline{u_i s} = -\frac{3l_2}{q} \left[\overline{u_i u_k} \frac{\partial S}{\partial x_k} + \overline{s u_k} \frac{\partial U_i}{\partial x_k} + \frac{g_i}{\rho_o} \overline{s \rho'} + f_k \varepsilon_{ikl} \overline{u_l s} \right] \quad \text{(A.22)}$$

where the shear production, P_s, is

$$P_s \equiv -\overline{u_i u_j} \frac{\partial U_i}{\partial x_j} \quad \text{(A.23)}$$

the buoyant production, P_b, is,

$$P_b \equiv -\psi g_i \overline{u_i s} \quad \text{(A.24)}$$

where $\psi = (\partial \rho / \partial S) / \rho_0$ and is the salinity contraction, and the dissipation term, ε, is,

$$\varepsilon \equiv \frac{q^3}{\Lambda_1}. \quad \text{(A.25)}$$

The scheme used in this study is Mellor-Yamada 2.5. This level has characteristics of the Mellor-Yamada Level 2 scheme, however is not entirely the same. Mellor-Yamada Level 2 differs from Mellor-Yamada Level 2.5 in that all advection and diffusion terms are neglected with the assumption,

$$\frac{Uq^2}{L} = \frac{a^2 q^3}{\Lambda} \quad \text{(A.26)}$$

where terms with an order of a^2 are eliminated. Mellor-Yamada Level 2.5 only assumes that the advection and diffusion terms in (A.17) are ignored, and therefore may be rewritten as,

$$2\overline{u_k s} \frac{\partial S}{\partial x_k} = -\frac{2q}{\Lambda_2} \overline{s^2} \quad \text{(A.27)}$$

The other three equations in Mellor-Yamada Level 2.5 remain the same as Mellor-Yamada Level 3, (A.20) to (A.22).

To simplify the calculation of the Mellor-Yamada Level 2.5 equations, two major assumptions are applied to (A.20) to (A.22) to create the Mellor-Yamada Level 2.5 boundary layer approximation equations. First, The Coriolis terms are neglected due to its insignificance in the turbulence terms. Next, the boundary layer approximation is utilized, where changes in the vertical direction are more prominent than changes in the horizontal direction, therefore allowing for all horizontal advection and diffusion terms to disappear from the equations, resulting in the equations below, (note that the remaining equations describing the Mellor-Yamada Level 2.5 scheme are no longer in tensor notation due to the elimination and simplification of terms as described)

$$\frac{D}{Dt}\left(\frac{q^2}{2}\right) - \frac{\partial}{\partial z}\left[lqS_q \frac{\partial}{\partial z}\left(\frac{q^2}{2}\right)\right] = P_s + P_b - \varepsilon \tag{A.28}$$

$$\overline{u^2} = \frac{q^2}{3} + \frac{l_1}{q}\left[-4\overline{wu}\frac{\partial U}{\partial z} + 2\overline{wv}\frac{\partial V}{\partial z} - 2P_B\right] \tag{A.29}$$

$$\overline{v^2} = \frac{q^2}{3} + \frac{l_1}{q}\left[2\overline{wu}\frac{\partial U}{\partial z} - 4\overline{wv}\frac{\partial V}{\partial z} - 2P_B\right] \tag{A.30}$$

$$\overline{w^2} = \frac{q^2}{3} + \frac{l_1}{q}\left[2\overline{wu}\frac{\partial U}{\partial z} + 2\overline{wv}\frac{\partial V}{\partial z} + 4P_B\right] \tag{A.31}$$

$$\overline{uv} = \frac{3l_1}{q}\left[-\overline{uw}\frac{\partial V}{\partial z} - \overline{vw}\frac{\partial U}{\partial z}\right] \tag{A.32}$$

$$\overline{wu} = \frac{3l_1}{q}\left[-\left(\overline{w^2} - C_1 q^2\right)\frac{\partial U}{\partial z} + \psi g\overline{us}\right] \tag{A.33}$$

$$\overline{wv} = \frac{3l_1}{q}\left[-\left(\overline{w^2} - C_1 q^2\right)\frac{\partial U}{\partial z} + \psi g\overline{vs}\right] \tag{A.34}$$

$$\overline{us} = \frac{3l_2}{q}\left[-\overline{uw}\frac{\partial S}{\partial z} - \overline{ws}\frac{\partial U}{\partial z}\right] \tag{A.35}$$

$$\overline{vs} = \frac{3l_2}{q}\left[-\overline{vw}\frac{\partial S}{\partial z} - \overline{ws}\frac{\partial V}{\partial z}\right] \tag{A.36}$$

$$\overline{ws} = \frac{3l_2}{q}\left[-\overline{w^2}\frac{\partial S}{\partial z} + \psi g\overline{s^2}\right] \tag{A.37}$$

where shear production and buoyant production are now defined in only the z-direction as,

$$P_s \equiv -\overline{wu}\frac{\partial U}{\partial z} - \overline{wv}\frac{\partial V}{\partial z} \tag{A.38}$$

$$P_b \equiv -\psi g\overline{ws}. \tag{A.39}$$

At this point, (2.12) may be defined in the scheme. The eddy viscosity and diffusivity coefficients may be calculated with the equations below,

$$\begin{aligned} K_z &= lqS_M \\ K_s &= lqS_H \end{aligned} \tag{A.40}$$

where S_M and S_H are stability functions dependent on Ri, and q can be solved from the turbulent transport equation.